# Interaction ondes-écoulement moyen et impact sur la variabilité de la moyenne atmosphère

Alexis Mariaccia

université PARIS-SACLAY

# Interaction ondes-écoulement moyen et impact sur la variabilité de la moyenne atmosphère

*Waves-medium flow interaction and impact on the variability of the middle atmosphere*

**Thèse de doctorat de l'université Paris-Saclay**

École doctorale n° 129, sciences de l'environnement d'Île-de-France (SEIF)
Spécialité de doctorat : Géosciences
Graduate School : Géosciences, climat, environnement et planètes.
Référent : Université de Versailles Saint-Quentin-en-Yvelines

Thèse préparée dans l'unité de recherche **LATMOS (Université Paris-Saclay, UVSQ, CNRS)**, sous la direction de **Philippe Keckhut**, Physicien, HDR, UVSQ et le co-encadrement de **Alain Hauchecorne**, Directeur de Recherche Emérite, HDR, CNRS

**Thèse soutenue à Guyancourt, le 4 décembre 2023, par**

**Alexis MARIACCIA**

## Composition du jury

### Membres du jury avec voix délibérative

| | |
|---|---|
| **Hélène BROGNIEZ**<br>Professeure des universités à l'UVSQ, HDR, LATMOS | Présidente |
| **Nathalie HURET**<br>Professeure des universités à l'Université Clermont Auvergne, HDR, OPGC | Rapportrice et Examinatrice |
| **Christine LAC**<br>Ingénieur Général des Ponts, des Eaux et des Forêts, HDR, CNRM | Rapportrice et Examinatrice |
| **Elisabeth BLANC**<br>Directrice de recherche, HDR, CEA-DAM DASE | Examinatrice |
| **Riwal PLOUGONVEN**<br>Professeur à l'École Polytechnique, HDR, LMD | Examinateur |

THESE DE DOCTORAT
NNT : 2023UPASJ025

université PARIS-SACLAY | ÉCOLE DOCTORALE Sciences de l'Environnement d'Île-de-France (SEIF)

**Titre :** Interaction ondes-écoulement moyen et impact sur la variabilité de la moyenne atmosphère

**Mots clés :** Moyenne atmosphère, Variabilité, Échauffement stratosphérique soudain, Inversion de température mésosphérique, Température, Vent

**Résumé :** La moyenne atmosphère s'étend de 10 à 90 km et englobe à la fois la stratosphère (10 à 50 km) et la mésosphère (50 à 90 km). L'équilibre présent dans la moyenne atmosphère est le résultat de la propagation verticale d'ondes atmosphériques de petites et grandes échelles redistribuant le moment angulaire à travers l'atmosphère. Ces ondes perturbent notablement le flux moyen lorsqu'elles se brisent, déposant ainsi leur quantité de mouvement et leur énergie, ce qui impacte la circulation générale. De plus, cette interaction onde-écoulement moyen est responsable de l'existence de phénomènes régissant la variabilité observée dans la moyenne atmosphère. Notamment, les deux plus marquants sont les échauffements stratosphériques soudains (ESSs) et les inversions de température mésosphériques (ITMs). Plus spécifiquement, les ESSs se manifestent en hiver par une augmentation de la température de la calotte polaire (40 à 60 K) et un affaiblissement du vortex polaire pouvant même inverser les vents d'ouest pour les cas les plus extrêmes. Un vortex polaire perturbé peut ensuite influencer la météo troposphérique au cours des mois suivants en générant, par exemple, des vagues de froid intenses. Les ITMs représentent une augmentation inattendue de la température (10 à 50 K) se produisant dans la mésosphère pendant plusieurs jours et s'étendant sur des milliers de kilomètres. De plus, les ITMs peuvent poser des problèmes importants pour la rentrée en toute sécurité des fusées, des navettes spatiales ou des missiles dans l'atmosphère suscitant davantage d'intérêt pour cet événement. Ainsi, pendant de nombreuses années, ces deux phénomènes ont été étudiés par la communauté scientifique cherchant à comprendre leur mécanisme d'apparition et leurs effets sur l'atmosphère. L'émergence de la technologie LiDAR et l'amélioration des produits de réanalyse archivant le climat passé ont rendu leur étude plus accessible.

Dans cette thèse, l'objectif est d'apporter des avancées dans la compréhension et la description des phénomènes ESS et ITM grâce à de nouvelles observations LiDAR acquises à l'Observatoire de Haute-Provence (44°N, 6°E) et à la dernière génération de produit de réanalyse, ERA5, couvrant la période de 1940 à aujourd'hui. Pour commencer notre étude de ces phénomènes à travers les données ERA5, nous avons initialement évalué la capacité d'ERA5 à reproduire la variabilité dans la moyenne atmosphère en la comparant aux observations LiDAR. Nous avons constaté que la variabilité stratosphérique observée pendant l'hiver, y compris celle générée par les ESSs, est reproduite avec précision dans la réanalyse ERA5. Cependant, le modèle ne parvient pas à reproduire cette précision à la fois dans la stratosphère d'été et dans la mésosphère, quelle que soit la saison, en raison soit de l'absence ou de la simulation imprécise des événements ITMs. De plus, nous présentons de nouvelles observations de la température et du vent co-localisées pendant les événements ITMs et évaluons comment ERA5 simule le vent en présence de ITMs. Une décélération du vent se produit dans la même gamme d'altitude que l'augmentation de la température, ce qui confirme le rôle des ondes de gravité dans l'apparition de ce phénomène. À la lumière de ces résultats, la réanalyse ERA5 contenue dans la stratosphère et la troposphère a été utilisée exclusivement pour étudier, premièrement, les principaux déroulés de la stratosphère d'hiver modulés par le timing des ESSs, et ensuite, leurs liens verticaux tout au long des mois d'hiver. De manière intéressante, nous avons découvert qu'en hiver dans l'hémisphère nord, la stratosphère suit quatre scénarios distincts qui présentent des couplages stratosphère-troposphère différents. Notamment, nous avons identifié des précurseurs de surface notables associés à ces scénarios qui pourraient potentiellement avoir des applications pour la prévision saisonnière.

université PARIS-SACLAY | ÉCOLE DOCTORALE Sciences de l'Environnement d'Île-de-France (SEIF)

**Title :** Waves-medium flow interaction and impact on the variability of the middle atmosphere
**Keywords :** Middle atmosphere, Variability, Sudden stratospheric warming, Mesospheric inversion layer, Temperature, Wind

**Abstract :** The middle atmosphere spans from 10 to 90 km and comprises the stratosphere (10 to 50 km) and the mesosphere (50 to 90 km). The equilibrium in the middle atmosphere results from the vertical propagation of small- and large-scale atmospheric waves redistributing the angular momentum across the atmosphere. These waves notably perturb the mean flow when they break, depositing their momentum and energy impacting the general circulation. Moreover, this wave-mean flow interaction is responsible for phenomena governing the observed variability in the middle atmosphere. Notably, the two most dramatic are the sudden stratospheric warmings (SSWs) and the mesospheric inversion layers (MILs). Specifically, SSWs manifest in winter by increasing the polar cap temperature (40 to 60 K) and weakening the polar vortex, which can reverse the westerly winds for the most extreme cases. A perturbed polar vortex can then impact the tropospheric weather in the following months by generating, for instance, severe cold air outbreaks. MILs represent an unexpected increase in temperature (10 to 50 K) occurring in the mesosphere, lasting several days and spanning thousands of kilometers. Moreover, MILs can represent significant issues for the safe reentry of rockets, space shuttles, or missiles into the atmosphere, sparking more interest in this phenomenon. For many years, the scientific community has investigated these two phenomena to understand their mechanism of occurrence and their effects on the atmosphere. The emergence of LiDAR technology and improved reanalysis products archiving the past climate has made their study more accessible.

In this thesis, the objective is to make advancements in the understanding and the description of SSW and MIL phenomena with new LiDAR observations acquired at the Observatoire of Haute-Provence (44°N, 6°E) and the last generation of reanalysis product, ERA5, lasting from 1940 until the present. To commence our study of these phenomena through ERA5 data, we initially evaluated the capability of ERA5 in replicating the variability in the middle atmosphere by comparing it with LiDAR observations. We found that the observed stratospheric variability during wintertime, including the one generated by SSWs, is accurately reproduced in ERA5 reanalysis. However, the model cannot replicate this accuracy in the summer stratosphere and mesosphere, regardless the season, due to either the absence or imprecise simulation of MIL events. Additionally, we present new co-located temperature-wind observations during MIL events and assess how ERA5 simulates wind in the presence of MIL. A deceleration in wind occurs in the same altitude range as the temperature enhancement, supporting the role of gravity waves in the apparition of this phenomenon. In light of these findings, the ERA5 reanalysis in the stratosphere and the troposphere was solely used to study the main winter stratosphere unfoldings modulated by the timing of SSWs and their vertical links throughout winter months. Interestingly, we discovered that during wintertime in the northern hemisphere, the stratosphere follows four separate scenarios with distinct stratosphere-troposphere couplings. We found notable surface precursors associated with these scenarios that could potentially have applications for seasonal prediction.

# Remerciements

La thèse, c'est un peu trouver son chemin de Damas tous les jours. Dans mon cas, je ne pense pas avoir encore franchi le détroit du Bosphore mais une route semble se dessiner. Heureusement, lors de cette aventure de trois ans, j'ai eu la chance de bénéficier d'un entourage excellent, un entourage que je remercie chaleureusement. Je pense tout d'abord à mon directeur de thèse, Philippe Keckhut, avec qui j'ai eu le bonheur de travailler. Je le remercie pour son encadrement adapté, la confiance qu'il m'a accordée et qui m'a permis de développer mon autonomie ainsi que mon esprit critique. Ces nouvelles compétences, j'en suis sûr, me seront grandement utiles à l'avenir. Nos passionnants et enrichissants échanges vont me manquer. Je remercie également mon autre encadrant, Alain Hauchecorne, pour son savoir scientifique vertigineux dont j'ai eu la chance d'avoir accès au cours de cette thèse.

Une thèse, c'est aussi un laboratoire, le LATMOS pour moi, où j'ai pu faire la rencontre de personnes formidables que je n'oublierai pas. Je pense notamment à Mathieu Ratynski, mon collègue devenu ami, avec qui j'ai eu la chance de partager ces trois années au cours desquelles une réelle complicité s'est créée. Merci également à mes autres collègues du laboratoire, notamment Valentin Moulay et Ophélie McIntosh, avec qui j'ai pu partager des moments de détente agréables au cours de nos repas quotidiens, et, de temps en temps, en échangeant quelques balles de ping pong.

D'autre part, comme la thèse est avant tout un travail assez solitaire, l'ambiance en dehors du labo a aussi joué un rôle déterminant dans la bonne réalisation de celle-ci. Pour son immense contribution, je remercie tout particulièrement François-Xavier Chamoy (aka "FX"), en tant que colocataire et ami désormais, qui m'aura transmis sa joie, sa bonne humeur et son humour quotidiennement. De même, je remercie mes autres co-locatrices, notamment Flore de Langle, Pauline de Villèle et Camille Bouyé, pour leur gaieté rayonnante. Merci à vous la coloc "Alasseur".

Ces trois années resteront aussi dans ma mémoire pour ces conférences inoubliables où j'ai pu rencontrer des personnalités scientifiques inspirantes à Boulder, à Vienne et à Berlin.

Enfin, pour leur soutien constant depuis les premiers jours, je souhaite remercier les membres de ma famille. Pour sa présence, son intelligence, sa franchise, sa bienveillance, je remercie Hadrien dont je mesure aujourd'hui la chance de l'avoir comme frère. Aussi, je remercie particulièrement mes parents d'être toujours à mes côtés et de m'avoir rendu ambitieux et persévérant. J'aimerais remercier également ma grand-mère Geneviève, à qui je dédie à titre posthume cette thèse, pour son intelligence, sa gentillesse et sa générosité hors du commun qui continuent de m'inspirer aujourd'hui. Merci à eux et aux autres membres de ma famille qui ont été et sont encore présents pour moi.

Pour finir, comme je me souviens avoir prononcé ces mots "Non je ne vais pas faire une thèse ! Je ne pense pas avoir un profil de chercheur !" en début de Master, je ne me risquerai plus à une autre prédiction, néanmoins, je me sens confiant pour une nouvelle aventure scientifique. Merci.

*In its efforts to learn as much as possible about nature, modern physics has found that certain things can never be "known" with certainty. Much of our knowledge must always remain uncertain. The most we can know is in terms of probabilities.*

Richard P. Feynman

# Table des matières

# Introduction

La moyenne atmosphère (10 à 90 km) est une région de l'atmosphère terrestre comprenant la stratosphère (10 à 50 km) et la mésosphère (50 à 90 km). Longtemps restée inexplorée par impossibilité de procéder à des observations in-situ, les connaissances sur la moyenne atmosphère ont énormément avancé depuis la seconde moitié du 20ème siècle avec l'arrivée des nouvelles technologies capables de mesurer précisément cette partie de l'atmosphère (Shepherd, 2000). Les observations fusées ont notamment permis la découverte et une description précise des phénomènes s'y produisant et de comprendre leurs influences sur la circulation atmosphérique générale.

Ainsi, la moyenne atmosphère est aujourd'hui reconnue indispensable pour bien comprendre comment fonctionne le climat terrestre. Sa structure thermique et dynamique est désormais établie pour diverger nettement de son équilibre radiatif et pour fluctuer en fonctions des saisons (Andrews et al., 1987). Particulièrement dans la mésosphère, où, de façon inattendue, les températures de l'hémisphère d'été sont plus froides que celles de l'hémisphère d'hiver (Kellogg and Schilling, 1951). Cette situation paradoxale résulte de la circulation verticale induite par la circulation méridienne avec subsidence et réchauffement adiabatique au pôle hiver et ascendance et refroidissement adiabatique au pôle été. Cet équilibre observé est généré par la propagation d'ondes atmosphériques de petites et grandes échelles interagissant avec l'écoulement moyen et redistribuant le moment angulaire à travers l'atmosphère. La circulation méridienne qui se met en place permet le transport des masses d'air de l'hémisphère d'été vers l'hémisphère d'hiver (Plumb, 2002). Cette circulation a pour effet notable de transporter l'ozone, produit principalement à l'équateur, vers le pôle de l'hémisphère d'hiver où réside le jet stratosphérique de la nuit polaire, appelé vortex polaire (Butler et al., 2015). En effet, chaque hiver un vortex polaire

stratosphérique se forme au-dessus du pôle de 15 à 50 km et se caractérise par des vents forts soufflant d'Ouest en Est (Waugh et al., 2017). En moyenne, les vents sont d'Est dans l'hémisphère d'été tandis qu'ils sont d'Ouest dans l'hémisphère d'hiver. Ce champ de vent opère un filtrage des ondes dans la stratosphère et la mésosphère, particulièrement effectif dans l'hémisphère d'été où la variabilité est réduite (Lindzen, 1981).

Les observations au sein de la moyenne atmosphère ont révélé l'existence de phénomènes importants causés par différents processus physiques et chimiques perturbant la dynamique atmosphérique et le climat. Parmi ces phénomènes, les plus impactant sont les échauffements stratosphériques soudains (ESSs) appelés SSW (en anglais pour : sudden stratospheric warming) (Scherhag, 1952) et les inversions de température mésosphériques (ITMs) appelés MIL (en anglais pour : mesospheric inversion layer) (Schmidlin, 1976) qui gouvernent la variabilité observée dans la stratosphère et la mésosphère aux moyennes et hautes latitudes. La particularité de ces deux phénomènes est de générer une forte élévation de température qui altère la structure de la moyenne atmosphère en impactant la stabilité et en transférant de l'énergie au milieu (Meriwether and Gerrard, 2004).

En effet, les ESSs, qui se produisent presque uniquement dans l'hémisphère nord, peuvent augmenter la température de la stratosphère d'hiver jusqu'à 40-60 K sur quelques jours et ralentir le vortex polaire jusqu'à parfois inverser le jet de la nuit polaire (Butler et al., 2017). Selon le modèle de Matsuno (1971), c'est l'interaction des ondes planétaires, transportant du moment vers l'Ouest, avec la circulation moyenne, allant vers l'Est, qui est responsable de cette élévation de température de la calotte polaire et de l'affaiblissement du vortex polaire. A la suite d'un échauffement, le vortex polaire peut être déplacé en dehors du pôle ou scindé en deux tourbillons, ayant également pour effet de répartir l'ozone contenu dans le vortex (Charlton and Polvani, 2007). Ensuite, le vortex polaire perturbé peut impacter le temps dans la troposphère de différentes façons, en décalant les chemins des dépressions, leurs fréquences et leur intensité et provoquer des tempêtes de

froid à travers l'hémisphère (Afargan-Gerstman and Domeisen, 2020; Baldwin and Dunkerton, 2001; Baldwin et al., 2003; Charlton et al., 2004). Enfin, des observations ont montré que des refroidissements mésosphériques de l'ordre de 30-40 K se produisent lors de ESSs, confirmant l'influence de la stratosphère sur la température de la mésosphère. Ces refroidissements observés dans la mésosphère instaurent ensuite des conditions favorables à l'apparition d'ITM (Keckhut et al., 2012).

Les ITMs, qui se produisent principalement en hiver aux moyennes latitudes, représentent une couche de température entre 10 et 50 K au sein de la mésosphère couvrant des milliers de kilomètres pendant plusieurs jours (Meriwether and Gardner, 2000). Ainsi, l'étude des ITMs est devenue indispensable afin de bien comprendre la circulation globale de la moyenne atmosphère. De plus, l'intérêt pour ce phénomène s'est renforcé depuis que les ITMs représentent un enjeu substantiel pour les applications aéronautiques (fusées, navettes spatiales et missiles) et leur sécurité lors de leur ré-entrée dans l'atmosphère (Wing et al., 2020). Bien que le mécanisme d'apparition reste débattu, le déferlement des ondes de gravité et planétaires est pensé jouer un rôle significatif dans ce phénomène (France et al., 2015; Hauchecorne et al., 1987; Salby et al., 2002; Sassi et al., 2002). Néanmoins des investigations supplémentaires sont nécessaires pour vérifier ce mécanisme, notamment l'accès aux observations simultanées vent-température pendant un événement ITM afin d'étudier la transmission des ondes de gravité (Meriwether and Gerrard, 2004).

Ainsi, la propagation et la dissipation d'ondes atmosphériques transférant leur énergie et leur quantité de mouvement au milieu apparaît comme un mécanisme d'apparition prépondérant pour ces deux phénomènes. Bien paramétrer cette interaction onde-écoulement moyen représente par conséquent un défi majeur pour les prévisionnistes en particulier pour les ondes induisant des fluctuations aux fines échelles (McLandress, 1998). L'enjeu est double, car il est aujourd'hui admit qu'une meilleure description de la moyenne atmosphère au sein des modèles météorologiques améliore significativement

leurs prévisions dans les basses couches (Charlton-Perez et al., 2013).

Actuellement, bien que des avancées significatives dans la théorie, les observations et la modélisation de ces phénomènes ont été faites, il subsiste encore des informations manquantes sur les processus physiques responsables de l'apparition des ITMs et de l'impact des ESSs sur le climat troposphérique. A cause de ces lacunes, la plupart des modèles climatiques ne parviennent toujours pas à prédire avec précision l'apparition d'un ESS au sein de la stratosphère dégradant potentiellement la qualité de la prévision dans toutes les couches (Wu and Reichler, 2020).

En conséquence, les ESSs et ITMs sont toujours un actif champ de recherche au sein de la communauté scientifique qui continue de les observer et d'analyser leurs effets. Depuis plusieurs années, de nombreuses classifications des événements des ESSs ont été entreprises afin de déterminer les facteurs conduisant à un impact sur le climat troposphérique (Kodera et al., 2016; Mitchell et al., 2013; Nakagawa and Yamazaki, 2006). Cependant, bien que les échauffements majeurs avec un vortex polaire scindé semblent altérer davantage le temps dans les basses couches (Mitchell et al., 2013), des cas contradictoires existent suggérant que les causes à l'origine de ces effets restent encore mal compris. Néanmoins, la propagation de l'anomalie stratosphérique vers la tropopause semble déterminante dans ce processus (Karpechko et al., 2017).

Avec le temps, l'examen de la moyenne atmosphère a notamment été facilitée, d'une part, via l'essor de la technologie LiDAR (LIght Detection and Ranging) (Hauchecorne and Chanin, 1980) et, d'autre part, par l'amélioration des produits de réanalyses conservant les archives du climat passé (Trenberth et al., 2008).

En effet, l'avantage du LiDAR est de bénéficier d'une grande précision capable de capturer les perturbations de petites et grandes échelles en faisant un instrument de choix pour l'étude de la dynamique de la moyenne atmosphère. Parmi les rares stations d'observation possédant un LiDAR dans le monde, le LiDAR Rayleigh qui opère à l'Observatoire de Haute-Provence (OHP, 44°N, 6°E) depuis 1979 fournit la plus longue série de mesures

de température dans la moyenne atmosphère et sera exploitée dans ce travail (Wing et al., 2018b).

Au fil des années, en plus de s'étendre toujours davantage vers le passé, la description de la moyenne atmosphère dans les produits de réanalyses s'est affinée avec la progression des performances des modèles météorologiques permettant l'étude climatologique de ces phénomènes. Actuellement, la dernière génération de réanalyse ERA5, produite par le CEPMMT (Centre Européen pour les Prévisions Météorologiques à Moyen Terme), s'étend de 1940 à nos jours, et décrit l'état de la moyenne atmosphère jusqu'à environ 80 km, le faisant l'un des produits le plus utilisé pour l'étude de l'atmosphère (Hersbach et al., 2020).

Je me propose ainsi d'apporter de nouvelles avancées sur la compréhension et la description des phénomènes ESSs et ITMs à l'aide de nouvelles observations LiDAR et des nouvelles réanalyses ERA5.

Tout d'abord, dans le premier chapitre, je présenterai la structure générale de la moyenne atmosphère et les principales ondes atmosphériques interagissant avec l'écoulement moyen responsables des échauffements stratosphériques soudains et des inversions de température mésosphériques.

Le chapitre 2 sera dédié à la description des technique et des données utilisées ici pour étudier la variabilité de la moyenne atmosphère. Notamment, via les observations LiDAR acquises à l'OHP et les dernières réanalyses ERA5 produites par le Centre Européen.

Dans le chapitre 3, avant de procéder à l'étude des différents phénomènes au sein de la moyenne atmosphère avec la réanalyse ERA5, une première évaluation de sa variabilité de sa température est effectuée à l'aide de quinze années d'observations LiDAR à l'OHP. Nous verrons que les réanalyses ERA5 de température possèdent une excellente représentation de la variabilité observée dans la stratosphère d'hiver. Cette précision n'est en revanche pas retrouvée dans la mésosphère où la principale cause de variabilité est l'apparition des ITMs.

Ensuite, les premières observations simultanées de l'évolution du vent lors d'inversions mésosphériques seront rapportées dans le chapitre 4. Les profils de vent révèlent qu'une forte décélération du vent se produit dans la même couche où la température augmente confortant le rôle des ondes de gravité dans ce processus.

Le chapitre 5 sera consacré à l'introduction du concept de mémoire stratosphérique et de la connexion entre le milieu et la fin d'hiver. A l'aide d'une nouvelle classification, nous montrerons que le vortex polaire stratosphérique tend à suivre quatre scénarios influencés par le timing des ESSs. Dans le chapitre 6, je me servirai de cette nouvelle classification pour étudier le couplage stratosphère-troposphère au cours de l'hiver afin de déterminer pour chaque scénario les potentiels précurseurs et les réponses troposphériques induites par la stratosphère.

Enfin les conclusions générales ainsi que les perspectives de ce travail seront données.

### Objectifs de la thèse

- Dans un premier temps, l'objectif consistera à évaluer la capacité des réanalyses ERA5 à reproduire la variabilité observée dans la moyenne atmosphère, en s'intéressant tout particulièrement au résultat concernant la période hivernale. Cette évaluation sera menée en comparant les données d'ERA5 aux observations LiDAR recueillies à l'OHP de 2005 à 2020. Il est essentiel d'examiner le biais moyen ainsi que la capacité d'ERA5 à reproduire la variabilité saisonnière, tant en hiver qu'en été, afin de valider la fiabilité et la précision des analyses, y compris le modèle numérique et l'assimilation des observations. Ceci vise à vérifier la capacité du système à reproduire les amplitudes des phénomènes se produisant dans la moyenne atmosphère, en particulier ceux générant les variations les plus marquées, tels que les échauffements stratosphériques et les inversions de température mésosphériques. Cette étude s'avère nécessaire avant d'entreprendre l'analyse de ces phénomènes à l'aide des nouvelles réanalyses.

- Dans un second temps, nous montrerons de nouvelles observations simultanées inédites de vent et température lors de phénomènes d'inversions de température mésosphériques. Cette nouvelle information, notamment sur le profil de vent, est nécessaire afin de mieux comprendre les mécanismes de formations de ces phénomènes. Nous verrons qu'une forte décélération du vent est observée dans la même gamme d'altitude où est observée l'inversion de température. Ainsi, ce nouveau résultat renforce l'idée selon laquelle les ondes de gravité jouent un rôle crucial dans l'apparition de ce phénomène. L'objectif sera aussi de comparer ces observations de vent lors d'inversions mésosphériques avec les réanalyses ERA5 pour évaluer la capacité des analyses à reproduire l'impact de ce phénomène à la fois sur le vent et la température.
- Ensuite, les 70 hivers allant de 1950 à 2020 stockés dans les réanalyses ERA5 seront utilisés afin d'étudier la différence physique entre les échauffements finaux avec des timings différents et la mémoire stratosphérique au cours de l'hiver. Puis, l'objectif sera d'établir une nouvelle classification des hivers basée sur leurs typologies des vents zonaux modulées par le timing des échauffements stratosphériques. L'intérêt de cette nouvelle approche est de comprendre dans quelle mesure les hivers de l'hémisphère nord suivent des évolutions prévisibles au cours du temps. Une investigation complémentaire sera de relier ces scénarios identifiés à des processus dynamiques spécifiques comme les ondes planétaires. Ceci permettra de mieux comprendre comment la dynamique affecte différemment les scénarios.
- Enfin, la classification établie précédemment servira à étudier le couplage stratosphère-troposphère au sein des différents scénarios. Cette étude supplémentaire a pour objectif de comprendre comment la troposphère affecte et est potentiellement affectée par la stratosphère en fonction de tel ou tel scénario. L'intérêt est donc de montrer l'importance du timing des échauffements stratosphériques ou de leur absence dans le déroulé de l'hiver à la fois dans la stratosphère et la troposphère. Une

autre motivation sera d'établir d'éventuels précurseurs dans les mois précédents l'apparition des échauffements ou des hivers sans perturbations. Cette investigation vise entre autre à étudier comment l'évolution de la stratosphère est en partie influencée par les conditions troposphériques du début d'hiver.

# 1 - Structure générale de la Moyenne Atmosphère

## 1.1 . Généralités sur l'atmosphère

L'atmosphère constitue cette fine couche gazeuse, appelé "air', comprise entre la surface terrestre et l'espace. Par convention, l'altitude de la surface est associée au niveau de la mer, tandis que la frontière précise entre l'atmosphère et l'espace reste difficile à définir de manière exacte. L'une des fonctions premières de l'atmosphère est de retenir une partie de l'énergie émise vers l'espace depuis la Terre. En effet, sans atmosphère, la température à la surface de la Terre serait en moyenne de -18°C (Zhong and Haigh, 2013). Ainsi son premier rôle est de générer un effet de serre pour réchauffer les basses couches. Sa présence est donc indispensable pour permettre l'habitabilité sur Terre et la survie de la biosphère terrestre.

L'atmosphère se compose de différentes couches qui se distinguent par leurs propriétés physiques, notamment la variation de température avec l'altitude. Ces couches sont généralement définies comme la troposphère, la stratosphère, la mésosphère, la thermosphère et l'exosphère. Chacune de ces couches joue un rôle spécifique dans les processus atmosphériques et présente des caractéristiques uniques. De plus, comme aucune frontière fermée n'existe entre ces différentes couches, les échanges de masses et d'énergie sont permises afin de maintenir l'équilibre de l'atmosphère.

En tant que milieu en contact avec la surface terrestre, les océans et l'espace, l'atmosphère est le théâtre de nombreux processus physiques, chimiques et biologiques. Ces processus appliquent donc des contraintes à l'air, considéré comme un fluide sur le plan physique, qui sont responsables de la circulation atmosphérique et des différents phénomènes météorologiques.

### 1.1.1 . Composition de l'atmosphère

L'air, composant l'atmosphère, contient différentes espèces chimiques dont les concentrations varient. Les premiers constituants de l'atmosphère sont l'azote et l'oxygène qui représentent ensemble 98.65% de la masse totale de l'atmosphère sèche. Le gaz noble argon en représente 1.28%. Ainsi, l'ensemble des autres espèces présentes dans l'atmosphère, telles que les gaz à effet de serre comme le dioxyde de carbone, le méthane, l'ozone ou encore la vapeur d'eau, représentent moins de 0.1% de la masse totale (Seinfeld and Pandis, 2016). Comme ces principaux constituants ne possèdent pas de sources dans la stratosphère et la mésosphère, leurs concentrations restent quasiment constantes dans l'atmosphère. En revanche, les autres ayant des sources et réservoirs importants connaissent une variabilité temporelle et spatiale importante du fait de la dynamique. En particulier, la vapeur d'eau peut représenter une partie variable de l'air humide dans la troposphère (0 à 3%) suivant les conditions de température et d'humidité. En revanche, dans la stratosphère et la mésosphère elle ne dépasse pas quelques ppm.

A partir de la thermosphère, la hausse de la distance moyenne parcourue par les molécules s'explique par la prise de contrôle du mélange par la diffusion moléculaire sur les mouvements de fluide macroscopique qui gouvernent sous 100 km. La communauté scientifique dénomme l'homosphère cette région de l'atmosphère où le mélange par tourbillons domine, tandis que la région dominée par la diffusion moléculaire est référée comme l'hétérosphère. Ces deux régions sont séparées par l'homopause à environ 110 km où les deux processus sont considérés comme d'égale importance. La principale variabilité de ces constituants est verticale.

### 1.1.2 . Structure statique de l'atmosphère

Comme mentionné précédemment, l'atmosphère est composée de plusieurs couches définies par leurs gradients de températures, positifs ou négatifs (voir Figure 1.1).

- **la troposphère** s'étend de la surface à une altitude variant avec la latitude et la saison, 7 km au pôle et 18 km à l'équateur. Le gradient de température y est négatif,

i.e., la température décroît avec l'altitude à peu près de 6.5 K/km pour atteindre un minimum d'environ -55°C à la tropopause. Ce minimum est causé principalement par l'émission infrarouge de la vapeur d'eau et des nuages. Elle concentre environ 80% de la masse l'atmosphère et 99% de la vapeur d'eau atmosphérique. L'instabilité atmosphérique au sein de la troposphère est à l'origine du mélange vertical des masses d'air, processus connu sous le nom de convection, responsable de la formation des nuages, des précipitations et des phénomènes météorologiques (tempêtes, cyclones, ouragans). D'autre part, la majorité des particules et gaz à effet de serre se trouvent en suspension dans la troposphère polluant l'air et réchauffant la surface et refroidissant les hautes couches. La limite supérieure séparant la troposphère de la stratosphère constitue la tropopause.

- **la stratosphère** se situe entre la tropopause (7 à 18 km) et la stratopause à 50 km. Cette couche est caractérisée par une forte stabilité atmosphérique causée par son gradient de température positif. En effet l'air contenu dans la stratosphère se réchauffe avec l'altitude car l'ozone ($O_3$) absorbe les rayons ultraviolets solaires UV-B et UV-C en partis nocifs pour la vie sur Terre. Ainsi, environ 90% de l'ozone atmosphérique se trouve dans la stratosphère où son pic de concentration se trouve entre 20 et 25 km. L'ozone est principalement produit par photochimie à l'équateur où davantage de rayonnement solaire (photons) parvient et réagit avec les molécules d'oxygène ($O_2$).
- **la mésosphère** s'étend de la stratopause (50 km) à la mésopause (90 km). La température y décroît à nouveau avec l'altitude causée par la diminution de la concentration en ozone. Ainsi, c'est une couche instable thermiquement ce qui favorise les mouvements verticaux d'air. La mésopause, qui marque la limite supérieure de la mésosphère, est la zone la plus froide de l'atmosphère terrestre, avec des températures descendant souvent en dessous de -90°C.
- **la thermosphère** se trouve entre la mésopause (90 km) et la limite extérieure de

l'atmosphère, l'exosphère qui se situe à environ 500 km. Cependant, cette limite dépend fortement de l'activité solaire. Comme pour la stratosphère, elle est caractérisée par un gradient de température positif. L'air y est réchauffé par l'absorption des rayons ultraviolets de très courtes longueurs d'ondes par le dioxygène. La température peut y osciller entre 300°C et 1600°C en fonction de l'activité solaire.

En première approximation on peut considérer une atmosphère statique soumise uniquement aux forces thermodynamiques (pression, densité et température). Comme l'air peut-être assimilé à un gaz parfait, i.e., son énergie interne ne dépend que de la température, on peut donc relier sa pression et sa température par la loi des gaz parfaits :

$$p = \rho R T, \tag{1.1}$$

où R est la constante de gaz pour l'air sec (=287 J.K$^{-1}$.kg$^{-1}$). Cette relation montre entre autre qu'à pression constante, une parcelle d'air plus chaude aura une densité plus faible. Ainsi l'air chaud tend à monter tandis que l'air froid tend à descendre. Dans le cadre d'une atmosphère statique, les forces de pression verticales (poussée d'Archimède) sont contre balancées par la force de gravité. On appelle cet équilibre, l'équilibre hydrostatique qui s'exprime par la relation suivante :

$$\frac{\partial p}{\partial z} = -\rho g \tag{1.2}$$

Cette relation impose donc une diminution de la pression avec l'altitude. La plus part des modèles font l'approximation de l'équilibre hydrostatique pour la conservation du moment vertical (Andrews et al., 1987).

### 1.1.3 . Contrôle de la circulation atmosphérique : Forces et énergie

L'atmosphère n'est pas un système statique mais bien dynamique dont la source d'énergie est le soleil. A cause de l'inclinaison de le Terre et de son cycle saisonnier, davantage de rayonnement solaire et donc d'énergie sont reçus dans les régions tropicales

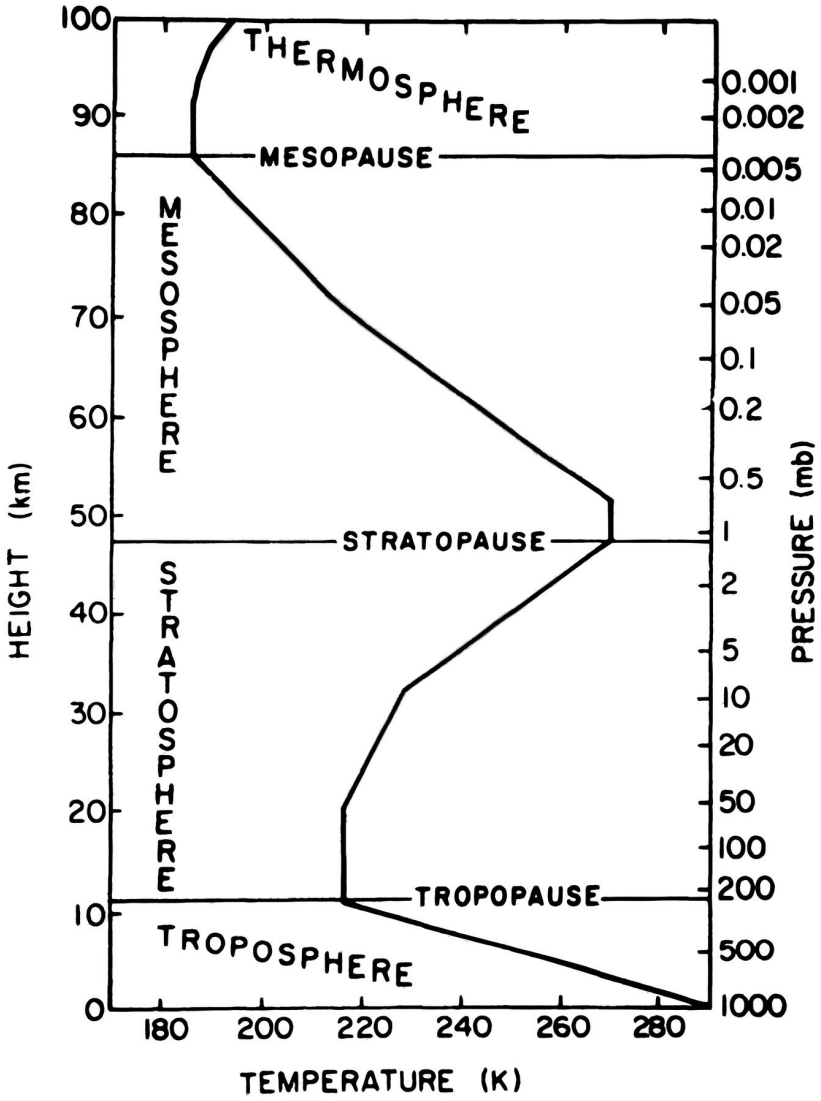


Figure 1.1 – Profil standard de température aux moyennes latitudes d'après US Standard Atmosphere (1976). (Source : Andrews et al. (1987))

alors qu'un déficit est observé dans les régions polaires (Salby, 2012). Ainsi, un transport de masses se met en place afin d'équilibrer et de répartir le surplus d'énergie reçue autour de l'équateur.

Parmi les différentes forces agissant sur les masses d'air, les forces de pression associées au gradient de température entre les régions tropicales et les régions polaires constituent le principal moteur de la circulation troposphérique. Ces forces de pression ont pour principal effet de transporter les masses d'air chaudes de l'équateur, soumises à de forts mouvements convectifs, vers les hautes latitudes où les masses d'air sont plus froides. La zone de transition de ces masses d'air est à l'origine du front polaire aux moyenne latitudes où le gradient de température est le plus élevé.

Cependant, les forces thermodynamiques ne peuvent expliquer à elles seules l'ensemble de la circulation atmosphérique. En effet d'autres forces dites mécaniques sont responsables des mouvements des masses d'air : la force de gravité, la force de Coriolis causée par la rotation de la Terre et les forces de friction induites par les ondes atmosphériques. La force de Coriolis joue notamment un rôle important dans la formation des courants-jets par équilibre géostrophique. Par exemple, l'équilibre des forces de gradient de pression, causée par le gradient thermique, et la force de Coriolis génèrent des courants de vents forts aux moyennes latitudes au niveau de la tropopause, appelés jet stream. Ce jet stream joue ensuite un rôle important dans la formation et le déplacement des systèmes météorologiques à moyenne échelle tels que les dépressions extratropicales. Tout particulièrement, nous verrons que les ondes et marées atmosphériques interagissent avec l'écoulement moyen et jouent un rôle primordial dans la circulation atmosphérique, notamment au sein de la moyenne atmosphère.

### 1.1.4 . Ondes et perturbations

Les ondes atmosphériques sont omniprésentes dans l'atmosphère et interagissent avec l'écoulement moyen en lui apportant de l'énergie et de la quantité de mouvement. Concrètement, une onde se manifeste par les mouvements périodiques (oscillations) de

particules de fluide chacune se déplaçant avec une phase légèrement différente de celle des particules voisines (Nappo, 2012a). Les ondes se propagent, pour la plus part, de la troposphère jusque dans la mésosphère où leurs amplitudes croissent avec la chute de la densité atmosphérique. Bien qu'il est impossible de voir une onde à l'oeil nu nous pouvons voir leurs effets sur l'atmosphère.

Ainsi, selon la théorie linéaire introduite par Hines (1960), les ondes sont "cachées" dans les perturbations des écoulements moyens. Mathématiquement, cela revient à décrire l'écoulement comme une somme d'un flux moyen et d'une perturbation. Par exemple, si $\bar{u}$ représente le vent moyenné zonalement sur une longitude et $u'$ la déviation à cette moyenne, alors le champ de vent complet s'écrit :

$$u(x,t) = \bar{u} + u'(x,t), \tag{1.3}$$

où $u'$ est de la forme :

$$u'(x,t) = A_x \sin(kx - \omega t + \phi), \tag{1.4}$$

avec $k$ le vecteur d'onde horizontal, $\omega$ la fréquence de l'onde et $\phi$ une phase. En revanche, ce modèle ne prend pas en compte les interactions onde-onde qui existent dans l'atmosphère mais qui peuvent être négligées pour des effets dynamiques de premier ordre (Nappo, 2012b). Plusieurs types d'ondes existent avec des échelles spatiales et temporelles différentes qui peuvent être catégorisées en fonction de leurs mécanismes de rappel.

- **Les ondes de gravité** ou ondes de flottabilité sont générées par la fluctuation d'une parcelle d'air autour d'une altitude d'équilibre dans un fluide stable stratifié soumis à la gravité. Leurs sources sont principalement les systèmes convectifs, l'orographie ou encore les fronts atmosphériques. Les ondes de gravité se propagent horizontalement et verticalement jusque dans la mésosphère où elles déferlent lorsque leur vitesse de phase est proche de la vitesse du vent moyen. La fréquence maximale de leurs oscillations est donnée par la fréquence de Brunt-Väisälä ($N$) tandis que la

fréquence minimale correspond au paramètre de Coriolis ($f$). Elles possèdent des longueurs d'ondes verticales inférieures à 10 km et des longueurs d'ondes horizontales allant de quelques dizaines à un millier de kilomètres. Enfin leurs périodes vont de dizaines de minutes à quelques heures. Ces phénomènes de petites échelles et leurs effets associés sont difficiles à paramétrer dans les modèles météorologiques dont les résolutions restent encore trop larges.

- **Les ondes de Rossby** ou ondes extra-tropicales planétaires sont des perturbations d'ondes variant longitudinalement qui sont générées par la fluctuation de la force de Coriolis avec la latitude. Précisément, le mécanisme de rappel est lié à la conservation de la vorticité potentielle. Ainsi, comme leur nom l'indique, leur extension horizontale est d'échelle planétaire avec des longueurs d'ondes horizontales de plusieurs milliers de kilomètres. Elles sont caractérisées par des périodes s'étendant de 5 à 16 jours en fonction des modes. Les ondes de Rossby se propagent uniquement dans un écoulement moyen allant à l'est (condition d'hiver) avec une vitesse de phase se propageant à l'ouest par rapport à l'écoulement moyen. Elles déferlent principalement dans la haute stratosphère où la densité est faible entraînant un freinage de l'écoulement à l'origine du phénomène des échauffements stratosphériques soudains (ESSs).
- **Les ondes planétaires équatoriales**, incluant les ondes de Kelvin, les ondes de Rossby équatoriales et les ondes mixtes de Rossby-gravité, sont des ondes générées par les mouvements convectifs au niveau de l'équateur. Le mécanisme de formation résulte d'un piégeage le long de l'équateur causée par la rotation de la terre. Ces ondes ne se propagent qu'entre 20°S et 20°N. Leurs périodes vont de 4 à 15 jours avec des longueurs d'onde allant jusqu'à des dizaines de milliers de kilomètres. Une particularité des ondes de Kelvin est leur déplacement vers l'est contrairement aux ondes de Rossby et ondes mixtes de Rossby-gravité. Ces ondes perturbent la circulation moyenne au niveau de l'équateur en impactant la variabilité des précipitations

et en générant notamment l'oscillation quasi-biennale.

- **Les marées atmosphériques** sont des oscillations de pression atmosphériques de l'ordre de 1 hPa causées par l'effet de réchauffements diurnes cycliques des masses d'air par le Soleil. Cette alternance jour/nuit est donc caractérisée par un maximum à 12h et un flux nul durant la nuit. La période associée aux marées est donc de 24h mais contient des sous-harmoniques de 12, 8 et 6h. Ces perturbations se propagent vers l'ouest en s'amplifiant dans la mésosphère et la thermosphère avant de se dissiper vers 120 km. Ce phénomène gouverne la variabilité du vent et de la température au sein de la basse thermosphère (Forbes, 1995).

Au cours de ce travail, nous nous intéresserons tout particulièrement à la variabilité de la moyenne atmosphère générée par l'effet des interactions entre l'écoulement moyen et les ondes de Rossby et les ondes de gravité.

### 1.1.5 . Équations primitives

Les équations régissant l'état et le mouvement de l'atmosphère, associé donc à un gaz compressible autour d'une sphère en rotation, sont bien connues. Néanmoins, elles sont généralement simplifiées en tenant compte des ordres de grandeur des différents termes en fonction des phénomènes étudiés. En particulier, l'équation du moment vertical peut être remplacée par l'équilibre hydrostatique, la force de Coriolis associée à la composante horizontale de la rotation de la Terre est négligée, enfin la distance $r$ entre un point dans l'atmosphère et le centre de la Terre est remplacée par un rayon moyen $a$. L'ensemble des équations obtenues à la suite de ces approximations s'appellent les équations primitives (Andrews et al., 1987). De plus, il est préférable d'utiliser des coordonnées verticales en Log-pression que la hauteur géométrique.

$$z = -H \ln (p/p_s)$$

Ainsi, les équations primitives en coordonnées Log-pression sur la sphère prennent

la forme suivante :

L'équilibre du moment dans les directions zonales et méridionales :

$$\frac{Du}{Dt} - \left(f + \frac{u\tan\phi}{a}\right)v + \frac{\Phi_\lambda}{a\cos\phi} = X, \tag{1.3.a}$$

$$\frac{Dv}{Dt} + \left(f + \frac{u\tan\phi}{a}\right)u + \frac{\Phi_\phi}{a} = Y \tag{1.3.b}$$

L'équilibre hydrostatique dans la verticale :

$$\Phi_z = \frac{R}{H}\theta\,\mathrm{e}^{\kappa z/H} \tag{1.3.c}$$

La conservation de la masse (équation de continuité) :

$$\frac{[u_\lambda + (v\cos\phi)_\phi]}{a\cos\phi} + \frac{(\rho_0 w)_z}{\rho_0} = 0 \tag{1.3.d}$$

La relation thermodynamique entre le chauffage diabatique et le taux de variation de la température potentielle :

$$\frac{D\theta}{Dt} = Q \tag{1.3.e}$$

Ici, $\Phi$ représente le géopotentiel, $\theta$ la température potentielle, $f = 2\Omega\sin\phi$ le paramètre de Coriolis et les composantes de vitesse sont définies dans les coordonnées horizontales ($\lambda$, $\phi$ = longitude, latitude) comme :

$$(u, v, w) = \left[(a\cos\phi)\frac{D\lambda}{Dt}, a\frac{D\phi}{Dt}, \frac{Dz}{Dt}\right], \tag{1.5}$$

où $D/Dt$ est le matériel de dérivation, correspondant au taux de changement suivant le mouvement du fluide au cours du temps, dont l'expression dans les coordonnées présentes est :

$$\frac{D}{Dt} = \frac{\partial}{\partial t} + \frac{u}{a\cos\phi}\frac{\partial}{\partial\lambda} + \frac{v}{a}\frac{\partial}{\partial\phi} + w\frac{\partial}{\partial z} \tag{1.6}$$

Les composantes horizontales de friction, ou les forçages mécaniques non conserva-

teurs sont exprimés par les termes $X$ et $Y$ et le chauffage diabatique est représenté par le terme $Q$. Ainsi, l'ensemble de ces équations permet de décrire une large gamme de phénomènes de petites et grandes échelles et les perturbations du flux atmosphérique. Nous verrons notamment qu'il est possible à partir de ces équations de décrire les interactions ondes-écoulement moyen responsables de larges perturbations au sein de la moyenne atmosphère.

## 1.2 . Dynamique de la Moyenne Atmosphère

Depuis la seconde moitié du XXe siècle, nos connaissances et notre compréhension de la moyenne atmosphère, comprenant la stratosphère et la mésosphère, ont énormément avancé (Shepherd, 2000). En effet, longtemps restée inexplorée par incapacité technologique de sonder l'atmosphère à ces altitudes, il a fallu des décennies et des observations considérables, contribuant chacune pour une partie de l'atmosphère, pour reconstituer les champs de vent et de température globaux. Ces derniers ont confirmé l'importance des effets dynamiques au sein de la moyenne atmosphère. Aujourd'hui, il est clair que les ondes atmosphériques se propageant et redistribuant le moment angulaire ont un rôle central dans la circulation méridienne et verticale des masses d'air de la moyenne atmosphère. En effet, on estime que l'énergie transférée par les ondes atmosphériques dans la mésosphère est équivalente à l'énergie solaire absorbée par la surface (Meriwether and Gerrard, 2004). En plus de la circulation, les ondes sont aussi connues pour être à l'origine de phénomènes induisant de fortes variations de température. En particulier, les deux phénomènes majeurs qui contrôlent la variabilité de la moyenne atmosphère qui sont : les échauffements stratosphériques soudains (ESSs) et les inversions de température mésosphériques (ITMs).

### 1.2.1 . Champs de vents et de température

La Figure 1.2 montre les champs zonaux climatologiques de vent zonal et de température de la moyenne atmosphère aux solstices de Janvier et Juillet. Selon l'évolution de ces champs, il apparaît évident qu'ils suivent une alternance saisonnière. De plus, ces champs diffèrent significativement des champs prévus par l'équilibre radiatif indiquant que l'équilibre atteint résulte d'autres forçages (Andrews et al., 1987). En effet, le champ de température en moyenne climatologique montrent que la mésosphère d'hiver est plus chaude que la mésosphère d'été. De façon similaire, les vents zonaux ne sont pas croissants avec l'altitude comme attendu mais changent de direction vers 80 km fermant le jet.

Les champs de vents zonaux climatologiques confirment l'existence de différents jets dans l'atmosphère : le jet-stream au niveau de la tropopause aux moyennes latitudes ($\sim$40° latitude/$\sim$10 km) dans les deux hémisphère toute l'année avec des vents soufflant vers l'est. Ensuite, les jets localisés dans la stratosphère et mésosphère sont opposés entre l'hémisphère d'été et l'hémisphère d'hiver. Ainsi le jet de l'hémisphère d'hiver, appelé communément le jet de la nuit polaire, souffle vers l'est tandis que le jet de l'hémisphère d'été souffle vers l'ouest. Enfin, les jets de la moyenne atmosphère se ferment vers 80 km et laissent apparaître des jets de vents opposés dans la basse thermosphère.

Ces champs sont le résultat de la circulation eulérienne moyenne méridienne et verticale, circulation dite diabatique qui induit un chauffage de la moyenne atmosphère dans l'hémisphère d'hiver et un refroidissement dans l'hémisphère d'été. Nous verrons dans la partie suivante que les forces de friction générées par les ondes jouent un rôle central dans cette circulation et l'équilibre de l'atmosphère atteint.

### 1.2.2 . Circulation méridienne moyenne

La Figure 1.3 schématise la circulation méridienne au solstice des masses d'air au sein de la moyenne atmosphère où se produisent les effets de friction par les ondes. Comme mentionné précédemment, la circulation troposphérique, principalement contrôlée par

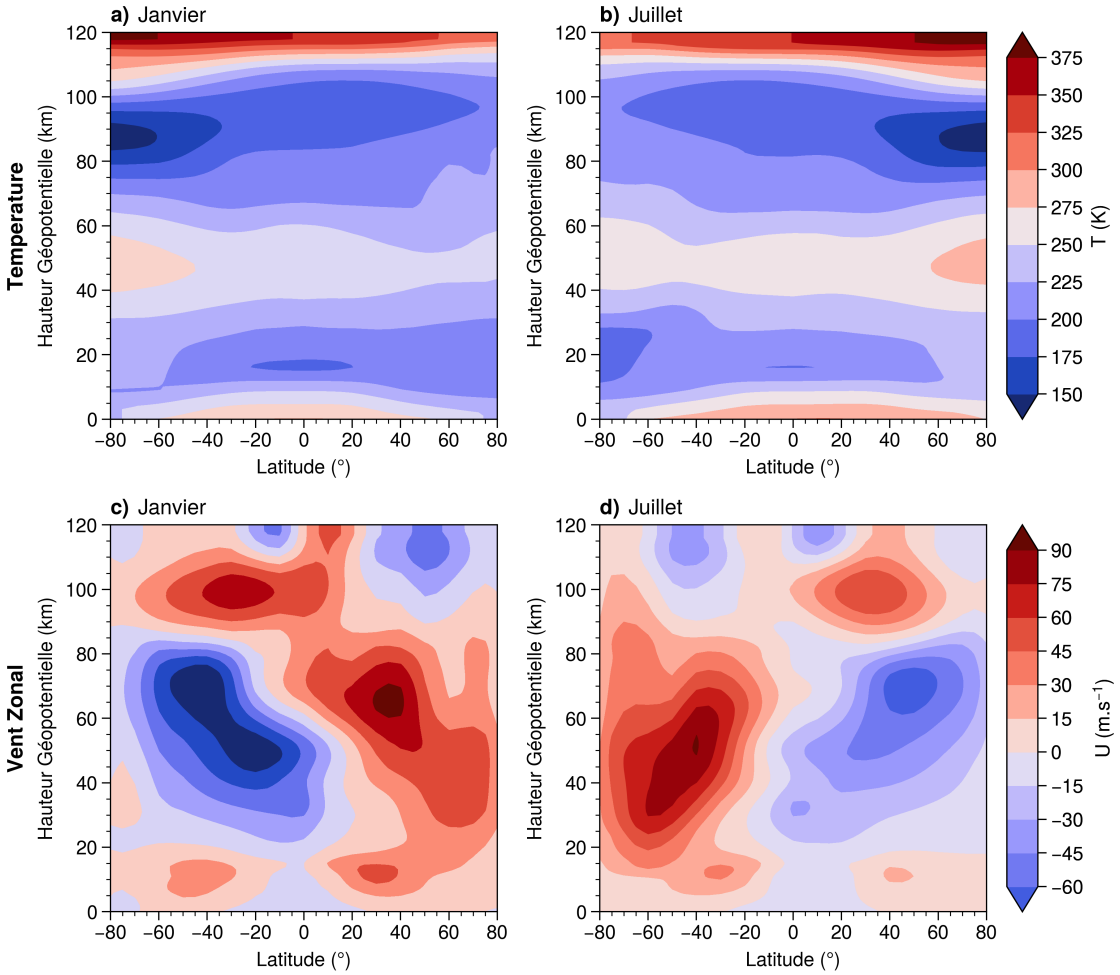


Figure 1.2 – Moyennes zonales de température pour les mois de Janvier (a) et Juillet (b) et des vents zonaux pour les mois de Janvier (c) et Juillet (d) d'après les données CIRA-86. (Source : Fleming et al. (1990))

les forces de pression, transporte les masses d'air chaudes de l'équateur vers les pôles tout au long de l'année. Dans la troposphère tropicale, le cellule de Hadley est principalement contrôlée par le forçage du gradient thermique de latitude (Plumb, 2002).

La circulation stratosphérique, connue sous le nom de circulation de Brewer-Dobson (Butchart, 2014), a été découverte par Brewer (1949) et Dobson (1956) à partir des observations de vapeur d'eau et d'ozone, respectivement. En effet, cette circulation au sein de la stratosphère a pour effet notable de transporter les masses d'air contenant l'ozone, principalement produit à l'équateur, vers le pôle.

Ainsi, quatre régions peuvent être identifiées dans la stratosphère : l'hémisphère d'été, les tropiques, la surf zone et le vortex polaire de l'hémisphère d'hiver. A toutes les saisons, une circulation vers le pôle dans les deux hémisphères de la basse stratosphère est causée par des perturbations de l'onde de Rossby à l'échelle synoptique. Ces perturbations sont associées à des instabilités baroclines responsables également d'un flux retour vers l'équateur proche de la surface à l'origine de poussées d'air froid (Shepherd, 2007). Cependant, aux plus hautes altitudes de la stratosphère, les hémisphère d'été et d'hiver possèdent une asymétrie fondamentale.

L'hémisphère d'hiver est caractérisé par des vents d'ouest en moyenne de la surface à la mésosphère autorisant la propagation des ondes planétaires depuis la troposphère et un plus large spectre d'ondes de gravité avec des vitesses de phase d'est et d'ouest. Les ondes planétaires se brisent par intermittence au sein de la surf zone de la stratosphère hivernale brassant l'air et redistribuant le moment angulaire générant une circulation vers le pôle (McIntyre and Palmer, 1983).

Tandis que dans l'hémisphère d'été, l'inversion des vents entre la troposphère et la stratosphère empêche la propagation des ondes planétaires et filtre une grande partie des ondes de gravité ne laissant passer que celles aux grandes longueurs d'ondes verticales avec des vitesses de phase horizontale allant vers l'est (Lindzen, 1981). Ces ondes de gravité tendent à déferler ensuite à de plus hautes altitudes ($\sim$85 km) au sein de la

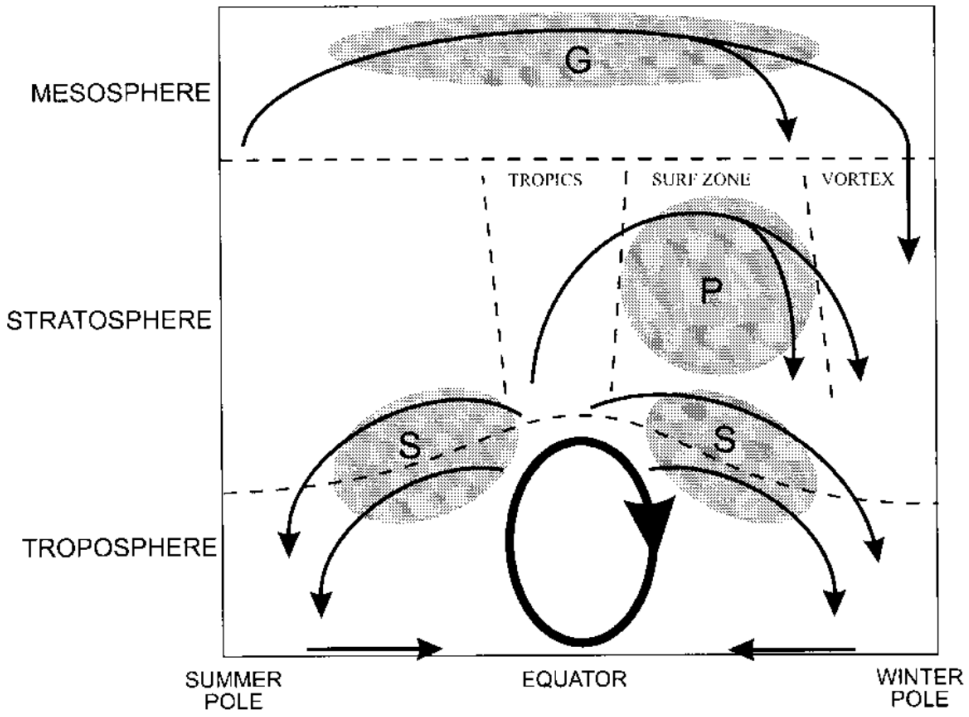


Figure 1.3 – Schéma de la circulation méridienne moyenne résiduelle : L'ellipse épaisse indique la cellule de Hadley troposphérique, alimentée par la chaleur. Les ombres indiquent les régions de déferlement d'ondes responsables de la circulation dans l'atmosphère moyenne. "S" représente les ondes synoptiques, "P" les ondes planétaires et "G" les ondes de gravité. L'ascension induit un refroidissement adiabatique et la descente un réchauffement adiabatique. (Source : Plumb (2002))

mésosphère où elles exercent un forçage sur les vents anti-cycloniques. Une circulation vers le haut et vers l'équateur s'en suit pour des raisons de conservation de la masse sur la sphère. Cette circulation refroidit adiabatiquement les masses d'air arrivant dans la mésosphère d'été.

Les vents de l'hémisphère d'hiver agissent également comme un filtre variable de la transmission des ondes de gravité qui peuvent passer à travers elles. Ces ondes de gravité tendent à déferler à des altitudes plus basses (à partir de $\sim$65 km) ralentissant les vents d'ouest. Ce forçage à son tour instaure une circulation au sein de la mésosphère transportant les masses d'air vers le pôle avec un effet de pompage vers le bas pour satisfaire

encore la conservation de la masse. En fin de compte, les masses réchauffent adiabatiquement la mésosphère et la stratopause de l'hémisphère d'hiver aux hautes latitudes. Ce mécanisme de circulation est parfois exprimé comme un contrôle descendant ("downward control" en anglais) (Haynes et al., 1991).

Les champs montrés précédemment sont donc le résultat de la circulation eulérienne moyenne méridienne et verticale, circulation dite diabatique qui induit un chauffage de la moyenne atmosphère dans l'hémisphère d'hiver et à un refroidissement dans l'hémisphère d'été.

### 1.2.3 . Variabilité saisonnière observée aux moyennes latitudes

La Figure 1.4 montre la variabilité de température journalière au sein de la moyenne atmosphère au-dessus de l'OHP. Ainsi, il est clair que la variabilité avec l'altitude admet une composante saisonnière forte. Cette variabilité admet un maximum de plus de 10 K en Décembre-Février à la fois dans la haute stratosphère ($\sim$40 km) et dans la mésosphère (60-70 km) alors qu'un minimum de $\sim$3 K est observé entre Avril et Octobre à ces mêmes altitudes. Cette différence de variabilité provient de la propagation d'ondes planétaires dans des vents soufflant à l'est en hiver et leurs blocages au cours de l'été. Dans la stratosphère d'hiver, la variabilité est notamment causée par les interactions entre les ondes planétaires et l'écoulement moyen qui sont à l'origine d'échauffements stratosphériques soudains (ESSs) augmentant la température de plusieurs dizaines de degrés.

Au sein de la mésosphère d'hiver, un minimum de variabilité est observé au-dessus de la stratopause, aux alentours de 55 km, correspondant à une zone de transition entre les échauffements de la haute stratosphère et le refroidissement de la mésosphère. En été, ce minimum s'étend jusque 65 km, altitude à partir de laquelle la variabilité reste forte tout au long de l'année. Au-dessus de ces minimums, la variabilité de la mésosphère est principalement gouvernée par le déferlement des ondes de gravité et l'apparition des inversions de température mésosphériques augmentant la température de dizaines de degrés sur plusieurs jours (Hauchecorne et al., 1991). On remarque notamment que les

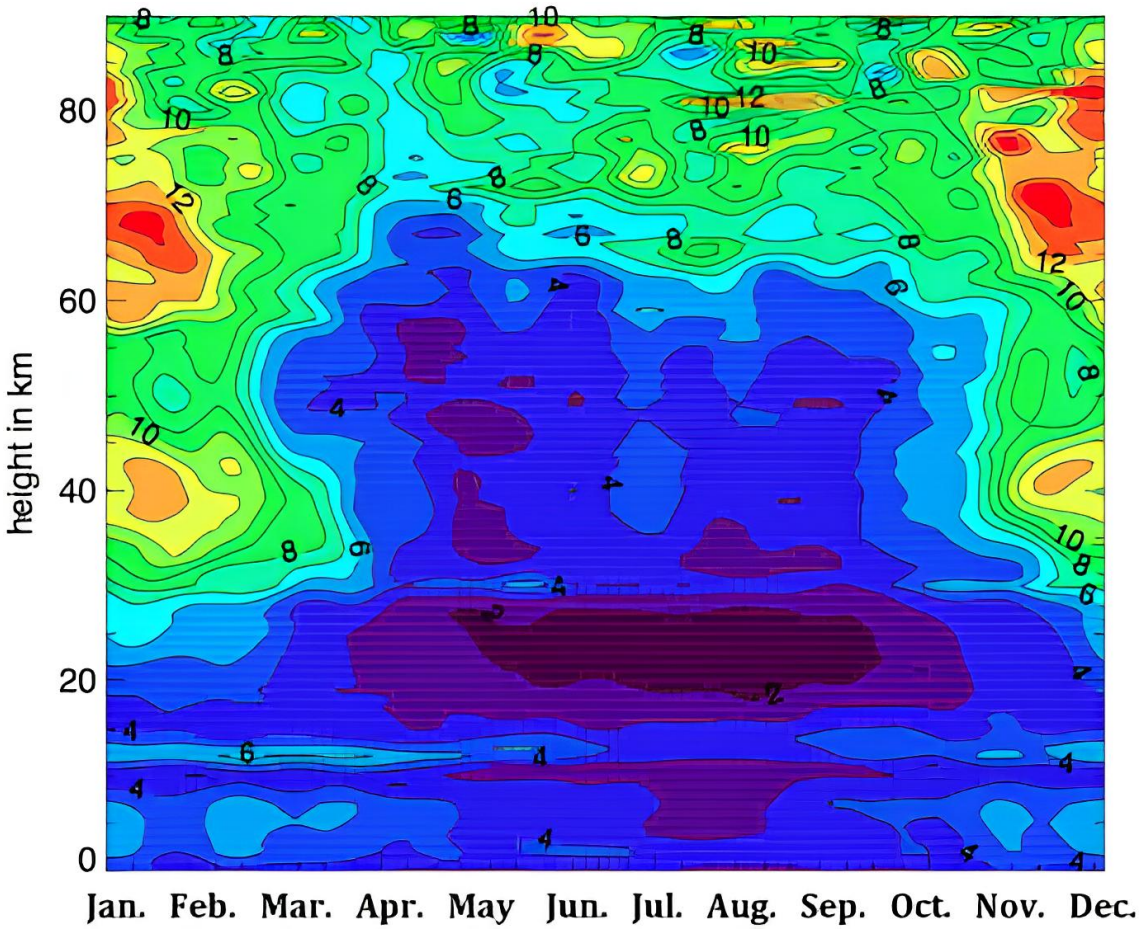


Figure 1.4 – Déviation standard moyenne de la température journalière au-dessus de l'OHP sur la période 1979-1998. (Source : Keckhut et al. (2012))

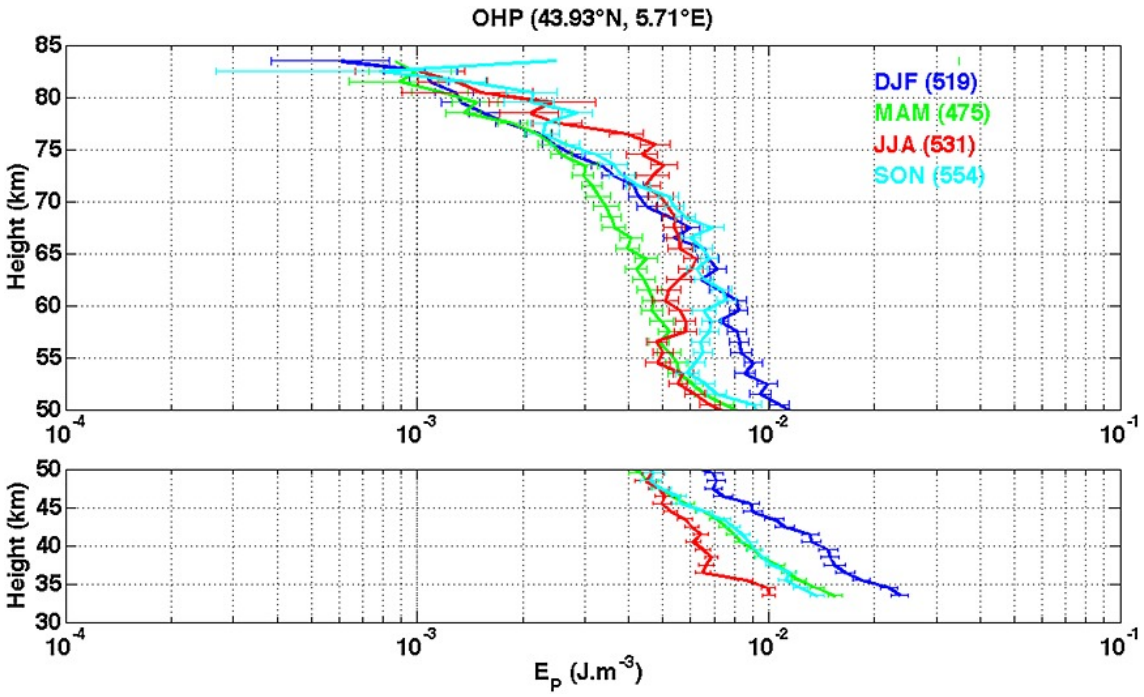


Figure 1.5 – Profils verticaux de l'énergie potentielle par unité de volume (en J.m-3) dans la haute stratosphère et la mésosphère obtenus à l'OHP, moyennés sur l'hiver (décembre-janvier-février, ligne bleue), le printemps (mars-avril-mai, ligne verte), l'été (juin-juillet-août, ligne rouge) et l'automne (septembre-octobre-novembre, ligne cyan). Les barres d'erreur horizontales indiquent l'incertitude $\pm 1\sigma$ de la médiane. Le nombre de profils utilisés pour la moyenne saisonnière est indiqué. Notez l'échelle logarithmique de l'axe des x. (Source : Mzé et al. (2014))

maximums de variabilité résident plus hauts dans la mésosphère en été qu'en hiver. Cette différence est à relier avec l'altitude de déferlement des ondes de gravité qui suit un cycle saisonnier, plus haute en été qu'en hiver (voir Figure 1.5).

De façon similaire aux ondes planétaires, le déferlement des ondes de gravité se produit à une altitude dite critique lorsque leurs vitesses de phase égalisent celles de l'écoulement moyen (voir Figure 1.6). Cependant, les ondes de gravité arrivant dans la mésosphère ont été au préalable filtrées par les vents moyens. Ainsi uniquement les ondes avec des vitesses de phase allant à l'ouest peuvent se propager dans l'hémisphère d'hiver.

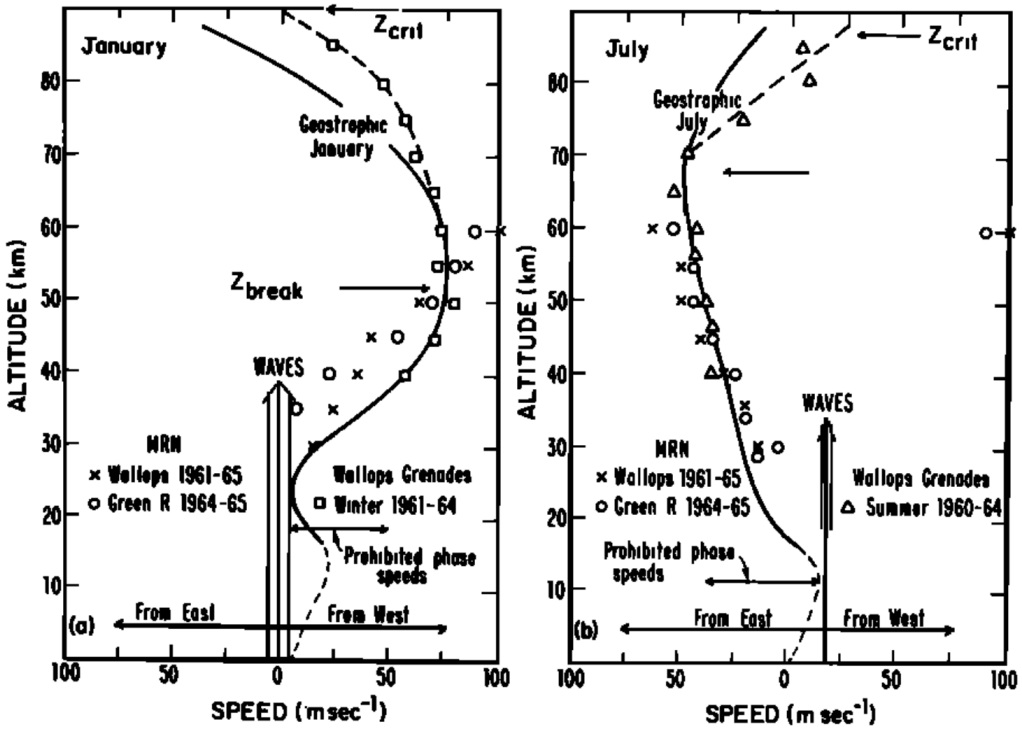


Figure 1.6 – Vent zonal en fonction de l'altitude dans la ceinture de latitude 30°-45°N d'après les sondes fusées. (a) Résultats pour janvier ; (b) résultats pour juillet. Les vents géostrophiques dérivés des sondages de température et les vitesses de phase permises et interdites pour les ondes de gravité mésosphériques d'origine troposphérique. (Source : Lindzen (1981))

## 1.3 . Principaux phénomènes contrôlant la variabilité

### 1.3.1 . Les échauffements stratosphériques soudains (ESSs)

#### Description

Comme montré sur la Figure 1.2, en moyenne, un jet de la nuit polaire avec des vents d'ouest, aussi appelé vortex polaire, se met en place dans l'hémisphère d'hiver lorsque la température de la stratosphère chute par manque d'ensoleillement. Ce vortex polaire reste centré au-dessus du pôle tout au long de l'hiver en piégeant les masses d'air très froides contenant l'ozone transporté depuis l'équateur (voir Fig. 1.7a). A la fin de l'hiver et au début du printemps, le vortex polaire disparaît avec le retour du rayonnement solaire et des vents d'est qui s'installent jusqu'à l'hiver prochain. Cependant, il arrive qu'au cours de l'hiver le vortex polaire soit fortement perturbé et par conséquent entraîne par une augmentation soudaine de température, pouvant aller de 40 à 60 K sur une semaine, accompagnée parfois d'une inversion du vent zonal. Ce phénomène, appelé échauffement stratosphérique soudain (en anglais : sudden stratospheric warming (SSW)), a été observé pour la première fois par Scherhag (1952) à l'aide de mesures réalisées par radiosondage au dessus de Berlin. Depuis lors, de nombreuses observations avec de meilleures résolutions sont venues compléter notre compréhension de la morphologie en trois dimensions des échauffements stratosphériques soudains. La Figure 1.7 représente une évolution typique du vortex polaire en hiver en période d'échauffement stratosphérique. Le vortex peut être déplacé en dehors du pôle et puis être scindé en deux tourbillons (voir Fig. 1.7b-c). Ces deux évolutions laissent apparaître des structures d'onde 1 (vortex déplacé) et d'onde 2 (vortex scindé) respectivement dont les contributions au champ de géopotentiel peuvent être calculées à partir d'une analyse de Fourier du signal à une même latitude. Cette analyse de l'activité dynamique sera utilisée dans l'article présentée dans la section 5.5.

Aujourd'hui, il est reconnu comme l'événement dynamique de grande échelle le plus

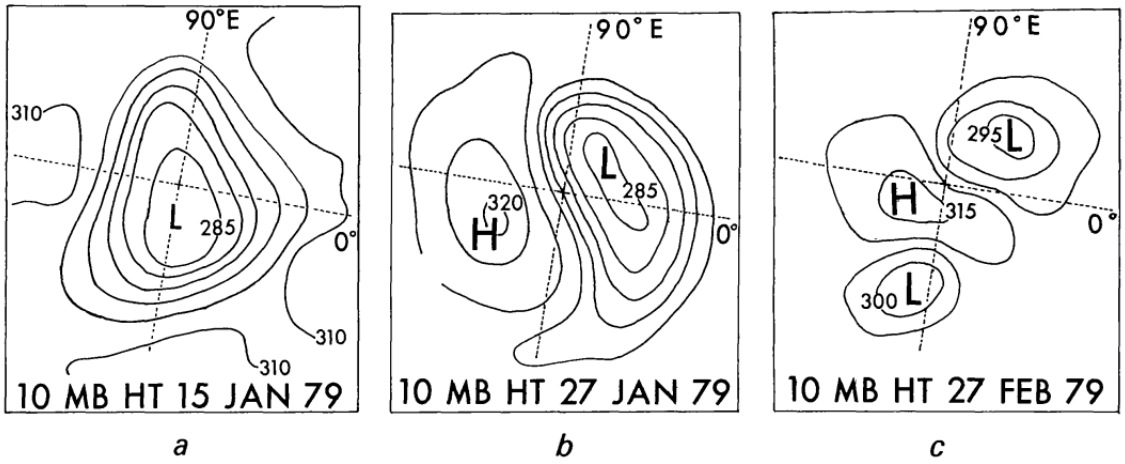


Figure 1.7 – Evolution de la topographie du champ de hauteur à 10 hPa dans l'hémisphère nord au début de l'année 1979. Les contours de hauteur sont indiqués en centaine de mètres et sont tracés à des intervalles de 500 m. L et H indiquent les minimums et maximums, respectivement. La région étudiée s'étend approximativement de 20°N jusqu'au pôle. Les lignes de longitude 0° et 90°E sont marquées. Le cadre (a) illustre le vortex polaire d'hiver normal, (b) montre la phase de pré-échauffement avec une forte perturbation de nombre d'onde 1 et (c) affiche une situation de post-échauffement avec une circulation anti-cyclonique dans la région polaire et une perturbation de nombre d'onde 2. (Source : Quiroz (1979))

spectaculaire se produisant au sein de la moyenne atmosphère. On sait depuis le modèle proposé par Matsuno (1971) que ce phénomène est la conséquence de l'interaction des ondes planétaires, se propageant depuis la troposphère, avec l'écoulement moyen dans la stratosphère. Étant donné que l'activité ondulatoire est fortement reliée à la présence d'orographie au sol et de la différence de température entre la mer et la terre, la quasi totalité des échauffements stratosphériques qui ont été observés se sont produits dans l'hémisphère nord. En effet l'hémisphère sud, avec moins de terres immergées, est caractérisé par un vortex polaire fort tout au long de l'hiver bien que des échauffements notables ont été recensés en 2002 et 2019 (Charlton et al., 2005; Rao et al., 2020).

Depuis lors, la communauté scientifique a cherché à classifier ces événements en fonction de différents critères caractérisant leur intensité, leur timing et leurs impacts sur la circulation stratosphérique. Au fil des années, seule la classification des ESSs suivante est restée largement utilisée : "Majeur", "Mineur", "Final" et "Canadiens" (Major, Minor, Final and Canadian en anglais). Cependant, bien qu'il n'existe toujours pas de définition claire associée à ces termes (Butler et al., 2017), le critère basé sur le vent zonal moyenné zonalement à 60°N-10hPa s'est imposé afin de qualifier les événements majeurs et finaux se produisant en milieu et fin d'hiver (Butler et al., 2015). Ainsi, il est admit que les événements dits "majeur" représentent les cas où le vent zonal moyen zonal à 60°N-10hPa s'est inversé en milieu d'hiver avant de revenir à une circulation d'Ouest. Les échauffements "finaux" représentent les cas où ce retour à des vents d'Ouest ne s'est pas produit. En revanche, bien que le critère sur le vent zonal ne soit pas communément appliqué aux événements dits "mineurs", il est admit qu'ils représentent les cas où le vortex polaire stratosphérique a été affaibli significativement sans inverser les vents (Butler et al., 2017). Les récents travaux de (Maury et al., 2016) ont permis d'établir le critère suivant permettant d'identifier les échauffements mineurs importants : si le vent zonal moyen zonal à 60°N-10hPa est devenu inférieur à 10 $m.s^{-1}$. Ce critère sera notamment utilisé plus tard afin de détecter tous les échauffements ayant un impact significatif sur l'évolution du vor-

tex polaire.

Ainsi un échauffement dit "majeur" induisant une inversion des vents dans la stratosphère se produit environ une fois tous les deux ans dans l'hémisphère nord (Charlton and Polvani, 2007; Domeisen, 2019). Cette fréquence est à l'origine de l'importante variabilité inter-annuelle observée (voir Figure 1.4) dans la stratosphère.

### Mécanismes

La description mathématique des échauffements stratosphériques et globalement de la moyenne atmosphère a été rendue possible à l'aide du développement des équations décrivant un fluide quasi-géostrophique sur le plan beta obtenues en simplifiant les équations primitives 1.3.a (voir Annexe A). Les ondes planétaires sont représentées comme des déviations à un écoulement moyen moyenné zonalement à l'aide les équations Eulériennes moyennes (Holton, 1980). En combinant l'ensemble de ces équations, il est possible d'obtenir la relation de dispersion des ondes et d'en déduire la relation suivante conditionnant la propagation verticale des ondes planétaires pour un fluide quasi-géostrophique :

$$0 < \bar{u} - c < \beta/k^2, \tag{1.7}$$

où $c$ est la vitesse de phase de l'onde, $\beta$ la variation du paramètre de Coriolis avec la latitude et $k$ le nombre d'onde horizontal. Cette équation impose donc que les ondes se propagent à l'ouest par rapport à un écoulement moyen allant à l'est et à une vitesse inférieure à $\beta/k^2$ pour pouvoir se propager verticalement. Cette condition de propagation explique pourquoi seules les conditions hivernales permettent la propagation des ondes planétaires avec de grandes longueurs d'ondes. Le blocage de la propagation des ondes s'effectue à l'altitude critique où $\bar{u} - c = 0$ à l'origine de l'apparition des échauffements.

Le principal intérêt de ces équations est de décrire les perturbations quasi-géostrophiques de vorticité potentielles induites par les ondes dans un écoulement où le rapport entre

la profondeur d'une colonne de fluide et la composante verticale de la vorticité absolue est conservé. Cependant, il est nécessaire d'utiliser les équations Eulériennes transformées quasi-géostrophiques, prenant en compte une circulation méridienne moyenne résiduelle, pour décrire correctement la réponse du flux moyen zonal aux perturbations d'ondes. Cette transformation permet entre autre d'obtenir l'équation du moment zonal moyen transformé suivante sur le plan beta :

$$\bar{u}_t - f_0 \bar{v}^* - \bar{X} = \rho_0^{-1} \nabla \cdot \mathbf{F}, \tag{1.8}$$

avec

$$\mathbf{F} \equiv (0, -\rho_0 \overline{v'u'}, \rho_0 f_0 \overline{v'\theta'}/\theta_{0z}), \tag{1.9}$$

où $\mathbf{F}$ est le flux d'Eliassen-Palm comprenant les termes de forçage tourbillonnaires par les ondes induisant des flux de moment et de chaleur agissant en combinaison. Le flux d'Eliassen-Palm permet de caractériser également la direction des ondes de petites amplitudes dans le plan méridien et est un excellent outil pour diagnostiquer les interactions onde-écoulement moyen (voir Figure 1.8). Il ressort qu'une divergence négative (positive) de ce flux est donc associée à une décélération (accélération) et à un échauffement (refroidissement) de l'écoulement moyen (Andrews, 1987). L'intérêt des équations Eulériennes transformées est de satisfaire le théorème de non accélération ($\nabla \cdot \mathbf{F} \equiv 0$), premièrement introduit par Charney and Drazin (1961), obtenu pour des perturbations linéaires et stationnaires se propageant dans un écoulement conservateur. En effet, ce théorème stipule que sous ces conditions les ondes ne peuvent pas induire de changement de l'écoulement moyen.

Andrews and McIntyre (1976, 1978) ont étendu ce résultat en tenant compte de la géométrie sphérique, des effets de friction ($X'$, $Y'$) et diabatiques ($Q'$) et en incluant les amplitudes d'onde variant au cours du temps ("onde transitoire"). Ce théorème généralisé

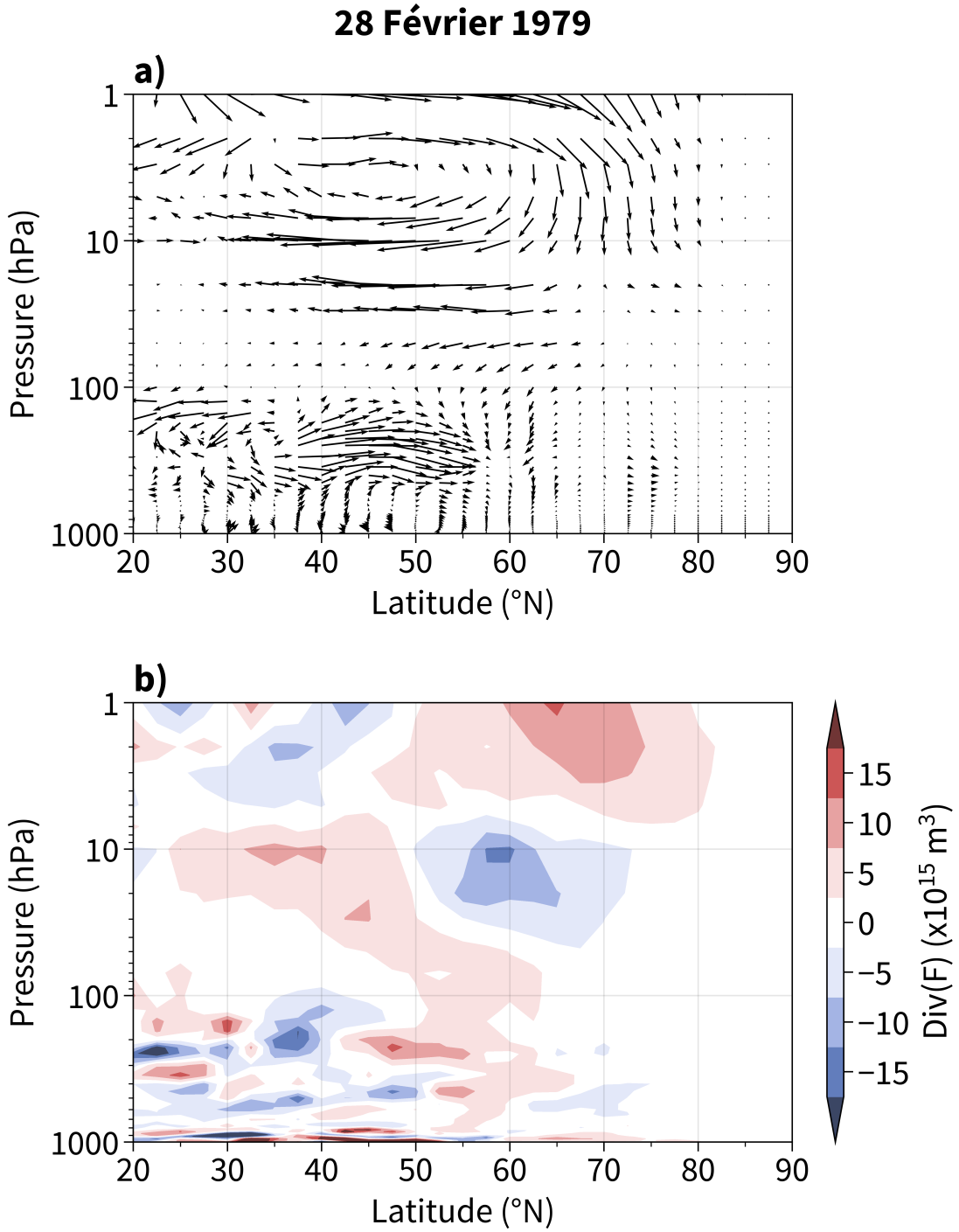


Figure 1.8 – Développement latitude-hauteur : (a) des vecteurs du flux d'Eliassen-Palm et (b) de sa divergence pour le jour du 28 Février 1979 lorsque la circulation stratosphérique est devenue anti-cyclonique à la suite d'un échauffement.

d'Eliassen-Palm prend la forme suivante :

$$\frac{\partial A}{\partial t} + \nabla \cdot \mathbf{F} = D + O(\alpha^3), \tag{1.10}$$

avec

$$A \equiv \frac{1}{2}\rho_0 \overline{\eta'^2} \bar{q}_y, \tag{1.11}$$

où $A$ représente la densité d'activité d'onde, $D$ une quantité contenant les effets de friction et diabatiques et $O(\alpha^3)$ les effets d'ondes non linéaires où $\alpha$ est l'amplitude de l'onde. Cette équation fait apparaître la dépendance de $\nabla \cdot \mathbf{F}$ aux propriétés physiques des effets d'onde transitoire et non conservatrice. En supprimant les termes de droite, l'équation 1.10 prend la forme d'une loi de conservation reliant la densité d'activité d'onde à la divergence du flux d'Eliassen-Palm ($\frac{\partial A}{\partial t} = -\nabla \cdot \mathbf{F}$). Cette forme est obtenue pour des ondes linéaires, conservatrices et transitoires nécessaire pour violer le théorème de non accélération énoncé précédemment.

A l'aide de simulations, Matsuno (1971) a montré que seule la propagation vers le haut de paquets transitoires d'ondes planétaires depuis la troposphère est capable de décélérer l'écoulement moyen zonal et d'élever la température proche du pôle comme on peut l'observer lors d'échauffements stratosphériques. Cette interaction onde-écoulement moyen est illustrée sur la Figure 1.9. Comme $\partial A/\partial t > 0$ au bord du paquet d'ondes alors il est attendu une divergence négative du flux d'EP proche du front du paquet générant une accélération vers l'ouest de l'écoulement moyen (Figure 1.9a). De plus, une partie de cette divergence négative sera équilibrée par le terme de Coriolis de la circulation méridienne moyenne résiduelle qui augmente induisant une circulation verticale requise par continuité (Figure 1.9b). Cette circulation vers le bas au nord et sous la région de la divergence du flux d'EP va réchauffer la région polaire et résulter en un échauffement stratosphérique.

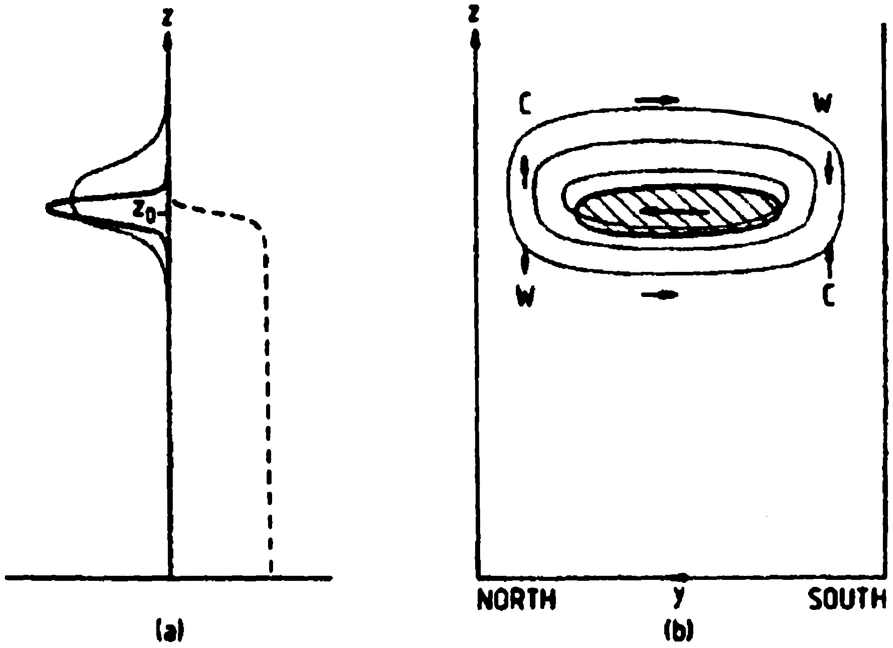


Figure 1.9 – Description schématique de l'interaction avec le flux moyen zonal d'un paquet d'onde planétaire transitoire se propageant verticalement pendant un échauffement stratosphérique. (a) Profils de hauteur du flux EP (pointillé), divergence du flux EP (ligne épaisse) et accélération du vent zonal moyen (ligne fine) et zo est l'altitude atteinte par le paquet d'onde. (b) Diagramme hauteur-méridional montrant la région où F < o (hachuré), contour de la décélération induite (lignes fines), et la circulation résiduelle ($v^*, w^*$) induite (flèches). Régions de chauffage (W) et de refroidissement (C) sont aussi indiquées. (Source : Andrews et al. (1987))

### Impacts

Au sein de la stratosphère, l'un des principaux impacts des échauffements stratosphériques est de redistribuer l'ozone accumulé au pôle en déplaçant le vortex polaire. Le vortex polaire restant habituellement d'ailleurs très fort et froid dans l'hémisphère sud, des nuages se forment favorisant la libération du chlore et du brome actifs qui détruisent l'ozone par réaction catalytique et sont responsables du trou de la couche d'ozone dans cette partie du monde. En plus des perturbations générées sur la circulation de la stratosphère, les échauffements stratosphériques sont désormais connus pour leurs impacts sur les basses couches qui peuvent influencer le climat à la surface jusqu'à deux mois suivant leurs apparitions. En effet, depuis les travaux de Baldwin and Dunkerton (2001) sur le mode annulaire de l'hémisphère nord (NAM pour Northern Annular Mode) représentant la variabilité dominante (Figure 1.10), on sait que l'anomalie générée dans la stratosphère lors d'un échauffement peut se propager dans la troposphère et atteindre la surface. Un des effets notables de cette propagation d'anomalie est d'engendrer une phase négative de l'Oscillation de l'Atlantique (OA) Nord avec des pressions plus hautes au pôle qu'aux moyennes latitudes. La phase négative de l'OA tend alors à générer des températures plus chaudes au pôle et plus froides aux moyennes latitudes et à déplacer le vent moyen vers l'équateur. Les conséquences sur le climat troposphérique sont nombreuses, comme l'apparition de vagues d'air froid ou le décalage vers l'équateur des parcours des dépressions dans l'Atlantique Nord ainsi que la modification de leur intensité et fréquence (Afargan-Gerstman and Domeisen, 2020).

Ainsi, ces impacts vers le bas révèlent que les échauffements stratosphériques sont des phénomènes emblématiques du couplage stratosphère-troposphère dans les deux sens au cours de l'hiver.

Comme les échauffements stratosphériques n'impactent pas tous la troposphère (voir premier échauffement de la Figure 1.10), de nombreuses classifications se basant sur différents critères ont été établies par la communauté scientifique pour déterminer les mé-

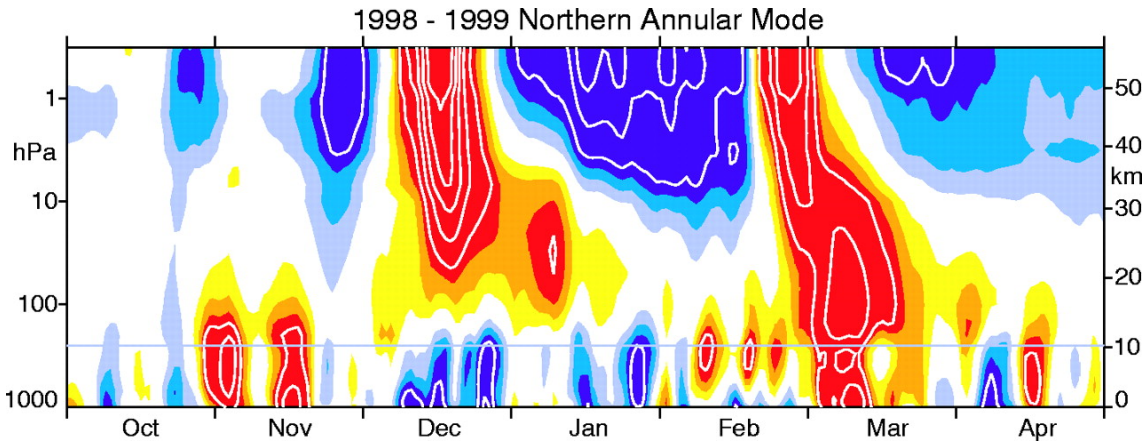


Figure 1.10 – Développement temps-hauteur du mode annulaire nord au cours de l'hiver 1998-1999. Les indices ont une résolution journalière et sont nondimensionnels. Le bleu correspond à des valeurs positives (vortex polaire fort) et le rouge à des valeurs négatives (vortex polaire faible). L'intervalle de contour est de 0,5, les valeurs entre -0,5 et 0,5 n'étant pas ombrées. La fine ligne horizontale indique la limite approximative entre la troposphère et la stratosphère. (Source : Baldwin and Dunkerton (2001))

canismes responsables de cette descente d'anomalies (Kodera et al., 2016; Mitchell et al., 2013). Aujourd'hui, l'impact des échauffements sur le climat troposphérique est encore imparfaitement décrit et les critères nécessaires pour exercer cette influence peu clairs bien que la descente de l'anomalie stratosphérique vers la tropopause semble être déterminante (Karpechko et al., 2017). Ainsi, mieux comprendre les mécanismes d'apparitions des échauffements est devenu d'un grand intérêt afin de potentiellement améliorer la prévision saisonnière compte tenu des temps caractéristiques du développement d'un échauffement. Dans cette thèse, l'importance des timings des échauffements sur la circulation stratosphérique au cours de l'hiver ainsi que leurs effets sur la circulation troposphérique seront étudiés en détail.

### 1.3.2 . Les inversions de température mésosphériques (ITMs)

#### Histoire

Le phénomène d'inversion de température mésosphérique (ITM) est reporté pour la première fois en 1960 par Stroud et al. (1960) (voir Figure 1.11) avec des mesures réalisées par fusées, ballons sondes ou radiosondes. Non conscients du phénomène, ils relèvent une élévation de température inattendue dans la haute mésosphère et suggèrent que la température de la mésosphère est dynamiquement contrôlée. Plusieurs études ont ensuite conforté cette idée en suggérant que les ondes de gravité sont responsables de la turbulence de la haute mésosphère (Hodges Jr., 1969; Lindzen, 1967; Lindzen and Blake, 1971; Lindzen and Chapman, 1968). C'est à partir des observations reportées par Schmidlin (1976) que le phénomène est pour la première fois identifié et que le terme "couche d'inversion mésosphérique" (Mesospheric Inversion Layer (MIL) en anglais) est introduit. Depuis lors, les inversions ont été largement observées à travers le monde à l'aide de satellites (Leblanc and Hauchecorne, 1997) et notamment avec l'essor de la technologie LiDAR (Duck et al., 2001; Hauchecorne et al., 1987). Aujourd'hui une ITM est connue comme étant une couche verticale d'environ 10 km où se produit une élévation de température (10-50 K) par rapport à la structure thermique caractéristique (Meriwether and Gardner, 2000; Meriwether and Gerrard, 2004). Ce phénomène apparaît assez souvent, en particulier aux moyennes latitudes de l'hémisphère d'hiver, et peut durer plusieurs jours et couvrir horizontalement des milliers de kilomètres (Leblanc and Hauchecorne, 1997).

La communauté a identifié deux types d'ITMs : "basse" se produisant entre 65 et 80 km et "haute" entre 85 et 100 km. Ces deux types d'inversions sont pensés posséder différents mécanismes de formations. Il est admit que les "basses" inversions seraient causées par la dissipation des ondes planétaires (Salby et al., 2002) tandis que les "hautes" inversions sont pensées être le résultat d'interactions non linéaires entre les marées atmosphériques et ondes de gravité (Meriwether and Gardner, 2000). Cependant, d'autres mécanismes sont probablement à l'oeuvre tel que la dissipation des ondes de gravité

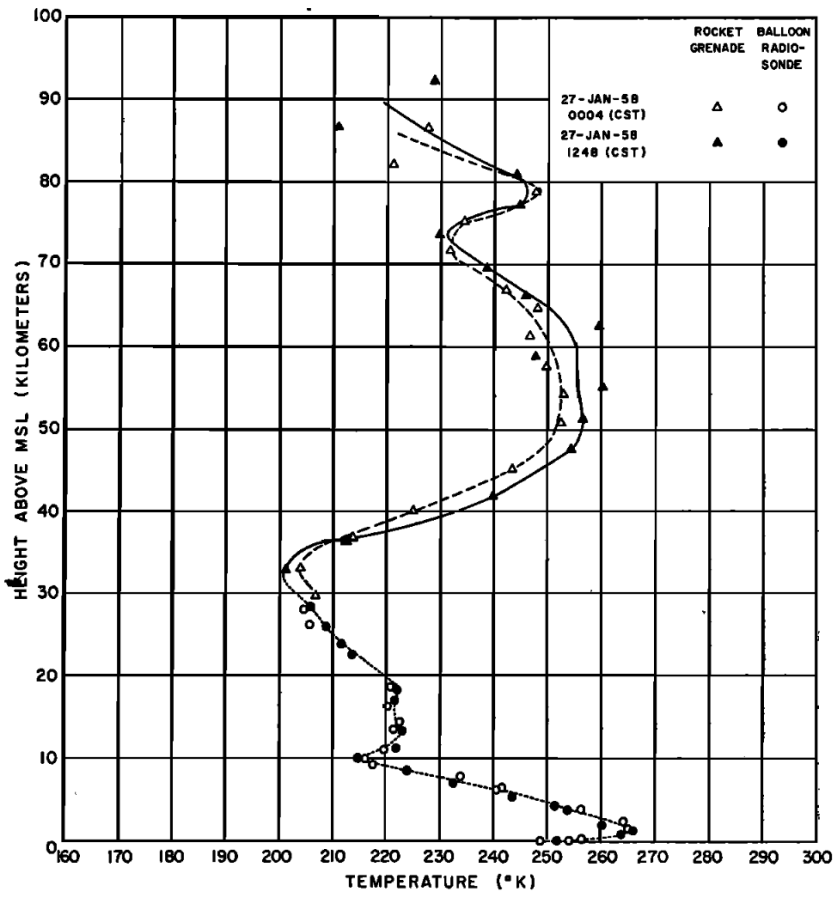


Figure 1.11 – Température en fonction de la hauteur au-dessus du MSL pour SM1.09 lancé le 27 janvier 1958 à 0004CST, et SM2.10 lancé le même jour à 1249 CST, Fort Churchill, Canada. Une inversion de température mésosphérique est visible entre 70 et 90 km. (Source : Stroud et al. (1960))

(Hauchecorne et al., 1987; Sassi et al., 2002), notamment pour les basses MIL, ou le chauffage chimique pour les hautes MIL (Meriwether and Mlynczak, 1995; States and Gardner, 2000).

### Rôle des ondes de gravité

Néanmoins, bien qu'il n'y ait actuellement pas de consensus sur les mécanismes de formation, plusieurs études mènent à admettre que les ondes de gravité auraient un rôle indispensable dans l'apparition des inversions mésosphériques basses. Par exemple, les

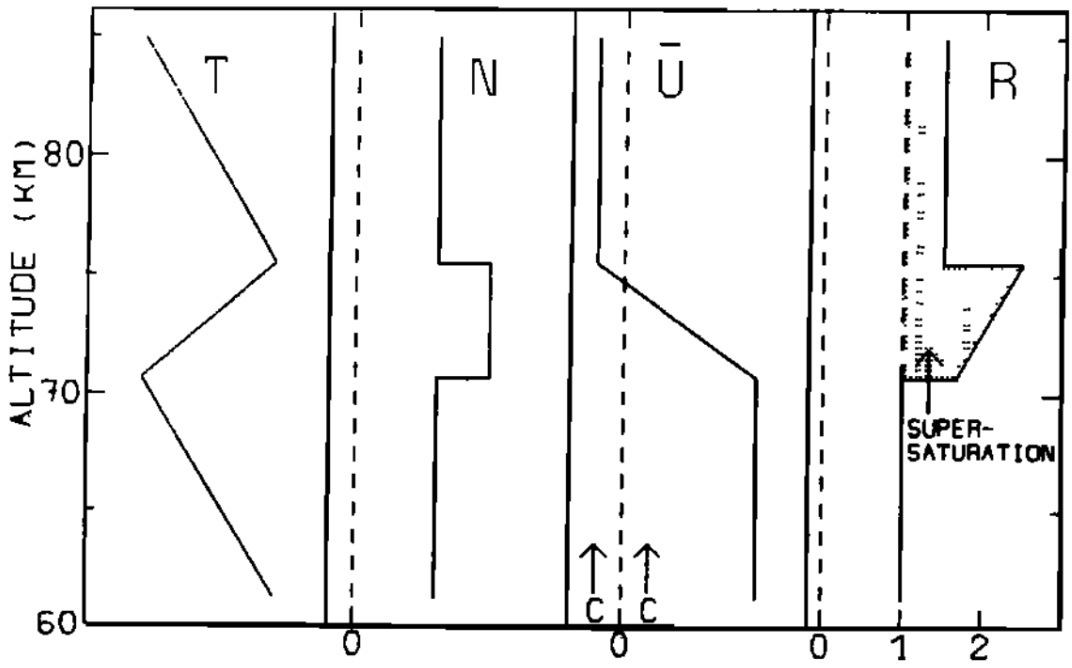


Figure 1.12 – Représentation schématique des profils verticaux de la température moyenne T, de la fréquence de Brunt-Väisälä N, du vent zonal moyen u et du rapport de saturation R = T'/T'$_s$, lors d'une inversion mésosphérique. (Source : Hauchecorne et al. (1987))

simulations réalisées par Sassi et al. (2002) ont montré que l'inversion mésosphérique disparaissait en ne maintenant que l'activité des ondes planétaires dans leur modèle. En effet, selon Hauchecorne et al. (1987), les ondes de gravité sont la principale cause de l'apparition et du maintient des basses inversions. Concrètement, le déferlement des ondes de gravité génère un dépôt de quantité de mouvement ralentissant les vents zonaux au-dessus du jet mésosphériques générant de la turbulence. Cette turbulence engendre alors un flux de chaleur provenant de la partie haute de la couche qui génère un échauffement adiabatique responsable de l'inversion de température. Ainsi cette couche favorise le déferlement continue des ondes de gravité qui peut maintenir l'inversion de température de plusieurs kelvins sur plusieurs jours. Les conditions atmosphériques nécessaires lors de l'apparition d'une inversion sont illustrées sur la Figure 1.12.

Cependant, le comportement du vent dans la moyenne atmosphère lors d'une inver-

sions mésosphérique reste encore à ce jour une information manquante cruciale pour bien comprendre et établir le mécanisme de formation à l'origine de ces phénomènes (Meriwether and Gerrard, 2004). Dans le chapitre 4.2, les premières observations co-localisées température-vent lors d'événements d'inversions de température mésosphériques seront présentées.

# 2 - Observations et base de données pour étudier la Moyenne Atmosphère

La découverte puis la compréhension des phénomènes survenant au sein de la moyenne atmosphère reposent en grande partie sur les observations effectuées à ces altitudes. En effet, la technique classique par radiosondage, mesurant la partie basse de l'atmosphère jusqu'à 25-30 km, a permis de découvrir l'existence des échauffements stratosphériques (Scherhag, 1952) ainsi que celle de l'oscillation quasi-biennale (Reed et al., 1961) dont les effets sont observables dans la basse stratosphère. Cependant, le sondage de la partie haute de la moyenne atmosphère a longtemps souffert de son inaccessibilité et de la disparité spatiale des observations à la surface du globe notamment entre les hémisphères Nord et Sud (voir Figure 2.1). Au cours des dernières décennies, des avancées significatives ont été réalisées dans la collecte de données à ces altitudes, grâce à des technologies de pointe et à des instruments sophistiqués qui ont été développés. Notamment, la technologie LiDAR est capable de capturer très fidèlement les fluctuations se produisant dans la moyenne atmosphère. D'autre part, l'étude climatologique de la moyenne atmosphère a aussi été permise par l'essor des modèles numériques de simulation du temps et des archives du climat passé, appelées réanalyses, s'améliorant toujours plus au fil des années.

## 2.1 . Techniques de mesure, modèles et base de données disponibles

La bonne caractérisation des phénomènes d'ESS et IMT passent donc par la qualité et la quantité des observations de température et de vent disponibles. L'observation des champs de vent et de température dans la moyenne atmosphère est obtenue à l'aide de différentes techniques de mesure in-situ ou de télédétection basés au sol ou à bord

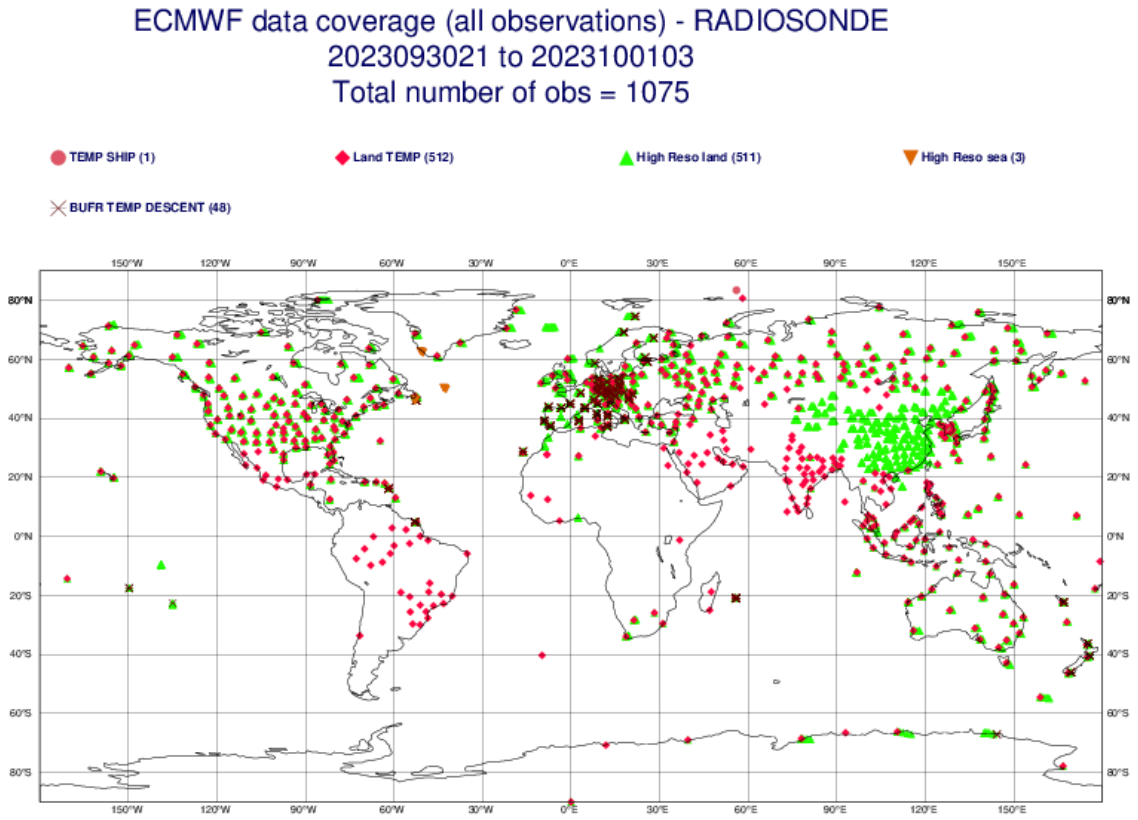


Figure 2.1 – Sites de radiosondages au sol (LAND) et à bord de navire (SHIP) couverts par les données du CEPMMT sur une fenêtre de 6h entre le 30/09/2023 et le 01/10/2023 (source : https://www.ecmwf.int/en/forecasts/quality-our-forecasts/monitoring-observing-system).

de satellites. Chacune de ces techniques possèdent une résolution spatiale et temporelle donnée et un domaine de validité propre (voir Figure 2.2).

- **Le Radiosondage (0-30 km)** est une technique de mesure qui consiste à envoyer des ballons-sondes équipés de capteurs dans l'atmosphère. Ces capteurs enregistrent des données telles que la température, l'humidité, la pression atmosphérique et la direction des vents à différentes altitudes. Ces informations sont transmises en temps réel depuis les ballons jusqu'aux stations au sol, ce qui permet de créer des profils verticaux de l'atmosphère. Les radiosondages sont connus pour capturer avec une bonne précision (0.2 K) les variations de température telles que celles liées aux ESSs (Schoeberl, 1978). Les inter-comparaisons ont montré un accord meilleur que 0.5 K confirmant la fiabilité de cette technique.
- **Les Fusées sondes** sont des véhicules spatiaux spécialement conçus pour effectuer des mesures et des observations verticales dans les couches supérieures de l'atmosphère terrestre. Historiquement, le développement des fusées a principalement été initié par les Allemands au cours des années 1930, ce qui a conduit à la création de la célèbre fusée V2, première fusée à atteindre l'espace (Seibert and Battrick, 2006). Après la Seconde Guerre mondiale, les fusées ont été largement utilisées des années 1960 aux années 1990 par les Américains (Keckhut et al., 1999), les Soviétiques (Kubicki et al., 2006) et les Japonais (Keckhut and Kodera, 1999), sur une quinzaine de sites répartis à travers le monde, dans le cadre de la course à l'espace. L'objectif consistait à réaliser une climatologie de cette région de l'atmosphère inconnue qui devait être traversée à l'aller et notamment au retour avec des enjeux de rentrée atmosphérique. Elles embarquent des instruments à bord qui mesurent généralement avec une bonne résolution diverses variables atmosphériques, telles que la température, la pression, la composition chimique, les particules chargées, les radiations, le vent etc. Cette technique a aussi été très utilisée pour étudier les variations de température des ESSs (Labitzke, 1981). Les principales méthodes ba-

sées sur les fusées pour mesurer la moyenne atmosphère sont :

- **Les datasondes (25 à 65 km)** ont joué un rôle vital entre les années 1970 et début des années 1990 pour fournir des observations de température dans la haute stratosphère et mésosphère (Finger et al., 1993). Bien qu'étant globalement arrêtée aujourd'hui, cette technique continue d'être employée pour des mesures telle que celle du vent à l'aide d'un radar capable de suivre sa descente (Lübken et al., 2016). Ainsi la datasonde contenant un ensemble de thermistances instrumentées est éjectée avec un parachute à retard stable ("starute" en anglais) au point le plus haut de la fusée (apogée). Cependant, au-dessus de 60 km, les incertitudes croient significativement (jusqu'à une dizaine de kelvin) à cause du chauffage aérodynamique, des effets de radiation, la constante de temps du thermistor qui exigent d'importantes corrections (Schmidlin, 1981). De plus, les datasondes ne peuvent être utilisées que sporadiquement et couvrir une période de temps limitée.
- **Les sphères tombantes (30-90 km)** utilisent les informations relatives à la position du radar et l'équation du mouvement pour calculer les données de densité, de température et de vent. Concrètement, la sphère est relâchée de la fusée typiquement vers 110 km avec un diamètre en général de 1 m et est suivie lors de sa descente par le radar (Schmidlin et al., 1991). Les données au-dessus de 90 km ne sont généralement pas exploitables à cause des incertitudes liées aux effets de traînée dérivés et la réponse de la sphère aux variations de densité et de vents. Cependant, les comparaisons avec les observations LiDAR de température lors d'ITM ont montré que les sphères tombantes possèdent un biais de l'ordre de 1 K dans la haute mésosphère causé par un ralentissement lors de la transition de super à sous-sonique. Les vents verticaux peuvent également être à l'origine d'erreurs vers 30 km (Lübken et al., 1994).
- **Les jauges d'ionisation (65-130 km)** aéroportées, en météorologie, sont des instruments lancés sur des fusées-sondes pour mesurer les propriétés de l'atmo-

sphère à haute altitude. Elles embarquent une sonde de détection avec un filament chauffé et une électrode anodique, comme les jauges d'ionisation au sol. Au fur et à mesure que la fusée monte, la diminution de la densité atmosphérique réduit le nombre de collisions avec le filament chauffé, ce qui entraîne une réduction des électrons émis et des molécules de gaz ionisées. Le courant d'ionisation qui en résulte est mesuré, et la pression, la densité et la température atmosphériques à différentes altitudes sont estimées sur la base de ces données. Cependant, au-dessus de 115 km, la sensibilité limitée de la jauge et l'effet inconnu de l'oxygène atomique génère des incertitudes trop importantes. Sous 90 km, des corrections liées à l'augmentation de la densité à l'intérieur de la fusée causée par sa vitesse doivent être appliquées (Friker and Lübken, 1992).

- **Le GPS Radio Occultation (0-30 km)** est une technique de télédétection atmosphérique utilisant les signaux satellites qui a joué un rôle important dans la caractérisation de l'atmosphère planétaire depuis les années 1960. Elle s'est notamment généralisé avec l'arrivée su système GPS (Global Positioning System). Concrètement, cette technique fonctionne en exploitant le retard des signaux micro-ondes des satellites GPS réfractés lors de leur passage à travers l'atmosphère. En effet, ils subissent un changement de fréquence et de phase en raison des variations de la densité de l'air. En mesurant précisément ces changements, on peut en déduire la température, l'humidité et la pression atmosphérique à différentes altitudes. Le GPS RO est généralement efficace pour la mesure de la troposphère et de la stratosphère et offre une résolution verticale de l'ordre de quelques centaines de mètres. La résolution temporelle peut atteindre quelques minutes (Khaykin et al., 2017; KUO et al., 2004). La constellation COSMIC-2 qui utilise cette technique surveille l'atmosphère tropicale actuellement (Schreiner et al., 2020).
- **Les Satellites opérationnels** sont spécialement conçus et utilisés pour surveiller et recueillir des données atmosphériques, océanographiques et environnementales

dans le but de soutenir les activités de prévision météorologique et de surveillance climatique. L'avantage premier est qu'ils permettent de couvrir l'ensemble du globe sur les différentes couches de l'atmosphère. La mesure de la température et du vent au sein de l'atmosphère s'effectue à l'aide de radiomètres (ex : AMSU (Advanced Microwave Sounding Unit)), de spectromètres (ex : IASI (Infrared Atmospheric Sounding Interferometer)) et de récepteurs GPS embarqués à bord de ces satellites (ex : METOP, NOAA, UARS). Par exemple, le radiomètre AMSU-A à micro-ondes multicanal sonde la température atmosphérique jusqu'à 45 km en mesurant la radiance émise au zénith dans les bandes d'absorption de l'oxygène (Funatsu et al., 2011; Karbou et al., 2005). Cependant, la résolution verticale des mesures se dégradent avec l'altitude passant de quelques centaines mètres dans la troposphère à quelques kilomètres dans la stratosphère et puis à des dizaines de kilomètres dans la mésosphère. Concrètement, ces instruments mesurent principalement la radiance sur différents canaux dont la majorité est émise par la troposphère et la stratosphère (Funatsu et al., 2016).

- **Les Satellites de recherche** sont généralement lancés dans le but de mener des expériences scientifiques et de collecter des données pour la recherche et la découverte. Leur mission est axée sur l'acquisition de connaissances scientifiques et la compréhension de phénomènes naturels. Contrairement aux satellites opérationnels, a durée de vie des satellites de recherche est souvent limitée car conçus pour des missions spécifiques à court terme. Par exemple, le radiomètre SABER (Sounding of the Atmosphere using Broadband Emission Radiometry) à bord du satellite TIMED (Thermosphere Ionosphere Mesosphere Energetics Dynamics) de la NASA a pour but de nous aider à mieux comprendre les processus physiques et chimiques au sein de la mésosphère et basse thermosphère, notamment en mesurant la température. Également, à bord du satellite Aura de la NASA, l'instrument Microwave Limb Sounder (MLS) utilise des signaux micro-ondes pour évaluer la température

de la stratosphère et analyser les éléments constitutifs de la haute troposphère. Dernièrement, le LiDAR Doppler à bord du satellite Aeolus a permis de mesurer des profils de vent jusqu'à 30 km afin d'étudier la dynamique de l'atmosphère terrestre. Cependant, les profils de température obtenus par SABER et MLS semblent posséder des biais importants dans la mésosphère (Wing et al., 2018a).

- **Les Modèles numériques climatiques** sont aujourd'hui largement utilisés pour étudier le climat, les prévisions atmosphériques et le changement climatiques (O'Neill et al., 2016). Ces modèles sont basés sur des équations mathématiques (Navier-Stokes) qui décrivent les processus physiques, chimiques et dynamiques de l'atmosphère, de l'océan, de la cryosphère (glaces), de la biosphère et de la lithosphère. Ces modèles divisent la Terre en une grille tridimensionnelle, où chaque cellule de la grille représente une région spatiale. Les équations sont résolues pour chaque cellule de la grille, en tenant compte des interactions entre les cellules voisines. Il existe plusieurs types modèles climatiques à travers le monde tels que les modèles de circulation générale (GCM en anglais) ou encore les modèles dits mécanistiques. Ces derniers permettent l'étude approfondie des mécanismes responsables de certains phénomènes en simulant certaines interactions. Parmi les GCMs, on distingue deux types de modèle avec des extensions verticales différentes : les "low-top" s'étendant jusqu'à la stratopause et "high-top" intégrant la mésosphère. Cependant, bien que les modèles "high-top" simulent mieux le climat dans la stratosphère (Charlton-Perez et al., 2013), ils ne s'accordent pas sur les prévisions des apparitions des ESSs (Ayarzagüena et al., 2020). De plus, comme les mécanismes d'apparition ainsi que les effets associés aux phénomènes ITM sont encore débattus, il n'est donc toujours pas possible d'établir une paramétrisation précise au sein des modèles nécessaire à leur bonne simulation.
- **Les Modèles statistiques** permettent d'accéder à la climatologie globale des différentes variables atmosphériques (température, vent zonal, densité et pression)

pour une valeur de géopotentiel donné. Le modèle CIRA (COSPAR International Reference Atmosphere, 1986) fournit ces données de 0 à 120 km d'altitude avec une résolution verticale de 2 km et de 5° en latitude (Fleming et al., 1990). Le modèle MSIS (Mass-Spectrometer-Incoherent-Scatter) constitue la partie haute du modèle CIRA (au-dessus de 100 km) (Hedin, 1987). Ces modèles sont utiles notamment pour initier la pression en haut de l'atmosphère lors de la reconstruction du profil de densité par acquisition LiDAR Rayleigh. Cependant, la principale contrainte de ce type de modèle est de ne pas simuler la variabilité empêchant une étude statistique des ITMs et ESSs.

- **Les Analyses météorologiques (0-80 km)** représentent la plus fidèle description de l'état atmosphérique mondial à un instant donné que l'on détient. Ces analyses correspondent à la prévision d'un modèle météorologique corrigée par les observations collectées (radiosondages, radar, satellites opérationnels...). Ainsi, la qualité de ces analyses s'est améliorée au cours du temps avec notamment la mise en orbite de nouveaux satellites fournissant davantage d'observations à assimiler. Certains centres météorologiques produisent désormais des réanalyses s'étendant jusque dans la mésosphère bien qu'aucune donnée ne soit assimilée dans cette couche. Parmi les différents produits de réanalyse existants on peut trouver : ERA5 (0 à 80 km), JRA-55 (0 à 50 km) et MERRA-2 (0 à 80 km). Actuellement, le produit ERA5 bénéficie de 137 niveaux verticaux lui conférant la meilleure résolution verticale parmi les différents produits disponibles (Hersbach et al., 2020).
- **Le LiDAR** (LIght Detection and Ranging) permet de sonder avec précision la haute stratosphère et la mésosphère en émettant verticalement un laser qui interagit avec les composants de l'atmosphère. Différents systèmes LiDAR permettent de dériver des profils de température (Rayleigh de 30 à 90 km, Sodium de 80 à 110 km), de vent (Doppler-Rayleigh de 30 à 90 km) ou encore la concentration d'Ozone (de 10 à 50 km). Cette technique a déjà fait ses preuves quant à sa capacité à capturer les

processus aux fines échelles (ondes de gravité) ainsi que les élévations de température associées aux ESSs et ITMs (Hauchecorne and Chanin, 1980; Keckhut et al., 2012; Mzé et al., 2014). Un autre avantage de cette technique est de permettre des comparaisons indépendantes avec les analyses météorologiques qui n'assimilent pas les observations LiDAR. En revanche, il n'existe actuellement qu'un nombre très limité de stations où opèrent des systèmes LiDAR ne permettant pas d'avoir une couverture horizontale idéale pour l'étude de certains phénomènes.

- **Le rayonnement OH (87 km)** (OH airglow en anglais) est un rayonnement nocturne issu de la désexcitation des molécules hydroxyles OH. Ces dernières sont formées en même temps que le dioxygène moléculaire par la réaction de l'ozone avec l'hydrogène atomique à ces altitudes. Ce processus photo-chimique résulte en une couche OH d'environ 8 km avec un pique de concentration vers 87 km. Avec les molécules de dioxygène ($O_2$), elles dominent le rayonnement terrestre dans les longueurs d'ondes infrarouges courtes (short wavelength infrared (SWIR) region en anglais). Comme ce rayonnement est un indicateur très réactif des modifications de la composition chimique, de la température et des conditions dynamiques à proximité de sa source d'émission (Bellisario, Christophe et al., 2020), les observations basées sur l'imagerie se sont avérées de grand intérêt pour étudier les configurations horizontales liées à la propagation d'ondes de gravité (Abreu and Yee, 1989; Le Du et al., 2022).

Comme l'objectif de cette thèse est de mieux décrire et comprendre les phénomènes d'ESS et ITM, il est nécessaire d'utiliser, en grand nombre, des données fidèles à la réalité afin de permettre une approche comparative et statistique. Parmi les différentes techniques de mesure encore actives, il résulte que seule la technique LiDAR est capable de fournir des observations de qualité de vent et de température dans toute la moyenne atmosphère. Il apparaît que la représentation climatologique au sein des modèles statistiques ne soit tout simplement pas adaptée, par définition, à l'étude de la variabilité

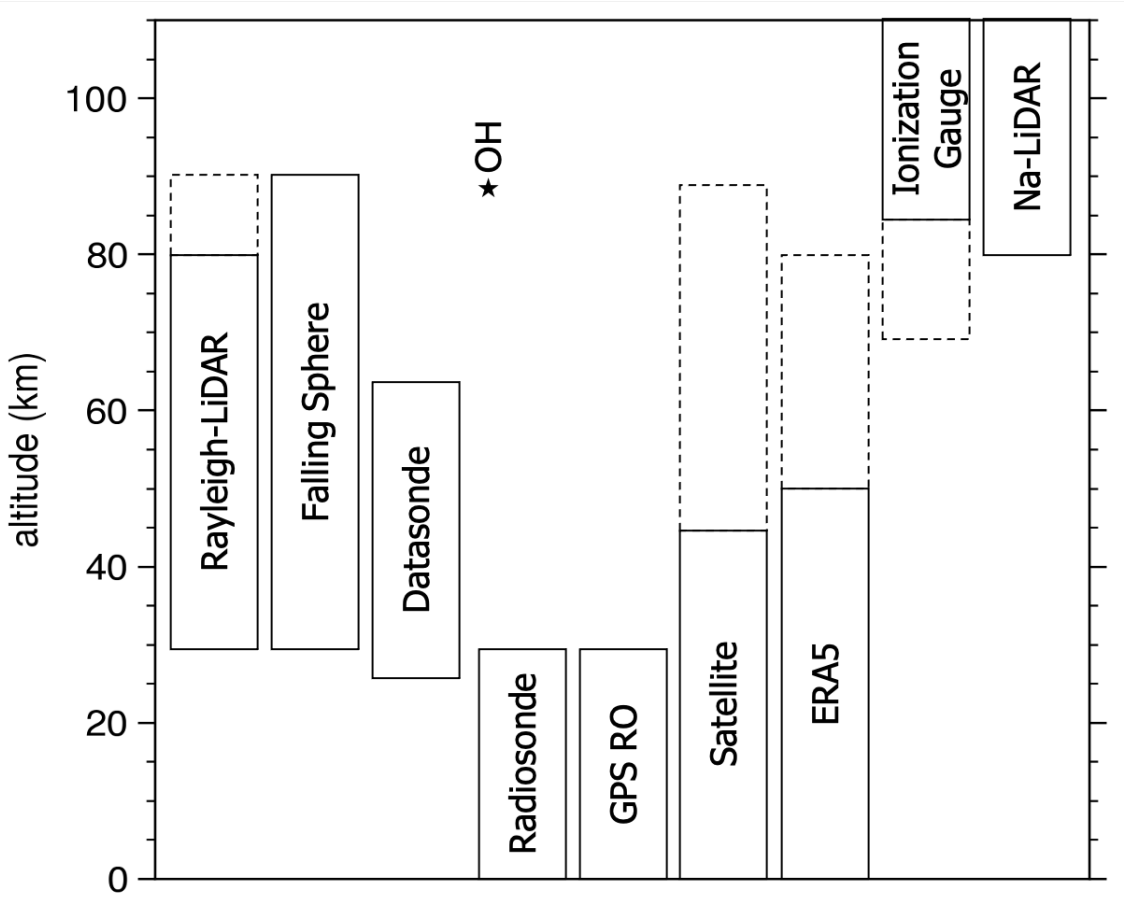


Figure 2.2 – Plage de hauteurs typiques des différentes techniques et données existantes pour mesurer et étudier la moyenne atmosphère. Les mesures individuelles peuvent s'écarter considérablement des fourchettes indiquées en raison de la variabilité des conditions d'observation et/ou de la performance des instruments. En pointillé, les altitudes où les technique et les données ne fournissent pas une fine résolution ou possèdent des incertitudes élevées ou une couverture sporadique.

dans la moyenne atmosphère mais peut servir d'élément de comparaison aux observations réalisées. L'utilisation des modèles climatiques via leurs prévisions et des modèles mécanistiques est envisageable et souhaitable pour mieux comprendre certains configurations et mécanismes associés aux ESSs et ITMs mais ne sera pas entreprise ici. Les analyses météorologiques qui assimilent des observations jusque dans la haute stratosphère et couvrent une longue période apparaissent appropriées pour permettre une étude inter-annuelle des phénomènes tel que les ESSs. En revanche, les analyses ne bénéficient d'aucune donnée assimilée dans la mésosphère contraignant le modèle à simuler la variabilité uniquement à partir d'équations mathématiques. Ainsi, afin d'étudier les ITMs, il apparaît évident d'utiliser les observations LiDAR capables de capturer fidèlement les fluctuations de vent et de température à l'origine de la variabilité sur ces gammes d'altitudes. Concernant les ESSs, en plus des observations LiDAR dans la haute stratosphère, les réanalyses assimilant le plus d'observations à l'aide de modèles météorologiques très performants sur de longues périodes semblent être les plus appropriées pour étudier ce phénomène. Parmi les produits de réanalyses existant, nous utiliserons la réanalyse ERA5 qui couvre actuellement la plus longue période (1940 à nos jours) avec le plus grand nombre de niveaux verticaux.

## 2.2 . Principe et fonctionnement de la technologie LiDAR

Depuis les années 1970, le sondage de la moyenne atmosphère a connu une révolution avec l'arrivée de la technologie LiDAR (Light Detection and Ranging) signifiant "détection et estimation de la distance par la lumière" (Collis, 1970). Le principe physique repose sur l'envoi vertical d'un faisceau laser dans l'atmosphère interagissant avec les constituants atmosphériques. L'analyse ultérieure de ce même faisceau laser retourné vers l'émetteur permet de remonter à des informations sur la structure de l'atmosphère (densité, température, concentration moléculaire, vitesse). Ainsi, le LiDAR utilise les ondes électromagnétiques proches du spectre visible contrairement à la technique du RADAR

Figure 2.3 – Photo d'un tir LiDAR réalisé à l'OHP. (Source : Yann Delcambre)

utilisant les ondes radio de grandes longueurs d'ondes. L'utilisation d'un laser par le LiDAR garantit une source lumineuse directionnelle, monochromatique, polarisée, d'amplitude élevée et cohérente. La plupart des applications requiert la détermination de la distance d'un objet à l'aide de LiDAR pulsé qui mesure le temps que met le faisceau (photon) pour revenir. D'autres LiDARs, visant à mesurer la vitesse d'un objet, émettent quant à eux une fréquence bien définie afin de déterminer le décalage de fréquence entre l'onde émise et celle reçue.

L'un des principaux avantages de cette technique est la haute résolution verticale des mesures permettant l'étude des phénomènes dynamiques aux fines échelles à courts termes tels que les ondes de gravité. De plus, comme le LiDAR est une technique non intrusive n'interférant pas avec le milieu observé, il permet des observations in situ sans perturbation. En fin de compte, le LiDAR présente la capacité de réaliser des mesures continues sur de longues durées, ouvrant ainsi la possibilité d'analyser les variations sai-

sonnières sur des périodes étendues (Hauchecorne et al., 1991). Cependant, cette technique est fortement dépendante des conditions météorologiques requérant un ciel sans nuages. De plus, en fonction du paramètre atmosphérique étudié, il existe plusieurs systèmes LiDAR utilisant différents types d'interactions rayonnement-matière : les diffusions Rayleigh, Mie, Raman, l'absorption ou la fluorescence possédant chacune des gammes d'altitude accessibles propres.

Par exemple, le LiDAR dit Rayleigh basé sur la rétrodiffusion Rayleigh des molécules d'air permet de mesurer la densité atmosphérique et d'en déduire la température via l'équilibre hydrostatique. Cette mesure est réalisée dans la région comprise entre 30 et 90 km où une diffusion moléculaire pure est attendue. Précisément, le principe de cette mesure repose sur le comptage de photons rétrodiffusés par les couches atmosphériques. L'incertitude liée à ce comptage des photons suit une statistique de loi de Poisson qui varie comme l'inverse de la racine carrée du nombre de photons comptés et donc croit exponentiellement avec l'altitude. C'est pourquoi cela en fait un instrument de choix pour l'étude des phénomènes se produisant au sein de la moyenne atmosphère. Depuis 1979, un LiDAR Rayleigh opère à l'Observatoire de Hautes-Provence (OHP, 44°N-6°E) en France et fournit environ une dizaine de profils de température par mois allant de 30 à 90 km. Ceci en fait la plus longue série de profils de température de la moyenne atmosphère sur Terre. Ce LiDAR est intégré dans le réseau international NDACC (Network for the Detection of Atmospheric Composition Change) et a été mis en place dans le cadre du réseau dédié à la surveillance de l'ozone. Le principe de ce LiDAR ainsi que les erreurs associées à la mesure sont expliquées en détail dans Hauchecorne and Chanin (1980) et Keckhut et al. (1993).

D'autres LiDARs opèrent également à l'OHP, un LiDAR Ozone et un LiDAR Doppler permettant respectivement la mesure de concentration de l'ozone dans la stratosphère et la vitesse du vent dans la moyenne atmosphère (Wing et al., 2018b). Cependant, actuellement le LiDAR Doppler utilise le même faisceau laser que celui utilisé pour le LiDAR Ray-

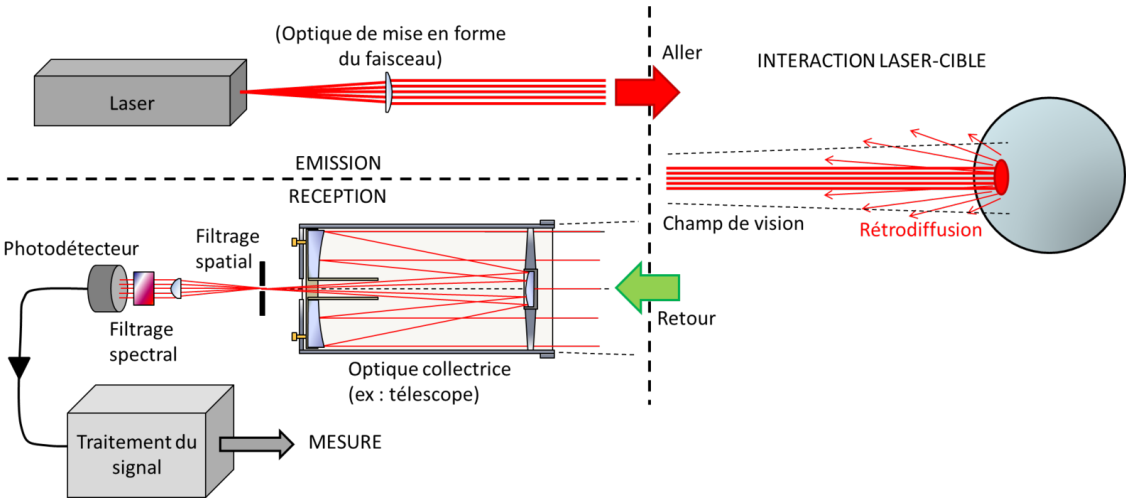


Figure 2.4 – Schéma de principe de fonctionnement d'un système LiDAR et de la mesure. (Source : https://fr.wikipedia.org/wiki/Lidar)

leigh Température empêchant des mesures simultanées avec ces deux instruments. Pour réaliser des mesures simultanées vent-température à l'OHP, les températures peuvent être acquises sur la voie off du LiDAR Ozone .

## 2.3 . Archives du climat passé : les réanalyses

### 2.3.1 . Principe

L'objectif des réanalyses météorologiques est de conserver la meilleure représentation des différentes variables physiques définissant l'état de l'atmosphère passé sur l'ensemble du globe. Ces nombreuses variables météorologiques conservées sont entre autre la température, la pression, le vent, l'humidité ou encore le géopotentiel. Ces archives du temps passé enregistrées dans des banques de données sont essentielles pour la communauté scientifique qui étudie l'évolution du climat au cours du temps et les variations saisonnières générées par les différents phénomènes météorologiques. Ces réanalyses sont aussi très utiles pour la validation de certains modèles climatiques et évaluer les prévisions météorologiques.

Concrètement, les réanalyses météorologiques sont construites à partir des analyses

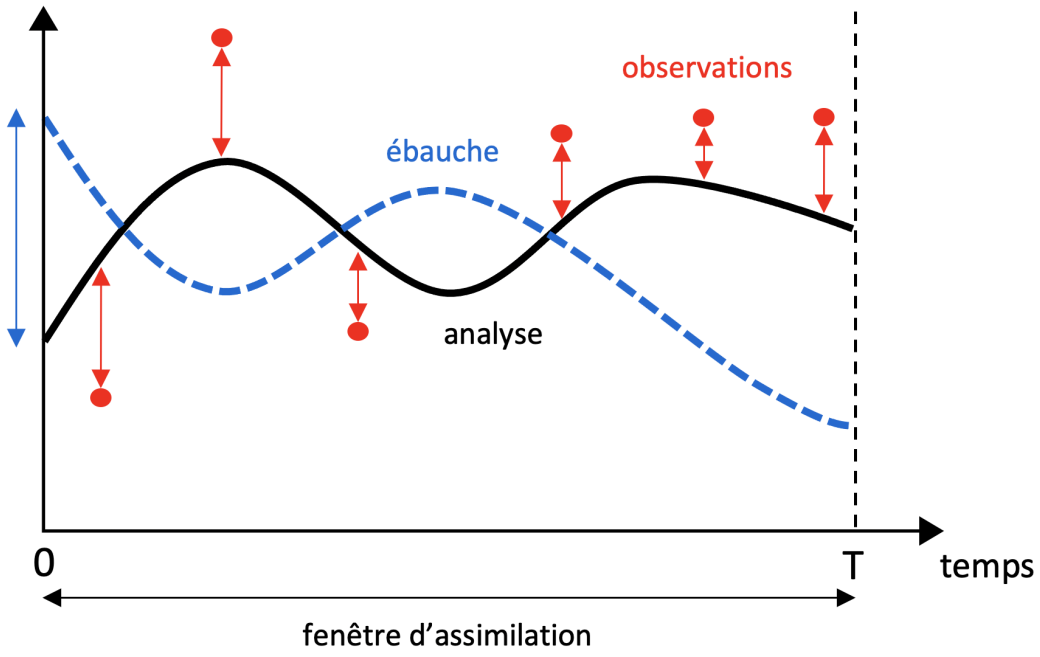


Figure 2.5 – Représentation simplifiée d'un schéma d'assimilation 4D-Var. On cherche à obtenir la trajectoire analysée du modèle (courbe pleine noire) qui soit à la fois proche des observations (cercles rouges) et de l'ébauche fournie par une prévision antérieure (courbe en tiretés bleue).

élaborées par les modèles de prévision numérique du temps. Les précédentes analyses sont générées par des modèles basés sur des équations physiques qui décrivent le comportement de l'atmosphère et de l'océan. Précisément, les analyses représentent le meilleur compromis entre une ébauche, c'est à dire une prévision récente d'un modèle météorologique réalisée, et les observations afin de conserver une représentation réaliste. Cette approche constitue l'assimilation de données par les modèles numériques de prévision du temps (Navon, 2009). On qualifie cette méthode de « 3D-Var » lorsque seule l'état du modèle et les observations valides au moment de l'analyse sont prises en compte. Elle est appelée « 4D-Var » lorsqu'elle inclut également l'évolution de ces éléments sur une période de temps donnée. Le principe de la 4D-Var est illustré sur la Figure 2.5. Ces modèles d'assimilation sont largement utilisés afin de prendre en compte les erreurs associées aux prévisions et aux observations. Les différentes sources d'observations assimilées sont entre autre les satellites, les radiosondages, les stations au sol, les avions et les bouées océaniques.

Ainsi, les réanalyses sont produites à partir de ces analyses, qui peuvent être corrigées à nouveau avec des observations supplémentaires, sur une grille horizontale et verticale bien définie et couvrant des décennies. Cependant, l'une des principales limites de cette approche est l'inhomogénéité de la couverture spatiale et temporelle des observations sur l'ensemble du globe. De plus, certaines observations comme la couverture nuageuse ou les précipitations sont compliquées à obtenir et peuvent conduire à des incertitudes dans les réanalyses.

### 2.3.2 . Les réanalyses ERA5

De nos jours, il existe plusieurs ensembles de réanalyses météorologiques utilisés par la communauté scientifique, tel que le produit NCEP/NCAR Reanalysis (Kalnay et al., 2018), le produit ERA-Interim (Dee et al., 2011) ou encore JRA-55 (KOBAYASHI et al., 2015) développés par des centres de recherche météorologique à travers le monde. Au fil des années, différents produits de réanalyses se sont succédés, chacun fournissant systéma-

tiquement à sa sortie une meilleure qualité de données que l'ancien produit. Ces améliorations sont notamment le fait de la disponibilité de nouvelles observations pouvant être assimilées ou par des modifications dans le modèle telles l'affinement de la résolution spatiale et temporelle ou encore une meilleure paramétrisation de processus physiques. Par exemple, la production des réanalyses ERA-Interim, couvrant la période 1979-2019 sur une grille de 80 km, a été stoppée en 2020 par le centre européen pour être définitivement remplacé par le nouveau produit ERA5, couvrant la période de 1940 à nos jours sur une grille de 31 km.

En effet, depuis 2016, dans le cadre du Service des changements climatiques de Copernicus (C3S), le centre européen CEPMMT (Centre Européen pour les Prévisions Météorologiques à Moyen Terme) produit la dernière génération de réanalyses, ERA5 (Hersbach et al., 2020). Ces réanalyses sont produites à l'aide du nouveau Système de Prévision Intégré Cy41r2 bénéficiant de décennies de développement dans la physique du modèle, la dynamique des noyaux et l'assimilation de données. L'état de l'atmosphère est reproduit toutes les heures sur une grille avec une résolution horizontale d'environ 31 km et sur 137 niveaux verticaux s'étendant de la surface à 0.01 hPa (environ 80 km).

Dans ce travail, les réanalyses ERA5 de température seront tout d'abord évaluées dans la moyenne atmosphère puis mises à profit afin d'étudier les phénomènes d'échauffements stratosphériques soudains et inversions de température mésosphériques.

# 3 - Évaluation de la variabilité au sein de la Moyenne Atmosphère dans les ré-analyses de température ERA5

## 3.1 . Introduction

Dans ce chapitre, nous procédons à l'évaluation des biais moyens ainsi qu'à l'examen de la capacité des réanalyses de température d'ERA5 à reproduire la variabilité observée dans la moyenne atmosphère aux moyennes latitudes au cours des saisons hivernales et estivales. Un autre objectif consiste à estimer l'incertitude du modèle dans la simulation de la variabilité saisonnière. Cette évaluation est menée en comparant les réanalyses à quinze années d'observations LiDAR recueillies à l'OHP entre 2005 et 2020. L'un des avantages notables réside dans le fait que les observations LiDAR de l'OHP, qui servent aujourd'hui de référence, capturent, avec une grande précision et une résolution verticale fine, les fluctuations engendrées par divers phénomènes de petites et grandes échelles. En effet, la localisation de l'OHP (44°N-6°E), en bordure du vortex polaire, se révèle idéale pour étudier les variations induites par les échauffements stratosphériques soudains et les inversions de température mésosphériques. En outre, les observations LiDAR permettent des comparaisons indépendantes, n'étant pas assimilées dans les réanalyses d'ERA5. Ainsi, les observations LiDAR de l'OHP se positionnent comme un choix privilégié pour évaluer de manière aussi précise que possible la qualité des réanalyses d'ERA5.

## 3.2 . Article

L’article ci-dessous a été publié dans le journal "Atmosphere" de MDPI le 31 janvier 2022.

*atmosphere*

MDPI

*Article*

# Assessment of ERA-5 Temperature Variability in the Middle Atmosphere Using Rayleigh LiDAR Measurements between 2005 and 2020

**Alexis Mariaccia [1,*], Philippe Keckhut [1], Alain Hauchecorne [1], Chantal Claud [2], Alexis Le Pichon [3], Mustapha Meftah [1] and Sergey Khaykin [1]**

[1] Laboratoire Atmosphères, Milieux, Observations Spatiales, UMR 8190, Institut Pierre-Simon Laplace, Université Versailles-Saint Quentin, Université Paris-Saclay, 78280 Guyancourt, France; philippe.keckhut@latmos.ipsl.fr (P.K.); alain.hauchecorne@latmos.ipsl.fr (A.H.); mustapha.meftah@latmos.ipsl.fr (M.M.); sergey.khaykin@latmos.ipsl.fr (S.K.)

[2] Laboratoire de Météorologie Dynamique/IPSL, CNRS, UMR 8539, École Polytechnique, 91120 Palaiseau, France; chantal.claud@lmd.ipsl.fr

[3] Commissariat à l'Energie Atomique (CEA), Direction des Applications Militaires (DAM), Campus Île-de-France (DIF) Bruyères-le-Châtel, 91297 Arpajon, France; alexis.le-pichon@cea.fr

* Correspondence: alexis.mariaccia@latmos.ipsl.fr

**Abstract:** In this study, the temperature biases and the ability of the ERA-5 product to reproduce the LiDAR variability in the 30–80 km altitude range were evaluated for the period 2005–2020, both for the winter and the summer months. During winter, temperatures from the ERA-5 dataset were in good agreement with LiDAR observations up to 45 km, while in the mesosphere, almost 70% of the ERA-5 profiles were cooler than those from LiDAR, except around 65 km. During summer, negative biases of −3 K were observed up to the stratopause, while significant positive biases of more than +10 K were found in the mesosphere. For the winter months, the variability observed by LiDAR, even during sudden stratospheric warming (SSWs) events, was reproduced accurately by the model in the upper stratosphere, but not in the mesosphere. Surprisingly, the LiDAR variability mainly due to propagating gravity waves in the summertime was also not reproduced by ERA-5 in the whole middle atmosphere. The model uncertainty associated with this variability, evaluated afterward with a new method, grew as expected with altitude and was more significant in winter than summer. A principal component analysis of the fluctuations of the temperature differences between the LiDAR and ERA-5 was performed to investigate the vertical coupling between 30 km and 70 km. The three first vertical modes illustrated 76% and 78% of the fluctuations of the temperature difference profiles in summer and winter, respectively, confirming the connection between the studied layers. The leading modes of the summer (49%) and winter (42%) possessed an anti-correlation between the upper stratosphere and the mesosphere, where fluctuations increased (at least ±5 K at 65 km) for both seasons due to the coarse vertical resolution in the model. The other modes showed an agreement between the LiDAR and ERA-5 fluctuations in the upper stratosphere and had a wave-like structure mainly located in the mesosphere, confirming that the model either overlooked or simulated imprecisely the gravity waves, leading to mesospheric inversions. Finally, SSWs impacted the ERA-5 temperature (deviation of ±3 K) some days before and after its trigger around the stratopause.

**Keywords:** middle atmosphere; winter; summer; temperature; LiDAR; ERA-5 reanalyses; polar vortex



**Citation:** Mariaccia, A.; Keckhut, P.; Hauchecorne, A.; Claud, C.; Le Pichon, A.; Meftah, M.; Khaykin, S. Assessment of ERA-5 Temperature Variability in the Middle Atmosphere Using Rayleigh LiDAR Measurements between 2005 and 2020. *Atmosphere* **2022**, *13*, 242. https://doi.org/10.3390/atmos13020242

Academic Editors: Andrey Koval and Alexander Pogoreltsev

Received: 3 December 2021
Accepted: 27 January 2022
Published: 31 January 2022



## 1. Introduction

Meteorological reanalyses provided by the European Centre for Medium-Range Weather Forecasts (ECMWF) are widely used for weather forecast and by the scientific community in order to access the atmospheric state at any time and to study the different atmospheric processes (e.g., [1–3]). Reanalysis, computed by the Integrated Forecasting

System (IFS) in the ECMWF model, is defined as being a combination of global available observations with a forecast using a sophisticated community numerical model coupling many different sub-systems including interacting radiative dynamical and chemistry processes. Such reanalyses have been regularly improved thanks to the availability of new observations or model improvements such as their spatial resolution, domain expansion, or new sub-grid processes' parameterizations. The top altitude and the number of levels increased as forecasts were improved. With these improvements, two types of general circulation model appear: the "high-top" models with a well-resolved stratosphere and the "low-top" models having a coarse resolution in the stratosphere and a lower top boundary [4]. Charlton-Perez et al. [5] compared different climate numerical models within the Fifth Coupled Model Intercomparison Project (CMIP5) experiment with different reanalysis packages MERRA, ERA-Interim, and ERA-40, revealing that high-top models simulate more accurately the stratospheric daily and interannual variability than low-top models. This issue is strong as the stratospheric circulation, which can affect the tropospheric weather (e.g., [6,7]), is therefore better reproduced by models that possess a mesosphere. Thus, adding more levels and the mesosphere domain within the models and the reanalysis packages has seen a growing interest for weather forecast and climate issues.

While the operational version of the ECMWF analysis uses a model in permanent evolution and avoiding any disruption on the analysis series, the ECMWF produces some reanalyses using the same methodology during the total period for climate issues. Since the beginning of reanalysis activities within the ECMWF community, the quality of the atmospheric reanalyses has continuously improved with the development of the forecast models, the new techniques of data assimilation, and the better quality of the new observations. As a result, several generations of reanalysis packages have succeeded each other, such as ERA-15, ERA-40, and ERA-Interim, by improving many aspects each time [8]. The production of the ERA-Interim reanalysis was stopped before 2020 to be replaced by the new and fifth-generation of global reanalysis built by ECMWF, the ERA-5 package, covering the entire mesosphere [9]. Temperatures in the ERA-5 dataset assessed here cover the period from 1950 to the present and implemented 137 verticals levels from the surface up to 0.01 hPa (approximately 80 km) [10]. However, most of the assimilated data are radio soundings lying from the surface to the lower stratosphere and satellite radiance measurements, whose weighting functions peak mainly in the troposphere and the stratosphere [11,12]. Therefore, no operational observations constrain the ERA-5 temperature reanalyses in the mesosphere. Even if the objective of increasing altitude range was primarily to improve the stratospheric part in pulling up the top-model boundary, it is interesting to assess the temperature accuracy both in the stratosphere and the mesosphere domain.

This is why several studies have been undertaken to assess the ERA-5 temperatures in the mesosphere by determining its existing temperature biases with, as in this study, Observatory of Haute-Provence (OHP) LiDAR observations. Some comparisons between LiDAR and the ECMWF operational analyses have already been performed over monthly periods [13,14] and recently above four stations between 1990 and 2017 [15]. A general agreement with LiDAR observations has been found in the upper stratosphere. Large biases have been already observed in the mesosphere, and larger variability in the upper stratosphere during winter than in summer was reported [13–15]. This difference between summer and winter is not surprising according to the circulation in the stratosphere [16] due to the wind reversal and the blocking of planetary wave propagation in summer. Temperature biases present in ERA-5 data have evolved with time with the inclusion of new satellite data in the data-assimilation system from COSMIC GPSRO and AMSU-A on NOAA-15 and then on NOAA-16 [17]. According to Marlton et al. [15], the intensification of the warm bias in the upper stratosphere above OHP between 2000 and 2007 is due to the introduction of AMSU-A data from NOAA-16.

In the present work, the temperature biases in the middle atmosphere in the ERA-5 dataset were updated with a seasonal approach for the period between 2005 and 2020.

The main novelty here, in order to pursue the previous studies, was the assessment of the variability of the model using LiDAR observations.

Systematic LiDAR observations performed within the Network for the detection of Composition Changes (NDACC) were used for trend estimates [18] and showed they can be used as a benchmark for time continuity for satellite cross-adjustment, long-term analyses, and numerical climate models [19,20].

The LiDAR variability, as well as its climatology have already been investigated at OHP in the south of France [16] and with LiDAR at different locations [21]. The interest of using the OHP LiDAR, in addition to the high quality of its temperature products [20], is the quasi constant number of measurements carried out each month, 10 on average here, allowing a good representation of dynamic phenomena on the scale of a few days. The observation of a polar stratospheric cloud by Keckhut et al. [22] confirms that the OHP located at mid-latitude in the Northern Hemisphere is nearly at the edge of the polar vortex and therefore ideally placed according to disturbances induced by planetary wave propagation and Sudden Stratospheric Warmings (SSWs) [23,24]. As only a few instruments cover the middle atmosphere, it is relevant to choose the OHP LiDAR to evaluate the dynamic representation of the ECMWF model at mid-latitudes in the Northern Hemisphere. Moreover, independent comparisons are allowed as the LiDAR observations are not considered in the assimilated data to construct reanalyses. While the upper atmosphere is mainly forced by surface and lower meteorological events, we propose an advanced analysis of the vertical correlation of the biases to study the processes linking the top and the bottom of the atmosphere. As cooling often accompanies the stratospheric warmings in the mesosphere, the impact of SSWs on the comparisons between the LiDAR and ERA-5 at the stratopause was also investigated.

The paper is organized as follows. The description of OHP Rayleigh-Mie LiDAR observations and ERA-5 reanalyses is given in the next section. In Section 3, the mean temperature difference profiles between the LiDAR and ERA-5 are computed both in winter and in summer. The model variability is assessed in Section 4. Afterward, a method is proposed to quantify the model uncertainty relative to the variability observed by the LiDAR in Section 5. Then, in Section 6, the main systematic biases between the LiDAR and ECMWF are analyzed. In Section 7, the impact of SSWs on the temperature differences at the stratopause is investigated. Finally, a conclusion is given in Section 8.

## 2. Data Description

### *2.1. OHP LiDAR*

The vertical temperature profiles used in this study came from the routine observations acquired by one of the LiDARs located at the Observatory of Haute-Provence (OHP, 44° N, 6° E). The physics principle of the Rayleigh LiDAR is based on the backscattering of a monochromatic emitted laser pulse by atmospheric molecules providing vertical air density profiles in relative values. More precisely, the backscattered photons by the sounded atmospheric layers are collected by a telescope. Then, the number of photons counted allows for deducing the vertical structure of the density. The hydrostatic equilibrium and the ideal gas law are afterward used to derive a 30–90 km temperature profile, where we expect a pure molecular scattering. The uncertainty attached to this photon-counting follows a Poisson law of statistics and is given by the square root of the number of photons received. The statistical uncertainty is the main limitation for LiDAR observations, and the potential biases are eliminated by robust instrumental design and regular inter-comparison exercises. A complete detailed description of the technique employed, as well as the uncertainties associated has already been presented in several publications [16,25].

The LiDAR Température et Aérosols (LTA) at OHP has measured nightly temperature in the middle atmosphere (M.A.) since 1979, providing around 15–20 mean profiles per month as the sky needs to be clear to perform an observation. This world's longest LiDAR temperature series have been implemented within the Network for the Detection of Composition Changes (NDACC) for trend studies [26,27] within the ozone-monitoring

program, as well as satellite validation [28]. A seeded Nd:YAG laser is used to produce a light pulse at 532 nm with a maximum power of 24 W. The LiDAR has a transmitted beam with a 30 Hz repetition rate and a time and vertical resolution respectively of nearly 3 min and 75 m (other LiDAR characteristics can be found in Keckhut et al. [25]). The time integration of the LiDAR (typically 2–6 h) and the vertical smoothing performed with a Hanning window over 2 km provide accurate temperature in the 30–90 km altitude range with 1 km sampling steps. The temperature uncertainties are mainly due to random errors and can attain an accuracy of 1 K from 30–70 km and 3 K at 80 km [25,29]. Statistical noise increases with altitude as soon as the air density decreases. The top part around 90 km could be affected by background noise estimates and initialization of the pressure profile with the MSIS-90 model [30] becoming rapidly negligible due to its exponential decrease. Despite these existing uncertainties, the OHP Rayleigh LiDAR can accurately capture perturbations generated by gravity waves in the mesosphere around 75 km, confirming the reliability of its temperature measurements at these altitudes [31]. Regular exercises are performed to check the LiDAR's capability to monitor the long-term temperature changes within the NDACC [28,32,33], and cross-comparisons with a mobile LiDAR allow checking the homogeneity of the network [33,34]. These temperature profiles are all archived in the National Ocean and Atmosphere Administration (NOAA) NDACC and the AERIS portals. The studied period here corresponds to the most recent data extending from 2005 to 2020, during which the OHP LiDAR acquired 1505 nights of observations, i.e., around 10 observations per month. There are no LiDAR data from September 2009 to September 2012 due to the presence of interference between two collocated LiDARs. Outside this period, the LiDAR data are spread uniformly [28].

Figure 1 illustrates the data used here and shows the evolution of the temperature profiles from the LiDAR and the ECMWF for three dates selected in January 2019 during which an SSW event occurred. Thus, according to these profiles, the model accurately simulated the magnitude of the warming in the upper stratosphere where SSWs occur, but not the temperature variations in the mesosphere where the vertical resolution decreases.

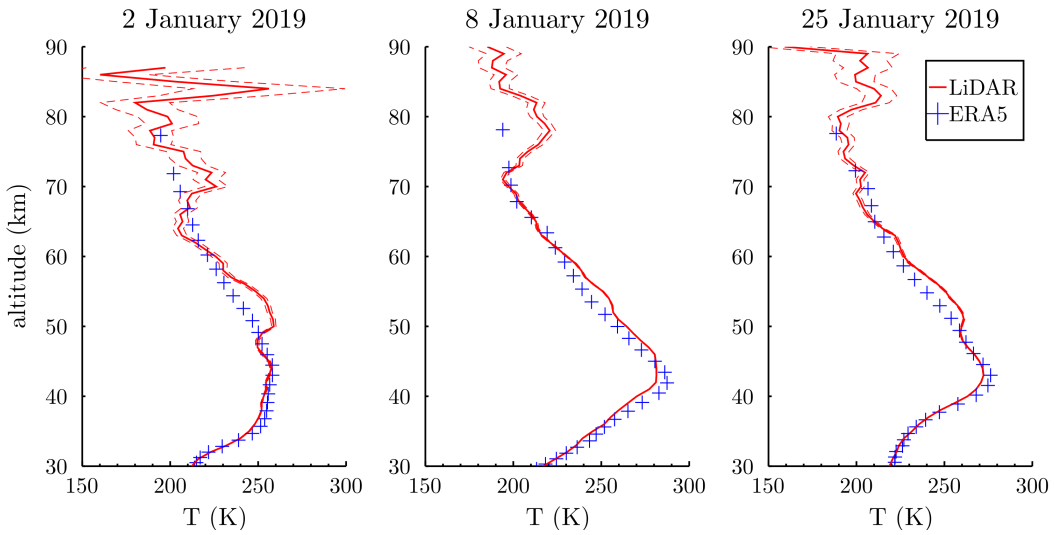


**Figure 1.** Temperature profiles from the LiDAR (red solid line) and the ECMWF (blue cross) for three dates selected in January 2019 during an SSW event. Instrumental errors from the LiDAR (red dashed lines) are added as well.

LiDAR observations are performed at night, and operations depend on a clear sky. Usually, observations are conducted during the first part of the night between 8 p.m. UTC and midnight and integrated over several hours. Here, temperature profiles from the ERA-5 product were extracted at the starting time of each LiDAR observation to perform individual comparisons. We considered that the average of ERA-5 temperature profiles over the observation time was not necessary as most of the LiDAR acquisitions last 2–3 h

and tidal effects are negligible over this small interval of time. Another interest in using LiDAR observations is that they are not assimilated data used to build the ERA-5 product and allow independent comparisons.

### *2.2. ECMWF: ERA-5 Product*

The new ERA-5 product benefits the updated ECMWF Integrated Forecast System (IFS) Cycle 41r2 and better model parametrizations of convection and microphysics. The ERA-5 output is produced throughout hourly on a 0.25° latitude–longitude grid and 137 vertical levels from the surface to the level pressure 0.01 hPa, enhancing both the temporal and spatial resolution compared to the 6 h ERA-Interim product computed on a 0.75 latitude–longitude grid with 60 vertical levels lying from the surface to 0.1 hPa. The distance between the OHP LiDAR and the selected grid cell of ERA-5 is estimated to be about 25 km. For these new reanalyses, a 12 h window between 09:00 UTC and 21:00 UTC and another from 21:00 to 09:00 UTC (the following day) are used by the assimilation system [10]. Currently, the period covered by the complete ERA-5 homogeneous analysis lies from 1950 to the present. The cold bias in the lower stratosphere from 2000 to 2006in the ERA-5 analyses is corrected in the new ERA-5.1 analyses [17].

In this study, we extracted ERA-5 temperatures at the nearest hour of the starting time of the LiDAR acquisition, and then, we compared them with the temperature observed by the OHP LiDAR. Firstly, we used a product to convert the 137 pressure levels into geometric altitude levels for each ERA-5 profile to compare them with LiDAR profiles. Since the vertical resolution is much better in the LiDAR data, we interpolated each LiDAR profile to the corresponding ERA5 profile before computing the difference. In addition, as the geometric altitude levels computed are different for each ERA5 profile, it was also necessary to re-interpolate afterward the differences between the LiDAR and ERA-5 over the altitude range 31–79 km (1 km step by step) in order to evaluate the systematic biases and the variability and to perform the PCA for both seasons.

## 3. Assessment of Systematic Differences between ERA-5 and the OHP LiDAR

### *3.1. Result*

Due to the variability, two seasons of 3 months were considered. The periods selected correspond to 3 months for both winter (December, January, February) and summer (June, July, August) to avoid the transition period of spring and autumn seasons while the vortex appears and disappears at very different times from one year to another (Figure 2). The LiDAR data possess 368 profiles for the winter season and 381 profiles for the summer season over the period 2005–2020.

In wintertime, LiDAR observations and ERA-5 profiles are in good agreement up to 45 km (Figure 2) with a slight warm bias of the model around 40 km (−1 K). This agreement was also retrieved by Marlton et al. [15], who found a temperature bias of ±1 K up to 1 hPa, confirming the good thermal representation of the model in the stratosphere. This good agreement at zonal mean levels at all latitudes, but with limb sounder observations, was also reported in Wright and Hindley [35], confirming the quality of the ERA-5 product in the stratosphere. In the mesosphere, the biases of the temperature differences are all positive and highly significant (+7 K on average between 50 km and 80 km) and exhibit two maxima of +7 K and +13 K at around 55 km and 75 km, respectively. The temperature differences of the LiDAR and model were assumed to follow a normal law distribution. Therefore, standard deviations in the mesosphere indicate that almost 70% of the ERA-5 profiles are cooler than the temperature derived from LiDAR data, except around 65 km, where differences are minor with a mean difference of +3 K. The LiDAR and ECMWF temperature profiles well illustrate this mean behavior in winter shown in January (Figure 1). Similar results were found above Sodankylä in Finland during December 2015 by Ehard et al. [14], who concluded that these temperature deviations in the mesosphere were amplified by the last horizontal resolution upgrade, as well as by the new cycle of the data-assimilation system.

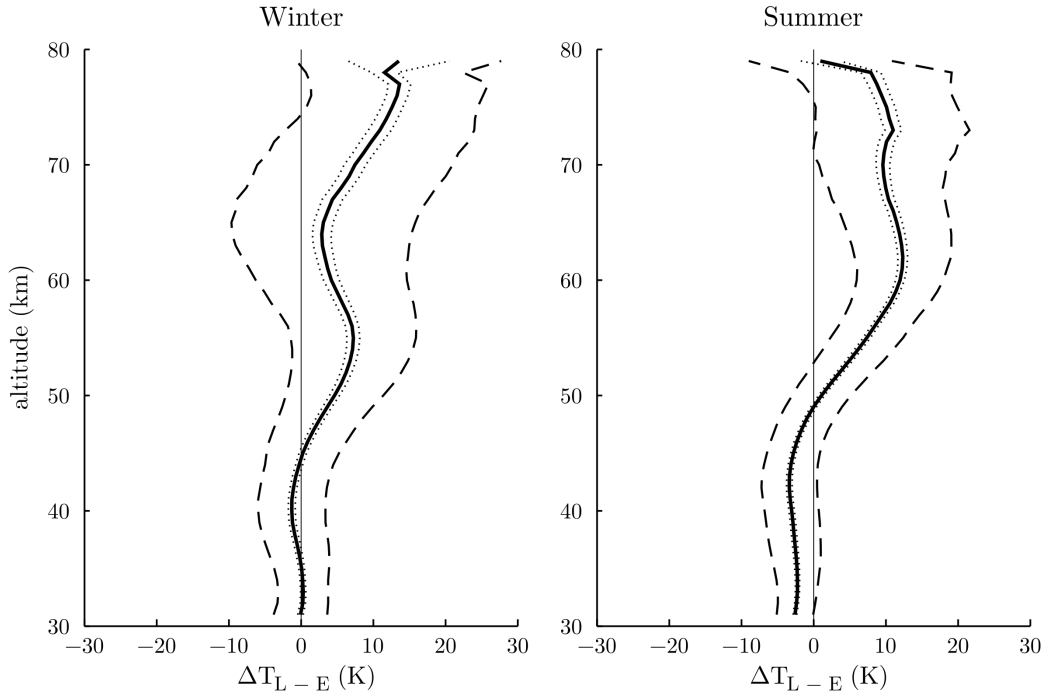


**Figure 2.** Mean of the temperature difference profiles (bold black lines) between the LiDAR and ERA-5 computed between 2005 and 2020 for both seasons. Dotted and dashed black lines represent respectively the 95% confident interval and the standard deviation.

Regarding the summer period, comparisons show a similar vertical pattern. However, differences in the upper stratosphere are more considerable and more significant with quasi constant negative biases of −3 K. The same behavior in the upper stratosphere was observed by Marlton et al. [15], who found a slight warm bias of the model during the summer months. A positive bias is observed in the entire mesosphere with a mean difference of +10 K around 60 km without decreasing at 65 km, as observed for the winter months. Thus, the trend in the mesosphere during winter is enhanced in summer, where almost all of the ERA-5 profiles are cooler than the LiDAR observations. In the next section, to complete the previous studies focusing only on the model biases, the evaluation of the ERA-5 product is further pursued by studying the model's ability to simulate the seasonal variability.

### *3.2. Discussion of Winter Biases in the Mesosphere*

In Figure 1, the warming between 50 km and 60 km observed by the LiDAR and temperature inversions occurring around 70 km are not present in the ERA-5 temperature profiles. At first glance, we could be tempted to explain the absence of the warming between 50 km and 60 km in the ERA-5 profiles by the SSW occurring in the lower part affecting the ERA-5 temperature in the mesosphere. However, this difference between the LiDAR and ERA-5 tends to decrease when the temperature increases in the upper stratosphere. Interestingly, this difference observed is retrieved in the profile of mean temperature differences for the winter months (Figure 2). Moreover, few SSW events (18) are covered by LiDAR observations over the studied period, while the mean biases in winter are computed over 368 profiles. This result suggests that the temperature differences in the mesosphere are not due to the occurring SSW, but to, first, systematic biases in the model and fluctuations at small scales, essentially due to gravity waves, observed by the LiDAR, but not simulated by the model in the mesosphere. Indeed, even though gravity waves with large amplitudes are well parameterized in ERA-5 and a vertical smoothing over 2 km has been applied on the LiDAR data, it can maintain observed perturbations whose

scales are sub-grid. In order to confirm that this model bias is not related to an imperfect simulation of SSWs, we studied afterward the model variability and the error associated.

## 4. Study of the Model Variability

### *4.1. Winter*

In order to assess the temporal variation of the modeled temperature, the individual temperature differences between the LiDAR and the ECMWF ($\Delta T_{L-E}$) were calculated over the three respective months of winter and summer at each altitude. The individual temperature deviations of ERA-5 profiles to their seasonal mean ($\Delta T_{E-ESM}$) and of the LiDAR profiles to their seasonal mean ($\Delta T_{L-LSM}$) were similarly computed to allow comparisons with $\Delta T_{L-E}$. In this section, two comparisons were investigated, the one between $\Delta T_{L-E}$ and $\Delta T_{L-LSM}$ and the one between $\Delta T_{E-ESM}$ and $\Delta T_{L-LSM}$. Motivated by the divergence observed between the mean of the temperature difference profiles (Figure 2), these comparisons aimed to assess both the capacity of the model to reproduce the variability observed in the LiDAR measurements and the model divergence to the LiDAR seasonal mean. In the linear regression equations computed between temperature differences $\Delta T_{L-E}$ and $\Delta T_{L-LSM}$, the slope coefficient represents how the observed variability is reproduced in ERA-5 and the y-intercept represents the model bias. Concretely, a slope coefficient of one means that the model behaved as the seasonal mean and did not reproduce the observed variability. This is the opposite for comparisons between $\Delta T_{E-ESM}$ and $\Delta T_{L-LSM}$.

Comparisons at 40 km during winter (Figure 3a) showed an excellent agreement (slope coefficient of one with zero bias) between $\Delta T_{E-ESM}$ and the temperature fluctuations observed with the LiDAR $\Delta T_{L-LSM}$. In addition, the value computed for the determination coefficient ($r^2 = 0.89$) confirmed the quality of the linear regression applied here. Both temperature fluctuation distributions revealed a bi-modal function with two maxima centered at −10 K and +20 K. This bi-modal distribution was already shown in Angot et al. [23], who concluded that the second peak was associated with SSW events. Despite this high variability, the model succeeded in reproducing the same temperature evolution with its seasonal climatology as the LiDAR observations in the upper stratosphere during winter. The temperature differences between the LiDAR and ERA5 ($\Delta T_{L-E}$) were afterward corrected by the linear regression ($\Delta T_{L-E} - y$), i.e., we subtracted from each $\Delta T_{L-E}$ value the corresponding $y(\Delta T_{L-LSM})$, in order to remove the model biases and the variability common to $\Delta T_{L-E}$ and $\Delta T_{L-LSM}$. The small normal distribution found for $\Delta T_{L-E} - y$ with a standard deviation of 4.6 K (Figure 3c) was associated with noise either due to the LiDAR instrumentation or due to model and assimilation effects for the ECMWF. A disagreement was noted in the mesosphere. For example, at 70 km (Figure 3d), the slope coefficient between ERA-5 fluctuations and LiDAR fluctuations decreased down to 0.2, showing that a large part of the variability observed with the LiDAR was not included in the meteorological model. This trend was true in the whole mesosphere. The evolution of the slope coefficients between $\Delta T_{E-ESM}$ and $\Delta T_{L-LSM}$ showed that the excellent agreement found in the upper stratosphere decreased from the stratopause (Table 1). This calculation confirmed that the model had a climatology cooler than the LiDAR in the mesosphere during winter. However, around 65 km, the mean difference still exhibited a small bias of +3 K. This suggests that mean differences between both climatologies and the capability to reproduce the LiDAR variability by the model are independent issues. When the differences between the LiDAR and ERA-5 ($\Delta T_{L-E}$) were compared with the LiDAR fluctuations ($\Delta T_{L-LSM}$), a linear correlation was found with relative large slope coefficients reaching values as large as 0.8 (Table 1), suggesting that the ECMWF model does not reproduce a significant part of the variability observed by the LiDAR.

Indeed, the slope coefficient between $\Delta T_{L-E}$ and $\Delta T_{L-LSM}$ increased from the stratopause, suggesting that the ECMWF model tends to behave as the LiDAR climatology in the mesosphere. The opposite evolution of the slope correlation coefficient over the altitude was observed between $\Delta T_{E-ESM}$ and $\Delta T_{L-LSM}$.

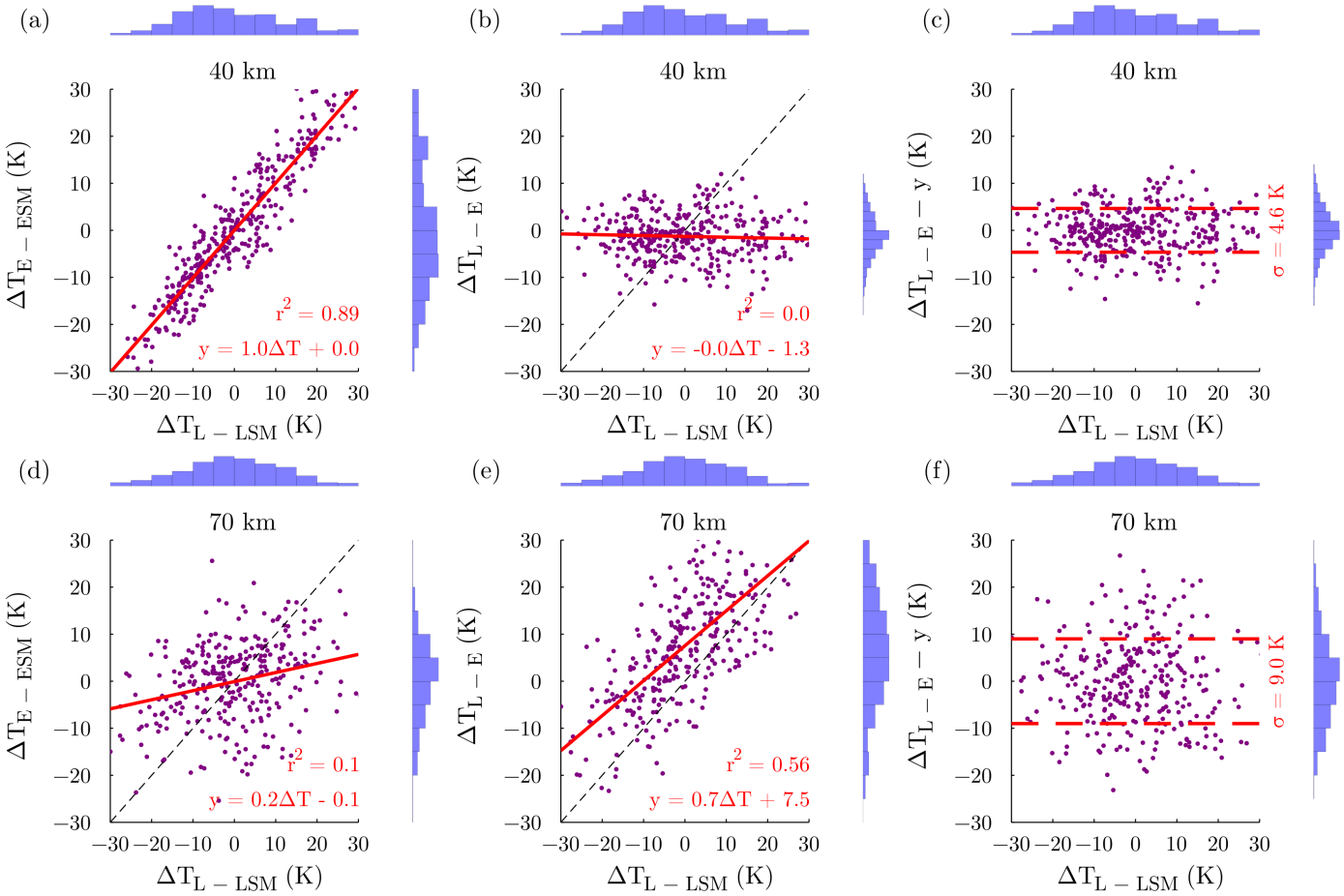


**Figure 3.** Comparisons of thetemperature differences between ERA-5 and its seasonal mean ($\Delta T_{E-ESM}$) and between the LiDAR and ERA-5 ($\Delta T_{L-E}$) with the temperature differences between the LiDAR and its seasonal mean ($\Delta T_{L-LSM}$) at 40 km (**a**,**b**) and 70 km (**d**,**e**) during winter. The correlation between these comparisons was computed with a linear regression (solid red line), and the associated determination coefficient ($r^2$) is displayed. A perfect correlation without bias is illustrated by the black dashed line. The temperature differences between the LiDAR and the ECMWF corrected by the linear regression ($\Delta T_{L-E} - y$) are shown at 40 km (**c**) and 70 km (**f**). The distributions (blue bars) of the temperature differences are added at the top for the x-axis and on the right for the y-axis.

**Table 1.** Numerical values of the slope coefficients at different altitudes for the winter season between the ERA-5 fluctuations ($\Delta T_{E-ESM}$) and the LiDAR fluctuations ($\Delta T_{L-LSM}$), calculated from their respective seasonal mean, and between the LiDAR and model temperature differences ($\Delta T_{L-E}$) and the LiDAR fluctuations ($\Delta T_{L-LSM}$). Mean biases calculated simultaneously are also provided, as well as the determination coefficient of the regression analysis ($r^2$).

| **Winter** | | **35 km** | **40 km** | **45 km** | **50 km** | **55 km** | **60 km** | **65 km** | **70 km** | **75 km** |
|---|---|---|---|---|---|---|---|---|---|---|
| $\Delta T_{E-ESM}/\Delta T_{L-LSM}$ | coef | 1 | 1 | 0.8 | 0.6 | 0.4 | 0.3 | 0.2 | 0.2 | 0.2 |
| | bias (K) | 0 | 0 | 0 | 0 | 0 | 0 | −0.1 | −0.1 | −0.4 |
| | $r^2$ | 0.88 | 0.89 | 0.8 | 0.54 | 0.28 | 0.12 | 0.1 | 0.1 | 0.14 |
| $\Delta T_{L-E}/\Delta T_{L-LSM}$ | coef | 0 | 0 | 0.2 | 0.4 | 0.6 | 0.7 | 0.8 | 0.7 | 0.5 |
| | bias (K) | 0.1 | −1.3 | 0.2 | 4.6 | 7.2 | 4.2 | 3 | 7.5 | 12.8 |
| | $r^2$ | 0 | 0 | 0.18 | 0.4 | 0.39 | 0.54 | 0.56 | 0.56 | 0.38 |

The link between these coefficient evolutions could be that the model parametrization led the model to behave as its climatology in the layers where perturbations responsible for

the variability were not perfectly simulated. This result implies that a restoring force to the climatology acts in the model to prevent an inconsistent representation of the mesosphere. In the winter stratosphere, most of the variance is due to the propagation of planetary-scale waves having large amplitudes, sometimes leading to SSWs [36]. Consequently, we can conclude that planetary waves are well reproduced in ERA-5. In contrast, the temperature variance in the winter mesosphere, primarily due to propagating and breaking gravity waves causing mesospheric inversions around 65 km, is not reproduced in ERA-5. The main reason is the coarse vertical resolution of the model in the mesosphere, preventing simulation perturbations at small scales.

Finally, the evolution of the biases associated with the comparisons between $\Delta T_{L-E}$ and $\Delta T_{L-LSM}$ followed, as expected, the mean of the temperature difference profiles (Figure 2a). When temperature differences between the LiDAR and model ($\Delta T_{L-E}$) were corrected by this linear correlation (Figure 3c,f), residual differences were obtained with a distribution shape close to a normal distribution. This suggests that the standard deviation of this quantity increasing with altitude can be related to noise, including instrumental LiDAR noise and other model effects such as the smoothing effect or a restoring force to the climatology.

### *4.2. Summer*

As opposed to the winter period, a small correlation with a slope coefficient of 0.1 is found at 40 km in summer between temperature differences $\Delta T_{E-ESM}$ and $\Delta T_{L-LSM}$ (Figure 4a).

Surprisingly, significant correlations were observed between temperature differences $\Delta T_{L-E}$ and temperature LiDAR deviation from its own climatology $\Delta T_{L-LSM}$ (Figure 4b), with a slope coefficient of 0.9 and a negative bias of −3 K. This bias is in good agreement with previous comparisons (Figure 2). This high correlation suggests that ERA-5 temperatures are close to the climatology. This result is not limited to the stratosphere, and similar comparisons were obtained in the mesosphere (Figure 4d) with a slope coefficient of 0.1 at 70 km. Again in the mesosphere, the linear correlation of the differences between ERA-5 and the LiDAR also indicates significant correlations with a slope coefficient of 0.7 at 70 km (Figure 4d) and a large positive bias of +9.9 K, in good agreement with the mean comparisons (Figure 2). Hence, the model did not reproduce the summer variability observed in the LiDAR data. These results confirm the model's trend to behave as the LiDAR climatology when the model does not reproduce the observed variability.

According to previous observations [37], the summer stratosphere is characterized by a weak variability, while a more substantial variability is observed in the upper mesosphere due to inversions occurring mainly in the 70–80 km altitude range. The temperature variance in the summer stratosphere is caused by propagating gravity waves, whose amplitudes are likely smaller in ERA-5 than in the observations and, unlike winter, by the impossible propagation of planetary waves in the middle atmosphere at this period [38]. As the winter, the few available levels between 70 km and 80 km in ERA-5 prevent reproducing the small amplitudes of gravity waves and their breaking, causing mesospheric inversions.

Moreover, it is impossible to infer, as opposed to the winter months, whether the model's ability to reproduce the variability is impacted or not by the mean difference between both climatologies. As expected, $\Delta T_{L-E} - y$ increases with altitude, lying from 2 K at 40 km to 5 K at 70 km (Figure 4c,f), meaning that the model uncertainty is greater in winter than in summer. Again, the evolution of the biases (Table 2) is consistent with the mean temperature difference profile (Figure 2b) during summer.

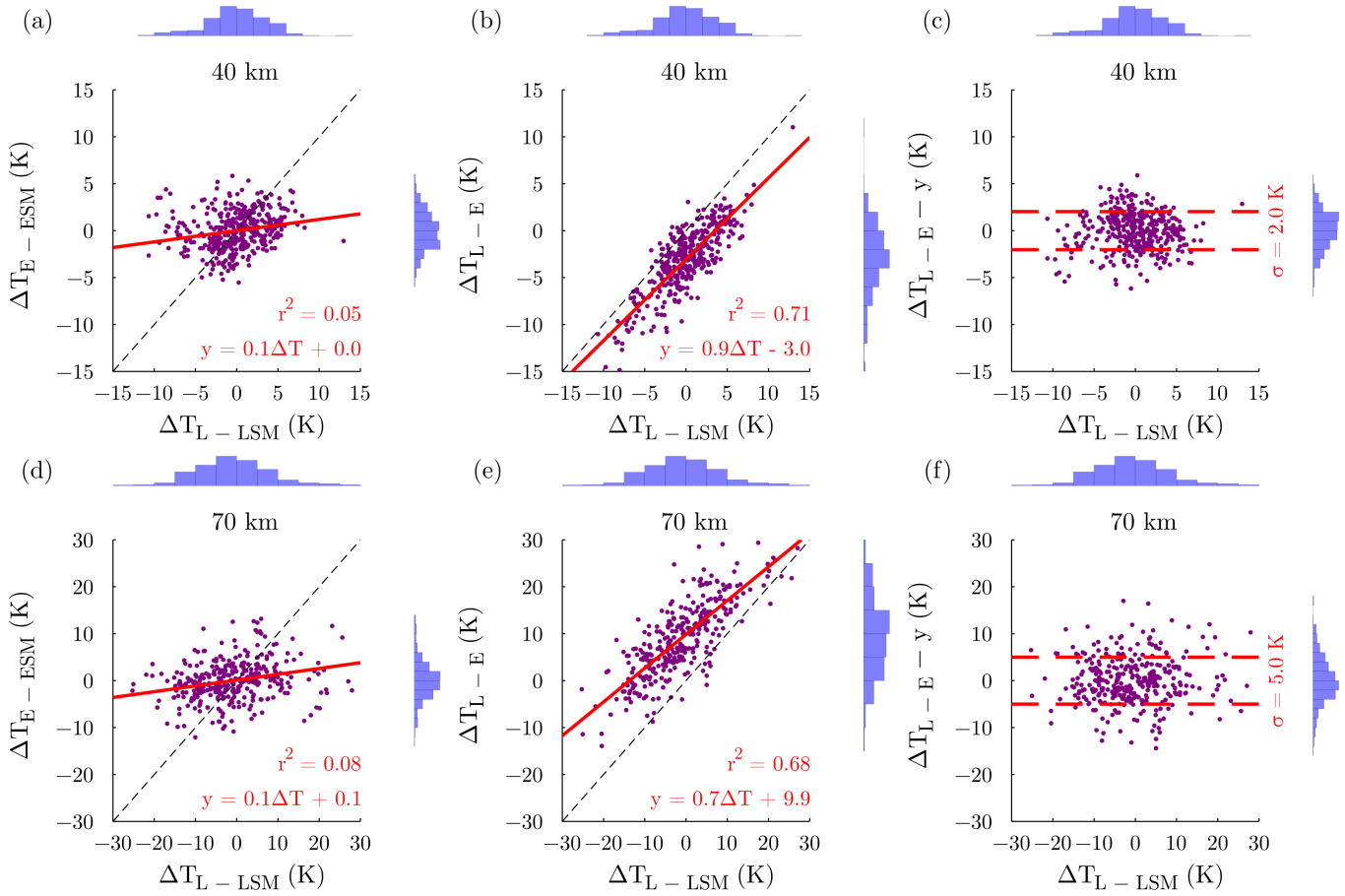


**Figure 4.** Comparisons of the temperature differences between ERA-5 and its seasonal mean ($\Delta T_{E-ESM}$) and between the LiDAR and ERA-5 ($\Delta T_{L-E}$) with the temperature differences between the LiDAR and its seasonal mean ($\Delta T_{L-LSM}$) at 40 km (**a**,**b**) and 70 km (**d**,**e**) during summer. A perfect correlation without bias is illustrated by the black dashed line. The temperature differences between the LiDAR and the ECMWF corrected by the linear regression ($\Delta T_{L-E} - y$) are shown at 40 km (**c**) and 70 km (**f**). The same information regarding the performed linear regressions and the distribution of temperature differences as contained in Figure 3 are displayed.

**Table 2.** The same information as contained in Table 1, but for the summer season.

| Summer | | 35 km | 40 km | 45 km | 50 km | 55 km | 60 km | 65 km | 70 km | 75 km |
|---|---|---|---|---|---|---|---|---|---|---|
| $\Delta T_{E-ESM}/\Delta T_{L-LSM}$ | coef | 0.1 | 0.1 | 0.2 | 0.2 | 0.1 | 0.1 | 0.1 | 0.1 | 0 |
| | bias (K) | 0 | 0 | 0 | 0 | 0 | 0 | 0 | 0.1 | −0.5 |
| | $r^2$ | 0.04 | 0.05 | 0.12 | 0.08 | 0.04 | 0.06 | 0.07 | 0.08 | 0 |
| $\Delta T_{L-E}/\Delta T_{L-LSM}$ | coef | 0.9 | 0.9 | 0.8 | 0.8 | 0.9 | 0.8 | 0.8 | 0.7 | 0.6 |
| | bias (K) | −2.3 | −3 | −2.8 | 1.1 | 7.3 | 12 | 11.6 | 9.9 | 11.3 |
| | $r^2$ | 0.76 | 0.71 | 0.69 | 0.69 | 0.68 | 0.63 | 0.72 | 0.68 | 0.56 |

## 5. Evolution of the Model Uncertainty

Independent of the biases observed in the model, it is interesting to estimate the model variability and the associated uncertainty, which is usually difficult to quantify. This uncertainty is due mainly to intrinsic errors in the assimilation process [39] and to its coarse resolution, reducing the parameterization quality of small-scale atmospheric processes such as gravity waves or mesospheric inversions. Thereby, statistical comparisons between the LiDAR and ERA-5 allow evaluating the model variability not observed by that LiDAR that can be associated with an estimate of the model uncertainty for the vertical

LiDAR resolution. According to Keckhut et al. [28], the LiDAR succeeds in capturing the fluctuations at small scales generated by breaking gravity waves over the studied altitude range. Thus, as the measured temperature is the sum of the mean plus fluctuations, we can decompose the variance observed by the LiDAR $\sigma^2_{LiDAR}$ and the variance simulated by the model $\sigma^2_{Model}$ as follows:

$$\sigma^2_{LiDAR} = \sigma^2_{LargeScale} + \sigma^2_{SmallScale} + \sigma^2_{LiDARNoise}, \quad (1)$$

and:

$$\sigma^2_{Model} = \sigma^2_{LargeScale} + \sigma^2_{ModelUncertainty}, \quad (2)$$

where $\sigma^2_{LargeScale}$ and $\sigma^2_{SmallScale}$ are the real geophysical variances at large and small scales, respectively $\sigma_{LiDARNoise}$ the median of the LiDAR instrumental errors and $\sigma^2_{ModelUncertainty}$ the uncertainty associated with the model variance. Here, we propose a method to estimate this model uncertainty, which includes small-scale and short-period variability not represented in the ECMWF [13], by using the linear correlation found between $\Delta T_{L-E}$ and $\Delta T_{L-LSM}$:

- First, the temperature differences between the LiDAR and the ECMWF ($\Delta T_{L-E}$) were compared to the temperature differences between the LiDAR and its seasonal mean ($\Delta T_{L-LSM}$) at each altitude;
- Afterward, the temperature differences between the LiDAR and the ECMWF ($\Delta T_{L-E}$) were corrected by the linear correlation found with the LiDAR temperature fluctuation ($\Delta T_{L-LSM}$) in order to remove their common variability and the model biases;
- Finally, from Equations (1) and (2), we can express the global uncertainty including the model uncertainty and small-scale fluctuations not simulated with this relation:

$$\sigma^2_{GlobalUncertainty} = \sigma^2_{SmallScale} + \sigma^2_{ModelUncertainty} = \sigma^2_{(\Delta T_{L\text{-}E}-y)} - \sigma^2_{LiDARNoise}, \quad (3)$$

  where $\sigma_{(\Delta T_{L-E}-y)}$ is the standard deviation of the temperature differences between the LiDAR and the model corrected by the linear regression (Figures 3c,f and 4c,f).

As expected, the model uncertainty and fluctuations at a small scale grow with altitude in both seasons and are higher in winter than in summer in the whole middle atmosphere (Figure 5). The global uncertainty increases from 3–7 K and from 1–4 K between 30 km and 70 km during winter and summer, respectively. In winter, the LiDAR variability reaches a maximum at 40 km, corresponding to the propagation of planetary waves and the effect of the SSWs. Then, the LiDAR variability decreases until the stratopause region and slightly increases up to 80 km. In the upper stratosphere during winter, a large part of the LiDAR variability (65% at 40 km) is reproduced by the model, which could explain the excellent agreement found previously between $\Delta T_{E-ESM}$ and $\Delta T_{L-LSM}$. However, from the stratopause region to 70 km, only a tiny part of the LiDAR variability is reproduced by the model (36% in average), which could explain here the bad agreement found between $\Delta T_{E-ESM}$ and $\Delta T_{L-LSM}$. This result is not surprising because, as discussed in Sections 3.2 and 4.1, a more significant part of small-scale fluctuations observed by the OHP LiDAR is supposed to be not simulated by the model in the mesosphere. Concretely, the variance generated by small-scale fluctuations contributes more to the global uncertainty in the mesosphere than in the upper stratosphere due to the degradation of the model resolution. Above 70 km, the global uncertainty is poorly estimated, while LiDAR uncertainties (initialization, background noise estimation) are likely overestimated (see Section 2.1). Indeed, LiDAR instrumental errors increase exponentially with altitude to reach more than 3 K at 70 km (Figure 5). Therefore, the model uncertainty should not be considered beyond this altitude. In summer, the LiDAR variability is smaller than during winter. The model reproduces 54% of the LiDAR variability from 30–60 km, which is consistent with the model inability observed above to capture the variability in the summertime in the middle atmosphere. Above 60 km, the increase of the LiDAR variability

is explained by mesospheric inversions occurring at these altitudes in the summertime, which are not accurately captured by the ECMWF products either. However, the global uncertainty decreases slightly and remains constant in the upper mesosphere, where its evolution is expected to increase. This result is due to LiDAR instrumental errors that are too high at these altitudes to evaluate the total uncertainty accurately.

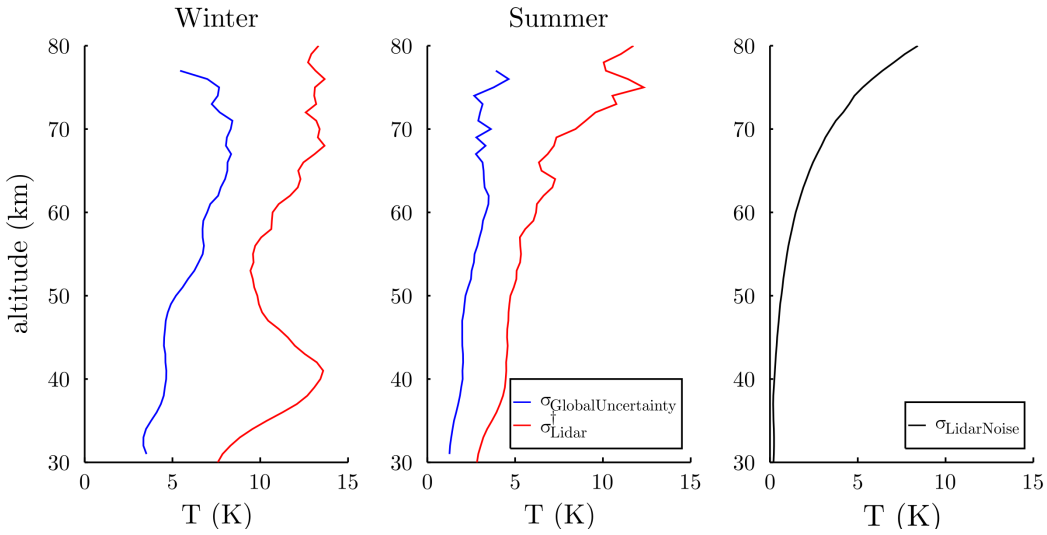


**Figure 5.** Model uncertainty estimates (blue solid lines) and atmospheric variability observed with the LiDAR (red solid lines) profiles corrected by the LiDAR noise during winter and summer in the 30–80 km altitude range. The median of the LiDAR instrumental errors $\sigma_{LiDARNoise}$ (black solid line) over the altitude is shown as well.

## 6. Temperature Differences and Vertical Coupling

The atmospheric variability is estimated by ERA-5 at each altitude level independently. However, as the atmosphere is a fluid, strong links exist between the different layers as the so-called stratosphere–troposphere coupling (e.g., [6,7]).

For this reason, a Principal Component Analysis (PCA) was performed on the fluctuations of the temperature differences between the LiDAR and ERA-5 to investigate vertical patterns in the observed and modeled variability reproduced. The PCA was computed over 368 profiles in winter and 381 in summer in the 30–70 km altitude range as the ERA-5 profiles suffer from a coarse resolution in the upper mesosphere. The three first modes explain 76% and 78% of the total variance in summer and in winter, respectively (Figures 6 and 7).

In summer, the leading mode, which corresponds to 49% of the total variability of the fluctuations (Figure 6a), has a clear anti-correlation between the upper stratosphere (+2 K at 40 km) and the mesosphere (−5 K at 70 km). This leading mode is illustrated by temperature profiles from the LiDAR and model for the date 23 August 2016 (Figure 8a). Numerous dates with the same vertical pattern have been found (not shown here), confirming that the PC1 computed represents a typical model behavior, i.e., the model tends to be warmer and cooler than LiDAR observations in the upper stratosphere and the mesosphere, respectively. However, the source responsible for this leading mode pattern is complicated as the compensations between the upper stratosphere and the mesosphere seem to be related to persisting biases and not small-scale phenomena. Two other modes, accounting for respectively 17% and 10% of the variability (Figure 6b,c), are more representative of the small-scale fluctuations not simulated in ERA-5. Both modes have a tiny signal (<1 K) in the upper stratosphere and possess a wave-like structure in the mesosphere, suggesting the presence of gravity waves causing temperature inversions [40].

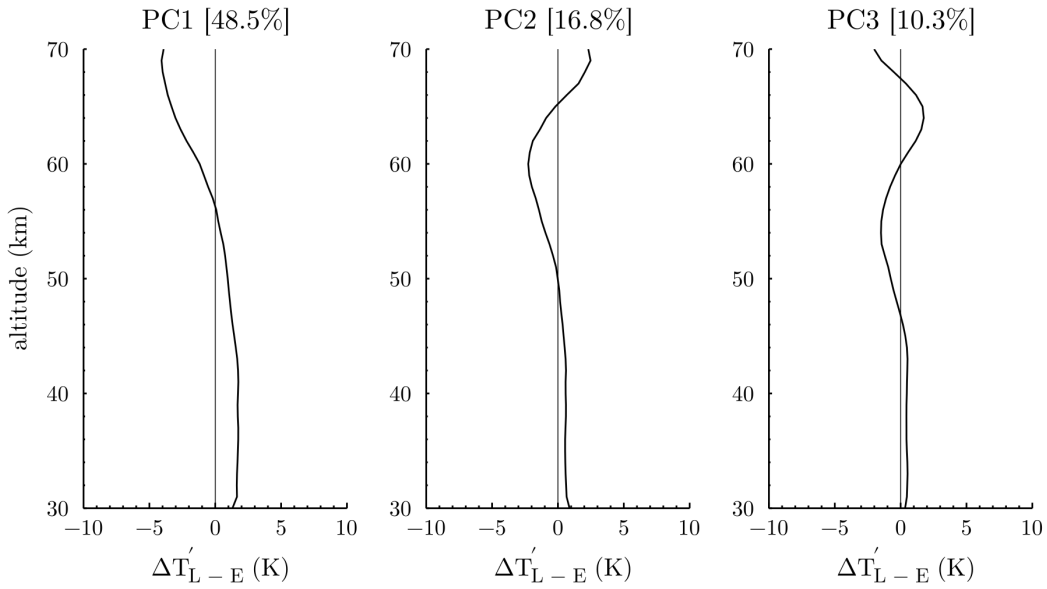


**Figure 6.** Vertical modes for the summer months (June, July, August) of the fluctuations of the temperature difference between the LiDAR and ERA-5, corresponding respectively to (PC1) 49%, (PC2) 17%, and (PC3) 10% of the variability.

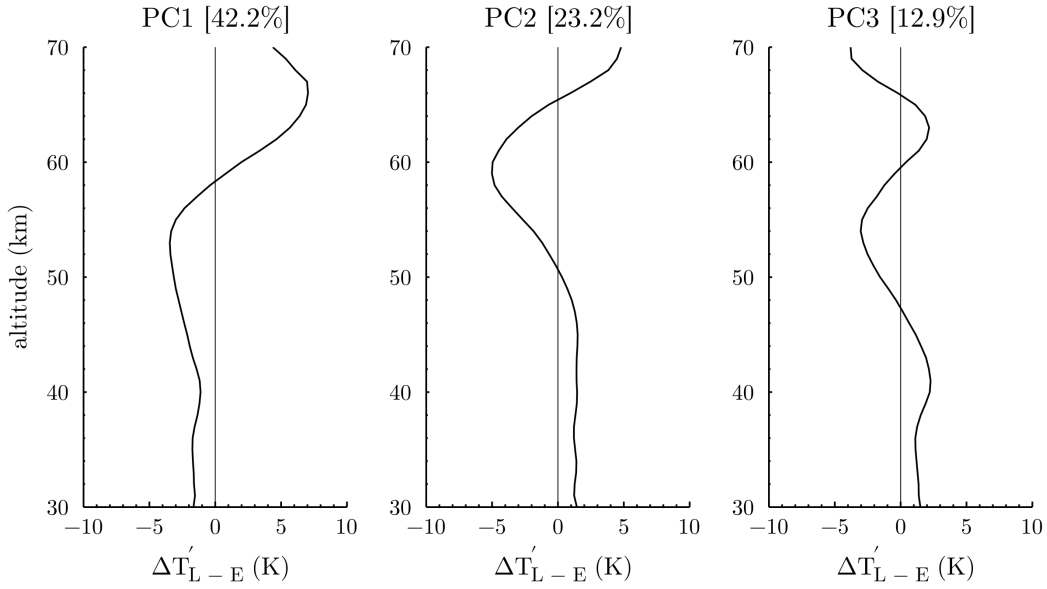


**Figure 7.** Vertical modes for the winter months (December, January, February) of the fluctuations of the temperature difference between the LiDAR and ERA-5, corresponding respectively to (PC1) 42%, (PC2) 23%, and (PC3) 13% of the variability.

Hence, these significant mesospheric fluctuations of 20–40 K over an atmospheric thickness of 5–10 km around 70 km are not reproduced by ERA-5 in summer (Figure 8b,c), confirming the hypothesis mentioned in Section 4-b. This trend of the model to overlook mesospheric inversions occurring at about 70 km is also illustrated with two dates in summer (Figure 8b,c). The examples shown here for the summer period confirm that ERA-5 is systematically cooler in the entire mesosphere and becomes warmer only when mesospheric inversions occur.

In winter, the three main modes explain 42%, 23%, and 13% of the variability of the temperature difference fluctuations. Similar to the summer, the first mode shows an anti-correlation between the upper stratosphere (−1 K at 40 km) with the lower mesosphere (−4 K at 55 km) and the upper mesosphere (+7 K at 65 km). The typical pattern of this

mode is illustrated by the LiDAR and model temperature profiles in Figures 1 and 8d. Interestingly, the summer and winter leading modes possess opposite patterns, suggesting that there is a connection between these two first modes. An investigation of the PC1 coefficient evolution over the studied period (not shown here) revealed a signal with opposite phases between summer and winter. Consequently, these first modes would not result from only an actual vertical coupling, but may represent seasonal fluctuations.

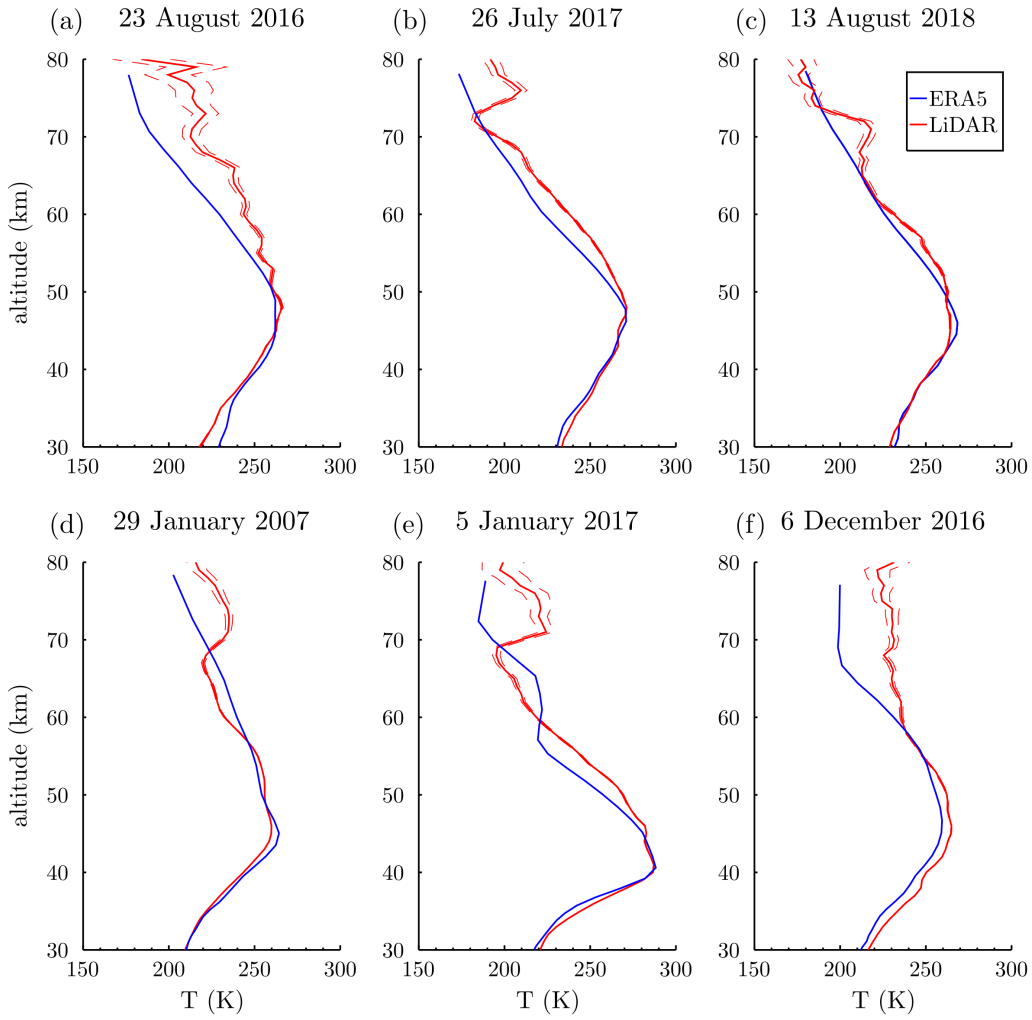


**Figure 8.** Temperature profiles from the LiDAR (solid red lines) and from the model (solid blue lines) for three dates in summer (**a**–**c**) and three dates in winter (**d**–**f**) chosen for illustrating the principal components found. Instrumental errors from the LiDAR are shown as well (red dashed lines).

The vertical patterns of the second and the third modes are likely associated with propagating atmospheric waves and mesospheric inversions occurring at lower altitudes than in summer [40,41]. Illustrations of the second and third modes are shown for three days in winter (Figure 8d–f). At first glance, the model sometimes tended to overlook (Figure 8d) a part of the mesospheric inversions during winter. However, contrary to the summer period, the model managed for some cases to simulate them, but often with a smaller magnitude and loweraltitude (Figure 8e), probably responsible for the bias reduction found at 65 km (Figure 2A). As mesospheric inversions are caused by breaking gravity waves, this seasonal difference should result from the model parametrization of gravity wave activity, which is supposed to be maximum in winter and minimum in summer [31,42]. Indeed, according to Strelnikova et al. [43], Gravity Wave Potential Energy Densities (GWPEDs) per unit volume ($E_{pV}$) in ERA-5 become smaller from 45 km and admit a seasonal cycle with a maximum

in winter and a minimum in summer. Here, as retrieved by Meriwether and Gardner [44], the mesosphere inversion layer altitude appears to be dependent on the seasons, i.e., lower in winter and higher in summer, at mid-latitudes. Hence, mesospheric inversions are challenging to simulate. Thanks to a 2D model, Hauchecorne and Maillard [45] were able to reproduce mesospheric inversions in winter with a parametrization of the drag, diffusion, and dissipation due to gravity wave breaking. The ECMWF has implemented in the ERA-5 reanalyses an artificial sponge layer effective above 10 hPa in order to reduce the unrealistic vertical wave reflection at the top model [14,46]. However, according to Ehard et al. [14], the sponge layer strongly damps the gravity wave activity above 45 km in the ERA-5 reanalyses, preventing the energy transport to the model top. Furthermore, Strelnikova et al. [43] found that $E_{pV}$ is smaller in ERA-5 and increases with altitude, admitting a seasonal cycle with a maximum in winter. Thus, these remarks should be considered as research leads for future updates and improvements of the last ECMWF model.

## 7. Impact of the SSWs on Temperature Differences

Several observations have shown that SSWs may increase the middle stratospheric temperature by more than 40 °C [47,48] in a span of a few days and influence the tropospheric weather for several weeks. These events are observed in the LiDAR temperature series over OHP [23,40]. However, these vast temperature deviations are still not well predicted by models [49]. Since SSWs are mainly driven by strong nonlinear processes, it is interesting to investigate how ERA-5 temperature reanalyses behave when these extreme events occur. According to the previous results, the magnitude of SSWs is well reproduced by the model in the upper stratosphere (Figure 3a). Thus, to investigate the impact of SSWs on the ERA-5 product, the temporal evolution of the temperature differences between the LiDAR and ERA-5 corrected by the model biases and the common variability $\Delta T_{L-E} - y$ 20 d before and after SSWs was studied in the middle atmosphere.

To detect any significant differences during one of the phases of an SSW, we considered differences according to the first day of the stratospheric warming. Day 0 is defined as the day when the zonal mean zonal wind is lower than 10 $ms^{-1}$ at 60° N and 10 hPa. This criterion is slightly different from major SSW's definition associated with wind reversal. This wind criterion was used here to include all major SSWs associated with coherent category as defined by Maury et al. [50]. Thus, the algorithm identified here 18 SSW events over the period 2005–2020, during which the OHP LiDAR carried out observations.

The results are not shown here, but no patterns were detected in most of the stratosphere, as well as in the mid- and upper mesosphere where differences $\Delta T_{L-E} - y$ appeared randomly distributed with time. The only pattern we can report is in the vicinity of the stratopause and the lower mesospheric levels (Figure 9). According to the moving mean, the model tended to be slightly cooler than LiDAR observations 5–20 d before that SSW happened with more than 60% of the temperature differences corrected, which were positive and with a mean of +1.7 K. As the days came close to the stratospheric warming, the model tended to be warmer. During the first 5 d after SSW, the model was mainly warmer than the LiDAR, with more than 75% of the temperature differences corrected, which were negative, and a mean of −2.5 K. Beyond five days after the SSW occurred, the model stayed within the dispersion and reproduced quite well the temperature observed by the LiDAR. ERA-5 reanalyses, even during a strong nonlinear event such as SSWs, allow representing quite well SSW evolutions except in the lower mesosphere a few days after the maximum of the event.

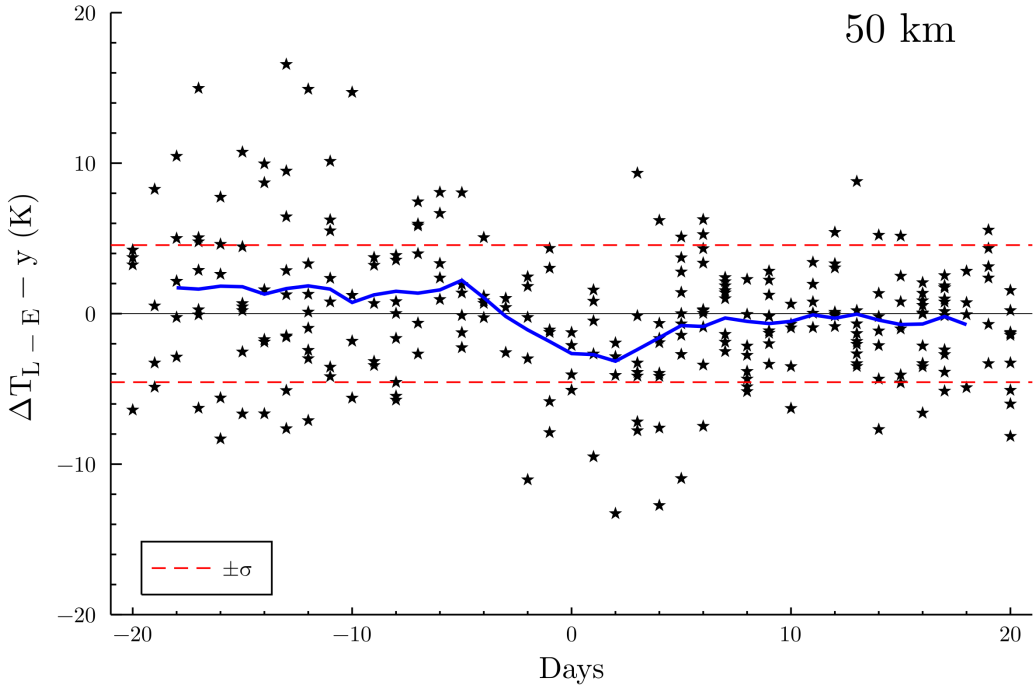


**Figure 9.** Evolution of the temperature differences at 50 km between the LiDAR and the ECMWF corrected by the linear regression 20 d before and after the mean zonal mean wind at 60° N and 10 hPa became inferior to 10 m.s$^{-1}$. The standard deviation computed over all values (red dashed lines) and the moving mean (blue solid line) computed over five days are displayed.

## 8. Conclusions

OHP LiDAR observations over the last fifteen years have been used as a benchmark to validate many satellite observations and were used here to assess the ERA-5 temperature reanalyses in the 30–80 km range at mid-latitudes.

Hence, in this study, the temperature assessments of the ECMWF model were carried out for both seasons, winter and summer, and only with the OHP station, as no other stations have been regularly measuring the middle atmosphere at mid-latitudes. First, the mean temperature differences between the LiDAR observations and the ECMWF model confirmed previous comparisons and showed a similar vertical pattern in winter and summer. A good agreement was found up to 45 km in winter, whereas a slight negative bias of −3 K up to 50 km was observed in summer. However, significant positive biases were found in the mesosphere for both seasons, indicating that the model climatology tends to be cooler than the LiDAR climatology. A reduction of the temperature bias was notable at 65 km for the winter months, likely due to mesospheric inversions, often simulated imprecisely by the model.

In order to pursue the previous studies focusing only on the temperature bias [13–15], a more detailed investigation of the model performance to reproduce the variability observed by the OHP LiDAR was carried out. In winter, the high variability due to SSWs, which characterizes the upper stratosphere, was well captured by the model, confirming that planetary waves are well reproduced in ERA-5. In the mesosphere, the model did not deviate from its seasonal mean and, therefore, did not reproduce most of the variability observed by LiDAR. Thus, it appears that the biases between the LiDAR and ERA-5 and the capability of the model to reproduce the variability in the mesosphere are not necessarily linked. In summer, the model did not reproduce the observed variability, neither in the upper stratosphere nor in the mesosphere. In the summer stratosphere, the reason was likely that ERA-5 simulates gravity waves whose amplitudes are smaller than in the observations. In the mesosphere, as for winter, the central part of gravity waves cannot be simulated in the model with its current vertical resolution. As a result, a restoring force to the climatology

acts on the model to keep a realistic representation of the mesosphere. In the mesosphere, the variability issue is similar for both seasons, while this altitude domain is mainly driven by gravity wave propagation and breaking, leading to mesospheric inversions. Hence, the model cannot accurately simulate mesospheric inversions responsible for the most considerable variability.

Of specific interest is the capability of the ERA-5 product to reproduce the observed variability in the upper stratosphere during winter. The damping of the variability in ERA-5 during summer in the stratosphere compared to winter has not been explained yet. A novelty of this work is the method suggested to estimate the model uncertainty associated with its variability. As the model uncertainty grows with the altitude, an accurate simulation of the natural variability for both seasons is limited, especially in the mesosphere.

In addition to this model variability assessment, the vertical coupling between the mesosphere and the upper stratosphere was investigated thanks to a principal component analysis of the fluctuations of the temperature differences between the LiDAR and ERA-5. The leading modes of both seasons revealed anti-correlations between the upper stratosphere and the mesosphere, illustrating the typical behavior of the model. Additionally, both first modes possess opposite patterns between winter and summer. The EOF coefficient evolution over the studied period suggests that the source of this connection would be due to seasonal fluctuations. On the other hand, the secondary modes for both seasons illustrate more the small-scale fluctuations not simulated in ERA-5. Indeed, the wave-like structure observed in these other modes suggests the presence of gravity waves, leading to mesospheric inversions, confirming, as inferred previously, either their absence in summer or their inaccuracy in winter in the ERA-5 temperature profiles.

As a significant part of the winter variability is due to SSWs, the study of their impact on the temperature reanalyses in the middle atmosphere was pursued here. It was found that SSWs influence ERA-5 temperatures around the stratopause several days before and after their trigger. Nevertheless, further studies about SSWs' representation in the models (start, evolution, duration, intensity, coupling, etc.) should be led with all LiDAR temperature series to assess their parametrization. These future investigations are of significant interest for the community using the ERA-5 product to accurately study SSWs' impacts on the bottom and the top of the atmosphere.

Finally, further investigations should be pursued to determine the origin of the model biases and explain the current limitation of the model to reproduce mesospheric inversions produced by gravity wave breaking. A first lead is the seasonal difference in the model ability observed here to simulate mesospheric inversions, which is undoubtedly due to the annual cycle of the gravity wave activity, i.e., maximum in winter and minimum in summer [31,42].

This study points out the need to assimilate more observations of the mesosphere, such as wind and temperature, to improve its representation in the model. However, only a few instruments measure this part of the atmosphere. Since 2018, the satellite Aeolus has been providing wind measurements up to 30 km that have demonstrated in the stratosphere their usefulness for model analyses [51]. Similar data should be added as infra-sound measurements deployed with the ARISE network [19] to complete the wind field representation at higher altitudes. Furthermore, some temperature profiles with high-repetitiveness overpasses can be derived from CubeSat constellation [34].

**Author Contributions:** Conceptualization, A.M., P.K. and A.H.; methodology, P.K., A.H., C.C. and M.M.; data curation and investigation, A.M.; resources, P.K., A.H. and C.C.; supervision, P.K., A.H. and C.C.; writing, A.M.; discussion, P.K., A.H., A.L.P., C.C., M.M. and S.K.; reviewing and revision, P.K., A.H., A.L.P., C.C., M.M. and S.K. All authors have read and agreed to the published version of the manuscript.

**Funding:** The French Educational Ministry with EUR IPSL and NDACC operations are supported by CNRS, CNES, and UVSQ.

**Institutional Review Board Statement:** Not applicable.

**Informed Consent Statement:** Not applicable.

**Data Availability Statement:** The data used in this publication were obtained as part of the Network for the Detection of Atmospheric Composition Change (NDACC) and are publicly available through the international NDACC website https://www-air.larc.nasa.gov/missions/ndacc/data.html and the French AERIS data portal http://cds-espri.ipsl.fr/NDACC/. The indications to download the ERA-5 data over 137 levels are given on the ECWMF website https://confluence.ecmwf.int/display/CKB/How+to+download+ERA-5. Additional and more detailed technical information is available at https://confluence.ecmwf.int/display/CKB/ERA-5%3A+data+documentation (accessed on 1 November 2021).

**Acknowledgments:** This work was a contribution to the MARTIC payload development supported by CNES and CNRS through the national program on remote sensing AO (Programme National de Télédétection Spatiale). The assessment of meteorological reanalyses using LiDAR have been initiated within the European H2020 ARISE project. We acknowledge the OHP station and their operators working on the site.

**Conflicts of Interest:** The authors declare no conflict of interest.

## References

1. Seviour, W.J.M.; Butchart, N.; Hardiman, S.C. The Brewer-Dobson circulation inferred from ERA-Interim. *Q. J. R. Meteorol. Soc.* **2012**, *138*, 878–888. [CrossRef]
2. Lee, C.; Smets, P.; Charlton-Perez, A.; Evers, L.; Harrison, G.; Marlton, G. The Potential Impact of Upper Stratospheric Measurements on Sub-seasonal Forecasts in the Extra-Tropics. In *Infrasound Monitoring for Atmospheric Studies: Challenges in Middle Atmosphere Dynamics and Societal Benefits*; Le Pichon, A., Blanc, E., Hauchecorne, A., Eds.; Springer International Publishing: Cham, Switzerland, 2019; pp. 889–907. [CrossRef]
3. Butler, A.H.; Seidel, D.J.; Hardiman, S.C.; Butchart, N.; Birner, T.; Match, A. Defining Sudden Stratospheric Warmings. *Bull. Am. Meteorol. Soc.* **2015**, *96*, 1913–1928. [CrossRef]
4. Hardiman, S.C.; Butchart, N.; Hinton, T.J.; Osprey, S.M.; Gray, L.J. The Effect of a Well-Resolved Stratosphere on Surface Climate: Differences between CMIP5 Simulations with High and Low Top Versions of the Met Office Climate Model. *J. Clim.* **2012**, *25*, 7083–7099. [CrossRef]
5. Charlton-Perez, A.J.; Baldwin, M.P.; Birner, T.; Black, R.X.; Butler, A.H.; Calvo, N.; Davis, N.A.; Gerber, E.P.; Gillett, N.; Hardiman, S.; et al. On the lack of stratospheric dynamical variability in low-top versions of the CMIP5 models. *J. Geophys. Res. Atmos.* **2013**, *118*, 2494–2505. [CrossRef]
6. Baldwin, M.P.; Thompson, D.W.J.; Shuckburgh, E.F.; Norton, W.A.; Gillett, N.P. Weather from the Stratosphere? *Science* **2003**, *301*, 317–319. [CrossRef] [PubMed]
7. Charlton, A.J.; O'neill, A.; Lahoz, W.A.; Massacand, A.C. Sensitivity of tropospheric forecasts to stratospheric initial conditions. *Q. J. R. Meteorol. Soc.* **2004**, *130*, 1771–1792. [CrossRef]
8. Uppala, S.M.; KÅllberg, P.W.; Simmons, A.J.; Andrae, U.; Bechtold, V.D.C.; Fiorino, M.; Gibson, J.K.; Haseler, J.; Hernandez, A.; Kelly, G.A.; et al. The ERA-40 reanalysis. *Q. J. R. Meteorol. Soc.* **2005**, *131*, 2961–3012. [CrossRef]
9. Dee, D.P.; Uppala, S.M.; Simmons, A.J.; Berrisford, P.; Poli, P.; Kobayashi, S.; Andrae, U.; Balmaseda, M.A.; Balsamo, G.; Bauer, P.; et al. The ERA-Interim reanalysis: Configuration and performance of the data assimilation system. *Q. J. R. Meteorol. Soc.* **2011**, *137*, 553–597. [CrossRef]
10. Hersbach, H.; Bell, B.; Berrisford, P.; Hirahara, S.; Horányi, A.; Muñoz-Sabater, J.; Nicolas, J.; Peubey, C.; Radu, R.; Schepers, D.; et al. The ERA5 global reanalysis. *Q. J. R. Meteorol. Soc.* **2020**, *146*, 1999–2049. [CrossRef]
11. Hoppel, K.W.; Eckermann, S.D.; Coy, L.; Nedoluha, G.E.; Allen, D.R.; Swadley, S.D.; Baker, N.L. Evaluation of SSMIS Upper Atmosphere Sounding Channels for High-Altitude Data Assimilation. *Mon. Weather. Rev.* **2013**, *141*, 3314–3330. [CrossRef]
12. Funatsu, B.M.; Claud, C.; Keckhut, P.; Hauchecorne, A.; Leblanc, T. Regional and seasonal stratospheric temperature trends in the last decade (2002–2014) from AMSU observations. *J. Geophys. Res. Atmos.* **2016**, *121*, 8172–8185. [CrossRef]
13. Le Pichon, A.; Assink, J.; Heinrich, P.; Blanc, E.; Charlton-Perez, A.; Lee, C.; Keckhut, P.; Hauchecorne, A.; Rüfenacht, R.; Kämpfer, N.; et al. Comparison of co-located independent ground-based middle-atmospheric wind and temperature measurements with Numerical Weather Prediction models. *J. Geophys. Res. Atmos.* **2015**, *120*, 8318–8331. [CrossRef]
14. Ehard, B.; Malardel, S.; Dörnbrack, A.; Kaifler, B.; Kaifler, N.; Wedi, N. Comparing ECMWF high-resolution analyses with LiDAR temperature measurements in the middle atmosphere. *Q. J. R. Meteorol. Soc.* **2018**, *144*, 633–640. [CrossRef]
15. Marlton, G.; Charlton-Perez, A.; Harrison, G.; Polichtchouk, I.; Hauchecorne, A.; Keckhut, P.; Wing, R.; Leblanc, T.; Steinbrecht, W. Using a network of temperature LiDARs to identify temperature biases in the upper stratosphere in ECMWF reanalyses. *Atmos. Chem. Phys.* **2021**, *21*, 6079–6092. [CrossRef]
16. Hauchecorne, A.; Chanin, M.L.; Keckhut, P. Climatology and trends of the middle atmospheric temperature (33–87 km) as seen by Rayleigh LiDAR over the south of France. *J. Geophys. Res. Atmos.* **1991**, *96*, 15297–15309. [CrossRef]

17. Simmons, A.; Soci, C.; Nicolas, J.; Bell, B.; Berrisford, P.; Dragani, R.; Flemming, J.; Haimberger, L.; Healy, S.; Hersbach, H.; et al. *Global Stratospheric Temperature Bias and Other Stratospheric Aspects of ERA5 and ERA5. 1*; European Centre for Medium Range Weather Forecasts: Reading, UK, 2020.
18. Funatsu, B.; Claud, C.; Keckhut, P.; Hauchecorne, A. Cross-validation of AMSU and LiDAR for long-term upper-stratospheric temperature monitoring. *J. Geophys. Res.-Atmos.* **2008**, *113*. [CrossRef]
19. Blanc, E.; Ceranna, L.; Hauchecorne, A.; Charlton-Perez, A.J.; Marchetti, E.; Evers, L.G.; Kvaerna, T.; Lastovicka, J.; Eliasson, L.; Crosby, N.B.; et al. Toward an Improved Representation of Middle Atmospheric Dynamics Thanks to the ARISE Project. *Surv. Geophys.* **2018**, *39*, 171–225. [CrossRef]
20. Wing, R.; Hauchecorne, A.; Keckhut, P.; Godin-Beekmann, S.; Khaykin, S.; McCullough, E.M.; Mariscal, J.F.; d'Almeida, E. LiDAR temperature series in the middle atmosphere as a reference data set—Part 1: Improved retrievals and a 20-year cross-validation of two co-located French LiDARs. *Atmos. Meas. Tech.* **2018**, *11*, 5531–5547. [CrossRef]
21. Leblanc, T.; McDermid, I.S.; Keckhut, P.; Hauchecorne, A.; She, C.Y.; Krueger, D.A. Temperature climatology of the middle atmosphere from long-term LiDAR measurements at middle and low latitudes. *J. Geophys. Res. Atmos.* **1998**, *103*, 17191–17204. [CrossRef]
22. Keckhut, P.; David, C.; Marchand, M.; Bekki, S.; Jumelet, J.; Hauchecorne, A.; Höpfner, M. Observation of Polar Stratospheric Clouds down to the Mediterranean coast. *Atmos. Chem. Phys.* **2007**, *7*, 5275–5281. [CrossRef]
23. Angot, G.; Keckhut, P.; Hauchecorne, A.; Claud, C. Contribution of stratospheric warmings to temperature trends in the middle atmosphere from the LiDAR series obtained at Haute-Provence Observatory (44° N). *J. Geophys. Res. Atmos.* **2012**, *117*. [CrossRef]
24. Hauchecorne, A.; Chanin, M.L. Density and temperature profiles obtained by LiDAR between 35 and 70 km. *Geophys. Res. Lett.* **1980**, *7*, 565–568. [CrossRef]
25. Keckhut, P.; Hauchecorne, A.; Chanin, M.L. A Critical Review of the Database Acquired for the Long-Term Surveillance of the Middle Atmosphere by the French Rayleigh LiDARs. *J. Atmos. Ocean. Technol.* **1993**, *10*, 850–867. [CrossRef]
26. Keckhut, P.; Claud, C.; Funatsu, B.M.; Hauchecorne, A.; Maury, P.; Khaykin, S.; Le Pichon, A.; Steinbrecht, W. Temperature trends observed in the middle atmosphere and future directions. In *Infrasound Monitoring for Atmospheric Studies*; Springer: Cham, Switzerland, 2019; p. 805. [CrossRef]
27. Steiner, A.K.; Ladstädter, F.; Randel, W.J.; Maycock, A.C.; Fu, Q.; Claud, C.; Gleisner, H.; Haimberger, L.; Ho, S.P.; Keckhut, P.; et al. Observed temperature changes in the troposphere and stratosphere from 1979 to 2018. *J. Clim.* **2020**, *33*, 8165–8194. [CrossRef]
28. Keckhut, P.; Randel, W.; Claud, C.; Leblanc, T.; Steinbrecht, W.; Funatsu, B.; Bencherif, H.; McDermid, I.; Hauchecorne, A.; Long, C.; et al. An evaluation of uncertainties in monitoring middle atmosphere temperatures with the ground-based LiDAR network in support of space observations. *J. Atmos. Sol.-Terr. Phys.* **2011**, *73*, 627–642. [CrossRef]
29. She, C.Y.; Yu, J.R.; Krueger, D.A.; Roble, R.; Keckhut, P.; Hauchecorne, A.; Chanin, M.L. Vertical structure of the midlatitude temperature from stratosphere to mesopause (30–105 km). *Geophys. Res. Lett.* **1995**, *22*, 377–380. [CrossRef]
30. Picone, J.M.; Hedin, A.E.; Drob, D.P.; Aikin, A.C. NRLMSISE-00 empirical model of the atmosphere: Statistical comparisons and scientific issues. *J. Geophys. Res. Space Phys.* **2002**, *107*, SIA 15–1–SIA 15–16. [CrossRef]
31. Mze, N.; Hauchecorne, A.; Keckhut, P.; Thétis, M. Vertical distribution of gravity wave potential energy from long-term Rayleigh LiDAR data at a northern middle latitude site. *J. Geophys. Res. Atmos.* **2014**, *119*, 12069–12083. [CrossRef]
32. Kurylo, M.J. Network for the detection of stratospheric change. In *Remote Sensing of Atmospheric Chemistry*; International Society for Optics and Photonics, SPIE: Bellingham, WA, USA, 1991; Volume 1491, pp. 168–174. [CrossRef]
33. Wing, R.; Steinbrecht, W.; Godin-Beekmann, S.; McGee, T.J.; Sullivan, J.T.; Sumnicht, G.; Ancellet, G.; Hauchecorne, A.; Khaykin, S.; Keckhut, P. Intercomparison and evaluation of ground- and satellite-based stratospheric ozone and temperature profiles above Observatoire de Haute-Provence during the LiDAR Validation NDACC Experiment (LAVANDE). *Atmos. Meas. Tech.* **2020**, *13*, 5621–5642. [CrossRef]
34. Keckhut, P.; Hauchecorne, A.; Meftah, M.; Khaykin, S.; Claud, C.; Simoneau, P. Middle-Atmosphere Temperature Monitoring Addressed with a Constellation of CubeSats Dedicated to Climate Issues. *J. Atmos. Ocean. Technol.* **2021**, *38*, 685–693. [CrossRef]
35. Wright, C.J.; Hindley, N.P. How well do stratospheric reanalyses reproduce high-resolution satellite temperature measurements? *Atmos. Chem. Phys.* **2018**, *18*, 13703–13731. [CrossRef]
36. Andrews, D.; Holton, J.; Leovy, C. *Middle Atmosphere Dynamics*; International Geophysics, Elsevier Science: New York, NY, USA; Academic Press: Cambridge, MA, USA, 1987.
37. Keckhut, P.; Hauchecorne, A.; Kerzenmacher, T.; Angot, G. Modes of variability of the vertical temperature profile of the middle atmosphere at mid-latitude: Similarities with solar forcing. *J. Atmos. Sol.-Terr. Phys.* **2012**, *75–76*, 92–97. [CrossRef]
38. Charney, J.G.; Drazin, P.G. Propagation of planetary-scale disturbances from the lower into the upper atmosphere. *J. Geophys. Res.* **1961**, *66*, 83–109. [CrossRef]
39. Kalnay, E. *Atmospheric Modeling, Data Assimilation and Predictability*; Cambridge University Press: Cambridge, UK, 2002. [CrossRef]
40. Hauchecorne, A.; Chanin, M.L.; Wilson, R. Mesospheric temperature inversion and gravity wave breaking. *Geophys. Res. Lett.* **1987**, *14*, 933–936. [CrossRef]
41. Leblanc, T.; Hauchecorne, A.; Chanin, M.L.; Rodgers, C.; Taylor, F.; Livesey, N. Mesospheric temperature inversions as seen by ISAMS in December 1991. *Geophys. Res. Lett.* **1995**, *22*, 1485–1488. [CrossRef]

42. Wilson, R.; Chanin, M.L.; Hauchecorne, A. Gravity waves in the middle atmosphere observed by Rayleigh LiDAR: 2. Climatology. *J. Geophys. Res.-Atmos.* **1991**, *96*, 5169–5183. [CrossRef]
43. Strelnikova, I.; Almowafy, M.; Baumgarten, G.; Baumgarten, K.; Ern, M.; Gerding, M.; Lübken, F.J. Seasonal Cycle of Gravity Wave Potential Energy Densities from LiDAR and Satellite Observations at 54° and 69° N. *J. Atmos. Sci.* **2021**, *78*, 1359–1386. [CrossRef]
44. Meriwether, J.W.; Gardner, C.S. A review of the mesosphere inversion layer phenomenon. *J. Geophys. Res. Atmos.* **2000**, *105*, 12405–12416. [CrossRef]
45. Hauchecorne, A.; Maillard, A. A 2-d dynamical model of mesospheric temperature inversions in winter. *Geophys. Res. Lett.* **1990**, *17*, 2197–2200. [CrossRef]
46. Kawatani, Y.; Hirooka, T.; Hamilton, K.; Smith, A.K.; Fujiwara, M. Representation of the equatorial stratopause semiannual oscillation in global atmospheric reanalyses. *Atmos. Chem. Phys.* **2020**, *20*, 9115–9133. [CrossRef]
47. Scherhag, R. Die explosionsartigen stratospherener warmungen des spatwinters. *Ber. Deut. Wetterd.* **1952**, *38*, 51–63.
48. Labitzke, K. Interannual Variability of the Winter Stratosphere in the Northern Hemisphere. *Mon. Weather. Rev.* **1977**, *105*, 762–770. [CrossRef]
49. Charlton, A.; Polvani, L. A New Look at Stratospheric Sudden Warmings. Part I: Climatology and Modeling Benchmarks. *J. Clim.* **2007**, *20*, 449–469. [CrossRef]
50. Maury, P.; Claud, C.; Manzini, E.; Hauchecorne, A.; Keckhut, P. Characteristics of stratospheric warming events during Northern winter. *J. Geophys. Res. Atmos.* **2016**, *121*, 5368–5380. [CrossRef]
51. Šavli, M.; Pourret, V.; Payan, C.; Mahfouf, J.F. Sensitivity of Aeolus HLOS winds to temperature and pressure specification in the L2B processor. *Atmos. Meas. Tech. Discuss.* **2021**, *2021*, 1–22. [CrossRef]

## 3.3 . Conclusions

Ainsi, les réanalyses ERA5 de température parviennent à reproduire de manière précise la variabilité observée en hiver dans la stratosphère, que ce soit pendant ou en dehors des périodes d'échauffements stratosphériques soudains. Les implications de ce résultat revêtent une grande importance pour les études ultérieures présentées dans cette thèse, où les réanalyses ERA5 seront largement employées en hiver dans la stratosphère. En revanche, cette bonne reproduction de la variabilité ne se retrouve pas dans la mésosphère, que ce soit en hiver ou en été, au sein des réanalyses ERA5. La principale preuve en est la simulation peu satisfaisante, voire inexistante, des phénomènes d'inversion de température mésosphérique. Ce constat n'est pas surprenant, étant donné que le modèle présente une faible résolution à ces altitudes et n'assimile pas d'observations dans la mésosphère. De plus, l'activité des ondes de gravité est considérablement réduite par la couche éponge située au-dessus de 50 km, ce qui entrave leur propagation. Cependant, même si la simulation des inversions au sein des profils de température d'ERA5 est imprécise, elle met en lumière l'existence de leurs paramétrisations dans le modèle, alors même que le mécanisme de leur formation suscite encore des débats. Étant donné que certaines théories suggèrent un ralentissement du vent dû au passage des ondes de gravité au niveau des inversions de température, il serait intéressant d'analyser le comportement du vent dans les réanalyses ERA5 lors de ces phénomènes. Dans le prochain chapitre, cette investigation sera menée en parallèle avec la présentation des premières observations simultanées de température et de vent lors des inversions de température mésosphériques.

# 4 - Nouvelles observations de vent lors d'inversions mésosphériques

## 4.1 . Introduction

Comme l'évaluation des réanalyses ERA5 l'a démontré, la variabilité de la mésosphère, largement influencée par les inversions de température, demeure actuellement insuffisamment simulée dans les modèles. Ce constat souligne l'impératif d'approfondir notre compréhension des effets des inversions sur cet environnement, en vue d'améliorer leurs paramétrisations au sein des modèles. De plus, une meilleure documentation des inversions mésosphériques revêt une grande importance pour diverses applications, telles que les vols de navettes spatiales, les trajectoires de missiles et de fusées lors de leur réentrée dans l'atmosphère.

Dans ce chapitre, nous présentons les premières observations LiDAR des vents en présence d'inversions de température mésosphériques, ainsi que les simulations effectuées par ERA5. L'objectif premier est de fournir une nouvelle perspective sur ces phénomènes en mettant en lumière leurs répercussions sur les schémas de vent. De plus, nous examinons le mécanisme de formation des inversions mésosphériques, en mettant en évidence le rôle probablement significatif des ondes de gravité dans leur initiation et leur maintien.

## 4.2 . Article

L'article ci-dessous a été publié dans le journal "Geophysical Research Letters" le 2 mai 2023.

Geophysical Research Letters

RESEARCH LETTER
10.1029/2022GL102683

# Co-Located Wind and Temperature Observations at Mid-Latitudes During Mesospheric Inversion Layer Events

**A. Mariaccia[1], P. Keckhut[1], A. Hauchecorne[1], S. Khaykin[1], and M. Ratynski[1]**

[1]Laboratoire Atmosphères, Milieux, Observations Spatiales, UMR 8190, Institut Pierre-Simon Laplace, Université Versailles-Saint Quentin, Université Paris-Saclay, Guyancourt, France

**Key Points:**

- First simultaneous wind and temperature observations in the altitude range 30–90 km during mesospheric inversion layer events
- According to these new observations, there is a strong wind deceleration occurring at the same altitude that the temperature inversion
- These results argue in favor of the mesospheric inversion layer's formation mechanism involving gravity wave dissipation

**Correspondence to:**

A. Mariaccia,
alexis.mariaccia@latmos.ipsl.fr

**Citation:**

Mariaccia, A., Keckhut, P., Hauchecorne, A., Khaykin, S., & Ratynski, M. (2023). Co-located wind and temperature observations at mid-latitudes during mesospheric inversion layer events. *Geophysical Research Letters*, *50*, e2022GL102683. https://doi.org/10.1029/2022GL102683

Received 5 JAN 2023
Accepted 24 FEB 2023

**Author Contributions:**

**Conceptualization:** A. Mariaccia, P. Keckhut, A. Hauchecorne, S. Khaykin
**Investigation:** A. Mariaccia
**Methodology:** A. Mariaccia, P. Keckhut, A. Hauchecorne, S. Khaykin
**Software:** A. Mariaccia
**Supervision:** P. Keckhut, A. Hauchecorne, S. Khaykin
**Validation:** P. Keckhut, A. Hauchecorne, S. Khaykin, M. Ratynski
**Visualization:** A. Mariaccia, P. Keckhut, A. Hauchecorne, M. Ratynski
**Writing – original draft:** A. Mariaccia
**Writing – review & editing:** P. Keckhut, A. Hauchecorne, S. Khaykin, M. Ratynski



**Abstract** The mesospheric inversion layer (MIL) phenomenon is a temperature enhancement (10–50 K) in a vertical layer (~10 km) lasting several days and spanning thousands of kilometers within the mesosphere. As MILs govern the mesospheric variability, their study is crucial for a better understanding of the middle-atmosphere global circulation. MIL phenomenon is also important for applications in aeronautics as perturbations in the mesosphere are significant issues for the safe reentry of rockets, space shuttles, or missiles. However, the description of this phenomenon remains incomplete, since no observations of MIL's effects on winds exist, hampering an understanding of the mechanisms responsible for their formation. This study investigates simultaneous wind-temperature observations in the altitude range of 30–90 km during MIL events. Strong winds deceleration occurred in the same altitude range as the temperature inversion, confirming the role of gravity waves in MIL's formation mechanisms.

**Plain Language Summary** Atmospheric waves propagate from the lower to upper layers, transferring their energy throughout the atmosphere. The mesosphere (50–90 km) is subject to these energy transfers, causing unexpected temperature increases (10–50 K) over a vertical layer (~10 km). These deviations are called mesospheric inversion layers (MILs). Though largely observed in temperature profiles, the MIL phenomenon remains misunderstood, as MIL's impacts on the wind in the middle atmosphere remain unknown. In this study, we first reported simultaneous wind-temperature observations between 30 and 90 km during MIL events. We observed a strong wind deceleration in the same altitude range where the temperature increases. This result argues in favor of the role of gravity waves in MIL's formation mechanisms.

## 1. Introduction

The mesosphere (50–90 km) is a substantial layer of the atmosphere where large and small-scale perturbations occur. These perturbations are caused by the propagation and breaking of atmospheric tides and waves from sources above and below, inducing deviations from its natural thermal structure. The so-called Mesospheric Inversion Layer (MIL) phenomenon is an especially significant perturbation that is now recognized to be responsible for a large part of the mesospheric variability. Moreover, MILs have garnered interest among researchers, since mesospheric perturbations are significant issues for applications in aeronautics, in particular the safe reentry of space shuttles and missiles (Wing et al., 2020). Indeed, since the first MIL phenomenon's signatures observed by rockets (e.g., Schmidlin, 1976; Stroud et al., 1960; Theon et al., 1967) that reported a non-expected positive lapse rate in the mesosphere, researchers have carried out numerous studies of MIL events (e.g., Cutler et al., 2001; Dao et al., 1995; Duck et al., 2001; Gan et al., 2012; Leblanc et al., 1995; Leblanc & Hauchecorne, 1997). An important review of the knowledge state on the MIL phenomenon has been carried out by Meriwether and Gardner (2000). The MIL phenomenon (henceforth referred to as simply MIL) is defined as a layer of about 10 km with enhanced temperature between 15 and 50 K, spanning over a thousand square kilometers over several days. MILs are currently known to occur quite often at low to mid-latitudes, preferentially in winter, and have been separated into two subtypes: the lower MIL, occurring between 65 and 80 km, especially in winter, and the upper MIL, occurring above 85 km. Different mechanisms have been suggested to explain their formation, such as planetary waves dissipation (France et al., 2015; Salby et al., 2002), gravity waves and tides interaction (Liu & Hagan, 1998; Meriwether & Gardner, 2000), and chemical heating (Meriwether & Mlynczak, 1995; Ramesh et al., 2013); however, these mechanisms remain not entirely described and are still an active research field. In particular, the wind behavior in the middle atmosphere (30–90 km) when a MIL event occurs remains an unanswered question, even though several studies have suggested its significant role in the MIL appearance (Meriwether & Gerrard, 2004). For instance, Hauchecorne et al. (1987) estimated the

role of gravity wave dissipation in the MIL's persistence, and showed that this process strongly depends on the temperature and the background wind. Salby et al. (2002) and Sassi et al. (2002) cfocused on the mechanism of MIL creation and revealed with simulations that the planetary wave breaking is supposed to occur in the same altitude range of a weak zonal wind region. The wind behavior during MIL events is an essential component of understanding the MIL phenomenon and, more broadly, the impacts on general middle atmosphere circulation. Although some studies have reported simultaneous wind-temperature observations in the middle atmosphere (e.g., Baumgarten, 2010; Stroud et al., 1960; Theon et al., 1967), most of them did not focus on the MIL phenomenon. Furthermore, some of these studies have detected MILs without knowing the phenomenon. For instance, Stroud et al. (1960) was unaware of the MIL phenomenon yet reported a temperature inversion at 80 km with strong wind shear at the same altitude without giving any explanation to this observed behavior.

Despite this supposed role, only two studies Huang et al. (1998), Huang et al. (2002) have reported simultaneous zonal wind and temperature observations from Na LiDAR in the altitude range 85–100 km in which a large wind shear associated with a MIL was detected. However, this incomplete description of the wind signature at upper MIL altitudes is insufficient for determining the entire shear profile and studying how gravity waves propagate from the stratosphere to the thermosphere (Le Du et al., 2022).

To date, all the theoretical and modeled wind behavior assumptions in the middle atmosphere during a MIL event have never been confirmed due to the absence of accurate co-located and simultaneous temperature and wind measurements with the former instruments (Meriwether & Gerrard, 2004). To our knowledge, the DYANA campaign, which took place in the northern hemisphere in 1990, is one the only during which Rayleigh LiDAR and falling spheres simultaneously measured temperature and wind, respectively, in the whole middle atmosphere. However, the characteristics of the MILs observed during this campaign were not studied, as this was not one of the main objectives. In addition, the falling sphere profiles suffer from significant smoothing and bias (see Figure 1) due to the large speed of the payload in the mesosphere, making this technique not enough reliable (Lübken et al., 1994). Since then, remote sensing techniques have been developed, particularly with the rise of the Doppler Rayleigh LiDAR technology capable of accurately measuring the temperature and wind in the atmospheric window of 30–90 km. Doppler LiDAR currently operates at the Observatoire of Haute-Provence (OHP) as well as Rayleigh LiDAR and Ozone LiDAR. The latter two LiDAR measuring the temperature and monitoring the ozone, respectively, making the OHP one of the rare station in the world where co-located and simultaneous wind-temperature observations in the middle-atmosphere are possible.

Our study aims to answer how the winds evolve during MIL events by providing the first time simultaneous temperature and wind observations in the altitude range of 30–90 km. The two observation data sets used here were acquired at Biscarrosse during the DYANA campaign in 1990 and at the OHP, located 550 km apart, in 2021/2022 winter. Biscarrosse and OHP stations exhibit a similar mesospheric climatology (Hauchecorne et al., 1991), making them well-situated for investigating the MIL's signature at both sites. Additionally, we explore how ERA5 reanalyzes simulated the wind and temperature during MIL events.

The publication is structured as follows. In Section 2, the data set from DYANA and Aeolus Validation campaigns as well as ERA5 reanalyzes are presented. Then, the method to identify and to characterize MIL events is described in Section 3. The temperature-wind observations for each selected date with MIL events are shown and commented in Section 4. Finally, mechanisms responsible for lower MILs are discussed, and perspectives are given in Section 5.

## 2. Data Description

### 2.1. The DYANA Campaign: Rayleigh LiDAR and Falling Spheres

The DYANA (DYnamics Adapted Network for the Atmosphere) campaign was conducted in the northern hemisphere over a large horizontal area from January to March 1990 in order to explore the middle atmosphere dynamics (10–100 km). This campaign was designed to improve the lack of horizontal coverage missing during previous campaigns. The main dynamical objectives were to study the large, medium, and small-scale variations generated by planetary waves, gravity waves, tides, and turbulence. Another aim was to inter-compare measurements in order to cross-check experimental methods. Thus, several techniques were employed during these 3 months to measure temperature and density from multiple ground-based stations. The set of these techniques with their monitored height range was: rocket bornes (90–115 km), falling spheres (30–90 km), Rayleigh LiDAR

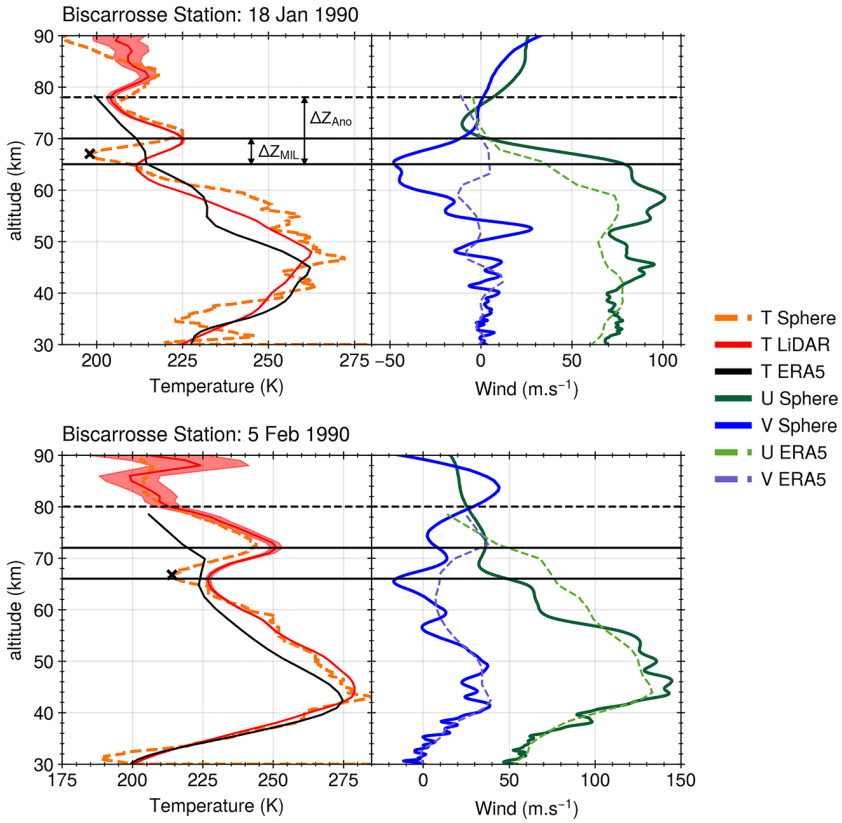


**Figure 1.** Temperature and wind profiles measured at Biscarrosse from falling spheres and Rayleigh LiDAR between 30 and 90 km for two dates during the DYANA Campaign. The statistical noise (red shaded area) of the LiDAR temperature signal is displayed. The two horizontal black solid lines indicate, respectively, the derived bottom and top of the MIL detected by the Rayleigh LiDAR. The horizontal dashed line represents the altitude of the potential total extension of the temperature anomaly ($\Delta Z_{Ano}$). The black cross points out the bottom of the MIL measured from falling spheres. In addition, the ERA5 temperature-wind profiles extracted for each date are shown.

(30–90 km), sodium LiDAR (80–105 km), data sondes (25–65 km) and radiosondes (0–32 km). These different instruments occasionally carried out coordinated temperature and density measurements at the exact location and approximately the same periods (about 1 hr) to perform inter-comparisons. For instance, the station based in southwest France at Biscarrosse (44°N–1°W) benefited from simultaneous observations from Rayleigh LiDAR and falling spheres. During the campaign, falling spheres were released at about 110 km altitude to obtain density, temperature, and wind profiles in the middle atmosphere. A detailed description of the falling sphere technique can be found in Engler (1965) and Jones and Peterson (1968). At the ground, a Rayleigh LiDAR measured the density profile by counting the number of photons from which the temperature was inferred by assuming hydrostatic equilibrium in the 30–90 km range, where a pure molecular backscattering is expected. The vertical resolution of LiDAR temperature profiles is typically 200 m. The Rayleigh Lidar method and the technical information about the LiDAR located at Biscarrosse have been described in Hauchecorne et al. (1991). The complete description of the DYANA campaign and its objectives have been reported in Offermann (1994). The presentation of each instrumental technique and the inter-comparison results are shown in Lübken et al. (1994). In the measurements data set carried out at Biscarrosse in 1990, eight dates of co-located and simultaneous temperature-wind observations are available.

### 2.2. Aeolus Validation Campaign: OHP LiDARs

In August 2018, in the frame of the Living Planet Program, the Aeolus satellite was launched by the European Space Agency in order to provide global wind profiles from the surface to 30 km for a 3 years period (Straume et al., 2020). The Aeolus satellite measures horizontal line-of-sight winds with a Doppler wind LiDAR named

ALADIN (Atmospheric LAser Doppler Instrument), which is the first-ever Doppler Wind LiDAR embarked on a satellite. In the meantime and in order to assess and validate Aeolus wind observations, ground-based Doppler LiDAR observations within the AboVE-2 (Aeolus Validation Experiment) were undertaken at the Observatory of Haute-Provence (OHP, 44°N, 6°E) (Ratynski et al., 2022). Moreover, the double-edge technique for wind profiling, first demonstrated at OHP (Chanin et al., 1989; Garnier et al., 1992), is realized in ALADIN Rayleigh channel. Several co-located LiDARs have been monitoring the middle atmosphere at the OHP within the Network for the Detection of Composition Changes (NDACC) for decades. Since 1993, a LIOvent Doppler LiDAR has been measuring the wind velocities at OHP, providing the first lidar-based wind climatology in the middle atmosphere (Souprayen et al., 1999). The principle, using the Rayleigh backscattering at 532 nm, is based on the Doppler shift between the emitted and the backscattered laser light caused by the displacement of scattering molecules relative to the LiDAR. The detection of Doppler shift is performed employing a double-edge Fapbry-Perot interferometer. The complete description of the Doppler LiDAR's technique and the instrument design at OHP has been reported in Chanin et al. (1989) and more recently in Khaykin et al. (2020).

Finally, an Ozone LiDAR has been monitoring the ozone as part of the Network for the Detection of Stratospheric Changes. The Ozone LiDAR's principle rests on the differential absorption LiDAR technique requiring the emission of two simultaneous laser wavelengths, 308 (absorbing) and 355 (non-absorbing) nm here, with differential absorption by ozone to provide its vertical profile. The method and the technical information about the Ozone LiDAR at OHP have been described in several studies (e.g., Godin-Beekmann et al., 2003; Wing et al., 2018). Thus, in order to perform simultaneous wind and temperature measurements at OHP, the temperature observations can also be derived by the Ozone LiDAR in off mode by using only the non-absorbing channel (355 nm). Therefore, in addition to the DYANA campaign data set, we benefited from 44 dates of simultaneous observations of temperature and wind carried out at the OHP from 2018 to 2022.

### 2.3. ERA5 Reanalyzes

The ERA5 reanalyzes are the last generation of reanalyzes, archiving the past climate on earth from 1950 to the present, produced by the ECMWF (European Center Medium for Weather Forecast) since 2016. These ERA5 reanalyzes are produced with a 4DVar assimilation scheme and the integrated system forecast Cycle 41r2. The ERA5 output is constructed every hour on a 0.25° latitude-longitude grid and 137 vertical levels lying from the surface to the level pressure 0.01 hPa (approximately 80 km). More technical information about ERA5 reanalyzes can be found in Hersbach et al. (2020). Here, in order to pursue investigations on how the ECMWF model simulates the MIL phenomenon already undertaken in Mariaccia et al. (2022), ERA5 wind and temperature reanalyzes are extracted at the nearest hour of the mid of acquisitions for the six dates shown above Biscarrosse and the OHP (Figures 1 and 2).

## 3. Method for Identifying and Characterizing MILs

Here, in order to identify MIL events within the temperature profiles, we followed the method developed by Leblanc and Hauchecorne (1997) and Fechine et al. (2008), which has been applied in numerous previous studies (e.g., Ardalan et al., 2022; Cutler et al., 2001; Leblanc et al., 1998). According to them, a MIL is identified when these three criteria are observed:

- The MIL bottom must be at least 5 km above the stratopause and the MIL top below 90 km.
- The temperature perturbation must be significant relative to the measurement uncertainty, that is, Terr $< \Delta T$.
- Finally, the temperature amplitude must be $2\sigma$ larger than the temperature fluctuations expected by gravity waves at these altitudes. According to Mzé et al. (2014), gravity waves are expected to generate perturbations of 1.6 K at 50 km and 4 K at 75 km.

Afterward, we characterized each observed MIL by computing their amplitude, thickness, and gradient similarly to the method developed in Figure 2 in Ardalan et al. (2022). Thus, for each observed temperature profile, our algorithm identified two altitudes: the altitude of the bottom MIL from which the temperature gradient reverses and the altitude of the top MIL where the temperature maximum is reached. These two altitudes are pointed out with horizontal solid lines in Figures 1 and 2 which delimit the observed MIL's altitude range ($\Delta Z_{MIL}$). Finally, the altitude corresponding to the potential extension of the temperature anomaly is determined when the temperature profile returns to the standard climatology, which is arbitrarily determined. Thus, amplitudes of temperature

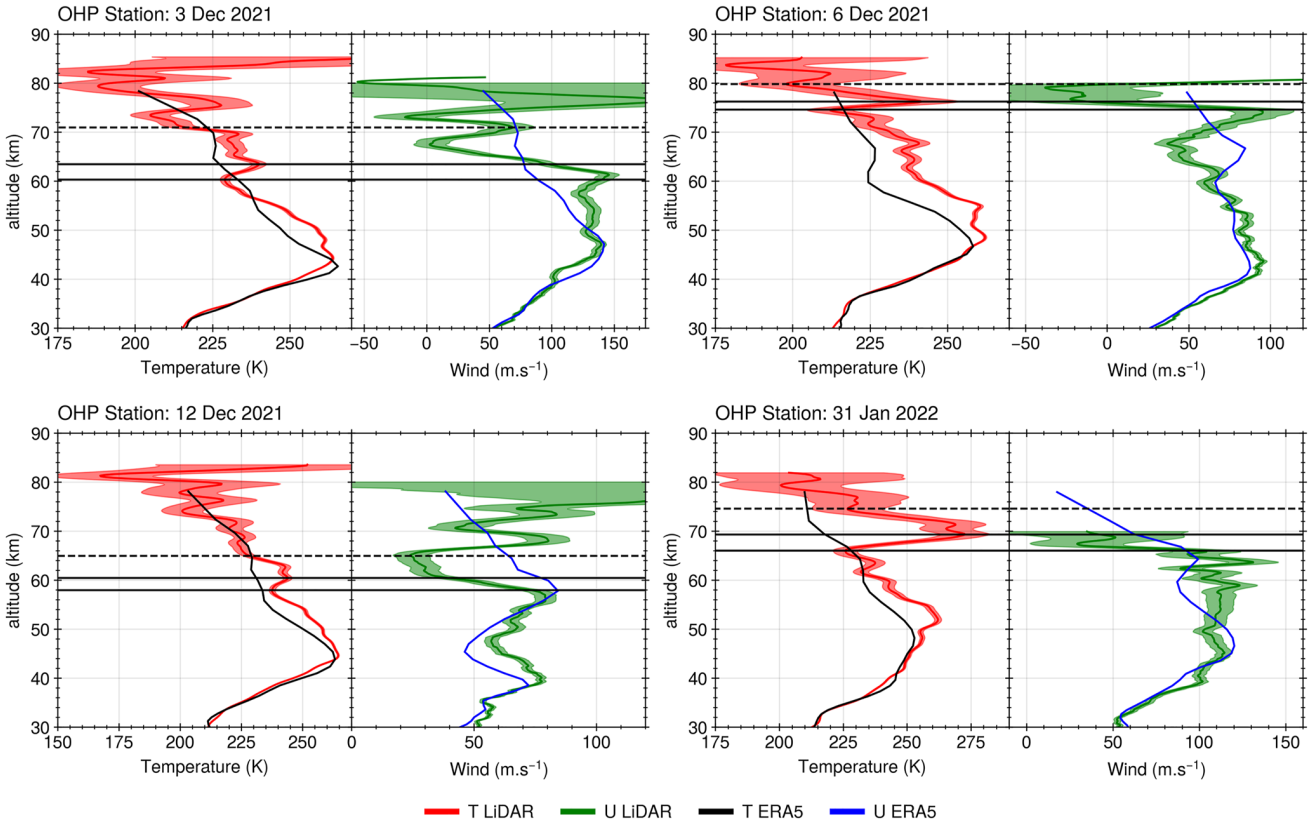


**Figure 2.** Temperature (red) and zonal wind (green) profiles measured for four dates in 2021/2022 winter from the Ozone LiDAR (temperature mode) and the Doppler LiDAR, respectively, located at the OHP. The statistical noise (shaded area) associated with these profiles is displayed. The three horizontal black lines indicate the same MIL's features that in Figure 1. Additionally, ERA5 temperature (black) and wind (blue) reanalyzes profiles are shown for these four dates.

increase ($\Delta T$) within the MIL is computed over the $\Delta Z_{MIL}$ thickness (Figure 1) for each profile. Zonal ($\Delta U$) and meridional ($\Delta V$) wind deviations are computed over the thickness $\Delta Z_{MIL}$ since the reversal of temperature gradients remains a better indicator than a wind drop to identify MIL's signature.

## 4. Results

### 4.1. DYANA Campaign in Biscarrosse

As a result, only two dates in the data from the DYANA campaign possess lower MIL presences which are exploitable. Figure 1 shows temperature zonal and meridional wind profiles measured by LiDAR and falling spheres. Simulated temperature profiles are provided by ERA5 for these two cases in the middle atmosphere during which lower MILs were present. According to these profiles, it is evident that a connection exists between the temperature and wind evolutions, that is, a wind deceleration occurs when the temperature increases, sometimes leading to a wind reversal for both meridional and zonal winds. Moreover, this wind deceleration tends to start at an altitude around the altitude where the temperature inversion starts. For instance, on 18 January 1990, the observed MIL illustrates well this temperature-wind connection with a temperature increase of 13.6 ± 0.8 K, causing the deceleration of the total wind lying from 92 m.s$^{-1}$ to 12 m.s$^{-1}$. While for the MIL observed on 5 February 1990, a total wind deceleration of around 14 m.s$^{-1}$ is found for a temperature elevation of 24.4 ± 3 K. Thus, the magnitude of the wind deceleration is not necessarily linearly linked with the temperature amplitude of the MIL. However, these wind deceleration values possess uncertainties since they are computed on the vertical domain where the positive temperature gradient is observed and not in the altitude range where the wind drop occurs. Nevertheless, this method captures the wind deceleration process during a MIL phenomenon.

The temperature measured by the falling sphere is compared with the collocated LiDAR temperature profile for the same dates. As a result, falling spheres' temperatures are systematically lower than LiDAR's temperatures

between 65 and 70–75 km for the two dates. Lübken et al. (1994) have reported that this difference is about 5 K between 65 and 77 km and is mainly due to drag uncertainty associated with the sphere descent that has a significant impact during the transition from super to sub-sonic at these altitudes. Thus, on 18 January 1990, the LiDAR detected the MIL bottom at around 65 km, while the falling sphere temperature profiles exhibit the MIL bottom higher near 68 km. However, the bottom of the MIL observed by the LiDAR corresponds better to the altitude where zonal and meridional winds start to decrease. Furthermore, the temperature profile from the falling spheres possesses a noise not realistic between 30 and 40 km, caused by an effect of vertical winds (Lübken et al., 1994), absent in the LiDAR profile. Therefore, to characterize mesospheric inversions with minimum uncertainty, only the temperature profiles acquired from Rayleigh LiDAR during the DYANA campaign are used to compute MIL's temperature amplitudes.

However, we notice that the ERA5 reanalyzes imprecisely simulated the magnitude, thickness, and altitude of the temperature inversion for these two dates. Surprisingly, for both dates, the zonal and meridional winds deceleration processes associated with the MIL are simulated with realistic magnitudes in ERA5 but starting at lower altitudes than in spheres' observations.

### 4.2. AboVE-2 Campaign at OHP

After applying the MIL identification method to the 44 available temperature profiles, we found only four cases during 2021/2022 winter in which a lower MIL was identifiable.

The main reason for these few identified MIL events is the challenge of measuring wind in the mesosphere due to the dependence on sky transparency. Furthermore, many actual wind observations possess weak signals, limiting the accurate detection of lower MILs during this period. For the recent observations, only zonal wind measurements were performed by the Doppler LiDAR during 2021/2022 winter to facilitate the inter-comparisons with the collocated Aeolus observations, which measures essentially the zonal component of winds. Nevertheless, as the zonal wind is often more significant than the meridional wind in the mesosphere by a factor of 10, we supposed that a zonal wind reduction implies very likely a total wind deceleration.

Figure 2 shows temperature and zonal wind profiles observed above the OHP for these four dates in the mesosphere where lower MILs were detected. Similar zonal wind deceleration behavior, as observed in Figure 1, is found within the lower MILs. In addition, the altitudes at which the temperature increases match well with those where the zonal wind starts to decelerate, similar to previous observations (Figure 1), confirming the temperature-wind connection. Afterward, we computed the MIL's characteristics by following the method described in Section 3 for these four MIL events. For instance, on 3 December 2021, the MIL detected was characterized by a temperature elevation of 11.1 ± 3.9 K associated with a zonal wind deceleration of 43.3 ± 17 $m.s^{-1}$. However, according to the wind observations, the zonal wind dropped over a larger altitude range than the one where the temperature increased. Therefore, this computed zonal wind fluctuation is lower than the one observed, which is, in reality, around 150 $m.s^{-1}$ (Figure 2). Consequently, these computed zonal wind amplitudes possess uncertainties due to the employed method. These results illustrate the Doppler LiDAR's capacity to capture strong wind fluctuations over narrow layers. For instance, on 6 December 2021, a zonal wind deceleration of 105.5 ± 57.5 $m.s^{-1}$ associated with a temperature elevation of 29.5 ± 19.2 K are computed over a layer of 1.65 km. Finally, the MIL events on 12 December 2021 and 31 January 2020, respectively, possess temperature elevations of 6.5 ± 2.9 K and 46.8 ± 14.3 K associated with zonal wind decelerations of 34.3 ± 10.1 $m.s^{-1}$ and 59.4 ± 68.7 $m.s^{-1}$. These computed values confirm, unlike those above Biscarrosse, that large temperature amplitudes within MILs tend to be directly related to substantial wind deceleration. Thus, over these six MIL events, we found a mean temperature gradient of 7.5 $K.km^{-1}$ associated with a mean zonal wind deceleration gradient of 21 $m.s^{-1}.km^{-1}$.

On 3 December 2021, a second MIL was present at 75 km in the temperature profile, but the altitude range of the wind observations at this altitude does not allow to derive wind deceleration of this MIL. Despite this uncertainty, the Doppler LiDAR technique is an excellent instrument for documenting MIL's effects on winds. Finally, unlike the two MILs above Biscarrosse, ERA5 temperature and wind reanalyzes did not reproduce MILs' presence for these four dates above the OHP.

## 5. Discussion and Perspectives on Mechanisms Responsible for Lower MILs

From the above results concerning co-located temperature and wind observations in the mesosphere during MIL events (Figures 1 and 2), we can determine that MIL's formation involved systematic wind drops within the

altitude range where the temperature increases. Unfortunately, these results are insufficient to precisely determine how the zonal wind deceleration magnitude varies with a specific temperature increase. Indeed, the computed amplitudes possess several uncertainties, such as the possibility of observations carried out outside the MIL center and the presence of other geophysical processes. Moreover, the method employed here to characterize MILs is better suited for capturing temperature amplitudes than for capturing wind shears within MILs. Consequently, further simultaneous temperature-wind observations are necessary to quantify the wind-temperature interconnection accurately.

Among the reported existing mechanisms, the observed connection between temperature and wind supports the theory of MIL's formation mechanism, first introduced by Hauchecorne et al. (1987), which is based on breaking gravity waves inside a thin layer. Since the zonal wind is westerly at all altitudes from the troposphere to the mesosphere in winter, only gravity waves with a westward phase can propagate up to the mesosphere and break at a critical layer where the phase speed becomes close to the background wind (Lindzen, 1981). When a gravity wave breaks and dissipates, the associated momentum transfer decreases the zonal wind above the mesospheric jet, generating turbulence. This turbulence then produces downward vertical heat flux from the upper layer, which generates adiabatic warming responsible for temperature inversion. Thus, this generated turbulence layer favors a continuous breaking of gravity waves which can sustain a temperature inversion layer of tens of kelvins for several days. These perturbations that occur during a MIL event are illustrated in Figure 7 in Hauchecorne et al. (1987), with a schematic representation of the vertical profiles of the mean temperature and the mean zonal wind matching the observations reported in this article. Finally, the results found in Hauchecorne and Maillard (1990), who have simulated a temperature inversion with a 2D model that implies a wind drop by the breaking of gravity waves inside a thin layer, strengthen the notion that this mechanism is essential in MIL's formation.

The research done by Sassi et al. (2002) further supports this idea. The authors simulated a lower MIL events between 70 and 80 km at mid-latitudes with the breaking of planetary waves, which generates warming in the upper stratosphere and cooling in the lower mesosphere favorable toward MIL's appearance. Their analysis shows that such lower MIL events occur in a weak westward wind region produced by the deposition of momentum from westward gravity waves known to occur above 70 km (Mzé et al., 2014). Additionally, when they remove the gravity wave activity in their model, the positive temperature lapse rate created in the mesosphere disappears, confirming the crucial role of gravity waves in the lower MIL's formation and persistence.

Figure 1 shows that the ERA5 reanalyzes are sometimes able to simulate the wind deceleration phenomenon with similar magnitude to the observations reported here, whereas the temperature inversion is nearly overlooked. Nevertheless, for most cases, particularly over the OHP, Figure 2 shows that ERA5 reanalyzes did not capture temperature and wind fluctuations in the mesosphere during MIL events. As already discussed in Mariaccia et al. (2022), the coarse vertical resolution of the model at these altitudes prevent the simulation of such fluctuations. The authors also mention that, the bad representation of the mesosphere is enhanced by the lack of assimilated observation by the model at these altitudes. Furthermore, the sponge layer implemented in the model probably damps the gravity wave energy propagation up to the mesosphere which is necessary for MIL's apparition and sustainability. The realistic MIL characteristics statistics simulated by the Whole Atmosphere Community Climate Model (WACCM), which benefit from a better vertical resolution in the mesosphere than ERA5 (France et al., 2015), suggests that the resolution improvement is the first crucial step in the MIL's simulation achievement. Thus, the new results given above suggest that MIL's formation mechanisms should be considered as a first lead to pursue the elaboration of an accurate theory on the lower MIL's apparition. Future investigations are necessary to test how the energy transfer from gravity wave dissipation in the mesosphere can create background wind drops and temperature increases as those reported here. The elaboration of a new 3-D mechanistic model, in the same manner, that the one developed by Hauchecorne and Maillard (1990) should be pursued, but with a better vertical resolution to simulate temperature inversions by reducing locally wind.

However, the instrumental error associated with the Rayleigh LiDAR grows less quickly than for the Ozone LiDAR. This result is expected, as the Ozone LiDAR was not designed for measuring temperature. Similarly, the Doppler LiDAR observations still suffer from large instrumental errors in the higher mesosphere impacting the study of MIL's effects on zonal wind. Therefore, in order to improve our description of the MIL phenomenon, more wind observations performed by LIOwind Doppler LiDAR with meridional winds are required in addition to temperature measurements to benefit more extensive statistics of simultaneous wind temperature. Furthermore, the improvement of this technique to reduce instrumental errors in the upper mesosphere should

be pursued. Finally, the development of technical instruments capable of measuring the turbulence generated by gravity waves within MILs should be undertaken (Hauchecorne et al., 2016).

## Data Availability Statement

The OHP ground-based lidar data can be obtained via NDACC lidar database https://ndacc.larc.nasa.gov/. The indications to download the ERA-5 data over 137 levels are given on the ECWMF website https://confluence.ecmwf.int/display/CKB/How+to+download+ERA5.

**Acknowledgments**
We gratefully thank the personnel of Station Gerard Megie at OHP (Frederic Gomez, Francois Dolon, Francois Huppert and others) for conducting the lidar observations. The work related to Aeolus validation has been performed in the frame of Aeolus Scientific Calibration & Validation Team (ACVT) activities under support of CNES Aeolus project. The temperature measurements have been obtained as part of as part of the Network for the Detection of Atmospheric Composition Change (NDACC). The falling sphere data as well as the lidar data from Centre d'Essai des Landes (CEL) have been acquired in the frame of the DYANA campaign implying Direction Générale de l'Armement (DGA). This work was performed within the framework of the European ARISE project and was funded by the French Educational Ministry with EUR IPSL.

## References

Ardalan, M., Keckhut, P., Hauchecorne, A., Wing, R., Meftah, M., & Farhani, G. (2022). Updated climatology of mesospheric temperature inversions detected by Rayleigh lidar above observatoire de haute Provence, France, using a k-mean clustering technique. *Atmosphere*, *13*(5), 814. https://doi.org/10.3390/atmos13050814

Baumgarten, G. (2010). Doppler Rayleigh/Mie/Raman lidar for wind and temperature measurements in the middle atmosphere up to 80 km. *Atmospheric Measurement Techniques*, *3*(6), 1509–1518. https://doi.org/10.5194/amt-3-1509-2010

Chanin, M.-L., Garnier, A., Hauchecorne, A., & Porteneuve, J. (1989). A Doppler lidar for measuring winds in the middle atmosphere. *Geophysical Research Letters*, *16*(11), 1273–1276. https://doi.org/10.1029/gl016i011p01273

Cutler, L. J., Collins, R. L., Mizutani, K., & Itabe, T. (2001). Rayleigh lidar observations of mesospheric inversion layers at poker flat, Alaska (65 n, 147 w). *Geophysical Research Letters*, *28*(8), 1467–1470. https://doi.org/10.1029/2000gl012535

Dao, P. D., Farley, R., Tao, X., & Gardner, C. S. (1995). Lidar observations of the temperature profile between 25 and 103 km: Evidence of strong tidal perturbation. *Geophysical Research Letters*, *22*(20), 2825–2828. https://doi.org/10.1029/95gl02950

Duck, T. J., Sipler, D. P., Salah, J. E., & Meriwether, J. W. (2001). Rayleigh lidar observations of a mesospheric inversion layer during night and day. *Geophysical Research Letters*, *28*(18), 3597–3600. https://doi.org/10.1029/2001gl013409

Engler, N. A. (1965). *Development of methods to determine winds, density, pressure, and temperature from the robin falling balloon*. (Tech. Rep.). Dayton University Ohio Research Institute.

Fechine, J., Wrasse, C., Takahashi, H., Mlynczak, M., & Russell, J. (2008). Lower-mesospheric inversion layers over Brazilian equatorial region using timed/saber temperature profiles. *Advances in Space Research*, *41*(9), 1447–1453. https://doi.org/10.1016/j.asr.2007.04.070

France, J., Harvey, V., Randall, C., Collins, R., Smith, A., Peck, E., & Fang, X. (2015). A climatology of planetary wave-driven mesospheric inversion layers in the extratropical winter. *Journal of Geophysical Research: Atmospheres*, *120*(2), 399–413. https://doi.org/10.1002/2014jd022244

Gan, Q., Zhang, S. D., & Yi, F. (2012). Timed/saber observations of lower mesospheric inversion layers at low and middle latitudes. *Journal of Geophysical Research*, *117*(D7). https://doi.org/10.1029/2012jd017455

Garnier, A., Chanin, M. L., Hauchecorne, A., & Porteneuve, J. C. (1992). Laser device for measuring wind speeds at medium altitudes by using a Doppler effect. (US Patent 5,088,815).

Godin-Beekmann, S., Porteneuve, J., & Garnier, A. (2003). Systematic dial lidar monitoring of the stratospheric ozone vertical distribution at observatoire de haute-Provence (43.92 n, 5.71 e). *Journal of Environmental Monitoring*, *5*(1), 57–67. https://doi.org/10.1039/b205880d

Hauchecorne, A., Chanin, M.-L., & Keckhut, P. (1991). Climatology and trends of the middle atmospheric temperature (33–87 km) as seen by Rayleigh lidar over the south of France. *Journal of Geophysical Research*, *96*(D8), 15297–15309. https://doi.org/10.1029/91jd01213

Hauchecorne, A., Chanin, M. L., & Wilson, R. (1987). Mesospheric temperature inversion and gravity wave breaking. *Geophysical Research Letters*, *14*(9), 933–936. https://doi.org/10.1029/GL014i009p00933

Hauchecorne, A., Cot, C., Dalaudier, F., Porteneuve, J., Gaudo, T., Wilson, R., et al. (2016). Tentative detection of clear-air turbulence using a ground-based Rayleigh lidar. *Applied Optics*, *55*(13), 3420–3428. https://doi.org/10.1364/AO.55.003420

Hauchecorne, A., & Maillard, A. (1990). A 2-d dynamical model of mesospheric temperature inversions in winter. *Geophysical Research Letters*, *17*(12), 2197–2200. https://doi.org/10.1029/GL017i012p02197

Hersbach, H., Bell, B., Berrisford, P., Hirahara, S., Horányi, A., Muñoz-Sabater, J., et al. (2020). The ERA5 global reanalysis. *Quarterly Journal of the Royal Meteorological Society*, *146*(730), 1999–2049. https://doi.org/10.1002/qj.3803

Huang, T.-Y., Hickey, M. P., Tuan, T.-F., Dewan, E. M., & Picard, R. H. (2002). Further investigations of a mesospheric inversion layer observed in the aloha-93 campaign. *Journal of Geophysical Research*, *107*(D19), ACL17-1–ACL17-8. https://doi.org/10.1029/2001JD001186

Huang, T. Y., Hur, H., Tuan, T. F., Li, X., Dewan, E. M., & Picard, R. H. (1998). Sudden narrow temperature-inversion-layer formation in aloha-93 as a critical-layer-interaction phenomenon. *Journal of Geophysical Research*, *103*(D6), 6323–6332. https://doi.org/10.1029/97JD03076

Jones, L. M., & Peterson, J. W. (1968). Falling sphere measurements, 30 to 120 km. In R. S. Quiroz (Ed.), *Meteorological investigations of the upper atmosphere: Proceedings of the American meteorological society symposium on meteorological investigations above 70 kilometers, Miami beach, Florida, 31 May–2 June 1967* (pp. 176–189). American Meteorological Society. https://doi.org/10.1007/978-1-935704-37-9_21

Khaykin, S. M., Hauchecorne, A., Wing, R., Keckhut, P., Godin-Beekmann, S., Porteneuve, J., et al. (2020). Doppler lidar at observatoire de haute-Provence for wind profiling up to 75 km altitude: Performance evaluation and observations. *Atmospheric Measurement Techniques*, *13*(3), 1501–1516. https://doi.org/10.5194/amt-13-1501-2020

Leblanc, T., & Hauchecorne, A. (1997). Recent observations of mesospheric temperature inversions. *Journal of Geophysical Research*, *102*(D16), 19471–19482. https://doi.org/10.1029/97jd01445

Leblanc, T., Hauchecorne, A., Chanin, M.-L., Rodgers, C., Taylor, F., & Livesey, N. (1995). Mesospheric temperature inversions as seen by ISAMS in December 1991. *Geophysical Research Letters*, *22*(12), 1485–1488. https://doi.org/10.1029/94gl03274

Leblanc, T., McDermid, I. S., Keckhut, P., Hauchecorne, A., She, C. Y., & Krueger, D. A. (1998). Temperature climatology of the middle atmosphere from long-term lidar measurements at middle and low latitudes. *Journal of Geophysical Research*, *103*(D14), 17191–17204. https://doi.org/10.1029/98JD01347

Le Du, T., Keckhut, P., Hauchecorne, A., & Simoneau, P. (2022). Observation of gravity wave vertical propagation through a mesospheric inversion layer. *Atmosphere*, *13*(7), 1003. https://doi.org/10.3390/atmos13071003

Lindzen, R. S. (1981). Turbulence and stress owing to gravity wave and tidal breakdown. *Journal of Geophysical Research*, *86*(C10), 9707–9714. https://doi.org/10.1029/jc086ic10p09707

Liu, H.-L., & Hagan, M. E. (1998). Local heating/cooling of the mesosphere due to gravity wave and tidal coupling. *Geophysical Research Letters*, *25*(15), 2941–2944. https://doi.org/10.1029/98gl02153

Lübken, F.-J., Hillert, W., Lehmacher, G., Zahn, U., Bittner, M., Offermann, D., et al. (1994). Intercomparison of density and temperature profiles obtained by lidar, ionization gauges, falling spheres, datasondes and radiosondes during the DYANA campaign. *Journal of Atmospheric and Terrestrial Physics*, *56*(13), 1969–1984. (Dynamic Adapted Network for the the Atmosphere). https://doi.org/10.1016/0021-9169(94)90023-X

Mariaccia, A., Keckhut, P., Hauchecorne, A., Claud, C., Le Pichon, A., Meftah, M., & Khaykin, S. (2022). Assessment of ERA-5 temperature variability in the middle atmosphere using Rayleigh lidar measurements between 2005 and 2020. *Atmosphere*, *13*(2), 242. https://doi.org/10.3390/atmos13020242

Meriwether, J. W., & Gardner, C. S. (2000). A review of the mesosphere inversion layer phenomenon. *Journal of Geophysical Research*, *105*(D10), 12405–12416. https://doi.org/10.1029/2000jd900163

Meriwether, J. W., & Gerrard, A. J. (2004). Mesosphere inversion layers and stratosphere temperature enhancements. *Reviews of Geophysics*, *42*(3). https://doi.org/10.1029/2003RG000133

Meriwether, J. W., & Mlynczak, M. G. (1995). Is chemical heating a major cause of the mesosphere inversion layer? *Journal of Geophysical Research*, *100*(D1), 1379–1387. https://doi.org/10.1029/94jd01736

Mzé, N., Hauchecorne, A., Keckhut, P., & Thétis, M. (2014). Vertical distribution of gravity wave potential energy from long-term Rayleigh lidar data at a northern middle-latitude site. *Journal of Geophysical Research: Atmospheres*, *119*(21), 12069–12083. https://doi.org/10.1002/2014JD022035

Offermann, D. (1994). The DYANA campaign: A survey. *Journal of Atmospheric and Terrestrial Physics*, *56*(13), 1639–1657. (Dynamic Adapted Network for the the Atmosphere). https://doi.org/10.1016/0021-9169(94)90002-7

Ramesh, K., Sridharan, S., & Vijaya Bhaskara Rao, S. (2013). Dominance of chemical heating over dynamics in causing a few large mesospheric inversion layer events during January–February 2011. *Journal of Geophysical Research: Space Physics*, *118*(10), 6751–6765. https://doi.org/10.1002/jgra.50601

Ratynski, M., Khaykin, S., Hauchecorne, A., Wing, R., Cammas, J.-P., Hello, Y., & Keckhut, P. (2022). Validation of Aeolus wind profiles using ground-based lidar and radiosonde observations at la Réunion Island and the observatoire de haute Provence. *EGUsphere*, 1–33. https://doi.org/10.5194/egusphere-2022-822

Salby, M., Sassi, F., Callaghan, P., Wu, D., Keckhut, P., & Hauchecorne, A. (2002). Mesospheric inversions and their relationship to planetary wave structure. *Journal of Geophysical Research*, *107*(D4), ACL4-1–ACL4-13. https://doi.org/10.1029/2001JD000756

Sassi, F., Garcia, R. R., Boville, B. A., & Liu, H. (2002). On temperature inversions and the mesospheric surf zone. *Journal of Geophysical Research*, *107*(D19), ACL8-1–ACL8-11. https://doi.org/10.1029/2001JD001525

Schmidlin, F. (1976). Temperature inversions near 75 km. *Geophysical Research Letters*, *3*(3), 173–176. https://doi.org/10.1029/gl003i003p00173

Souprayen, C., Garnier, A., Hertzog, A., Hauchecorne, A., & Porteneuve, J. (1999). Rayleigh–Mie Doppler wind lidar for atmospheric measurements. I. instrumental setup, validation, and first climatological results. *Applied Optics*, *38*(12), 2410–2421. https://doi.org/10.1364/AO.38.002410

Straume, A. G., Rennie, M., Isaksen, L., de Kloe, J., Marseille, G.-J., Stoffelen, A., et al. (2020). Esa´s space-based Doppler wind lidar mission Aeolus—First wind and aerosol product assessment results. *EPJ Web of Conferences*, *237*, 01007. https://doi.org/10.1051/epjconf/202023701007

Stroud, W. G., Nordberg, W., Bandeen, W. R., Bartman, F. L., & Titus, P. (1960). Rocket-grenade measurements of temperatures and winds in the mesosphere over Churchill, Canada. *Journal of Geophysical Research*, *65*(8), 2307–2323. https://doi.org/10.1029/JZ065i008p02307

Theon, J. S., Nordberg, W., Katchen, L. B., & Horvath, J. J. (1967). Some observations on the thermal behavior of the mesosphere. *Journal of the Atmospheric Sciences*, *24*(4), 428–438. https://doi.org/10.1175/1520-0469(1967)024⟨0428:SOOTTB⟩2.0.CO;2

Wing, R., Hauchecorne, A., Keckhut, P., Godin-Beekmann, S., Khaykin, S., McCullough, E. M., et al. (2018). Lidar temperature series in the middle atmosphere as a reference data set–part 1: Improved retrievals and a 20-year cross-validation of two co-located French lidars. *Atmospheric Measurement Techniques*, *11*(10), 5531–5547. https://doi.org/10.5194/amt-11-5531-2018

Wing, R., Martic, M., Hauchecorne, A., Porteneuve, J., Keckhut, P., Courcoux, Y., et al. (2020). Atmospheric density and temperature vertical profile retrieval for flight-tests with a Rayleigh lidar on-board the French advanced test range ship monge. *Atmosphere*, *11*(1), 75. https://doi.org/10.3390/atmos11010075

## 4.3 . Conclusions

Il est clair que les inversions de température mésosphériques sont caractérisées par une forte décélération du vent dans la même tranche d'altitude où l'augmentation de température se produit. Ces nouvelles observations confortent l'idée selon laquelle le mécanisme de formation de ce phénomène repose bien sur le déferlement des ondes de gravité comme proposé par Hauchecorne et al. (1987) et testé par Hauchecorne and Maillard (1990).

De façon surprenante, les réanalyses ERA5 ont réussi parfois à simuler assez fidèlement la chute de vent mais pas l'augmentation de température associée à l'occurrence d'inversions mésosphériques. Néanmoins, la plupart des cas montrent que les réanalyses ERA5 sont incapables de reproduire les inversions mésosphériques à la fois dans les profils de température et de vent. Les principales causes de cette mauvaise représentation des fluctuations au sein de la mésosphère ont déjà été discutées précédemment. Tandis que, comme attendu, les profils ERA5 montrent une bonne représentation du vent et de la température au sein de la haute stratosphère confirmant à nouveau leur qualité à ces altitudes. Il n'est actuellement pas possible de connecter à l'aide des réanalyses la dynamique observée dans la stratosphère avec celle de la mésosphère. Notamment afin de comprendre l'éventuelle connexion des inversions au cours de l'hiver avec l'apparition des échauffements stratosphériques soudains.

C'est pourquoi les données ERA5 au sein de la mésosphère ne seront pas utilisées dans la suite de la thèse focalisant sur les échauffements stratosphériques soudains. Ainsi, uniquement les réanalyses ERA5 s'étendant jusqu'à la stratopause ($\sim$1hPa) seront employées dans les prochaines investigations visant à étudier l'impact des échauffements sur le déroulé des hivers et le couplage stratosphère-troposphère.

# 5 - Concept de mémoire stratosphérique au cours de l'hiver

## 5.1 . Introduction

Dans ce chapitre, les réanalyses ERA5 sont utilisées comme base de données pour l'étude de l'évolution de la stratosphère d'hiver de l'hémisphère nord influencée par les échauffements stratosphériques soudains au cours des précédentes décennies. Ainsi, pour bénéficier d'un échantillon représentatif, les 71 années allant de 1950 à 2020 sont extraites pour former 70 hivers.

Tout d'abord, deux nouvelles catégories caractérisant mieux la nature de l'apparition des échauffements stratosphériques finaux sont introduites : dynamique ou radiatif. Ensuite, la corrélation trouvée entre les mois des hivers à l'aide du vent et de la température polaire permet d'introduire le concept de mémoire stratosphérique. Enfin, ce travail de mémoire stratosphérique est poursuivie en établissant une nouvelle classification des évolutions des hivers au sein de la stratosphère soulignant l'importance du timing des échauffements stratosphériques soudains dans le déroulement des hivers.

## 5.2 . Échauffements stratosphériques finaux : Dynamiques ou Radiatifs

Au sein de la stratosphère, la direction des vents s'inverse entre l'hiver et l'été. En hiver, en l'absence de rayonnement solaire, la région polaire se refroidit, engendrant la formation d'une vaste dépression connue sous le nom de vortex polaire. Autour de ce vortex, les vents soufflent de l'ouest vers l'est. Avec le retour du soleil réchauffant l'atmosphère polaire au printemps, le vortex polaire s'estompe pour céder la place à un anticyclone, autour duquel les vents s'inversent, soufflant désormais de l'est vers l'ouest. Cette tran-

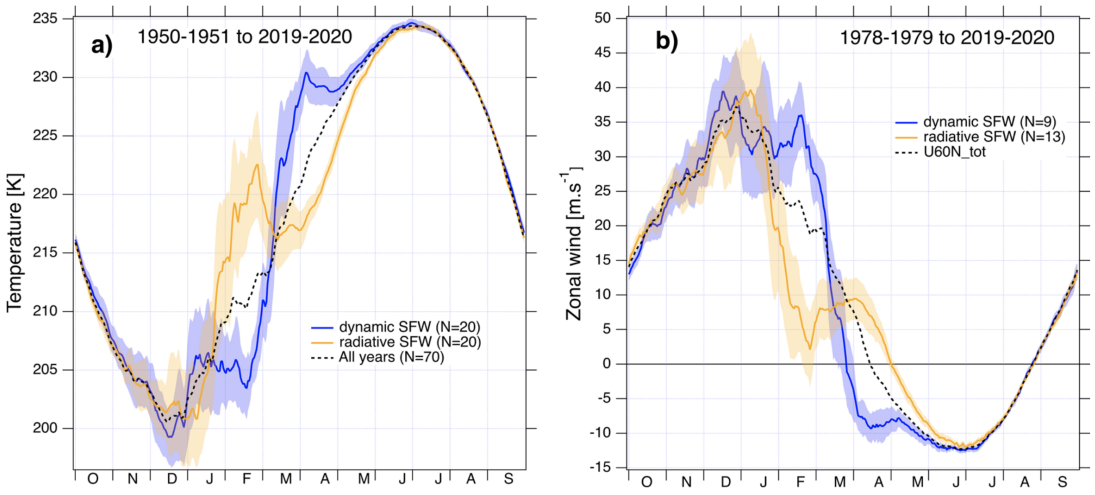


Figure 5.1 – Évolution (a) de la température polaire et (b) du vent zonal à 60°N pour le composite dynamique en bleu foncé et le composite radiatif en orange. La zone ombrée représente le niveau de confiance de 95% (2 écarts types) sur les valeurs moyennes. La ligne noire pointillée représente l'évolution moyenne sur les 70 ans de données. (Source : Hauchecorne et al. (2022))

sition entre les régimes de vents d'ouest en hiver et de vents d'est en été est désignée sous le terme d'« échauffement stratosphérique final (ESF) ». Habituellement catégorisé en fonction de leurs dates d'apparitions, soit tôt ou tardif (Waugh and Rong, 2002), une nouvelle classification basée sur l'anomalie de température a été introduite récemment par Hauchecorne et al. (2022).

Les auteurs démontrent que l'inversion de la circulation zonale au début du printemps peut se dérouler en douceur et progressivement, principalement influencée par le réchauffement radiatif dû au soleil dans la région polaire. À l'inverse, cette inversion peut être précoce et brutale, accompagnée d'une rapide augmentation de la température polaire et d'un décroissement rapide des vents zonaux, cela sous l'effet de l'activité des ondes planétaires, similaire à un échauffement stratosphérique soudain au milieu de l'hiver.

Les auteurs ont établi deux groupes composites, regroupant respectivement 20 années marquant une transition en douceur (composite ESF radiatif) et 20 années marquant une transition brusque (composite ESF dynamique). La figure 5.1 illustre une différence

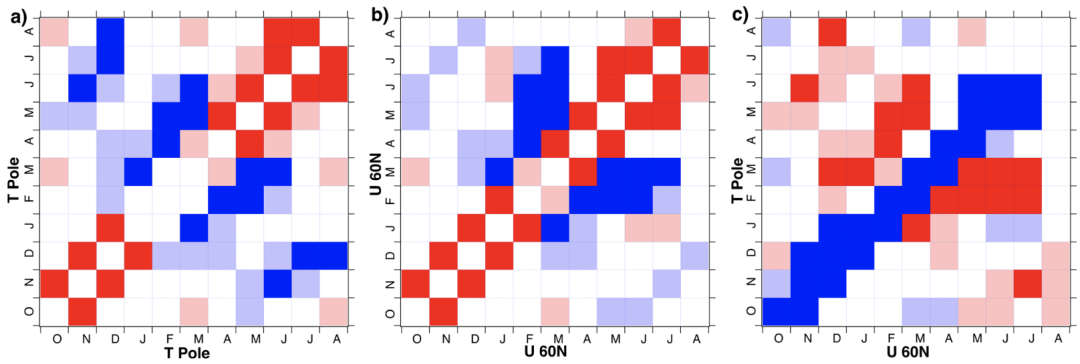


Figure 5.2 – Niveau de confiance de la corrélation entre les valeurs moyennes mensuelles de 2 mois de l'année pour les corrélations : (gauche) température-température, (milieu) vent-vent et (droite) température-vent. +1 à +2 $\sigma$ rouge clair, > +2 $\sigma$ rouge foncé, -2 à -1 $\sigma$ bleu clair, < -2 $\sigma$ bleu foncé. Pour la corrélation entre deux mois d'une même variable (panneaux de gauche et du milieu), la diagonale est laissée en blanc et le chiffre est symétrique par rapport à la diagonale. (Source : Hauchecorne et al. (2022))

hautement significative entre ces deux composites quant à l'évolution de la température polaire et des vents zonaux à 60°N au cours de l'année. Plus particulièrement, ces résultats mettent en évidence que les hivers caractérisés par un ESF dynamique ont tendance à ne pas présenter d'événements de réchauffement stratosphérique soudain au milieu de l'hiver, tandis que ceux avec un ESF radiatif ont davantage de probabilités d'enregistrer de tels événements. Cette observation suggère l'existence d'une sorte de mémoire dans la stratosphère.

## 5.3 . Corrélation intra-hivernale

Pour tester cette hypothèse de mémoire de la stratosphère, la corrélation temporelle entre les anomalies moyennes mensuelles du vent zonal à 60°N et la température polaire est présentée sur la Figure 5.2. Il résulte que l'état du vortex polaire sur un mois donné, que se soit la température ou le vent zonal, est anticorrélé avec son état 2 à 3 mois plus tôt. Le début de l'hiver est anticorrélé avec le milieu de l'hiver et le milieu de l'hiver avec la fin de l'hiver et le début du printemps.

L'explication suggérée implique une réduction de l'activité des ondes planétaires à la

suite d'un ESS permettant au vent zonal de reprendre de la force et conduisant à un refroidissement dans la région polaire. Le vent zonal et la température polaire présentent également tous deux une corrélation pendant les mois d'été (juin à août), indiquant une mémoire persistante de la stratosphère polaire d'été après l'ESF. Comme attendu, la température et le vent zonal sont anticorrélés à plus de 95% sur le même mois. La stratosphère d'été garde la mémoire de son état en avril-mai après l'ESF jusqu'à fin juin.

## 5.4 . Nouvelle classification des évolutions hivernales de la stratosphère

Compte tenu de la connexion intra-hivernale au sein des hivers soulignée précédemment, une nouvelle approche est élaborée afin de poursuivre ce travail de mémoire stratosphérique en étudiant l'impact des timings des échauffements stratosphériques soudains sur le déroulé des hivers. Cette nouvelle méthode consiste à classifier les typologies des hivers en se basant sur les principaux modes de variabilité des anomalies de vent zonal des 70 hivers étudiés dans Hauchecorne et al. (2022). Dans cette section, l'étude rapportant cette nouvelle classification est présentée. Celle-ci vise notamment à montrer que la stratosphère d'hiver de l'hémisphère nord suit des scénarios typiques se répétant au fil des années avec des activités dynamiques singulières. De plus, cette nouvelle approche tenant compte de tous les échauffements dits "importants", comprenant les majeurs et mineurs, permet de focaliser davantage sur le timing du phénomène que sur son intensité. Ainsi, contrairement aux précédentes classifications focalisant surtout sur des échauffements majeurs, cette méthode permet de se concentrer sur l'étude de l'évolution des hivers au fil des années.

## 5.5 . Article

L'article ci-dessous a été publié dans le journal « Journal of geophysical research » dans la catégorie « Atmospheres » le 7 juillet 2022.

JGR Atmospheres

RESEARCH ARTICLE
10.1029/2022JD036662

# Classification of Stratosphere Winter Evolutions Into Four Different Scenarios in the Northern Hemisphere

**A. Mariaccia[1], P. Keckhut[1], and A. Hauchecorne[1]**

[1]Laboratoire Atmosphères, Milieux, Observations Spatiales, UMR 8190, Institut Pierre-Simon Laplace, Université Versailles-Saint Quentin, Université Paris-Saclay, Guyancourt, France

**Key Points:**

- The winter stratosphere in the northern hemisphere tends to follow four typical scenarios
- The different scenarios show how the mid-winter is connected with the winter end
- The modes contain the information of important sudden stratospheric warmings timings

**Correspondence to:**

A. Mariaccia,
alexis.mariaccia@latmos.ipsl.fr

**Citation:**

Mariaccia, A., Keckhut, P., & Hauchecorne, A. (2022). Classification of stratosphere winter evolutions into four different scenarios in the northern hemisphere. *Journal of Geophysical Research: Atmospheres*, *127*, e2022JD036662. https://doi.org/10.1029/2022JD036662

Received 19 FEB 2022
Accepted 30 JUN 2022

**Author Contributions:**

**Conceptualization:** A. Mariaccia
**Investigation:** A. Mariaccia, P. Keckhut
**Methodology:** A. Mariaccia, P. Keckhut, A. Hauchecorne
**Project Administration:** P. Keckhut, A. Hauchecorne
**Software:** A. Mariaccia
**Supervision:** P. Keckhut, A. Hauchecorne
**Validation:** P. Keckhut, A. Hauchecorne
**Visualization:** A. Mariaccia
**Writing – original draft:** A. Mariaccia



**Abstract** Among the 70 northern hemisphere winters from 1950 to 2020, 61 have been classified into four independent scenarios with a new technique based on analyzing empirical orthogonal functions of stratospheric zonal wind fluctuation patterns at the edge of the polar vortex. These four scenarios represent a typical zonal wind evolution in the stratosphere modulated by timings of stratospheric warmings occurring in winter. First, there are three scenarios (January mode, February mode, and Double mode) for which the polar vortex generally breaks down with a reversing of zonal winds in midwinter, known as sudden stratospheric warmings (SSWs) events, at different times. The last one is a non-perturbed scenario with two under-modes for which only the timing of the polar vortex transition to its summer state differs, either radiative or dynamical. Consistently with these wind patterns, the wave-1 and wave-2 anomaly evolutions confirm that these scenarios are associated with independent dynamics behaviors and significant differences between wave-1 and wave-2 activities. We found that the wave-1 anomaly evolutions drop systematically for each scenario when the stratospheric winds weaken, while this correlation with the wave-2 anomaly evolutions is not observed for all scenarios. These different dynamical behaviors confirm that the scenarios are either mainly dynamically driven by wave-1 or both driven by wave-1 and wave-2. Until early December, the modes possess similar increasing evolutions of the wave-1 activity due to the seasonal cycle. After, the scenarios separate, suggesting that the mechanisms responsible for the winter unfolding act in the previous months.

## 1. Introduction

Each year in both hemispheres, when the summer is finishing, a cold polar vortex with westerly winds forms in the stratosphere as the incoming solar radiation decreases. During its radiative life cycle, stratospheric warmings affect the position and the structure of the polar vortex leading to a vortex breakdown and the reversing of the westerly winds for the most extreme cases (Baldwin et al., 2021), the so-called sudden stratospheric warmings (SSWs) events observed for the first time by Scherhag (1952). Then, with the arrival of the following spring, this vortex weakens and decays when the winds return to their easterly summer state. Since their discovery, much evidence has shown that SSWs impact afterward the tropospheric circulation confirming the existence of the two-way stratospheric-tropospheric dynamical coupling (Baldwin & Dunkerton, 2001; Labitzke, 1981; Thompson & Wallace, 2001).

Indeed, the birth mechanism of SSWs, according to the models developed by Matsuno (1971) and Andrews et al. (1987), implies an interaction between the mean flow and upward propagating planetary waves from the troposphere to the stratosphere. However, as sources of planetary waves are mainly the orography or the high-temperature gradient between ocean and land, nearly all observed SSWs occurred in the Northern Hemisphere (NH). In contrast, the polar vortex in the Southern Hemisphere (SH) generally remains very strong in wintertime due to the small amplitude of planetary waves. Although one exception with a major SSW can be raised during the SH spring of 2002 (Charlton et al., 2005; Krüger et al., 2005). While in the NH, major SSWs, on average, occur about six times per decade (Charlton & Polvani, 2007) with a substantial variability over decades (Domeisen, 2019).

Since SSWs are observed and studied, the scientific community has been searching to classify them according to several physical criteria illustrating their impact on the evolution of the polar vortex. Over the years, only the following classification of SSWs into four categories referring to their magnitude and timing has remained widely used: Major, Minor, Final, and Canadian warmings. However, still, nowadays, no clear definition for these four SSW types exists, resulting in different classifications among the studies (Butler et al., 2017).

Initially based on the rising of the temperature within the vortex by the World Meteorological Organization (WMO) for the International Years of the Quiet Sun in 1964, the definitions of major SSWs given in the literature have evolved and are now almost exclusively defined according to the reversal from westerly to easterly of the stratospheric zonal winds at the edge of the vortex (Butler et al., 2015). These current definitions include the distinction between major SSWs and final stratospheric warmings (FSWs) corresponding to the last inversion of the climatological winter westerlies to summer easterlies in the stratosphere. Similarly, the definition of minor SSWs is now based on a strong stratospheric wind deceleration without reversing the polar winds (e.g., Maury et al., 2016). Finally, there is still no consensus on the classification of Canadian warmings (warming occurring in early winter with an eastward shift of the Aleutian high), that is, whether or not they must be differentiated from major SSWs when winds reverse (Butler et al., 2015).

For many years, the attention has been focused primarily on major SSWs as they substantially impact the polar vortex and the weather in the troposphere. Indeed, numerous tentative classifications of major SSWs have been explored according to different criteria. For instance, Charlton and Polvani (2007) (hereafter CP07) introduced a classification of major SSWs based on the vortex geometry, that is, the vortex is either displaced off of the pole or split into two distinct vortices. It has been found that split events occur mainly in January and February, and displaced events occur mainly in December and March. Mitchell et al. (2013), who improved the classification technique developed by CP07, concluded that displacements and splitting vortex events later influence the tropospheric weather differently.

Other studies have attempted to classify major SSWs according to their low impact, and the tropospheric response (Charlton-Perez et al., 2018; Domeisen, 2019; Kodera et al., 2016). However, the occurrence of major SSWs limits these classifications since they overlooked the minor SSWs, occurring more frequently during winters and weakening the vortex significantly but without reversing the winds (Maury et al., 2016), preventing, in fine, a complete understanding of the mean stratospheric changes. The advantage of this study is that the classification is based on the winter evolutions and not on the SSW type in mid-winter, and therefore no winters are discarded.

Regarding FSWs, on the other hand, a criterion based on their timing of occurrence has generally been used to classify them into "early" or "late" events (Waugh & Rong, 2002). In the NH, the generation of early FSWs is similar to the one for SSWs events, which tend to be also wave-driven (Vargin et al., 2020). In contrast, late FSW events are more radiatively-driven as the polar vortex weakens with the increase of incoming solar radiation. Recently, Butler and Domeisen (2021), who undertook a new classification of FSWs according to the dominant wave geometry prior to reversing the winter westerlies in both hemispheres, have found that wave-1 events tend to shift the polar vortex toward Eurasia in the NH. In contrast, wave-2 events are the precursor of an elongated or split vortex over Canada and eastern Asia. Hauchecorne et al. (2022), in addition to their new classification of FSWs from 1950 to 2020 according to their nature and their occurrence, either "dynamical" or "radiative" events, investigated the seasonal memory of the stratosphere. They found that the polar vortex on a given month is anti-correlated with its state 2–3 months earlier and that the stratosphere keeps a memory of its state of April–May until at least July.

This work aims to improve our overall understanding of the handling of winters by investigating principal winter typologies and inferring how the early winter is related to the mid-winter and then how the mid-winter influences the early spring. The novelty here is that we pursue the investigation of the stratosphere memory initiated by Hauchecorne et al. (2022) over the same period with a new technique of classification of winters based on the principal component analysis of the evolution of the polar vortex. To our knowledge, it is the first time that this type of classification has been undertaken and, in addition, by using the new ERA-5 reanalyzes of wind at 10 hPa-60°N produced by the European Center for Medium-Range Weather Forecasts (ECMWF). The other solid motivation for this new classification is its usefulness for improving the models' weather prediction in the stratosphere.

This paper is organized as follows: A detailed description of the data used as well as an illustration of the wave contributions (wave-1 and wave-2) to the vortex geometry during two SSWs are given in the next section. Then, the distribution of major and important SSWs (ISSWs) and FSWs is shown and discussed in Section 3. The method and the result of the classification are presented in Section 4. In Section 5, a more detailed characterization of each scenario is done. The mean evolutions of the wave amplitudes for each scenario are presented and discussed in Section 6. Finally, a discussion and a conclusion are given in Section 7.

## 2. Data Description

Wind and geopotential data used here are extracted at 10 hPa-60°N for the 1950–2020 period from the final product of reanalyzes ERA-5 built by the ECMWF. The ERA-5 reanalysis package is constructed thanks to worldwide observations provided by multiple sources (satellites, radiosondes, aircraft, rocketsondes, and other surface observations), which are assimilated with a 4D Var system (Hersbach et al., 2020). This last generation of reanalyzes benefits the updated ECMWF Integrated Forecast System IFS 41r2, improved bias correction techniques, and a better model parametrization of convection and microphysics than in the last ERA-Interim package (Dee et al., 2011). The ERA-5 output is produced hourly on a global horizontal resolution of 31 km and 137 vertical levels extending from the surface to the level pressure of 0.01 hPa (approximately 80 km). The ERA-5 package covers a period from 1950 to the present, providing the most extended reanalyzes series. Furthermore, recent studies evaluating ERA-5 reanalyzes in the middle atmosphere have confirmed their accuracy in the stratosphere in wintertime. For instance, Marlton et al. (2021) have found a good thermal representation up to 3 hPa and, in addition, Mariaccia et al. (2022) have shown that the model reproduced the variability accurately in the upper stratosphere during winter.

Thus, for this study, we dispose of wind and geopotential reanalyzes at 10 hPa-60°N to form the 70 winters between 1950 and 2020. For the years between 2000 and 2006, reanalyzes are from the re-run ERA-5.1 correcting the cold bias of the temperature in the lower stratosphere observed in ERA-5 for this period (Simmons et al., 2020). The zonal mean zonal winds and the amplitudes of waves 1 and 2 are daily computed from 1 November to 1 June. Figure 1 shows zonal wind evolutions during two winters. Winter 1960/1961 illustrates an unperturbed winter case, that is, a strong polar vortex, finishing with an abrupt transition to easterly winds in March typical of a dynamical end. Butler and Domeisen (2021) classified the FSW of this winter as an "early" event of wave-1 type. While, winter 2017/2018 illustrates a perturbed winter case with a major SSW of wave-2 type (Rao et al., 2018) occurring in February and finishing mid-April with a slow transition to the summer mode characteristic of a radiative end.

The wave components are calculated from the Fourier Analysis of geopotential as described in Pawson and Kubitz (1996):

$$Z = \overline{Z} + \sum_{k=1}^{2} Z_k \cos k\left(\lambda - \delta_k^Z\right), \quad (1)$$

where the overline represents the zonal mean, and each zonal wavenumber $k$ is defined by its amplitude $Z_k$ and phase $\delta_k$. Here the phase corresponds to the longitude (east) of the maximum and lies in the range (0, 360/k). Figure 2 illustrates the decomposition of the stratospheric geopotential field for two dates after a major SSW. As expected, the wave-1 dominates for the vortex displacement event in January 2012 while the wave-2 dominates for the vortex splitting event in February 2018.

## 3. Distribution of SSWs From 1950 to 2020

### 3.1. Identifying the Different Type of SSWs

#### 3.1.1. Identification of Important SSWs

Most studies have focused on SSWs when wind reverses from westerly to easterly, the so-called major SSWs, as they strongly impact the vortex state. Nevertheless, their occurrence is about one every 2 years which limits the statistical study of their timing for a data set containing only 70 winters. Hence, to observe a temporal trend in the occurring of SSWs, it is necessary to add other SSWs that weak significantly the vortex without reversing winds, the so-called minor SSWs. As minor SSWs have stimulated a few interests, very few definitions based on objective criteria exist to classify these events. According to the WMO, a minor SSW is characterized by a substantial increase of temperature, at least 25° for 1 week or less at any stratospheric level in the winter hemisphere. However, this temperature criterion is ambiguous as another WMO report stated that major SSW has a temperature increase of at least 30° for the same period (Butler et al., 2015). Here, to keep a continuity with the major SSW definition, we used a new wind criterion based on the study of Maury et al. (2016) to select, in addition to major SSWs, the warmings which affect the vortex significantly without reversing the wind. For the

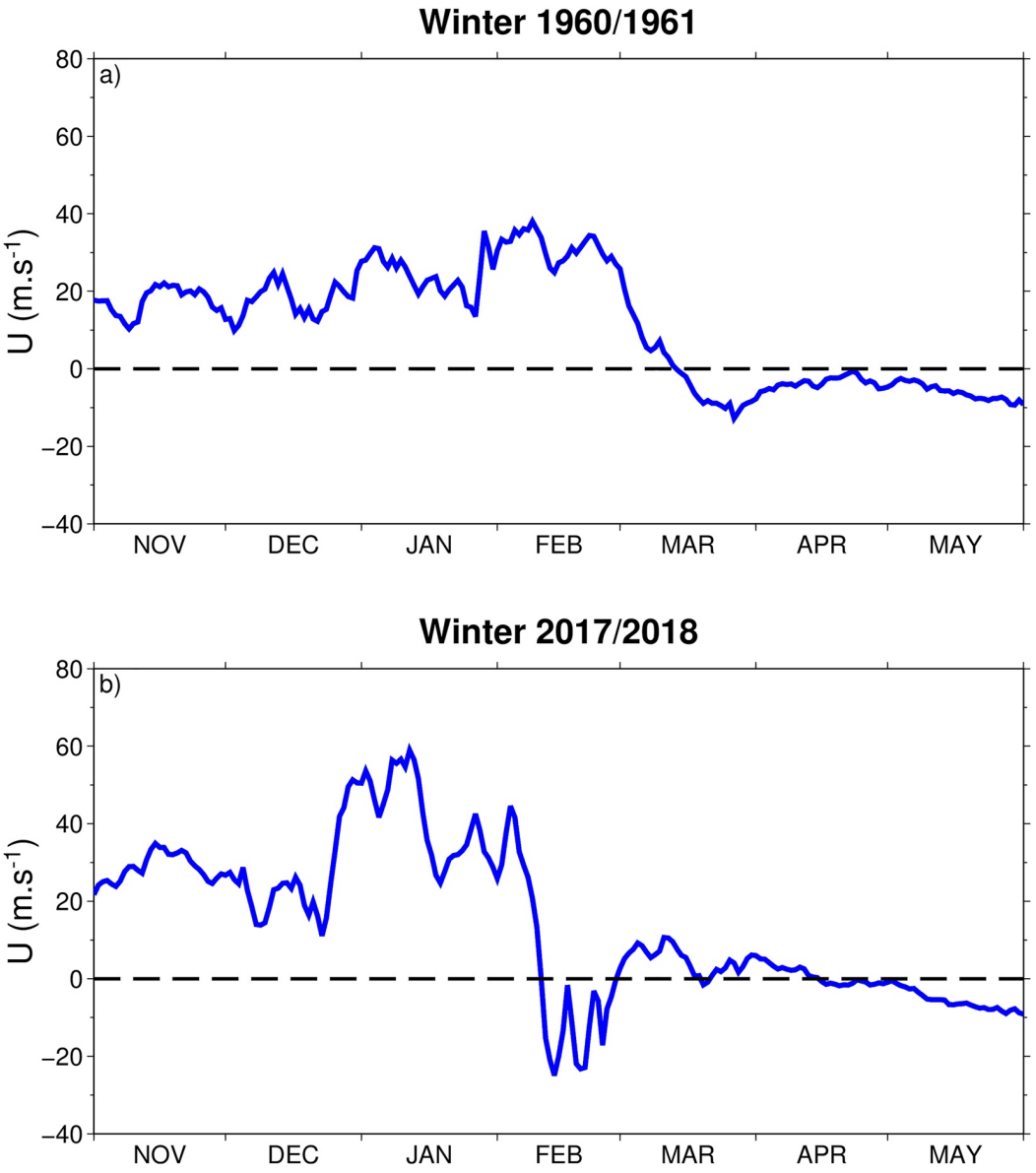


**Figure 1.** Evolution of zonal mean zonal wind (solid blue line) at 10 hPa-60°N for two winters illustrating a strong polar vortex finishing with an early and dynamical final stratospheric warming (FSW) of wave-1 type (a) and a polar vortex perturbed by a major sudden stratospheric warming of wave-2 type occurring in February and finishing with a late and radiative FSW (b).

remainder of this study, all these events will be referred to as the "ISSWs." The central date of each important SSW occurring during the 70 winters is determined as follows:

1. We search the first date $d$ from which the zonal mean of zonal wind at 60°N-10 hPa falls below 10 $ms^{-1}$, threshold sufficient to detect events reducing significantly the planetary wave propagation and from which the vortex can be considered as weak (Maury et al., 2016).
2. From $d$, if $u$ is not positive for at least 10 consecutive days before 30 April, the event is considered as an FSW event, and we stop to search other Important SSW. If not, the date $d$ is saved as a central date of Important SSW.
3. Then, a 20-day mask is applied to avoid accounting twice the same event. At $d + 20$, if $u$ is superior to 10 $ms^{-1}$ the algorithm continues to search other event. However, in the case where $u$ is still inferior to 10 $ms^{-1}$, we

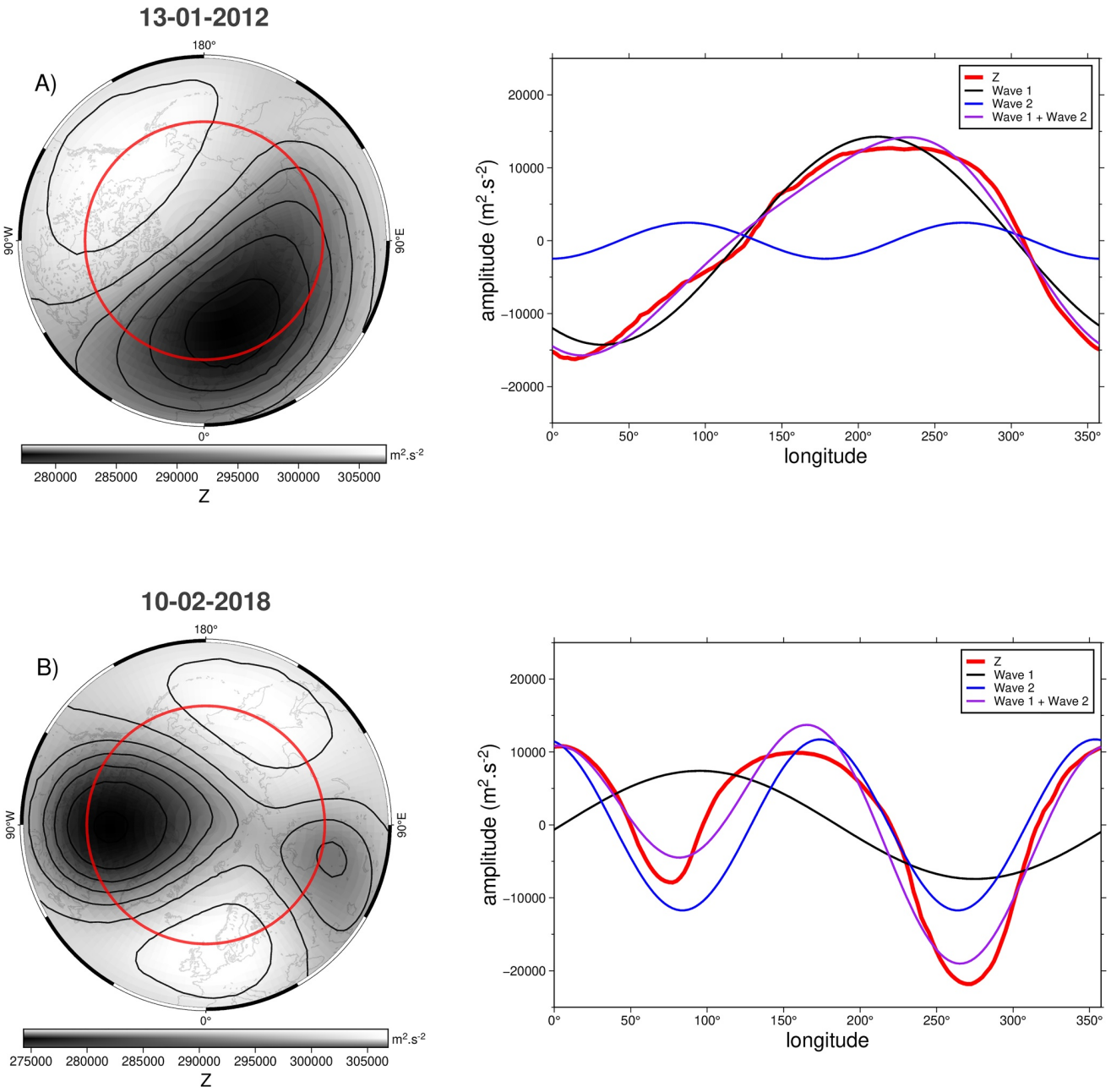


**Figure 2.** Geopotential contour at 10 hPa in the Northern Hemisphere for two dates showing two typical vortex evolutions (in black) after a sudden stratospheric warming: a displacement off of the pole (a) and a splitting into two vortices (b). The red circle is plotted on the 60°N and the geopotential evolution at this latitude is displayed on the right (red line). Contributions from wave-1 (black line) and wave-2 (blue line) to this geopotential are both displayed separately and together (purple line).

search the next date from which $u$ is superior to 10 $ms^{-1}$ and then the algorithm repeats the steps 1–3. If there is no date, the algorithm stops.

Here, we did not impose a warming duration, as performed in Maury et al. (2016) to separate minor from major SSWs, since only the ISSWs identification was needed for classifying afterward winters. With this algorithm, 105 important SSW events among the 70 winters have been detected, giving a ratio of 1.5 important SSW events per winter.

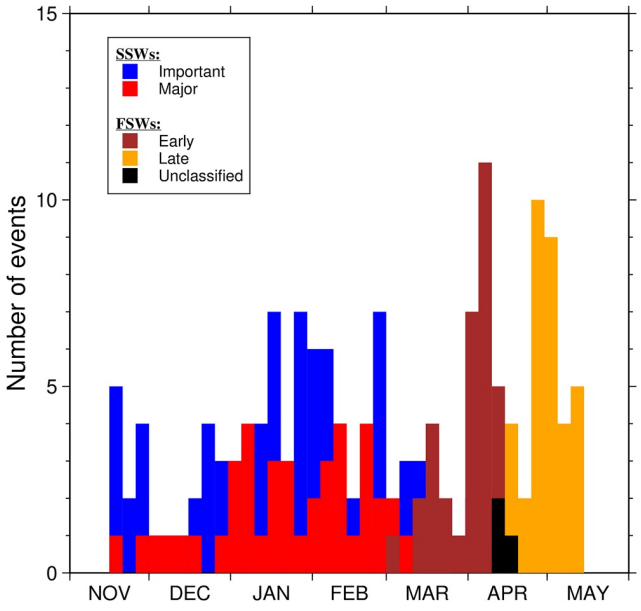


**Figure 3.** Distribution of Important sudden stratospheric warmings (SSWs) (in blue), Major SSWs (in red) and final stratospheric warmings, in either "early" (in brown) or "late" (in orange) events and unclassified (in black), into intervals of 5 days from 1 November to 1 June from 1950 to 2020.

#### 3.1.2. Identification of Major SSWs

The method used here to identify major SSWs is the same that proposed by Bancalá et al. (2012) which is based, as initiated by Charlton and Polvani (2007), on the zonal-mean zonal wind. The central date of the event is the day when the wind at 10 hPa-60°N reverses from westerly to easterly. Then, the algorithm searches the next day from which the wind becomes again westerly and then applies a 20-day mask. This interval, corresponding to the time necessary for the restoring of the polar vortex (Newman & Rosenfield, 1997), avoids to count several times the same event as the winds may oscillate around the 0 $ms^{-1}$ value. In the case where the day after this interval of 20 days has easterly wind, then the algorithm searches the next day having westerly wind superior to 5 $ms^{-1}$ to start again the searching for other major SSWs. Additionally, the algorithm searches the number of consecutive days of westerlies and the wind intensity following each event identified in order to detect if it corresponds to a FSW. Thus, an event is considered as a FSW whether the wind does not return to westerly for at least 10 consecutive days and that, among these days, the wind does not reach once 5 $ms^{-1}$. With this algorithm, 45 major SSWs have been detected among the 70 winters, which gives a ratio of 0.64 major SSW per year.

#### 3.1.3. Identification of FSWs

However, the previous method developed by Bancalá et al. (2012) is not retained for FSWs identification as it subsists a winter for which none central date of FSW was computed. Thus, in order to have an FSW central date for each winter, the identification of FSWs is carried out with the same method employed by Butler and Domeisen (2021). This method is also based on the westerly winds reversal at 10 hPa-60°N, consistent with the definition of major SSWs used above. The central dates of FSWs are the first date before 30 June when $u$ fall below 0 $ms^{-1}$ and do not return to westerly for more than 10 consecutive days. As a result, the median date of the 70 FSWs identified is 15 April. As in Butler and Domeisen (2021), we classified afterward as "early" event FSWs occurring 2 days prior to the median date and as "late" events those occurring 2 days after the median date. These two FSW types are illustrated in Figure 1. With this algorithm, 33 winters have been classified as "early" events, 32 winters as "late" events, and five winters remain unclassified. Recently, Hauchecorne et al. (2022), who used a criterion based on temperature anomaly, have shown that FSWs are either "dynamical" and early (with a positive temperature anomaly superior to +10 K as for mid-winter SSWs) or "radiative" and late (with temperature anomaly inferior to 0 K). Their method found 20 winters with a radiative end and 20 winters with a dynamical end among the 70 winters from 1950 to 2020.

The comparison between these two classifications reveals, first, a perfect agreement for the 20 winters with a dynamical end which are all classified as "early" here, and second, that among the 20 winters with a radiative end, 18 winters are considered as "late" and two are unclassified. These two winters with unclassified FSWs (1988/1989 and 2017/2018) have both a late transition occurring mid-April (see Figure 1b) characteristic of winters having a radiative end. Moreover, Butler and Domeisen (2021), who studied FSWs from 1958 to 2019 in the NH, classified these both winters with a "late" FSW. Consequently, and to keep a consistency with the classification carried out by Hauchecorne et al. (2022), these two winters are considered as having a late and radiative end for the remaining of this study.

The occurrence distribution of major and important SSW events, as well as FSW events identified with these algorithms, is shown in Figure 3.

### 3.2. Discussion on SSWs and FSWs Distribution

As expected, major SSWs occur mainly during the mid-winter, in January and February (Figure 3), when the planetary wave activity is very strong (Fusco & Salby, 1999), causing the weakening and then the breakdown of the vortex. The major SSW distribution shows two peaks in January and February with nearly the same number of events. Similar preferred timings for major SSWs have been observed in other studies, such as in Limpasuvan

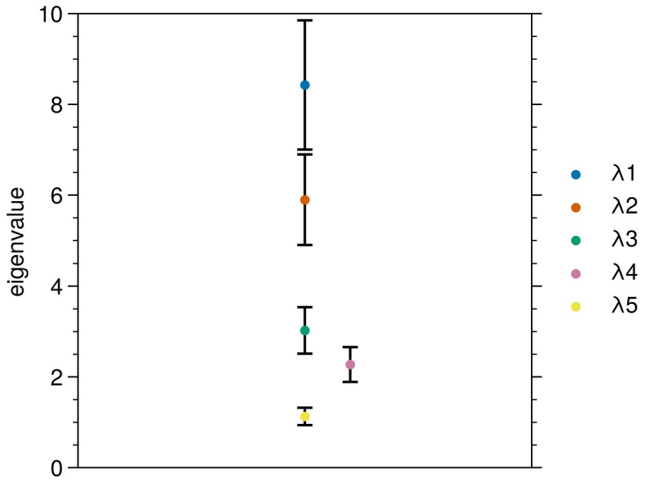


**Figure 4.** Schematic diagram of the first five eigenvalues $\lambda_\alpha$ associated with the first five empirical orthogonal function modes. The standard error for each eigenvalue, represented with the error bars, are computed with the North's "rule of thumb" for $N = 70$.

et al. (2004) who used 44 years of reanalyzes (1958–2001), suggesting that central dates of SSWs are not distributed randomly during winter. However, to our knowledge, none of them have been tempted to study this distribution as it is done here, that is, by searching how ISSWs' timings, illustrated by these peaks, influence afterward the winter evolutions. Thus, the major SSW distributions shown here constitute this study's first motivation to relate the preferential periods for which SSWs occur to a particular winter typology. However, despite these first trends observed, the number of major SSWs detected is insufficient to infer all the temporal trends in the occurrence of SSWs impacting the polar vortex significantly.

In order to complete and confirm the SSWs' timings, the distributions of ISSWs and FSWs are also studied. Indeed, the ISSWs detected with the method described above enhance the first peaks found previously with the major SSW distribution and make others appear, especially in November and March. Here, the early warmings in November represent mostly minor SSWs containing likely Canadian Warmings occurring at this period and characterized by an eastward shift of the Aleutian high (Labitzke, 1981).

Beyond mid-December, a continuum of ISSWs is observed during mid-winter, with at least three ISSWs occurring each week. A prominent peak of ISSWs with seven events overlaps the two peaks of major SSWs discussed above in January and February. These two first significant peaks confirm the previously observed trends with major SSWs during mid-winter, that is, some winters have been perturbed by either major or minor warming in mid-January or early February. Furthermore, a third thin peak with seven ISSWs is found at the end of February and March. Finally, some important warmings occur in December and March but with peaks less marked than the three others.

Unsurprisingly, the distribution of FSWs is separated into two major peaks, one before mid-April and the other in early May, pointing out the early and late FSWs, respectively (Butler & Domeisen, 2021). Hence, the median date of all FSWs, which is 15 April, appears to be a good criterion for classifying winters according to their ends. This result is of great interest as it confirms that SSWs and FSWs tend to occur at specific periods and not randomly. Thus, the following section aims to classify all of these winters in order to observe whether major winter evolution scenarios related to these privileged SSW and FSW timings exist.

## 4. Classification of Winters

This section describes the method employed here to determine the main scenarios of winter evolutions from 1 November to 1 June among the 70 winters since 1950. First, an empirical orthogonal function (EOF) is applied to the zonal mean zonal wind anomaly data set, composed of 70 winters of 213 days, in order to compute the main modes among winters. Here, the zonal wind anomalies are calculated by removing the daily mean over 70 years and dividing afterward by the standard deviation. As the EOF is very sensitive to winters with strong variability, only the first three modes were computed to avoid modes that do not represent observed scenarios (Figure 5). Additionally, in order to confirm that the first three modes are independent from each other, we computed the sampling errors for the eigenvalues associated with the five first EOFs with the following North's "rule of thumb" (North et al., 1982):

$$\delta\lambda_\alpha = \lambda_\alpha (2/N)^{1/2}, \tag{2}$$

where $\lambda_\alpha$ is the eigenvalue and $N$ is the number of realizations of a particular sample (70 here). The obtained results are displayed in Figure 4 and reveal that only the sampling errors associated with the third and fourth eigenvalues overlap by about 20%–30%. Consequently, the first three modes are not a linear mixture of the same eigenvector and can therefore be considered independent. Therefore, these modes illustrate the most important and common features of the winter polar vortex evolution.

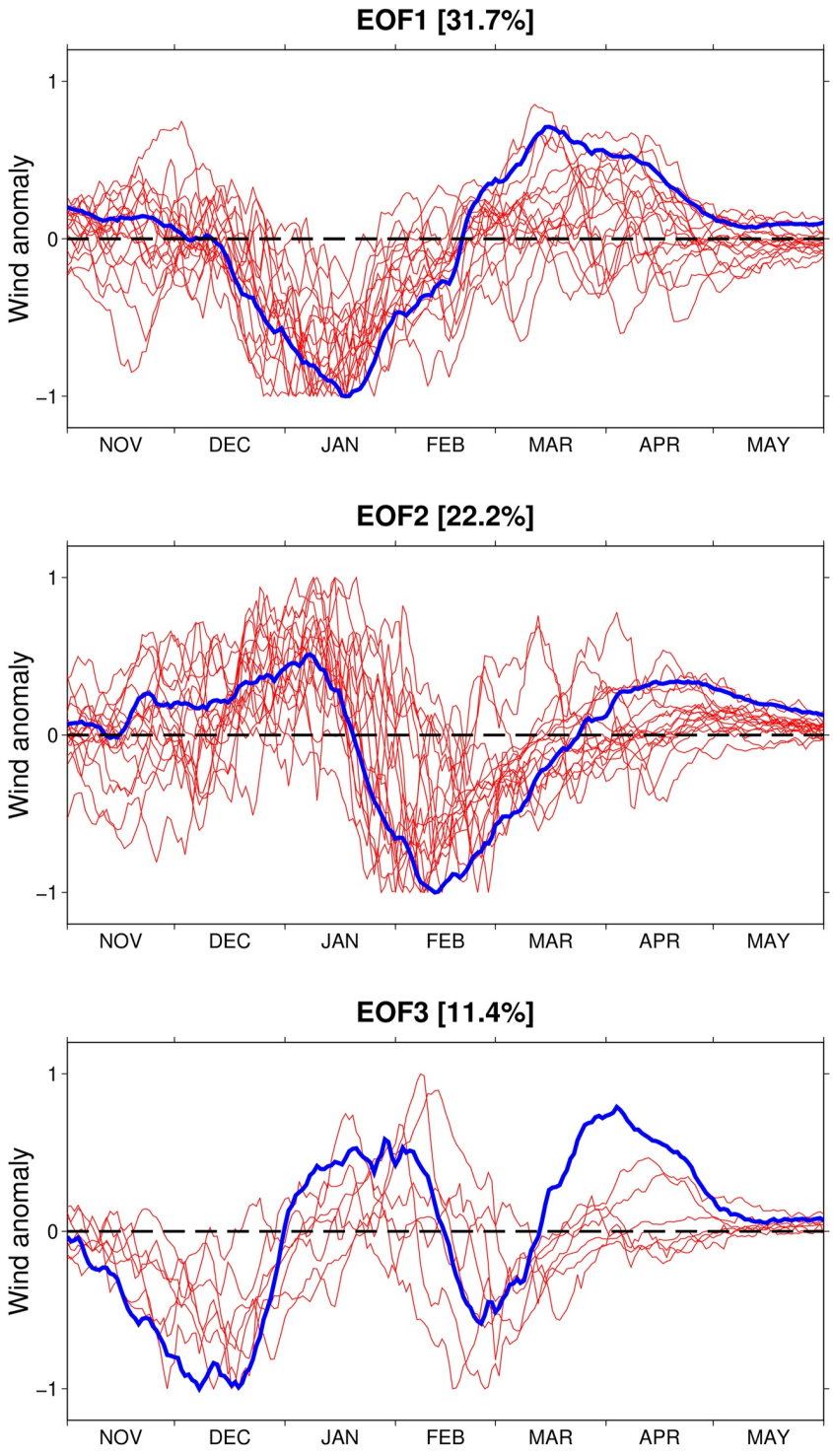


**Figure 5.** The first three empirical orthogonal functions (EOFs) (blue solid lines) of standardized wind anomalies for the 70 winters between 1950 and 2020 corresponding respectively to (EOF1) 31.7%, (EOF2) 22.2% and (EOF3) 11.4% of the variability. The winters associated with the curve fitting method to EOF1, EOF2, and EOF3 are illustrated by their wind anomaly evolution (red solid lines).

As a result, these EOF patterns illustrate typical physical evolutions of zonal winds in the winter stratosphere where, unsurprisingly, preferential timings of ISSWs contained in winters appear (Figure 5). These first three modes explain 65.3% of the wind fluctuations patterns revealing the main winter typologies and confirming the connection between the mid-winter and the winter end. Indeed, these evolutions reveal how the vortex evolved after an important SSW occurred. Here, EOF1 and EOF2 suggest that there will not be another one before the end of winter when an important SSW occurs in January and February. While, the EOF3 advances that when an important SSW occurs in December, there will be a second one at the end of February. Nonetheless, these suggested evolutions are not faultlessly followed by all associated winters.

The EOF1 (31.7%) represents the scenario with a single ISSW occurring in mid-January (hereafter January mode), and the EOF2 (22.2%) represents the scenario with a single ISSW occurring in February (hereafter February mode). Finally, the EOF3 (11.4%) represents the scenario with two important warmings occurring in December and March (hereafter Double mode). Thus, the patterns of these modes are consistent with the occurrence distribution of important SSW events observed in Figure 3 suggesting that peaks are related to specific scenarios. To perform the classification, we proceeded as follows:

- First, as these scenarios are related to perturbed polar vortex with ISSWs occurring in mid-winter, only the winters for which zonal wind became inferior to 10 $ms^{-1}$ once between 15 December and 1 March are selected to avoid considering Canadian warmings and FSWs. As a result, the algorithm identified 50 winters.
- Then, we normalized the three modes as well as the wind anomalies. Afterward, in order to associate these winters to the correct scenarios, a multiple curve fitting is employed by assuming that each winter is a linear combination of the three modes. This technique allows the weighting of the contribution of these three modes via a coefficient. Thus, we can decompose wind anomalies for each winter as follows:

$$\Delta \mathrm{U}_{\mathrm{w}_i} = k_1 \mathrm{EOF1} + k_2 \mathrm{EOF2} + k_3 \mathrm{EOF3}, \tag{3}$$

  where $\Delta U_{\mathrm{w}_i}$ is the wind anomaly for one winter $w_i$ and $k_1$, $k_2$, and $k_3$ are the coefficients associated to EOF1, EOF2, and EOF3 patterns, respectively.
- Finally, a winter is associated to the scenario with the highest coefficient and whether this coefficient is superior to 0.2 in order to classify only winters with patterns similar to EOF ones.

After several tests, we chose the coefficient threshold of 0.2 that allows for classifying, without making wrong associations, nearly all winters with similar patterns to EOF ones. As a result, 41 winters have been classified, 17 winters in the January mode, 17 winters in the February mode and 7 winters in the Double mode. The nine winters no classified possess similar coefficient magnitudes, all under 0.2, between the three scenarios indicating that they do not follow one precise scenario but more a combination of several different patterns. Consequently, the three main scenarios represent winter evolutions with ISSWs occurring in mid-winter.

After this first classification step, the 20 remaining winters represent the winter scenario nearly no perturbed during the mid-winter. This absence of disturbance makes the method based on the EOF useless to classify them as they do not have enough variability. Consequently, only the end of these winters, that is, when the vortex returns to its summer mode with easterly winds, is studied with a timing criterion. The method to classify FSWs used by Butler and Domeisen (2021) and described in Section 3.1.3 is therefore applied to the remaining winters. However, even though previous studies (Butler & Domeisen, 2021; Waugh & Rong, 2002) generally qualified FSW as "early" or "late" events, we classified the 20 remaining winters, similarly to Hauchecorne et al. (2022), into either radiative final warming mode (hereafter RFW mode) or dynamical final warming mode (hereafter DFW mode) for illustrating both their timing and the physical processes triggering them. Even though the DFW and RFW modes are under modes of the same scenario, they will be treated separately for the remaining of this study. As a result, the algorithm classified five and 15 winters in the RFW and DFW modes at the end of this last step, respectively. The result of this last classification is shown in Figure 7. The distribution of the 61 associated winters among these four scenarios and their occurrence over time are shown in Appendix A.

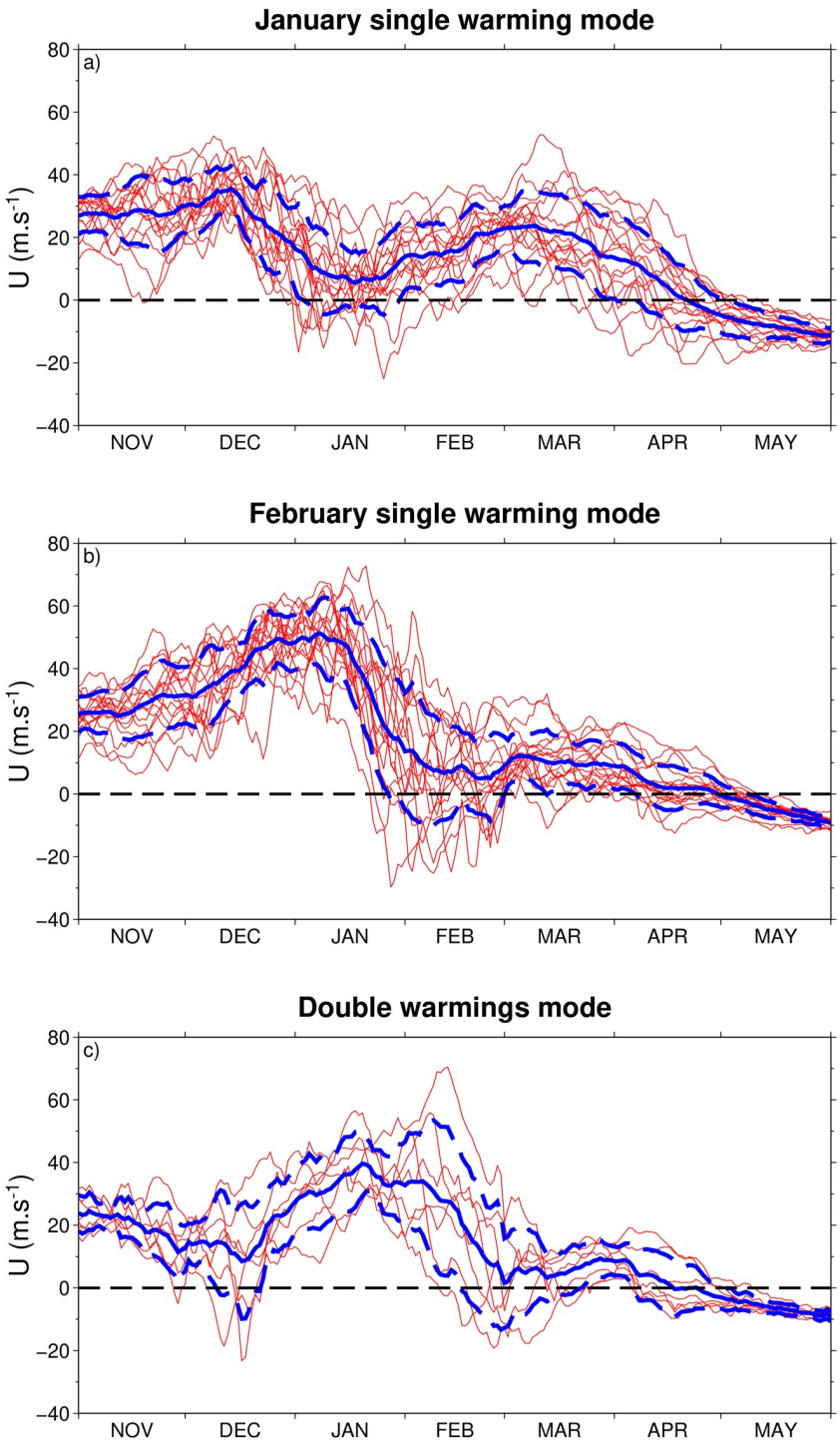


**Figure 6.** Evolutions of the zonal mean zonal wind at 10 hPa and 60°N for each winter (thin red lines) classified into the first three modes identified: the January single warming mode (a), the February single warming mode (b) and the Double warming mode (c). The blue solid and dashed lines show the mean and the standard deviation, respectively.

## 5. Characterization of Different Scenarios

Figure 6 illustrates the three scenarios identified with the principal component analysis by showing the mean evolutions of the wind at 10 hPa and 60°N of the associated winters. EOF evolutions (Figure 5) show clear

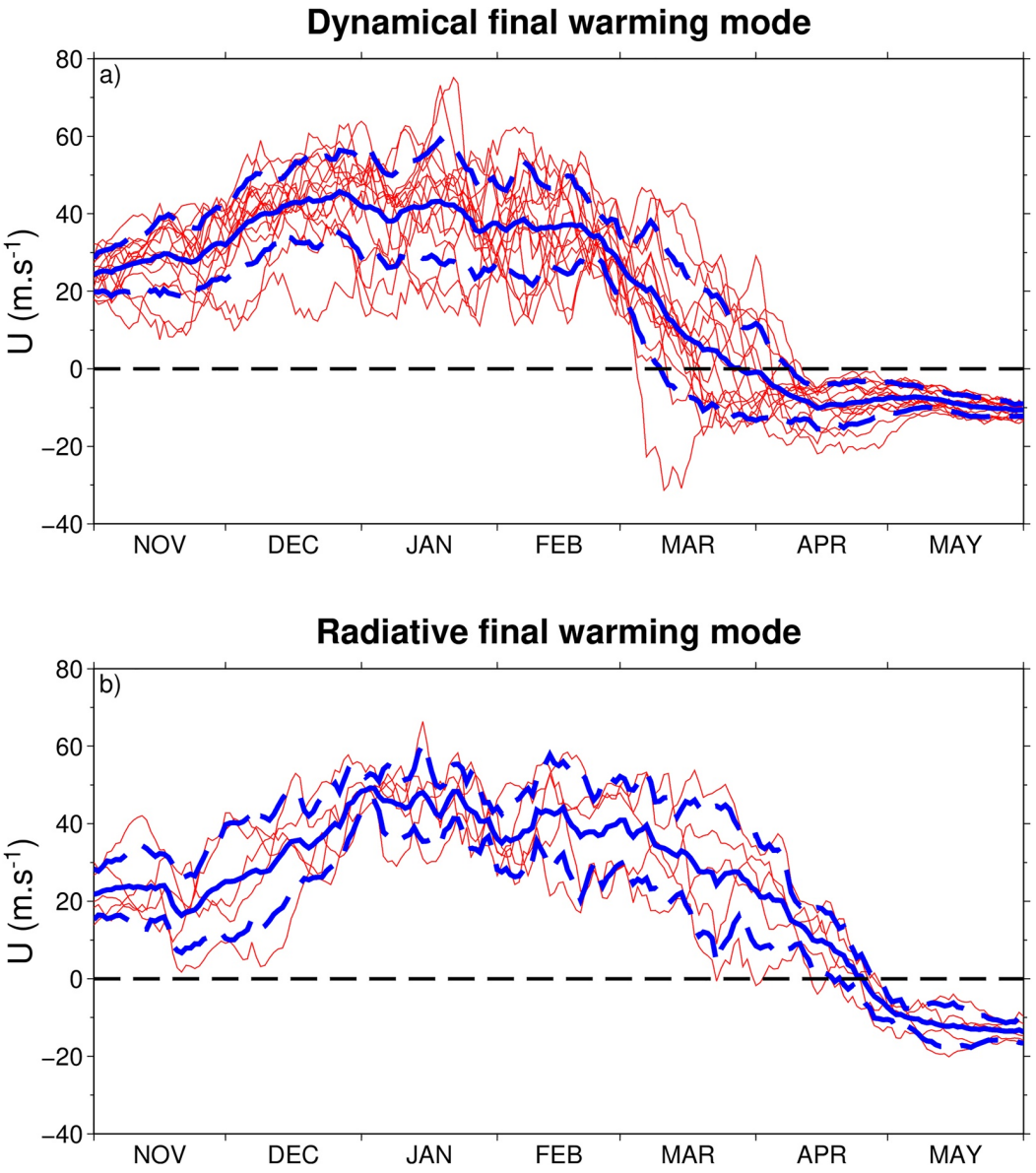


**Figure 7.** Evolutions of the zonal mean zonal wind at 10 hPa and 60°N for remaining winters (thin red lines) classified into the last scenario with two under-modes: the Dynamical final warming mode (a) and the Radiative final warming mode (b). The blue solid and dashed lines show the mean and the standard deviation, respectively.

anti-correlations between mid-winter and winter end. For instance, clear anti-correlation is found between January and March and between February and April for the EOF1 and EOF2, respectively, while the EOF3 presents an anti-correlation with a shorter interval between the end of February and early April. The anti-correlations between the early winter and the mid-winter are less marked in these modes. Nonetheless, this result confirms the conclusion by Hauchecorne et al. (2022), that is, the polar vortex on a given month is anti-correlated with its state 2–3 months earlier. Hence, according to the mean evolutions of these modes, the instant when important SSW occurs is a critical indicator for understanding the winter evolution afterward. The last winter scenario with its two under-mode, dynamical or radiative final warming, is also illustrated by the mean stratospheric wind evolutions at 10 hPa and 60°N of the associated winters in Figure 7. Table 1 reports the number of major SSWs, Canadian warmings, and FSW types among winters composing the four scenarios, determined with the methods detailed previously in Section 3.1, as well as the mean date of FSWs and their standard deviation.

**Table 1**
*Number of Radiative, Dynamical and Unclassified Final Stratospheric Warmings (FSWs) Among the Winters Classified Into the Four Scenarios*

| FSW type | January mode | February mode | Double mode | DFW mode | RFW mode |
|---|---|---|---|---|---|
| Radiative | 10 | 14 | 3 | 0 | 5 |
| Dynamical | 5 | 3 | 3 | 15 | 0 |
| Unclassified | 2 | 0 | 1 | 0 | 0 |
| Mean date of FSWs | 21 April | 28 April | 20 April | 28 March | 26 April |
| Standard deviation | 13 days | 12 days | 13 days | 11 days | 4 days |
| Major SSWs | 15 | 13 | 4 and 6 | 1 | 1 |
| Early warmings | 1 | 1 | 1 | 2 | 2 |

*Note.* The mean date of FSWs is displayed with the standard deviation. The number of winter with at least one major SSW and with an early warming are given as well.

For the January mode (Figure 6a), the vortex is, on average, enhanced during November even though Canadian warmings can occur at this period but without preventing the occurring of ISSWs in January. Indeed, the common point of these winters is that the vortex is slowed from mid-December due to the important SSW, very often major (almost 90% here), occurring around mid-January. Afterward, the vortex forms again with winds exceeding 20 $ms^{-1}$ on average from mid-February. Finally, the vortex falls down from the end of March to enter its summer mode preferentially with a radiative end or, sometimes, a dynamical end (see Table 1). The supposed reason these winter evolutions do not have a very marked preference end is that their SSW occur early enough in winter, making time necessary for the reforming of the vortex. According to Table 1, 10 winters finish with a radiative end, five finish with a dynamical end, and two winters remain unclassified. The FSWs occur on average on 21 April with a standard deviation of 13 days, confirming that ISSWs occurring in January do not influence the end type.

For the February mode (Figure 6b), the vortex is on average very strongly reinforced at the beginning of winter with winds lying from more than 20 $ms^{-1}$ at the start of November to more than 40 $ms^{-1}$ at the start of January. Then, the vortex is strongly decelerated from mid-January due to the important SSW occurring in February. Following this important SSW, which is often a major SSW, the vortex does not benefit from the necessary scale time to recover its previous state. Additionally, due to the seasonal variation in the radiation, the vortex strength starts to decrease gradually, preventing it from reaching its mid-winter strength. Therefore, the vortex remains very weak during the March month with winds at about 10 $ms^{-1}$ on average. For finishing, the vortex falls entirely at the end of April with a late and radiative end. These results are confirmed by Table 1 reporting that for more than 80% of winters composing the February mode, the algorithm has identified a radiative end occurring on average on 28 April with a standard deviation of 12 days. Furthermore, among these 17 winters, 13 major SSW events occurred, confirming that the vigorous intensity of the vortex breaking in February is strongly correlated to a radiative end. However, the warming in February did not prevent a dynamic end for three winters suggesting that other mechanisms drive the end type in addition of the timing of important SSW in mid-winter.

These results are in agreement with those found in Hu et al. (2014) who reported that winters with SSWs have a higher probability to finish with a late FSW than winters without SSWs.

For the Double warmings mode (Figure 6c), a first important SSW, major for more than half of winters, occurs around mid-December, causing the weakening of the vortex as soon as the November month has started. After this first significant warming, the vortex is reinforced until mid-January with winds exceeding 30 $ms^{-1}$ on average. Then a second important SSW, nearly every-time major, occurs at the end of February, weakening the vortex again. This last warming occurring lately in the winter prevents a complete restoration of the vortex and, therefore, leads it to its end. Thus, the mean final transition pattern of the Double mode is very similar to the one of the February mode. In contrast, there are as many winters with a radiative end as a dynamic end. The date of FSWs is, on average, on 20 April and a standard deviation of 13 days. This result confirms that the winter end, partly influenced by ISSWs' timings, is dynamically and radiatively driven (Butler & Domeisen, 2021; Salby & Callaghan, 2007). Winters with early FSWs possess a similar mechanism to mid-winter SSWs, that is, predominantly wave-driven, while late FSWs occur when winds weaken due to the changing solar radiation requiring less wave activity to break the vortex definitely (Vargin et al., 2020). However, these observed trends for the Double mode suffer from a few numbers of associated winters limiting their robustness. Therefore, more winters are necessary to confirm whether there is a preferred end type associated with this scenario.

While for the Dynamical and the Radiative modes belonging to the unperturbed vortex scenario, their mean winter evolutions are similar, that is, with no ISSWs from 15 December to 1 March, but with different end types (Figures 7a and 7b). The starting of winters is characterized by a strong enhancement of the polar vortex, with sometimes the presence of Canadian warmings occurring in November or in early December. Then, as the mid-winter is not perturbed by major SSWs, the polar vortex remains stable and strong until the arrival of the spring and the FSW. Regarding the Dynamical-mode, the FSW date is on average on 28 March with a standard deviation of 11 days, while for the Radiative-mode, the FSW date is on average on 26 April with a standard

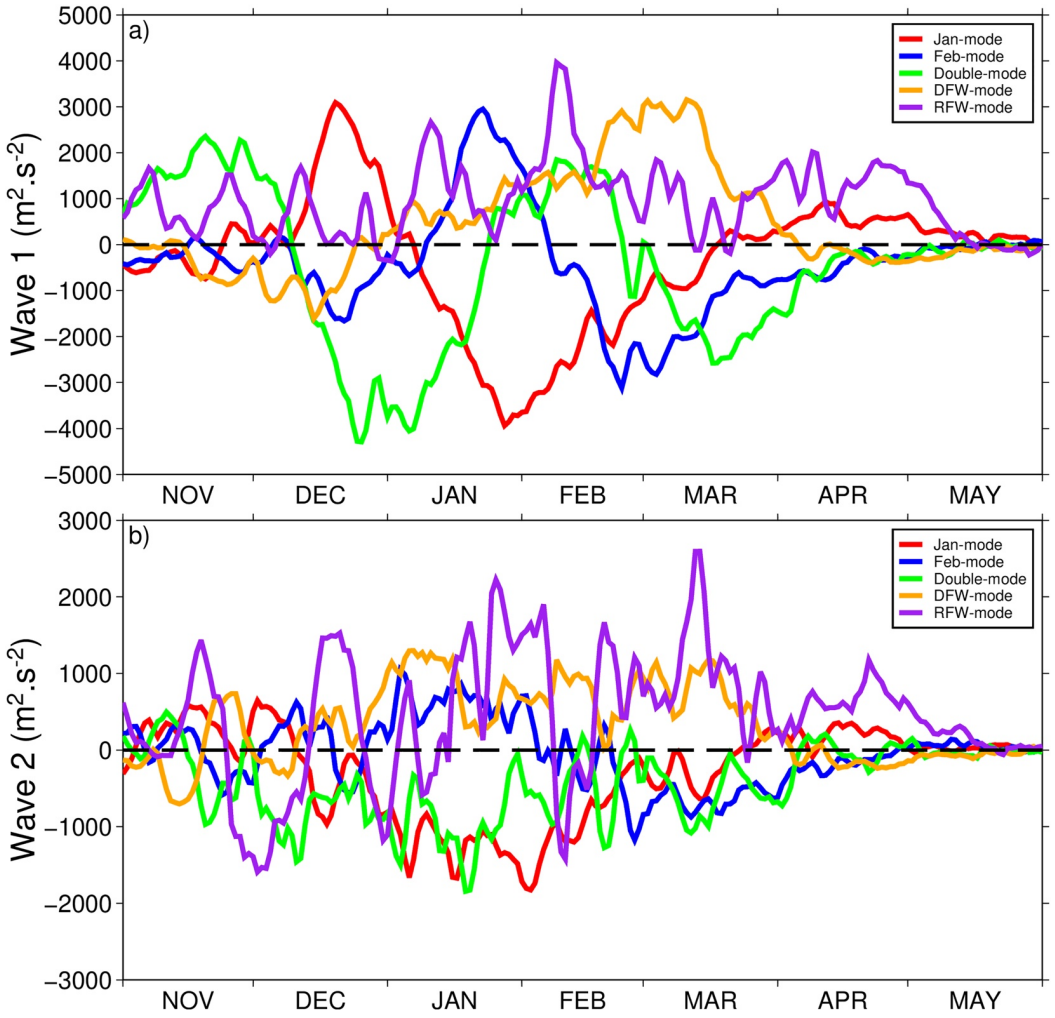


**Figure 8.** Mean evolutions of waves 1 (a) and 2 (b) amplitude anomalies for each scenario during the extended winter.

deviation of 4 days. Thus, there is almost 1 month on average separating the final warming dates between winters with a dynamical end and a radiative end. Finally, the unequal distribution of winters without ISSWs according to their FSW's timing, early and dynamical (15 winters) or late and radiative (five winters), is consistent with the trend observed in Hu et al. (2014).

How the timing of the ISSWs and FSWs for each scenario is preconditioned by the evolutions of the activities of planetary waves 1 and 2 is studied in the next section.

## 6. Evolution of Wave-1 and Wave-2 Activities

Figure 8 shows the mean anomalies evolutions of the planetary waves 1 and 2 during winter for each scenario obtained after to have removed the daily climatology computed over the 70 years. For all scenarios apart from the Double mode, the wave-1 anomalies remain near zero until early December, pointing out that the other modes follow the seasonal wave-1 activity increasing. In contrast, a constant strong positive wave-1 anomaly characterizes the exception of the Double mode in the same period preceding the important SSW occurring in December. Beyond early December, the wave-1 activities associated with the modes separate each other. The wave-2 anomalies for each scenario oscillate overall around zero until early December but with smaller amplitudes than for wave-1.

For the January mode, the mean anomaly amplitude of wave-1 strongly increases from early to mid-December, reaching its highest amplitude of more than 3,000 $m^2\ s^{-2}$, and then drops abruptly to reach an amplitude of almost −4,000 $m^2\ s^{-2}$ at the end of January. Afterward, the wave-1 anomaly increases again to become positive in mid-April and then starts to decrease definitely until the end of winter. On the other hand, the wave-2 anomaly remains overall negative, with a peak of almost −2,000 $m^2\ s^{-2}$ in early February. Therefore, winters associated with the January mode are mostly wave-1 driven. The evolution of the wave-1 anomaly amplitude is in perfect consistency with the formation and the reinforcement of the vortex in early winter as well as during February and the occurrence of the major SSW and FSW around mid-January and mid-April, respectively indeed, because upward propagating planetary waves from the troposphere to the stratosphere are possible only in a westerly circulation.

Regarding the February mode, the wave-1 anomaly drops from early December to mid-December, where a first minimum is reached, about −1,500 $m^2\ s^{-2}$. Afterward, the wave-1 activity strongly increases to reach a peak after mid-January with a similar amplitude, almost 3,000 $m^2\ s^{-2}$ that the one found in mid-December for the January mode. Then, the wave-1 anomaly drops suddenly to become negative and reaches the second minimum of −3,000 $m^2\ s^{-2}$ at the end of February. Beyond this moment, the wave-1 activity remains weaker than the seasonal climatology until the end of the winter. A similar evolution is found for the wave-2 anomaly, first increasing after December to reach a maximum with a positive peak of around 1,000 $m^2\ s^{-2}$ at mid-January, and then dropping to reach a minimum at the end of February before remaining negative until the winter end. Thus, this result shows that wave-1 and wave-2 drive the stratospheric circulation for winters associated with the February mode. As for the January mode, these evolutions are perfectly consistent with the vortex formation and its reinforcement during November and December and with the major SSW and the radiative end occurring in February and the end of April, respectively.

For the Double mode, after the positive anomaly in November, the wave-1 activity starts to decrease from early December until the end of December to reach a negative minimum of less than −4,000 $m^2\ s^{-2}$ while the wave-2 anomaly decreases constantly. Then, the wave-1 anomaly increases until early February to reach an activity similar to the November one, around 1,500 $m^2\ s^{-2}$. Afterward, the wave-1 anomaly drops again when the second important SSW occurs and reaches a second negative minimum in mid-March, almost −3,000 $m^2\ s^{-2}$. Finally, the wave-1 anomaly remains negative until the winter end. A similar evolution of the wave-2 activity to the January mode is found for the Double mode, that is, the wave-2 anomaly remains overall negative during winter. Thus, these mean evolutions of wave-1 anomalies are coherent with the timing of the two ISSWs occurring in the winters associated with the Double mode. Therefore, the first and the second ISSWs of these winters, occurring in mid-December and at the end of February, respectively, are preconditioned mostly by a wave-1 activity.

Consistently with the zonal wind evolutions shown in Figure 7, similar trends in the wave activities are found between the DFW and RFW modes. Indeed, the wave-1 and wave-2 activities associated with both modes remain overall stronger than the seasonal activity. The RFW mode is characterized by a wave-1 anomaly increasing slightly from early January to mid-February to reach a maximum of almost 4,000 $m^2\ s^{-2}$ and then dropping progressively until the end of May. While, for the DFW mode, the wave-1 anomaly increases from mid-December to reach a maximum in mid-March of 3,000 $m^2\ s^{-2}$ and then drops suddenly to reach an anomaly near zero in early April. We notice that, as expected, the DFW mode possesses a wave-1 activity stronger than the RFW mode from mid-February to mid-March. However, the opposite is found for the wave-2 activity in the same period. Regarding the wave-2 anomalies, the DFW mode possesses a general constant positive anomaly around 1,000 $m^2\ s^{-2}$ from early January to mid-March, while an oscillating evolution is observed for the RFW mode. A strong drop in the wave-2 activity is observed in early February for the RFW mode reaching less than −1,000 $m^2\ s^{-2}$, coinciding that the maximum of nearly 4,000 $m^2\ s^{-2}$ reached by the wave-1 anomaly. After this drop, the wave-2 activity increases to reach and finish with the same amplitude as the DFW mode. Even though a notable peak not expected in March of about 2,500 $m^2\ s^{-2}$ for the RFW mode is found, before decreasing until the end of May.

## 7. Discussion

Thus, the new classification technique employed here divided the 70 winters among four scenarios identified, representing each typical evolution of the stratospheric circulation during winter. However, as this method used to build the four composites is based on the stratospheric zonal wind patterns from 1 November to 1 June, the

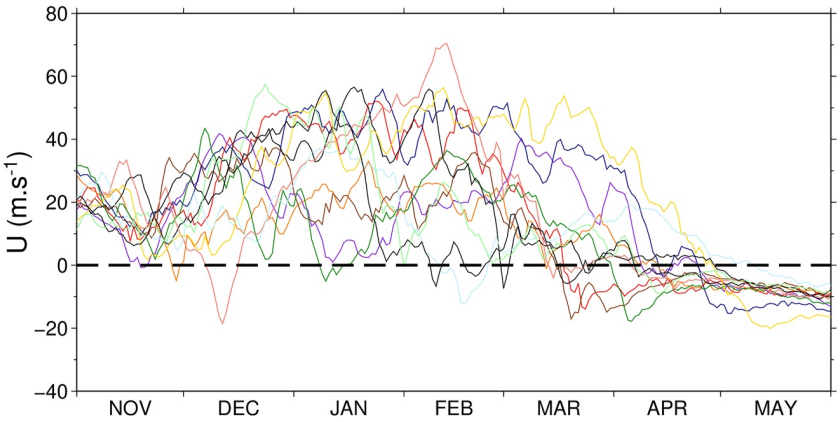


**Figure 9.** Evolution of the zonal mean zonal wind at 10 hPa and 60°N for each winter with an important warming occurring in November.

algorithm might have proceeded to the wrong winter associations. For instance, winters with an important SSW occurring at the end of January can be associated with the January mode while they should be associated with the February mode or inversely (see Figures 6a and 6b).

Nevertheless, the mean stratospheric zonal wind patterns found for each scenario testify that the algorithm correctly classified most of the winters. Additionally, their consistency with the mean evolutions of the waves' amplitudes constitutes further evidence that the algorithm identified real distinct scenarios with specific dynamical behaviors. Indeed, for example, only the quasi-stationary wave-1 tends to dominate during the pre-warming phase for winters associated with the January mode. While for the winters associated with the February mode, waves 1 and 2 tend to play an average role in the occurrence of the important SSW.

The mean evolutions of wave-1 anomaly amplitudes, especially from December, follow different typologies more marked with greater magnitude than the mean evolutions of wave-2 anomaly amplitudes. The main reason is that wave-1, in statistics, tends to play a significant role each time the vortex is strongly perturbed regardless of the vortex geometry, that is, either displacement or splitting events (Bancalá et al., 2012; Barriopedro & Calvo, 2014). Another reason is that the wave-2 anomaly evolutions for each winter are more abrupt and sudden than the constant evolutions observed for wave-1 prior to the important SSW occurring (not shown here). Consequently, the mean evolutions of wave-2 anomaly amplitudes shown in this study are less suitable markers than wave-1 activities to illustrate the different dynamics between scenarios. Finally, the common evolutions of the wave-1 amplitudes during November month are mainly due to the seasonal cycle of the wave activity. Beyond early December, the reasons the modes separate from each other remain unknown. Investigating the mechanisms influencing the winter unfolding and causing the divergence from this climatology of the wave activity for each mode should be pursued in future studies. The observed precursors in the mesosphere in Angot et al. (2012) should be considered a first lead up to 2 months before minor and major SSWs occur in the stratosphere.

Interestingly, from mid-February to mid-March, the wave-1 and wave-2 wave activities of the DFW mode are stronger and weaker than those of the RFW mode. However, as the DFW mode is expected to have stronger wave activity than the RFW mode at this period (Vargin et al., 2020), this result suggests, first, that dynamical FSWs are triggered mainly by the wave-1 activity and, second, that the wave-1 activity plays a role, more or less significant systematically, in all FSWs' triggering.

Identifying important warmings occurring in early winter, sometimes classified in the literature as Canadian warmings, which rarely reverse the zonal winds, is undertaken to investigate their influence on winter unfolding. Here, early warming is detected when the zonal wind became once inferior to 10 $ms^{-1}$ during November. Thanks to this wind criterion, 12 warming events have been detected, including the events classified as Canadian warmings by Labitzke (1981). According to the result of the classification, the winters with early warming do not have a preferred scenario (see Table 1), confirming the ability of the algorithm to capture the general trend even when unusual events occur. This result is confirmed in Figure 9 showing how the 12 winter evolutions with early warming identified in November follow different patterns.

The causes why this early warming does not prevent or influence the occurrence and the timing of an important SSW in the following months are not investigated here. Nevertheless, the likely reasons for this behavior are that early warmings are often weak, and the polar vortex is rapidly reinforced due to the radiation cooling. Furthermore, the Canadian warmings among these events mainly impact the lower stratosphere (Manney et al., 2001).

When we compare with the classifications carried out by Charlton and Polvani (2007), Mitchell et al. (2013), Barriopedro and Calvo (2014) and Afargan-Gerstman and Domeisen (2020) (not shown here), only the February mode tends to be associated with split events. Otherwise, the different scenarios identified here are neither related to a specific vortex geometry type, a certain wave geometry, or a precise downward impact after major SSWs. This result was expected as the vortex geometry is unrelated to a distinct wave geometry. Indeed, Bancalá et al. (2012), who investigated the wave geometry in the prewarming phase, classified major SSWs according to the dominant zonal wavenumber (wave-1 or wave-2 events). Additionally, Barriopedro and Calvo (2014) examined the El Nino-Southern Oscillation (ENSO) phase, either El Nino (EL) or La Nina (LN), during major SSWs and found amplification of wavenumber 1 preceding SSWs during EL phase and amplification of wavenumber 2 preceding SSWs during LN phase. However, the evolution of the vortex geometry toward a splitting or a displacement event during SSWs does not have a privileged ENSO phase or a specific wave geometry. Moreover, the vortex splitting event arises not only with a strong wave-2 activity but also with significant wave-1 activity.

Consequently, the timing of ISSWs and FSWs and, therefore, the winter typologies are independent of these characteristics. This absence of correlation is not surprising as the classification carried out here is based on the stratospheric circulation patterns influenced by the timing of ISSWs and FSWs, while the vortex structure, as well as the dominant wavenumber during the pre-warming phase, are influenced by the ENSO phase (Barriopedro & Calvo, 2014). Indeed, this new way to classify SSWs and FSWs, that is, focusing on winter typologies rather than only on the most extreme events, reveals how the mid-winter is connected to the winter end. Thus, the three perturbed scenarios identified here confirm the result found in Hauchecorne et al. (2022), especially from the mid-winter, that is, the vortex state on a given month is anti-correlated with its state 2–3 months earlier and are therefore further evidence of the stratospheric memory existence.

## 8. Conclusions

In this study, we have classified 61 winters among the 70 NH winters from 1950 to 2020 into four distinct scenarios with a new technique based on EOF analysis of the evolution of the anomaly of stratospheric zonal mean zonal winds extracted from the ERA5 package at the edge of the polar vortex. These four scenarios are influenced by the timings of ISSWs, including major and minor SSWs, and FSWs, giving an overview of the stratospheric memory, that is, how the mid-winter is connected to the winter end. The first advantage of this new method of classification is to focus on the winter typologies and not only on the major SSW events extending the number of winters classifiable.

Thus, the algorithm identified three perturbed scenarios with ISSWs occurring in mid-winter: the January mode (17 winters), the February mode (17 winters), and the Double mode (seven winters). Here nine winters among the perturbed winters possess atypical patterns and remain unclassified. Most of the time, the January mode is characterized by a major SSW occurring in mid-January and afterward a reinforcement of the vortex to finish preferentially radiatively or sometimes with a dynamical FSW. Here, we found that among the winters with an important SSW in January, 30% have a dynamical FSW, and 60% have a radiative FSW. Strong reinforcement of the vortex characterizes the February mode in early winter, often followed by a major SSW occurring in February, generally finishing (for 82% of cases here) with a radiative FSW confirming that ISSWs' timings influence the winter end. Winters with ISSWs tend to finish with a radiative FSW. Finally, the Double mode is characterized by a first important SSW occurring in mid-December and a second important SSW at the end of February to finish either with a radiative or dynamical end. However, contrary to the January and February modes, the few winters associated with the Double mode make it difficult to infer a robust trend for the privileged FSW type. Therefore, according to our results, the ISSWs' timings influence but are not the only mechanisms responsible for the triggering timing of FSWs.

Accordingly, the conclusion in Hauchecorne et al. (2022) is confirmed here with these first three scenarios, that is, the vortex on a given month is anti-correlated with its state 2–3 months earlier.

The last scenario represents undisturbed winters classified into two under-modes according to their end types, either late and radiative (five winters) or early and dynamical (15 winters), confirming that winters without ISSWs tend to finish with an early FSW.

Additionally, the mean evolutions of wave amplitudes associated with each scenario, especially the wave-1 evolutions, are consistent with the zonal wind patterns found, confirming the different dynamics behaviors between each scenario in the pre-warming phase. After a comparison with the classifications done by Mitchell et al. (2013), Barriopedro and Calvo (2014) and Afargan-Gerstman and Domeisen (2020), only the February mode tends to be related to a splitting vortex type after that important SSW occurred. Otherwise, the scenarios found here are not related to a typical vortex geometry, wave geometry, or tropospheric response. Furthermore, the unfolding of winters is not affected by ISSWs occurring in early winter, which are Canadian warmings for most of them, mainly because they are often weak and the polar vortex is rapidly reinforced by the radiative cooling and also as they tend to impact only the lower stratosphere (Manney et al., 2001).

Consequently, the main interests of this new classification are that the EOF analysis confirms mathematically that the observed winter patterns with similar preferential SSWs' timings follow independent modes illustrating typical physical evolutions. Second, this new way to classify ISSWs and FSWs according to their timings and impacts on the winter evolution aims to establish the connection between the mid-winter and the winter end. Finally, the objective classification of winters into these modes of variability improves our understanding of the stratosphere state, which is essential for seasonal forecasting in the lower layers. However, further researches are necessary to explain why the wintertime stratospheric winds follow these typologies and why one scenario occurs rather than another. Thus, several significant questions remain suspended:

- What are the precursors responsible for each scenario and the SSW timings?
- What causes the different wave-1 and wave-2 activities between the scenarios?
- On what depends on the winter end type when the polar vortex remains very strong?

and should be investigated in the future, thanks to the four composites determined here. Here, the wave-1 activities associated with the scenarios separate each other from early December, suggesting that the mechanisms responsible for their occurrence act in the previous months. A first lead should be the observed temperature anomalies in the mesosphere in Angot et al. (2012) up to 2 months before minor and major SSWs occur. Finally, further research on these winter scenarios can contribute to better modeling the stratospheric wintertime wind evolutions in climate models, improving their overall weather forecasting (Figure A1).

## Appendix A: Distribution of the 70 Winters

1. January single warming mode: (1950/1951, 1952/1953, 1954/1955, 1959/1960, 1967/1968, 1969/1970, 1970/1971, 1976/1977, 1984/1985, 1997/1998, 2001/2002, 2002/2003, 2003/2004, 2005/2006, 2011/2012, 2012/2013, 2018/2019).
2. February single warming mode: (1956/1957, 1957/1958, 1962/1963, 1972/1973, 1978/1979, 1980/1981, 1982/1983, 1986/1987, 1988/1989, 1989/1990, 1990/1991, 1994/1995, 2007/2008, 2008/2009, 2009/2010, 2016/2017, 2017/2018).
3. Double warmings mode: (1951/1952, 1965/1966, 1968/1969, 1979/1980, 1987/1988, 1998/1999, 2000/2001).
4. Unperturbed mode:
   Dynamical final warming mode: (1955/1956, 1958/1959, 1960/1961, 1963/1964, 1973/1974, 1974/1975, 1975/1976, 1985/1986, 1992/1993, 1995/1996, 1999/2000, 2010/2011, 2013/2014, 2014/2015, 2015/2016).
   Radiative final warming mode: (1961/1962, 1964/1965, 1966/1967, 1996/1997, 2019/2020).
5. Unclassified winters: (1953/1954, 1971/1972, 1977/1978, 1981/1982, 1983/1984, 1991/1992, 1993/1994, 2004/2005, 2006/2007).
6. Winters with an early warming: (1952/1953, 1958/1959, 1966/1967, 1968/1969, 1974/1975, 1976/1977, 1979/1980, 1987/1988, 1996/1997, 2000/2001, 2009/2010, 2016/2017).

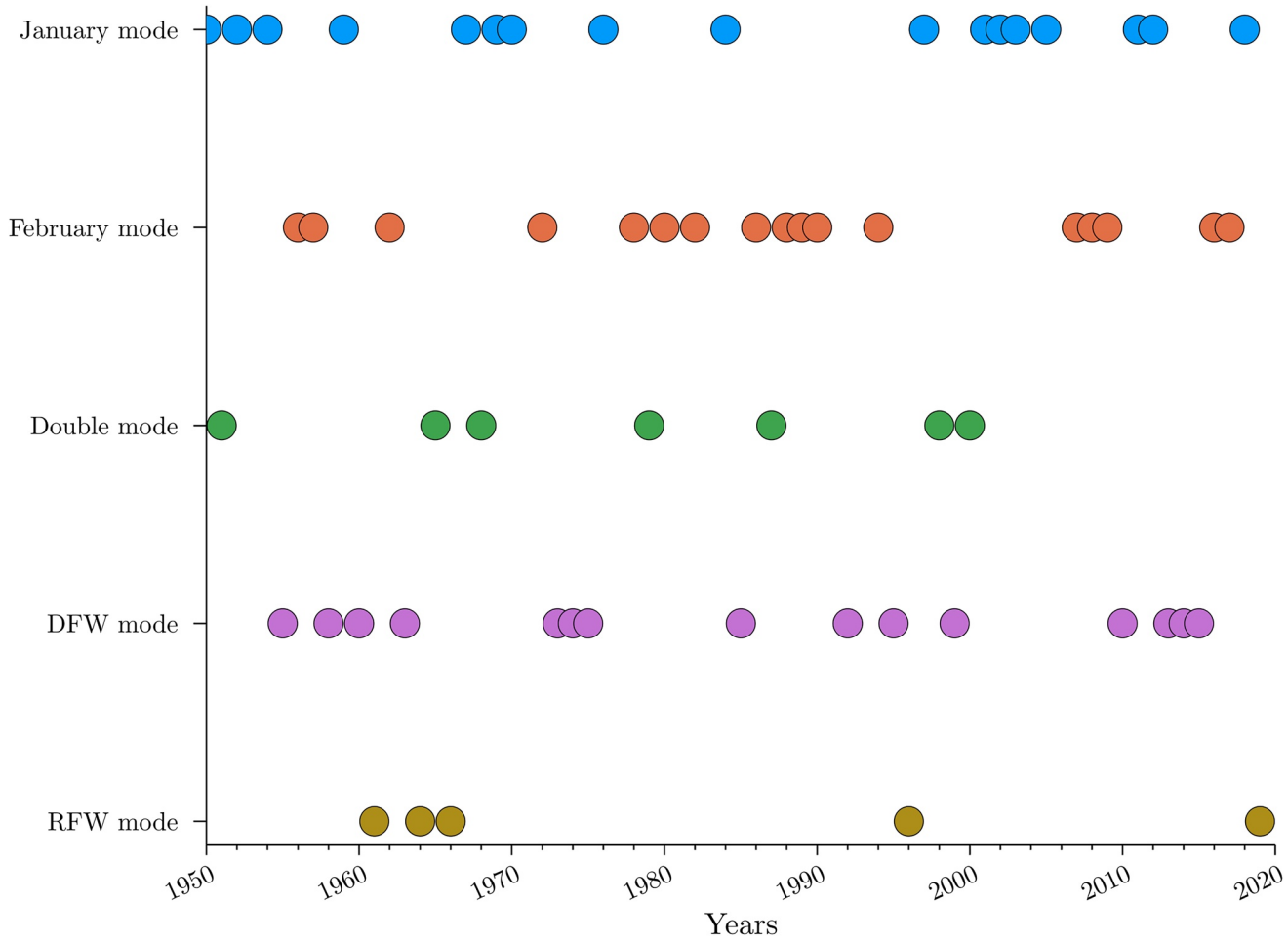


**Figure A1.** Distribution of the 70 winters among the five scenarios over time.

## Data Availability Statement

How to access ERA5 data on pressure levels from 1950 to the present is explained on the ECMWF website: https://confluence.ecmwf.int/display/CKB/How+to+download+ERA5#HowtodownloadERA5-OptionB:DownloadERA5familydatathatisNOTlistedintheCDSonlinecatalogue-SLOWACCESS Hersbach et al. (2018) was downloaded from the Copernicus Climate Change Service (C3S) Climate Data Store. Bell et al. (2020) was downloaded from the Copernicus Climate Change Service (C3S) Climate Data Store. The results contain modified Copernicus Climate Change Service information 2020. Neither the European Commission nor ECMWF is responsible for any use that may be made of the Copernicus information or data it contains.

**Acknowledgments**
This work was performed within the framework of the European ARISE project and was funded by the French Educational Ministry with EUR IPSL.

## References

Afargan-Gerstman, H., & Domeisen, D. (2020). Pacific modulation of the North Atlantic storm track response to sudden stratospheric warming events. *Geophysical Research Letters*, *47*(2), e2019GL085007. https://doi.org/10.1029/2019GL085007

Andrews, D., Holton, J., & Leovy, C. (1987). *Middle atmosphere dynamics*. Elsevier Science.

Angot, G., Keckhut, P., Hauchecorne, A., & Claud, C. (2012). Contribution of stratospheric warmings to temperature trends in the middle atmosphere from the lidar series obtained at haute-provence observatory (44°N). *Journal of Geophysical Research*, *117*(D21), D21102. https://doi.org/10.1029/2012JD017631

Baldwin, M., & Dunkerton, T. (2001). Stratospheric harbingers of anomalous weather regimes. *Science*, *294*(5542), 581–584. https://doi.org/10.1126/science.1063315

Baldwin, M. P., Ayarzagüena, B., Birner, T., Butchart, N., Butler, A. H., Charlton-Perez, A. J., et al. (2021). Sudden stratospheric warmings. *Reviews of Geophysics*, *59*(1), e2020RG000708. https://doi.org/10.1029/2020RG000708

Bancalá, S., Krüger, K., & Giorgetta, M. (2012). The preconditioning of major sudden stratospheric warmings. *Journal of Geophysical Research*, *117*(D4), D04101. https://doi.org/10.1029/2011JD016769

Barriopedro, D., & Calvo, N. (2014). On the relationship between ENSO, stratospheric sudden warmings, and blocking. *Journal of Climate*, *27*(12), 4704–4720. https://doi.org/10.1175/JCLI-D-13-00770.1

Bell, B., Hersbach, H., Berrisford, P., Dahlgren, P., Horányi, A., Muñoz Sabater, J., et al. (2020). ERA5 hourly data on pressure levels from 1950 to 1978 (preliminary version). [dataset]. Copernicus Climate Change Service (C3S) Climate Data Store (CDS). Retrieved from https://cds.climate.copernicus-climate.eu/cdsapp#!/dataset/reanalysis-era5-pressure-levels-preliminary-back-extension?tab=overview

Butler, A. H., & Domeisen, D. I. V. (2021). The wave geometry of final stratospheric warming events. *Weather and Climate Dynamics*, *2*, 453–474. https://doi.org/10.5194/wcd-2-453-2021

Butler, A. H., Seidel, D. J., Hardiman, S. C., Butchart, N., Birner, T., & Match, A. (2015). Defining sudden stratospheric warmings. *Bulletin of the American Meteorological Society*, *96*(11), 1913–1928. https://doi.org/10.1175/BAMS-D-13-00173.1

Butler, A. H., Sjoberg, J. P., Seidel, D. J., & Rosenlof, K. H. (2017). A sudden stratospheric warming compendium. *Earth System Science Data*, *9*(1), 63–76. https://doi.org/10.5194/essd-9-63-2017

Charlton, A. J., O'Neill, A., Lahoz, W. A., & Berrisford, P. (2005). The splitting of the stratospheric polar vortex in the southern hemisphere, September 2002: Dynamical evolution. *Journal of the Atmospheric Sciences*, *62*(3), 590–602. https://doi.org/10.1175/JAS-3318.1

Charlton, A. J., & Polvani, L. M. (2007). A new look at stratospheric sudden warmings. Part I: Climatology and modeling benchmarks. *Journal of Climate*, *20*(3), 449–469. https://doi.org/10.1175/JCLI3996.1

Charlton-Perez, A. J., Ferranti, L., & Lee, R. W. (2018). The influence of the stratospheric state on North Atlantic weather regimes. *Quarterly Journal of the Royal Meteorological Society*, *144*(713), 1140–1151. https://doi.org/10.1002/qj.3280

Dee, D. P., Uppala, S. M., Simmons, A. J., Berrisford, P., Poli, P., Kobayashi, S., et al. (2011). The ERA-interim reanalysis: Configuration and performance of the data assimilation system. *Quarterly Journal of the Royal Meteorological Society*, *137*(656), 553–597. https://doi.org/10.1002/qj.828

Domeisen, D. I. (2019). Estimating the frequency of sudden stratospheric warming events from surface observations of the North Atlantic oscillation. *Journal of Geophysical Research: Atmospheres*, *124*(6), 3180–3194. https://doi.org/10.1029/2018JD030077

Fusco, A. C., & Salby, M. L. (1999). Interannual variations of total ozone and their relationship to variations of planetary wave activity. *Journal of Climate*, *12*(6), 1619–1629. https://doi.org/10.1175/1520-0442(1999)012<1619:IVOTOA>2.0.CO;2

Hauchecorne, A., Claud, C., Keckhut, P., & Mariaccia, A. (2022). Stratospheric final warmings fall into two categories with different evolution over the course of the year. *Communications Earth & Environment*, *3*(1), 4. https://doi.org/10.1038/s43247-021-00335-z

Hersbach, H., Bell, B., Berrisford, P., Biavati, G., Horányi, A., Muñoz Sabater, J., et al. (2018). ERA5 hourly data on single levels from 1979 to present. [dataset]. Copernicus Climate Change Service (C3S) Climate Data Store (CDS). Retrieved from https://cds.climate.copernicus-climate.eu/cdsapp#!/dataset/reanalysis-era5-pressure-levels-preliminary-back-extension?tab=overview

Hersbach, H., Bell, B., Berrisford, P., Hirahara, S., Horányi, A., Muñoz-Sabater, J., et al. (2020). The ERA5 global reanalysis. *Quarterly Journal of the Royal Meteorological Society*, *146*(730), 1999–2049. https://doi.org/10.1002/qj.3803

Hu, J., Ren, R., & Xu, H. (2014). Occurrence of winter stratospheric sudden warming events and the seasonal timing of spring stratospheric final warming. *Journal of the Atmospheric Sciences*, *71*(7), 2319–2334. https://doi.org/10.1175/JAS-D-13-0349.1

Kodera, K., Mukougawa, H., Maury, P., Ueda, M., & Claud, C. (2016). Absorbing and reflecting sudden stratospheric warming events and their relationship with tropospheric circulation. *Journal of Geophysical Research: Atmospheres*, *121*(1), 80–94. https://doi.org/10.1002/2015JD023359

Krüger, K., Naujokat, B., & Labitzke, K. (2005). The unusual midwinter warming in the Southern Hemisphere stratosphere 2002: A comparison to Northern Hemisphere phenomena. *Journal of the Atmospheric Sciences*, *62*(3), 603–613. https://doi.org/10.1175/JAS-3316.1

Labitzke, K. (1981). Stratospheric-mesospheric midwinter disturbances—A summary of observed characteristics. *Journal of Geophysical Research*, *86*(C10), 9665–9678. https://doi.org/10.1029/JC086iC10p09665

Limpasuvan, V., Thompson, D. W. J., & Hartmann, D. L. (2004). The life cycle of the Northern Hemisphere sudden stratospheric warmings. *Journal of Climate*, *17*(13), 2584–2596. https://doi.org/10.1175/1520-0442(2004)017<2584:TLCOTN>2.0.CO;2

Manney, G. L., Sabutis, J. L., & Swinbank, R. (2001). A unique stratospheric warming event in November 2000. *Geophysical Research Letters*, *28*(13), 2629–2632. https://doi.org/10.1029/2001GL012973

Mariaccia, A., Keckhut, P., Hauchecorne, A., Claud, C., Le Pichon, A., Meftah, M., & Khaykin, S. (2022). Assessment of ERA-5 temperature variability in the middle atmosphere using Rayleigh lidar measurements between 2005 and 2020. *Atmosphere*, *13*(2), 242. https://doi.org/10.3390/atmos13020242

Marlton, G., Charlton-Perez, A., Harrison, G., Polichtchouk, I., Hauchecorne, A., Keckhut, P., et al. (2021). Using a network of temperature lidars to identify temperature biases in the upper stratosphere in ECMWF reanalyses. *Atmospheric Chemistry and Physics*, *21*(8), 6079–6092. https://doi.org/10.5194/acp-21-6079-2021

Matsuno, T. (1971). A dynamical model of the stratospheric sudden warming. *Journal of the Atmospheric Sciences*, *28*(8), 1479–1494. https://doi.org/10.1175/1520-0469(1971)028<1479:ADMOTS>2.0.CO;2

Maury, P., Claud, C., Manzini, E., Hauchecorne, A., & Keckhut, P. (2016). Characteristics of stratospheric warming events during northern winter. *Journal of Geophysical Research: Atmospheres*, *121*(10), 5368–5380. https://doi.org/10.1002/2015JD024226

Mitchell, D. M., Gray, L. J., Anstey, J., Baldwin, M. P., & Charlton-Perez, A. J. (2013). The influence of stratospheric vortex displacements and splits on surface climate. *Journal of Climate*, *26*(8), 2668–2682. https://doi.org/10.1175/JCLI-D-12-00030.1

Newman, P. A., & Rosenfield, J. E. (1997). Stratospheric thermal damping times. *Geophysical Research Letters*, *24*(4), 433–436. https://doi.org/10.1029/96GL03720

North, G., Bell, T., Cahalan, R., & Moeng, F. (1982). Sampling errors in the estimation of empirical orthogonal functions. *Monthly Weather Review*, *110*(7), 699–706. https://doi.org/10.1175/1520-0493(1982)110<0699:SEITEO>2.0.CO;2

Pawson, S., & Kubitz, T. (1996). Climatology of planetary waves in the northern stratosphere. *Journal of Geophysical Research*, *101*(D12), 16987–16996. https://doi.org/10.1029/96JD01226

Rao, J., Ren, R., Chen, H., Yu, Y., & Zhou, Y. (2018). The stratospheric sudden warming event in February 2018 and its prediction by a climate system model. *Journal of Geophysical Research: Atmospheres*, *123*(23), 13332–13345. https://doi.org/10.1029/2018JD028908

Salby, M. L., & Callaghan, P. F. (2007). Influence of planetary wave activity on the stratospheric final warming and spring ozone. *Journal of Geophysical Research*, *112*(D20), D20111. https://doi.org/10.1029/2006JD007536

Scherhag, R. (1952). Die explosionsartigen stratospherener warmungen des spatwinters. *Berichte des Deutschen Wetterdienstes*, *38*, 51–63.

Simmons, A., Soci, C., Nicolas, J., Bell, B., Berrisford, P., Dragani, R., et al. (2020). Global stratospheric temperature bias and other stratospheric aspects of ERA5 and ERA5.1. ECMWF Technical Memorenda No. 859. https://doi.org/10.21957/rcxqfmg0

Thompson, D., & Wallace, J. (2001). Regional climate impacts of the Northern Hemisphere annular mode. *Science*, *293*(5527), 85–89. https://doi.org/10.1126/science.1058958

Vargin, P. N., Kostrykin, S. V., Rakushina, E. V., Volodin, E. M., & Pogoreltsev, A. I. (2020). Study of the variability of spring breakup dates and Arctic stratospheric polar vortex parameters from simulation and reanalysis data. *Izvestiya, Atmospheric and Oceanic Physics*, *56*(5), 458–469. https://doi.org/10.1134/S0001433820050114

Waugh, D., & Rong, P.-P. (2002). Interannual variability in the decay of lower stratospheric arctic vortices. *Journal of the Meteorological Society of Japan*, *80*(4B), 997–1012. https://doi.org/10.2151/jmsj.80.997

## 5.6 . Conclusions

Ainsi, il apparaît que le vortex polaire tend à suivre quatre scénarios influencés par le timing des échauffements stratosphériques soudains importants et finaux. Plus précisément, trois de ces scénarios représentent des évolutions, dites "perturbées", au cours desquelles des échauffements se produisent tandis que le dernier scénario, dit "non perturbé", représente un vortex polaire fort tout au long de l'hiver. De plus, ces scénarios possèdent des évolutions spécifiques d'activité d'ondes planétaires, ondes 1 et 2, en accord avec leurs évolutions de vent zonal soulignant leur caractère singulier.

Ainsi, ces scénarios illustrent la connexion existante entre le milieu et la fin de l'hiver renforçant cette idée de mémoire stratosphérique introduite par Hauchecorne et al. (2022) et permettent de confirmer les conclusions établies précédemment. Tout d'abord, les hivers ayant eu un vortex polaire fort non perturbés tendent à connaître un échauffement final dynamique. D'autre part, il est clair que l'anticorrélation du vortex polaire avec son état 2-3 mois auparavant est avant tout le résultat des hivers perturbés. Cependant, les hivers associées à chaque scénario ne semblent pas reliées à une certaine géométrie du vortex polaire ou géométrie d'onde selon les précédentes classifications (Bancalá et al., 2012; Barriopedro and Calvo, 2014; Charlton and Polvani, 2007; Mitchell et al., 2013).

Ces nouveaux résultats démontrent l'importance du timing des échauffements dans le déroulé des hivers et améliorent notre compréhension du fonctionnement de la stratosphère essentielle pour la prévision météorologique. Malgré ces nouvelles trouvailles, les mécanismes responsables de l'apparition de ces différents scénarios restent à être élucidés. La séparation des évolutions de l'activité d'onde-1 à partir de début décembre suggère que les potentiels facteurs responsables de ces évolutions agissent en amont. Dans le prochain chapitre, le couplage stratosphère-troposphère sera étudié pour chaque scénario afin de rechercher d'éventuels précurseurs. Cette étude permettra entre autre d'établir une potentielle connexion tout au long de l'hiver entre les différentes couches.

# 6 - Couplage stratosphère-troposphère et précurseurs des scénarios

## 6.1 . Introduction

La nouvelle classification établie précédemment est exploitée afin d'étudier le couplage stratosphère-troposphère pour chaque scénario. L'intérêt est tout d'abord de confirmer que les scénarios déterminés représentent des évolutions singulières de l'état de l'atmosphère et pas seulement de la circulation stratosphérique. Ensuite, l'idée est de rechercher les précurseurs des scénarios dans les premiers mois de l'hiver et les potentiels impacts sur le climat troposphérique suivant l'apparition des échauffements.

Concrètement, l'étude du couplage entre les couches est réalisée en analysant les indices du mode annulaire nord, comme initié par Baldwin and Dunkerton (2001) (voir Figure 1.10), afin de capturer le principal mode de variabilité en hiver. Ainsi, les évolutions de ces indices donnent une visualisation de l'influence mutuelle des couches, notamment lors de l'apparition des échauffements stratosphériques soudains. L'avantage est de pouvoir comparer ces différentes évolutions avec celles reportées notamment dans Mitchell et al. (2013) afin d'évaluer l'importance de la géométrie du vortex polaire, soit déplacée ou scindée, dans le mécanisme de descente de l'anomalie stratosphérique post-échauffement.

Également, l'évolution de la divergence du flux d'Eliassen-Palm dans la troposphère et la stratosphère sera étudiée afin de confirmer les comportements dynamiques trouvés pour les différents scénarios. Enfin, les anomalies mensuelles de géopotentiel et de température au sol seront montrées pour chaque scénario afin de confirmer la potentielle présence de précurseurs et les impacts générées par les échauffements notamment via l'apparition ou non des phases négatives de l'oscillation Arctique nord.

## 6.2 . Article

L’article ci-dessous a été soumis au « Journal of geophysical research » dans la catégorie « Atmospheres ».

# Examination of the Stratosphere-Troposphere Coupling Over Winter Months With a Classification Based on the Timing of SSW events

**A. Mariaccia[1], P. Keckhut[1], and A. Hauchecorne[1]**

[1]Laboratoire Atmosphères, Milieux, Observations Spatiales, UMR 8190, Institut Pierre-Simon Laplace, Université Versailles-Saint Quentin, Université Paris-Saclay, 78280 Guyancourt, France.

**Key Points:**

- Distinct wave activity signals are diagnosed into both the troposphere and the stratosphere for each scenario.
- Each scenario possesses unique stratosphere-troposphere interaction in winter.
- Surface precursors in perturbed scenarios emerge in early winter, especially December.

Corresponding author: Alexis Mariaccia, alexis.mariaccia@latmos.ipsl.fr

**Abstract**

We have conducted an investigation into the coupling between the stratosphere and troposphere, focusing on perturbed and unperturbed scenarios of the northern hemisphere polar vortex. These scenarios were established in a previous study, which categorized the main winter typologies based on the timing of sudden stratospheric warmings (SSWs) and final stratospheric warmings (FSWs). Here, we further analyze the mass-weighted divergence of the Eliassen-Palm (EP) flux to confirm the association between these scenarios and the specific timing of momentum and heat flux deposition by planetary waves. Our analysis reveals that wave-1 and wave-2 contributions to this divergence confirm distinct wave activity effects in relation to these scenarios. Additionally, examining the evolutions of the Northern Annular Mode (NAM) provides further insight, demonstrating that these scenarios represent unique states of both the stratosphere and troposphere, which can mutually influence each other during the winter months. Of particular interest is the observation of descending stratospheric anomalies into the troposphere following SSWs, often accompanied by a negative phase of the Arctic Oscillation (AO). Notably, we have found interesting surface signals associated with perturbed scenarios in early winter, especially in December. These surface precursors display wave-like patterns that align with the diagnosed wave activity in the upper stratosphere. This finding establishes a potential connection between early winter tropospheric conditions and upcoming stratospheric states. Consequently, our results enhance our ability to anticipate the behavior of the polar vortex and its eventual surface impacts, thus holding significant implications for sub-seasonal to seasonal forecasts in the northern hemisphere.

## Plain Language Summary

The stratosphere-troposphere coupling is a dynamic and important area of research, as it is widely recognized that the interactions between the stratosphere and troposphere significantly impact each other, particularly during the winter season. It has been established that accurately representing this coupling in climate models can lead to improvements in weather forecasting. One prominent phenomenon that exemplifies this coupling is sudden stratospheric warming (SSW), which occurs due to interactions between planetary waves and the mean flow in the stratosphere. SSW events can have notable effects on the surface, including potential shifts in extra-tropical storm tracks and the occurrence of severe cold-air outbreaks. Given the significant impacts of SSWs, the scientific community has been actively working towards classifying these events based on their characteristics and impacts. In a previous study, a novel classification scheme was introduced, which identified four distinct scenarios for the northern hemisphere polar vortex based on the timings of SSWs and final stratospheric warmings (FSWs). In this paper, we aim to evaluate the stratosphere-troposphere coupling for each of these scenarios during the winter months, with the goal of identifying potential associated precursors.

## 1 Introduction

The understanding of stratosphere-troposphere coupling is a crucial aspect of improving seasonal weather predictions in atmospheric sciences (Sigmond et al., 2013; Domeisen et al., 2020). This field of research has gained significant attention due to the recognized mutual influence between the stratospheric polar vortex and the tropospheric circulation during the northern hemisphere winter (Waugh et al., 2017). One of the key models, developed by Matsuno (1971), explains that variations in the strength of the wintertime stratospheric circulation are a result of the interaction between the mean flow and upward propagating planetary waves that transport westward momentum from the troposphere. These interactions can give rise to sudden stratospheric warming (SSW) events, characterized by increased polar cap temperatures, weakened polar vortex, and even the reversal of westerly winds in extreme cases (Butler et al., 2017). The subsequent stratospheric circulation anomalies

can descend into the troposphere, influencing surface weather patterns over several weeks (Baldwin & Dunkerton, 2001; Waugh et al., 2017). Additionally, equatorial stratospheric cooling can also occur as a result of these events (Fritz & Soules, 1970; de Wit et al., 2015). Proposed mechanisms responsible for the downward propagation of stratospheric anomalies have been summarized in previous studies by Tripathi et al. (2015) and Kidston et al. (2015).

The northern hemisphere annular mode (NAM) is a commonly used measure for assessing stratosphere-troposphere coupling during SSW events (Baldwin & Thompson, 2009). Baldwin and Dunkerton (2001), for example, computed NAM indices from weak and strong vortex composites and observed that these events are often followed by negative and positive phases, respectively, of the Arctic Oscillation (AO) pattern at the surface, which can persist for up to two months. The stratospheric anomaly propagating downward has numerous consequences for tropospheric weather, including shifts in storm track locations, changes in the likelihood and intensity of mid-latitude storms, variations in the frequency of high-latitude blocking events, and the occurrence of cold air outbreaks across the hemisphere (Thompson & Wallace, 2001). However, it is worth noting that not all SSW events result in a systematic tropospheric response (Sigmond et al., 2013), and the same is true for final stratospheric warming (FSW) events (Butler & Domeisen, 2021). Therefore, there has been ongoing research in the scientific community to classify SSW and FSW events and understand the factors that determine their different impacts on tropospheric circulation.

Traditionally, extreme SSW events have been classified as "major" based on the reversal of westerly winds at 10hPa-60°N (Butler et al., 2015). However, even though being a relevant metric for detecting a perturbed polar vortex (Butler & Gerber, 2018), this criterion alone does not indicate whether the stratospheric anomaly propagates downward. Other studies have classified SSW events based on the geometry of the polar vortex, distinguishing between displaced and splitting types (Charlton & Polvani, 2007; Cohen & Jones, 2011; Seviour et al., 2013; Mitchell et al., 2013).

Although Mitchell et al. (2013) found that splitting types tend to propagate downward compared to displacement types, aligning with the upward fluxes of wavenumbers 1 and 2 observations of Nakagawa and Yamazaki (2006), this statistical difference was not consistently retrieved by Charlton and Polvani (2007) and Lehtonen and Karpechko (2016). This inconsistency was also reported in Maycock and Hitchcock (2015) confirming that the polar vortex geometry is not an optimal predictor of tropospheric impacts following SSWs. It is similar for the wave geometry criterion as downward impacts can occur after both wave-1 and wave-2 SSW events, as seen in the SSWs of January 2009 (wave-2 type) and January 2010 (wave-1 type) (Ayarzagüena et al., 2011; Kodera et al., 2015).

While some studies have directly classified SSWs based on their tropospheric responses, such as absorbing or reflecting types (Kodera et al., 2016), the persistence of stratospheric anomalies (Runde et al., 2016; Karpechko et al., 2017), or surface observations of the North Atlantic Oscillation (Domeisen, 2019) and North Atlantic storm track response (Afargan-Gerstman & Domeisen, 2020). Thus, these different researches highlight the trickiness in finding the most robust criteria responsible for the tropospheric responses occurring after SSWs. Nevertheless, even though the mechanism responsible for the descending effect is still unclear, persistence of anomalies in the lower stratosphere seem to play a crucial role in this process (Black & McDaniel, 2004; Hitchcock et al., 2013; Karpechko et al., 2017).

On the other hand, FSW events have been classified based on their timing and nature, distinguishing between "early" and "dynamical" or "late" and "radiative" events (Waugh & Rong, 2002; Hauchecorne et al., 2022). The occurrence mechanism between mid-SSWs and early dynamical FSWs, both driven by waves, is similar (Vargin et al., 2020). In addition to its effects on transport and mixing of stratospheric ozone (Waugh & Rong, 2002; Butler & Domeisen, 2021), the timing of the FSW can exert an influence on the tropospheric circulation and the sea ice thickness through autumn (Kelleher et al., 2020).

Recently, Mariaccia, Keckhut, and Hauchecorne (2022) proposed a new classification based on empirical orthogonal functions of stratospheric zonal wind fluctuation patterns at the edge of the polar vortex. Their study suggests the existence of four scenarios followed by the northern hemisphere winter stratosphere. Three of them are modulated by the timings of important SSW events (ISSWs) lumping all SSW events for which the zonal mean zonal wind at 10 hPa-60°N became inferior to 10 $m.s^{-1}$ in mid-wintertime. The advantage of this criterion is to take into account, in addition to major SSWs, the warmings weakening significantly the polar vortex without reversing the wind (Maury et al., 2016). The last scenario represents winters without ISSWs but differing in the timing of FSW (dynamical and early or radiative and late). This novel classification focuses on the entire winter evolution rather than specific SSW or FSW events, and it establishes a connection between mid-winter and winter end, highlighting the existence of a stratospheric memory as previously highlighted by Hauchecorne et al. (2022).

Interestingly, Monnin et al. (2022) conducted research on the impact of SSW timing on tropospheric reactions in Europe. The findings indicate that SSWs occurring in December and January have a more significant surface impact compared to SSWs in February and March. Therefore, this study provides strong motivation for investigating the coupling between the stratosphere and troposphere during winter months using the classification established in Mariaccia, Keckhut, and Hauchecorne (2022).

The primary objectives of this study are twofold: first, to demonstrate that this classification represents not only the unfolding of wintertime stratospheric circulation at the edge of the polar vortex but also typical stratosphere-troposphere couplings in the northern hemisphere during winter, and second, to investigate whether stratospheric anomalies descend into the troposphere and manifest as surface signals throughout the winter season in the northern hemisphere. Additionally, the study aims to identify potential precursors at the surface in the months leading up to significant stratospheric anomalies, which could provide insights for seasonal predictability.

The structure of the paper is organized as follows. Section 2 presents the data extraction process from the ERA5 product, as well as the methods used to compute the NAM indices and the divergence of Eliassen-Palm flux in the stratosphere-troposphere. Section 3 describes the four scenarios and their respective dynamical characteristics. Sections 4 and 5 provide an analysis of NAM evolutions and surface impacts for the perturbed and unperturbed scenarios. Then, the impacts on surface temperature in early and late winter are examined in Section 6. Finally, Section 7 presents the summary and conclusions of the study, along with a discussion of its implications for seasonal predictability and future research directions.

## 2 Data and Method

### 2.1 ERA5 reanalysis

Since 2016, the European Centre for Medium-Range Weather Forecasts (ECMWF) has been generating a state-of-the-art reanalysis data set called ERA5. All the technical description of the ERA5 reanalysis can be found in Hersbach et al. (2020). Initially covering the period from 1950 to the present, the ERA5 reanalysis benefited in 2023 of a further extension back to 1940 (Copernicus, 2023). However, as this study is based on the classification established with the winters from 1950 to 2020, this last available decade is not exploited here.

According to Bell et al. (2021), the ERA5 reanalysis possesses an accurate depiction of the SSW in 1952 confirming its fidelity in the pre-satellite era. Furthermore, recent studies have demonstrated that ERA5 temperature reanalysis accurately reproduces observed temperatures and their variability within the upper stratosphere during winter (Marlton et al., 2021; Mariaccia, Keckhut, Hauchecorne, Claud, et al., 2022). However, the mesosphere is

not as well represented in ERA5. Consequently, the ERA5 data set is particularly suitable for studying stratosphere-troposphere coupling over decades, specifically during the winter season.

ERA5 data is available at 37 pressure levels, covering the entire troposphere-stratosphere region from 1000 to 1 hPa, with 11 levels between 100 and 1 hPa. For our analysis, we extracted the daily variables required to compute the Northern Annular Mode (NAM) indices and Eliassen-Palm flux from ERA5 reanalysis data at these pressure levels. Our analysis covers a 2.5°×2.5°grid from 20°N poleward and spans from 1950 to 2020, encompassing a total of 70 winters. To evaluate the surface impacts of each composite, monthly means of air temperature at two meters above the surface (2m temperature) as well as the mean sea level pressure (MSLP) were extracted from 40°N poleward over the studied period. The winter season in our analysis starts on November 1st and concludes on May 1st, spanning a period of 182 days.

### 2.2 Calculating the NAM indices

The Northern Annular Mode (NAM), also known as the Atlantic Oscillation (AO), is a key measure of dynamic variability over hemispheric scale during the winter season. It is computed by determining the leading empirical orthogonal function (EOF) that captures the dominant patterns of variability. The computation of NAM indices enables us to assess the influence of stratospheric variability on the spatial patterns observed in the troposphere.

Several methods exist for computing NAM indices, including surface-based EOFs, height-dependent EOFs, and zonal-mean EOFs. Each method has its advantages and drawbacks. The first two methods have limitations in capturing realistic annular variability in the middle atmosphere, as well as computational costs. In contrast, the zonal-mean EOFs method, as described by Baldwin and Thompson (2009), based on daily averaged, zonally averaged, year-round geopotential height, consistently captures annular variability structures and is employed in this study.

To calculate the daily NAM indices ($y_l^d$), the following equation is used:

$$y_l^d = \frac{\overline{Z_l^d} W e_l}{(e_l)^T W e_l}, \tag{1}$$

where $\bar{Z_l^d}$ represents the zonal mean of the daily geopotential anomaly, $W$ is a vector used to spatially weight the NAM indices (cosine of latitudes), and $e_l$ denotes the leading EOF of all zonal mean daily geopotential anomalies. Thus, we computed NAM indices for the 70 winters spanning from 1950 to 2020 using Equation 1. Subsequently, we averaged the daily NAM indices over the winters associated with each mode to obtain the mean time-height development of the northern annular mode.

By applying this approach, we can analyze the behavior of the NAM and its link to stratospheric variability, providing valuable insights into the stratosphere-troposphere coupling over the winter season.

### 2.3 The Wilcoxon signed-rank test

To test if the median of anomalies across years composing each scenario is nonzero, Wilcoxon signed-rank tests were conducted. Here, we defined the alternative hypothesis in order to test whether the distribution is statistically less or greater than a distribution symmetric about zero. By performing these tests, we can therefore determine whether the observed differences possess a median statistically negative or positive (Wilcoxon, 1945).

### 2.4 The divergence of Eliassen-Palm flux

The Eliassen-Palm (EP) flux is a vector that characterizes the direction of small atmospheric waves as well as the magnitude of eddy heat flux and momentum flux (Eliassen & Palm, 1961). It serves as a valuable diagnostic tool for investigating wave-mean flow interactions and, consequently, the coupling between the stratosphere and troposphere (Kuroda & Kodera, 1999). The divergence of the EP flux provides information about the acceleration or deceleration of the zonal mean zonal wind.

In this study, ERA5 data has been extracted onto pressure levels and latitude degrees, and the divergence of the EP flux is computed using the methodology described by Jucker (2021). This approach accounts for spherical geometry, the aspect ratio of the figures, and the units of the vector components. The components of the EP flux in pressure coordinates are calculated using the equations introduced by Andrews et al. (1983):

$$f_\phi = -\overline{u'v'} + \overline{u}_p \frac{\overline{v'\theta'}}{\bar{\theta}_p}, \tag{2}$$

$$f_p = \left( f - \frac{1}{a\cos\phi} \frac{\partial(\bar{u}\cos\phi)}{\partial\phi} \right) \frac{\overline{v'\theta'}}{\bar{\theta}_p} - \overline{u'\omega'}, \tag{3}$$

where the notation follows the conventional usage, and primes and overbars represent perturbations and zonal means, respectively. Subscripts $\phi$ and $p$ refer to partial derivatives with respect to latitudes and pressure levels. $f$ denotes the Coriolis parameter, and $a$ represents the radius of the Earth. The unit of $f_\phi$ is $\mathrm{m}^2/\mathrm{s}^2$, and assuming pressure is in hPa, $f_p$ is in $\mathrm{m} \cdot \mathrm{hPa}/\mathrm{s}^2$. To obtain the natural form of divergence on the ($\phi$, $p$) plane, it is necessary to express the EP flux components in the scale units for $\phi$ and $p$ on the diagram, as outlined by Edmon et al. (1980):

$$\mathbf{F} = \left( \hat{F}_\phi, \hat{F}_p \right) = \frac{2\pi}{g} a^2 \cos^2\phi \left( f_\phi, a f_p \right). \tag{4}$$

where $\mathbf{F}$ represents the EP flux components in the desired scale units. Finally, the mass-weighted divergence of $\mathbf{F}$ is simply given by $\partial_\phi \hat{F}_\phi + \partial_p \hat{F}_p$ and is expressed in units of $\mathrm{m}^3$. In this study, the anomaly of EP flux divergence is computed daily for each winter on all pressure levels throughout the analyzed period. The mean divergence anomalies associated with the four different scenarios are presented in the subsequent section. The contributions of wave-1 and wave-2 to the mean divergence anomaly for each scenario are also calculated and can be found in the appendix section. However, a detailed discussion of their contributions will be provided in the following section.

## 3 The Dynamics of the Four Vortex Scenarios

A recent study by Mariaccia, Keckhut, and Hauchecorne (2022) classified 61 out of the 70 winters between 1950 and 2020 into four scenarios representing typical polar vortex evolutions. These scenarios include the January mode (17 winters), the February mode (17 winters), the Double mode (7 winters), and the unperturbed polar vortex evolution consisting of the Dynamical Final Warming (DFW) mode (15 winters) and the Radiative Final Warming (RFW) mode (5 winters). The complete list of winters associated with each scenario can be found in Mariaccia, Keckhut, and Hauchecorne (2022). For the remainder of this study, we will focus separately on the DFW and RFW modes. Mariaccia, Keckhut, and Hauchecorne (2022) also found that each scenario exhibits distinct wave-1 and wave-2 activities in the middle stratosphere, consistent with zonal wind patterns over the winter months. However, as this investigation focused on a specific point in the northern hemisphere

stratosphere (10 hPa and 60°N), further analysis is needed to confirm these trends at other altitudes and latitudes near the polar vortex edge.

To better understand the interaction between waves and the mean flow, we calculated the mean mass-weighted divergence anomaly of Eliassen-Palm flux for winters associated with perturbed and unperturbed scenarios. Figures 1 and 2 in this study show the divergence anomalies for perturbed and unperturbed scenarios, respectively. The wave-1 and wave-2 contributions to this divergence are provided in the appendix (Figures A1 and A2). We also examined the zonal mean zonal wind and temperature evolutions and their respective spread between 50°N and 70°N at 10 hPa to assess the effects of the EP flux divergence. These zonal mean evolutions closely resemble those reported by Mariaccia, Keckhut, and Hauchecorne (2022) at 60°N-10 hPa, confirming that the typologies identified in the northern hemisphere stratosphere are widespread.

Significant signals are mainly detected in the upper stratosphere where planetary waves break and deposit their momentum (Plumb, 2002). Negative (positive) divergence values correspond to the deceleration (acceleration) of zonal winds and temperature increase (decrease) linked with SSWs and FSWs (polar vortex reinforcements), as expected. The findings validate the impact of wave-mean flow interactions on weakening the zonal stratospheric circulation and heating the stratosphere. Presumably, the extension and elevation of the disparity signal are accountable for the sudden deceleration of zonal wind recorded at 10-hPa. For example, the February pattern (see Fig. 1b) displays a more pronounced decrease in wind speed over time compared to other patterns due to a negative divergence signal that extends and persists into the lower stratosphere. It is worth noting that in November and December, the divergence anomaly signals just above the surface are mostly positive and negative for the January and February patterns, respectively. Importantly, this means the opposition of dynamical activity highlights the probable interactions between the stratosphere and troposphere in early winter, which are responsible for the timing of the upcoming ISSW.

In contrast, the divergences linked to the DFW and RFW modes (shown in Fig. 2) exhibit frequent oscillations between positive and negative values during the winter in the upper stratosphere. These oscillations, which involve short-term momentum and heat flux depositions, are believed to be responsible for the undisturbed winters experienced in these modes. Thus, it seems that to produce a significant impact on the stratospheric circulation, longer durations of wave-mean flow interactions that generate momentum and heat flux are required, as evidenced in the perturbed scenarios.

Regarding the troposphere, divergence signals are very noisy and difficult to interpret on Figures 1 and 2. While, Figures A1 and A2 show, on average, more readable signals bringing a more complete picture of the dynamical activity in the troposphere and the stratosphere over winter months. First of all, the previous trends observed and reported in Mariaccia, Keckhut, and Hauchecorne (2022) are more widely confirmed here. Indeed, it is evident that the divergence associated with wave-1 possesses systematically a stronger magnitude than the one associated with wave-2 suggesting the preponderant role of wave-1 on the general observed dynamics. Additionally, the contributions of wave-1 and wave-2 to the divergence evolutions align with the wave activity analysis performed for each scenario. Consistently, the ISSW events in January and Double modes are predominantly driven by wave-1 (Fig. A1a-b-e-f), while the February mode exhibits contributions from both wave-1 and wave-2 (see. Fig. A1c-d). In the same way, it confirms that the dynamical FSW in the DFW mode is essentially driven by wave-1 and slightly by wave-2 (Fig. A2a-b), while, the RFW mode is characterized by oscillations of wave activities in the upper stratosphere (Fig. A2c-d).

Importantly, Figure A1 provides new insights into the impacts of wave-1 and wave-2 in perturbed scenarios. It is noteworthy that divergence anomaly signals, particularly those linked with wave-1, have a tendency to descend over time. Interestingly, these anomalous

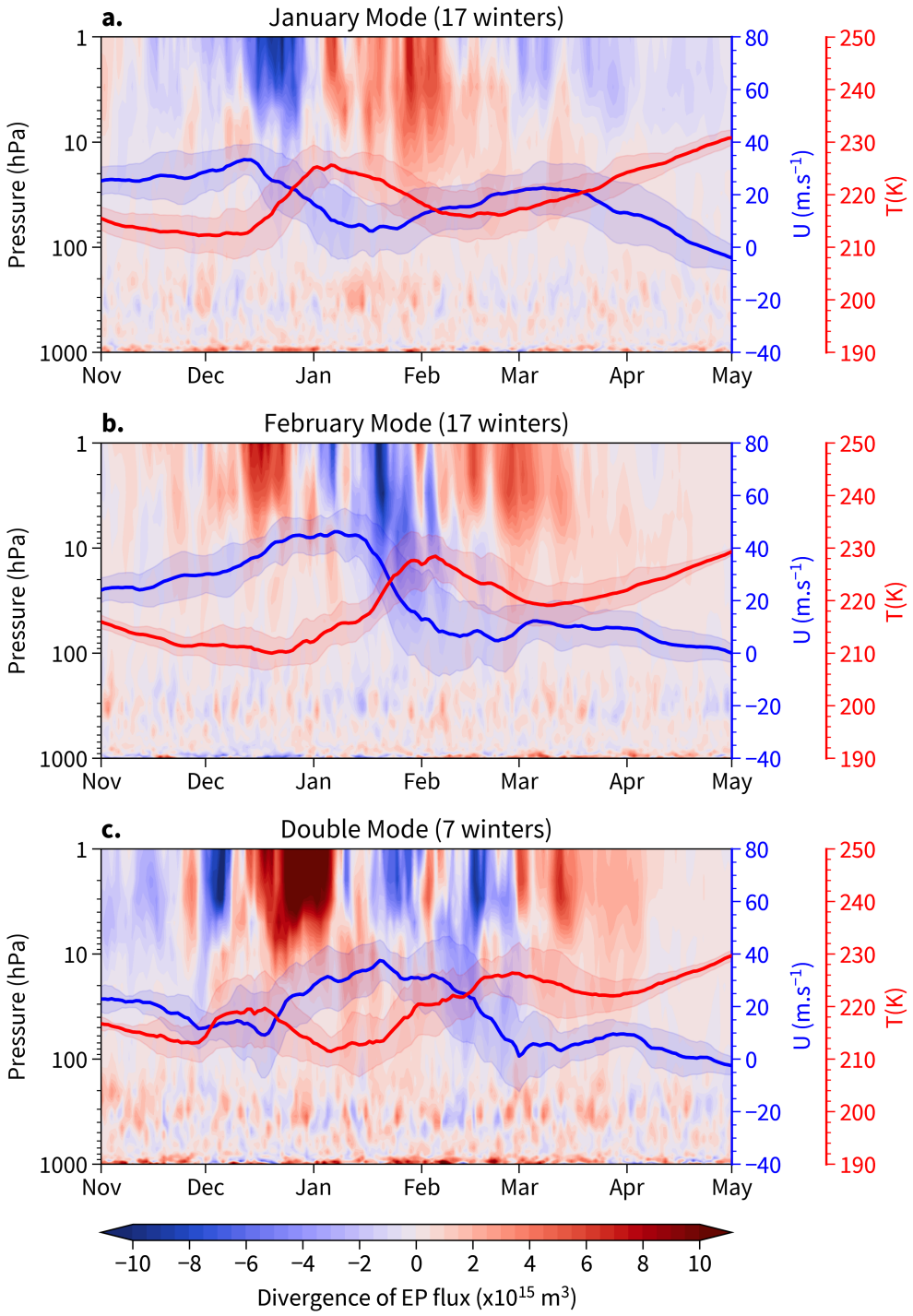


**Figure 1.** Mean time-height development of the anomaly of the mass-weighted divergence of Eliassen-Palm flux between 50 and 70°N for the three perturbed scenarios: the January Mode (a), the February Mode (b), and the Double Mode (c). Shaded negative (blue) and positive (red) values correspond to a deceleration and acceleration of the zonal wind, respectively. Solid blue and red lines represent mean evolution of zonal mean zonal wind and zonal mean temperature, respectively, computed over the latitude range 50-70°N at 10 hPa. Their respective shaded regions shows the associated standard deviation.

descents in January and Double modes extend to lower levels in the troposphere compared to those in the February mode. This finding suggests that the occurrence of ISSWs in winters linked to the February mode has a lesser impact on the troposphere compared to those in January and Double modes, which aligns with Monnin et al. (2022). Notably, comparable discrepancies are present between the upper stratosphere and the area around 350 hPa, particularly when a robust signal in the upper stratosphere is evident. This behaviour provides further evidence of the likely vertical connection between the stratosphere and the troposphere. Additionally, for both wave 1 and wave 2, there is an observable pattern of divergence signs that are often contradictory at approximately 650 hPa compared to those at approximately 350 hPa, indicating the presence of an anti-correlation within the troposphere.

Regarding the January mode, in December, it is clear that wave-1 and wave-2 possess opposite signals, indicating destructive interference in the upper stratosphere and the troposphere. Still in December, consistently with the first observations on Figures 1a-b, January and February modes display opposite wave-1 signals in the troposphere (Fig. A1a-c). More precisely, their respective tropospheric wave-1 signals show opposite alternative signs between the regions around 350 and 650 hPa. Another revealed novelty is the notable early tropospheric wave-2 signals in November for the February mode (Fig. A1d). Therefore, these early signals may be a precursor to the subsequent ISSW.

Regarding the unperturbed scenarios (Fig. A2), it is clear that the DFW and RFW modes possess distinct wave activity signals in both the stratosphere and troposphere all over the winter. Thus, these wave contributions hint that the FSW nature for winters without ISSWs is the result of very different dynamical behavior in the previous months. Unlikely the DFW mode, the RFW mode still displays oscillations in its wave-1 and wave-2 signals (Fig. A2c-d) and does not exhibit notable wave-1 signals in the troposphere before March (Fig. A2c). While, the DFW mode exhibits significant positive divergence anomaly both in the upper stratosphere and at 350 hPa in November and December (Fig. A2a). Noticeably, for the DFW mode, this first significant positive Wave-1 divergence anomaly found in the upper stratosphere propagates downward suggesting a potential impact in the troposphere in the following months. Noteworthy, still for the Wave-1 field, oppositely to the general observed trend, the DFW mode exhibits a positive divergence anomaly at 350 hPa in February whereas the signal is negative in the upper stratosphere. This result highlights that the wave effects in the troposphere are not systematically similar to those at the same period in the upper stratosphere but can be influenced by previous stratospheric anomalies.

Consequently, these new findings further support the previously reported dynamical behaviors and enhance our understanding of wave activities in different scenarios and their impacts on polar vortex evolutions. The observed tropospheric divergence signals in early winter can potentially indicate the divergence sign of the stratosphere and the timing of the upcoming SSW. Concretely, these results suggest that tropospheric wave activities in early winter can act as a predictor of the dynamical activity in the upper stratosphere in the following months. However, since the mean divergence anomaly signals are primarily located in the upper stratosphere, it is challenging to infer how momentum and heat flux anomalies affect the troposphere before and after the SSW's occurrence. Therefore, in the next section, we investigate the troposphere-stratosphere coupling by examining the NAM evolutions for each scenario.

## 4 Perturbed Vortex Scenarios

### 4.1 NAM evolutions

Figure 3 depicts the average time-height development of the NAM indices determined in the troposphere and stratosphere for the three disturbed situations: January, February, and Double modes. Solid black contour lines are present in the figure to indicate noteworthy

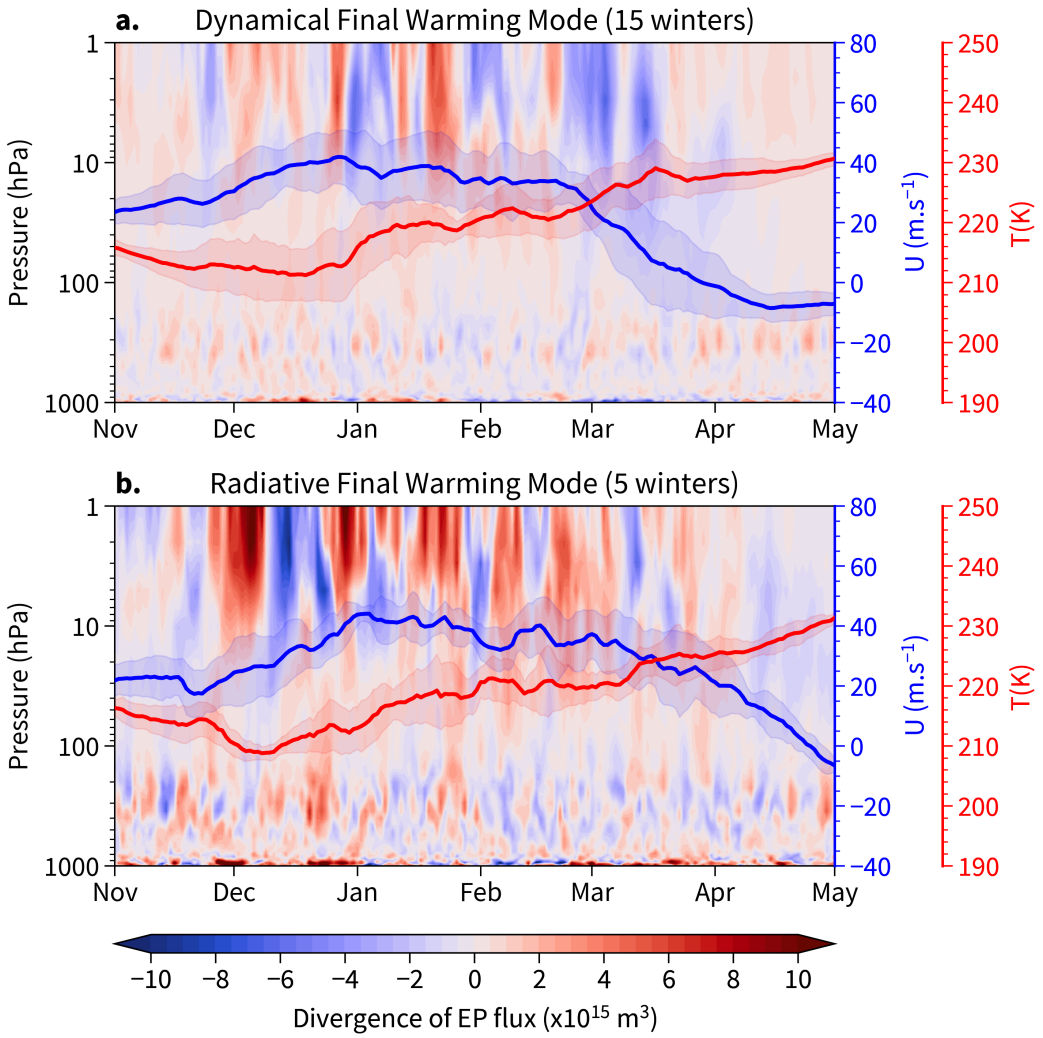


**Figure 2.** Mean time-height development of the anomaly of the mass-weighted divergence of Eliassen-Palm flux between 50 and 70°N for the two sub-modes composing the unperturbed scenario: the Dynamical Final Warming Mode (a) and the Radiative Final Warming Mode (b). Shaded negative (blue) and positive (red) values correspond to a deceleration and acceleration of the zonal wind, respectively. Solid blue and red lines represent mean evolution of zonal mean zonal wind and zonal mean temperature, respectively, computed over the latitude range 50-70°N at 10 hPa. Their respective shaded regions shows the associated standard deviation.

anomalies founded on the Wilcoxon signed-rank test. Feeble and warm polar vortex periods are manifested in red, and strong and cold periods in blue. These results are in line with earlier research that has shown that anomalies in the stratosphere possess longer time scales in contrast to fluctuations in the troposphere. Moreover, anomalies have a tendency to manifest initially in the upper stratosphere before descending downward (Baldwin & Dunkerton, 2001; Mitchell et al., 2013). Furthermore, anomalies that reach the lower stratosphere have a tendency to have longer durations compared to those in the upper stratosphere owing to the extended radiative time scale. Strong anomalies situated just above the tropopause demonstrate a greater chance of downward propagation into the troposphere, highlighting the crucial role played by this factor (Black & McDaniel, 2004). Notably, the NAM evolutions align with the divergence evolutions of EP flux observed in the perturbed scenarios (refer to Figure 1).

For the January mode (refer to Figure 3a), there are initial anomalies noticeable in early December, even though the area it covers is relatively small over a few days. These anomalies are positive, just above the tropopause, and negative at the surface. Towards the end of December, all levels of the stratosphere experience a simultaneous emergence of a significant positive anomaly associated with weak polar vortex events caused by an ISSW. This phenomenon propagates rapidly throughout the stratosphere with high significance between December and January, suggesting a potential wave resonance caused by barotropic mode excitation (Esler & Scott, 2005). It extends across the entire stratosphere and subsequently descends into the troposphere, reaching the Earth's surface notably in January. In February, a positive anomaly descends from the upper to lower stratosphere, with a slight rise at the tropopause which halts its propagation into the troposphere. Importantly, another positive anomaly occurs at the surface in late March, which could signify a delayed response within the troposphere to the strong positive anomaly observed earlier in March. Concurrently, a slight negative anomaly emerges in the upper stratosphere, cascading downwards to the lower stratosphere in April, but not pervading into the troposphere. The FSW, typically transpiring on or about April 20th (Mariaccia, Keckhut, & Hauchecorne, 2022), does not generate an intense signal in either the stratosphere or the troposphere. Thus, these results conform to the expected winter patterns linked with this scenario. This includes the occurrence of ISSWs in mid-January, followed by a minor strengthening of the polar vortex in March, with a conclusion in April. It is noteworthy that a mid- and upper stratospheric anomaly typically does not antecede the positive anomaly associated with the appearance of ISSWs in the final days of December. The lack of an anomaly can be attributed to the similarity in seasonal wave activity cycles up until mid-December for most winters (Mariaccia, Keckhut, & Hauchecorne, 2022), which results in a zero anomaly in the stratosphere at the start of winter. However, beyond mid-December, the mean wave activity linked to the scenarios starts to diverge. Nonetheless, the initial optimistic and pessimistic irregularities identified in early December above the tropopause and on the surface, respectively, may suggest early indications of the forthcoming ISSW.

In the case of the February mode (see Fig. 3b), a noticeable negative anomaly is found in the latter half of November above the tropopause for a few days. Thus, it is worth noting that the February mode starts oppositely to the January mode in the lower stratosphere region. Therefore, these significant negative deviations may represent first precursors of the timing of the following SSW. Then, a significant negative anomaly indicating strong polar vortex events emerges and covers simultaneously the entire stratosphere from mid-December to the end of January. Importantly, as this anomaly descends further toward the tropopause, it begins to significantly impact the troposphere, confirming the importance of this factor once again (Black & McDaniel, 2004). Subsequently, a positive anomaly primarily appears in the upper stratosphere at the end of January, with a tilted descending phase that later reaches the lower stratosphere, lasting until April. However, no significant descent into the troposphere is observed since the positive anomaly remains predominantly above 100 hPa, which is too high to affect the tropopause and enable downward propagation (Karpechko et al., 2017). Nevertheless, positive anomaly signals, whose only a small part is statistically

significant, emerge at the surface in March, suggesting a weak tropospheric response to this stratospheric anomaly on average. From March onward, a weak negative anomaly signal develops in the upper stratosphere, descending to the lower stratosphere, indicating the final formation of the polar vortex with weak winds before the occurrence of the FSW, often characterized by late and radiative events. Similar to the January mode, no significant deviation precedes the negative anomaly in December in the mid- and upper stratosphere, as explained earlier. Therefore, these findings align with the mean zonal evolution associated with the February mode, featuring a stratospheric circulation reinforcement in December and January, followed by a rapid zonal wind deceleration due to an ISSW occurring at the end of January, before a radiative FSW at the end of April.

Lastly, winters associated with the Double mode (see Fig. 3c) exhibit, on average, a positive anomaly in the troposphere from mid-November. Surprisingly, unlike the January and February modes, this anomaly appears to propagate upward from the surface and precedes another positive anomaly covering the entire stratosphere from mid-December, corresponding to the first ISSW's occurrence. This upward propagation suggests that the positive anomaly at the surface acts as a tropospheric precursor to the subsequent ISSW's appearance. Hence, this anomaly propagation exemplifies the bidirectional stratospheric-tropospheric dynamical coupling and its potential usefulness for seasonal-scale climate forecasts. The positive anomaly descends into the lower stratosphere and propagates into the troposphere from mid-January. Concurrently, a negative anomaly emerges in the upper stratosphere from the beginning of January, descending to the lower stratosphere by early February, indicating the reformation of the polar vortex. Starting from mid-February, a new positive anomaly emerges, covering both the stratosphere and troposphere until the end of March. Interestingly, the maximum positive anomaly is observed at low altitudes around 200 hPa, corresponding to the second ISSW's occurrence. Thus, similar to the previous two modes, these findings align with the unfolding of mean stratospheric winter circulation and wave activity for the Double mode (see Figure 1), featuring an initial ISSW in December, a subsequent one around the end of February, and a vortex restoration between the two. In April, a negative anomaly begins to develop in the upper stratosphere, corresponding to a tentative restoration of the polar vortex, which is interrupted by the FSW, often characterized by late and radiative events during this period. The absence of propagation of this negative anomaly suggests that the presence of tropospheric anomalies is unrelated.

In conclusion, these mean time-height evolutions of NAM indices indicate that these three perturbed scenarios possess distinct vertical structures influenced by the timings of ISSWs and FSWs. On the whole, positive anomalies generated by ISSWs tend to either cover simultaneously all levels in the stratosphere or to propagate downward progressively over one month to reach the lower stratosphere. Stratospheric anomalies generated by ISSWs in the January and Double modes descend more into the troposphere than those in the February mode. However, this behavior is not observed for FSWs, which are mostly radiative and do not tend to impact the troposphere significantly. Notably, both the stratosphere and troposphere exhibit weak signals in April. These findings affirm that the new classification determined in Mariaccia, Keckhut, and Hauchecorne (2022) not only represents different stratospheric wind scenarios but also repetitive typical spatial patterns that couple the stratosphere with the troposphere during Northern Hemisphere winters. In the next section, we will discuss the results and compare them to the past literature. Then, we will investigate the surface regions impacted in the Northern Hemisphere over the months for these three perturbed scenarios.

### 4.2 Discussion of NAM evolutions

Overall, the mean NAM evolutions associated with the perturbed scenarios bring a new interesting picture of the stratosphere-troposphere coupling enabling to discuss some factors thought to be important in the mechanism responsible for the propagation down to the surface. First and foremost, the descent and the persistence of the stratospheric

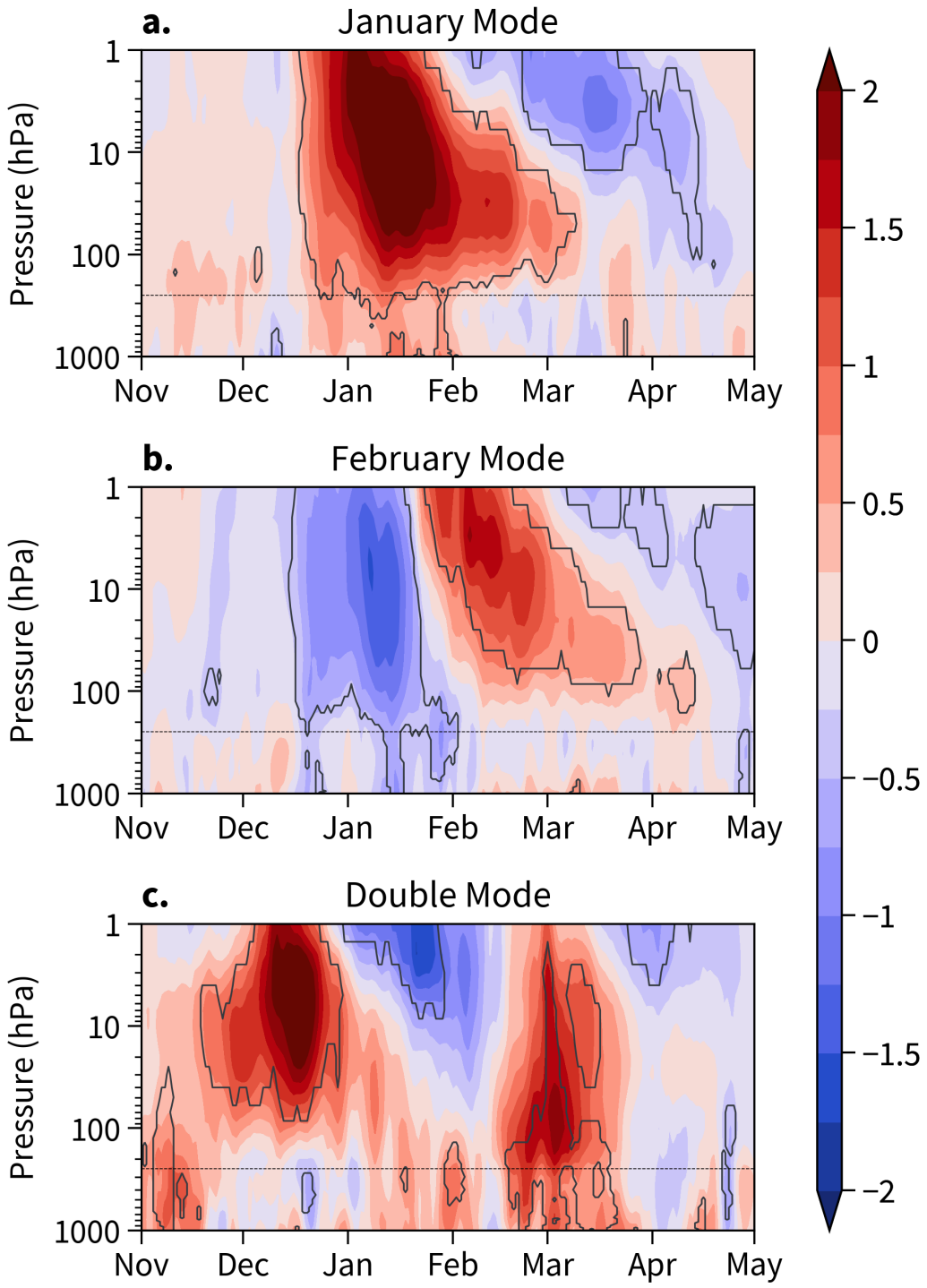


**Figure 3.** Mean time-height development of the northern annular mode indices for the winters associated with the three perturbed scenarios: the January Mode (a), the February Mode (b), and the Double Mode (c). The indices have daily resolution and are non-dimensional. Negative values (blue) corresponds to a strong polar vortex and positive values (red) to a weak polar vortex. The black lines contour areas with statistical confidence at the 95% level according to a Wilcoxon signed-rank test. The horizontal black dashed lines indicate the approximate delimitation between the troposphere and the stratosphere.

anomaly toward the tropopause, after an ISSW, appears crucial in order to penetrate into the troposphere as already underscored in previous studies (Black & McDaniel, 2004; Hitchcock et al., 2013; Karpechko et al., 2017).

One the other hand, interestingly, the NAM evolutions associated with the January and February modes align potentially with the conclusions drawn by Monnin et al. (2022) regarding the role of the timing of SSWs on the surface impacts. Indeed, as depicted on Figures 3, it is clear that ISSWs occurring in January are propagating more downward into the troposphere than ISSWs occurring later in February. Thus, it is likely that ISSWs occurring in January are followed by more pronounced surface impacts than ISSWs occurring later in February (Baldwin & Dunkerton, 2001). Therefore, this result potentially supports the role of the timing of ISSWs in the following tropospheric impacts reported in Monnin et al. (2022). According to the authors, early winter SSWs (Dec/Jan) experience more often stronger polar vortex anomalies since the stratospheric mean state is stronger than for late winter SSWs (Feb/Mar). However, although Monnin et al. (2022) found that early SSWs (Dec/Jan) do not propagate more downward than late SSWs (Feb/Mar), contrasting with our results, it is probable that this finding is the result of mixed winters belonging to the February and Double modes. Thus, an investigation of the correlation between downward propagation and surface impacts is needed to confirm this hypothesis. This point will be clarified in the sections 4.3 and 6 by studying the surface impacts over winter months for each perturbed scenario.

Finally, the January and February modes bear resemblance to the findings of Splitting and Displaced events in Mitchell et al. (2013) (see their Figure 4), respectively, and are also consistent with their seasonal distribution of splitting, displacement, and mixed events (see their Figure 3). However, the planetary wave activity related to these two scenarios, mainly wave-1 driven for the January mode whereas both wave-1 and wave-2 driven for the February mode, are in contradiction with this found agreement. It is therefore difficult to attribute a specific polar vortex geometry to winters associated with these scenarios without making assumptions with significant uncertainties. Moreover, as the splitting type's trend to impact more the troposphere than the displacement type seem to very sensitive to the SSW definition (Charlton & Polvani, 2007; Lehtonen & Karpechko, 2016; Maycock & Hitchcock, 2015), this feature appears to be less decisive than the persistence of the anomaly in the tropopause region (Karpechko et al., 2017) or potentially than the timing of ISSWs in predicting stratospheric anomaly descents and surface impacts.

### 4.3 Impacts on surface pressure

Figure 4 illustrates the evolution of monthly mean MSLP for the three perturbed scenarios from November to March. The stippled areas indicate the regions of highest significance according to the Wilcoxon signed-rank test.

For the January mode, it can be observed that winters begin in November with a few regions of high significance (see Fig. 4a): a positive anomaly over the Barents Sea and a negative anomaly in Western Europe. In December (see Fig. 4b), significant signals are found across the investigated area. Therefore, winters typically exhibit a pressure dipole with strong positive anomalies over Siberia and Asia, while significant negative anomalies cover the center and Northwest America. Interestingly, these surface signals display a wave-1-like pattern, coinciding with significant wave-1 activity diagnosed in the middle stratosphere before the occurrence of ISSWs for the January mode (see Fig. 8a in Mariaccia, Keckhut, and Hauchecorne (2022)). Thus, these results suggest that the surfaces patterns observed in November and December act as precursors to a specific wave-1 activity propagating upward from the troposphere and disturbing the stratospheric circulation, which in turn impacts the surface in the following months. This connection exemplifies the two-way troposphere-stratosphere coupling that takes place in the northern hemisphere during winter. In January (see Fig. 4c), which is when the ISSW is expected to occur for winters associated with this

mode, strong positive anomalies are observed at the pole and eastern Siberia, while negative anomalies are found in southern Europe and Northeast America. This pattern is typical of the negative phase of the AO generated after SSWs. It is consistent with the NAM indices showing a downward propagation of positive anomalies in January (see Fig. 3a). However, as emphasized by Lehtonen and Karpechko (2016), this signal is, in fact, the result of both the SSW and the regular weather anomaly present before the SSW. In February (see Fig. 4d), this positive anomaly signal extends further over northern Canada, while in March (Fig. 4e), it covers Iceland and a part of the Pacific, with an overall decrease in significance. Yet, according to the NAM evolution (Fig. 3a), no downward propagation due to the SSW in January occurs from February indicating that the troposphere evolves independently at this period. Consequently, the positive anomaly persisting at the pole until March is likely caused by this regular weather anomaly present initially in November and December. Supposedly, as the pressure anomalies exhibits wave-1 like patterns with a rotational motion over the months, it suggests the existence of a quasi-stationary wave-1 slowly propagating around the globe.

Regarding the February mode, surprisingly, opposite signals are observed compared to the January mode, particularly from November to January (Fig. 4f-g-h), confirming that these two modes possess very different initial surface conditions. In November, winters tend to have a negative anomaly over the Barents Sea, while a positive anomaly, is observed in Western Europe. In December, the previous negative anomaly covers a portion of Siberia, and another negative anomaly appears over the west of Greenland, while a positive anomaly is observed over the U.S. West Coast. Another positive anomaly is found over Western Europe but lacks high significance. Interestingly, this surface pattern exhibits a wave-2-like pattern, especially for the negative signals, aligning with the period when wave-2 activity in the stratosphere increases for this mode (Fig. 8b in Mariaccia, Keckhut, and Hauchecorne (2022)). Therefore, similar to the January mode, this surface pattern serves as an indicator of a future weak polar vortex generated by an ISSW in February. More generally, these results support the idea that November and December are crucial months for identifying and anticipating the occurring scenario. In January, a negative anomaly is present at the pole, while a positive anomaly is observed in western Europe. Again, this result aligns with the NAM indices computed for this mode, which indicate a descent of negative anomalies during this period. This pattern corresponds to the positive phase of the AO. Consistently with the NAM evolution obtained for the February mode (Fig. 3b), no significant signals are found in February when the ISSW is expected to occur (Fig. 4i), confirming that the anomaly does not reach the surface. Only a small positive anomaly signal in the Bering Sea tends to be recurrent in February, albeit with significance. Unlikely, in March (Fig. 4j), significant signals appear again with negative anomalies present over the north of the U.K. and Southwest America, while positive anomalies are found over Northeast America and Eastern China. As these signals have a Wave-2-like pattern, as seen in early winter, they may be caused by regular weather anomalies that are both a contribution of quasi-stationary Wave-1 and Wave-2 propagating in winter (Lehtonen & Karpechko, 2016). Therefore, these weak surface signals following the ISSW confirm that the overall troposphere evolves somewhat independently from the stratosphere. Additionally, these results are in agreement with the role of the timing of SSW on the following tropospheric impacts highlighted by Monnin et al. (2022) and argue in favor of the hypothesis discussed earlier as what the downward propagation near the tropopause also plays a role in this process.

Unlike the January and February modes, the Double mode exhibits strong signals in November (Fig. 4k), with a positive anomaly over the pole and the Barents Sea, while negative anomalies cover southern Europe and the Bering Sea. This pattern shares similarities with the one observed in December for the January mode, i.e., a wave-1-like pattern that can act as a precursor to the expected ISSW in the following month. In December (Fig. 4l), significant negative anomalies still with a wave-1-like pattern cover the North Atlantic Ocean and Eurasia, while a positive anomaly is present over the Bering Sea. Although

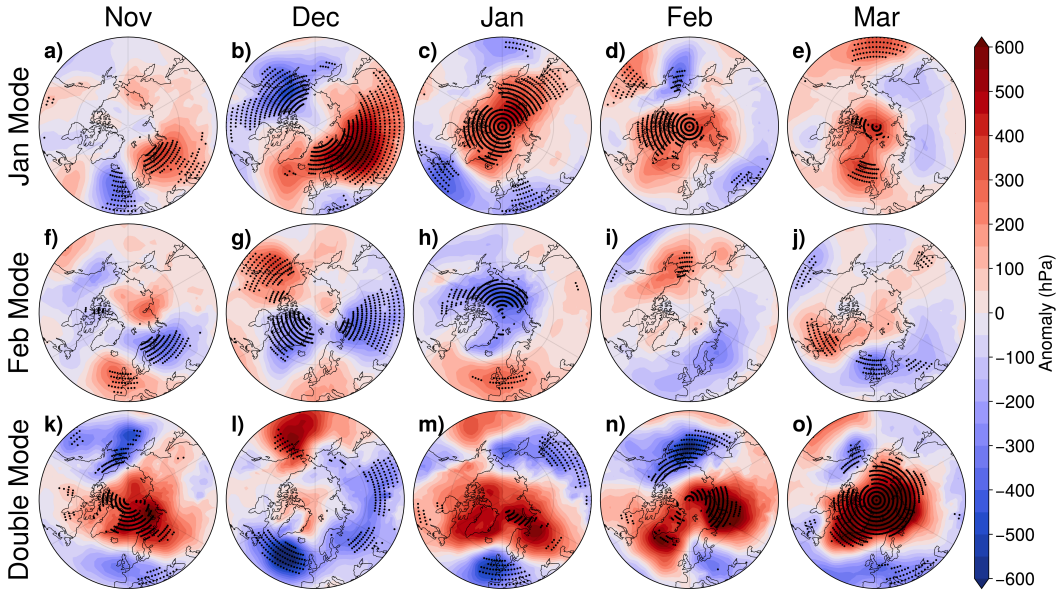


**Figure 4.** Monthly mean of MSLP anomaly from 40°N poleward in the northern hemisphere for the three perturbed scenarios from November to March. Blue and red shaded regions respectively correspond to negative and positive MSLP anomalies. Stippled areas show statistical confidence at the 95% level according to a Wilcoxon signed-rank test.

the first ISSW occurs in December, there is no immediate downward propagation of the positive anomaly, as shown in Figure 3c, where the descent into the troposphere occurs later in January and February. Consequently, these surface anomalies present in December probably represent the regular weather anomaly driving the surface patterns of winters associated with this mode. Then, a significant positive anomaly is found in January (Fig. 4m), covering North America, the pole, and the land around the Barents Sea, albeit with low significance. Meanwhile, negative anomalies are present in Western Europe and China. In February (Fig. 4n), a significant positive anomaly over northern Siberia suggests that the stratospheric anomaly finally reached the surface. Simultaneously, a significant negative anomaly is present over the Bering Sea. Finally, in March (Fig. 4o), a negative phase of the AO is observed again due to the effect of the second ISSW, with a significant positive anomaly covering the entire pole, Greenland, and a northern part of Siberia.

Thus, based on Figure 4, it is evident that these three perturbed modes exhibit distinct regular surface pressure anomaly before the occurrences of ISSWs. In addition, their surface pressure anomalies are differently impacted by ISSWs afterwards. For instance, there are similarities in the initial surface conditions and surface impacts between the January and Double modes, which are opposite to those observed for the February mode. Specifically, for the January and Double modes, a wave-1-like pattern is present at the surface in November and December, respectively, and the positive pressure anomaly tends to propagate from the stratosphere to the surface after an ISSW, generally inducing a negative phase of the AO. Surface anomalies are therefore driven by both regular pressure anomaly, probably caused by quasi-stationary Wave-1, and stratospheric anomaly generated by ISSWs. In contrast, the February mode displays a wave-2-like pattern at the surface in December and a positive phase of AO in January. The quasi absence of significant signals in February indicates that the troposphere evolves independently from ISSWs. However, in March, some significant Wave-2-like signals appear again meaning that ISSW and regular pressure anomalies have a late combined effect. Consequently, these perturbed scenarios exhibit precursors at the surface at the beginning of winter, particularly in December, which are likely responsible for

the observed wave activity in the stratosphere and, therefore, appear crucial for anticipating the subsequent stratospheric state. Regarding FSWs, their occurrence does not seem to significantly impact the surface, regardless of the perturbed mode, aligning with their NAM evolutions. The investigation of the unperturbed mode and its two sub-modes, DFW and RFW, is presented in the next section.

# 5 Unperturbed Vortex Scenario

## 5.1 NAM evolutions

Figure 5 presents the NAM indices for the DFW and RFW modes, following a similar format to Figure 3. In line with zonal wind evolutions (Fig. 2), both sub-modes exhibit a negative anomaly in the stratosphere, indicative of a persistent polar vortex that extends until the end of winter, finishing with either dynamical or radiative FSWs.

For the DFW mode (Fig. 5a), a negative anomaly forms on average in the stratosphere around 10 hPa starting in December. This negative anomaly propagates downward, gradually encompassing the entire stratosphere while intensifying until the end of February, reaching a peak around 30 hPa. The negative anomaly persists in the stratosphere until the end of February, at which point it initiates descent towards the troposphere, approaching the tropopause. Consequently, the negative anomalies reach the Earth's surface until the end of March. Interestingly, in early March, a positive anomaly appears at the top of the diagram. This positive anomaly corresponds to the occurrence of a dynamical FSW, which disrupts the polar vortex, resembling but with less intensity than the ISSWs observed in the three perturbed scenarios. Throughout March, this tilted positive anomaly propagates downward and reaches the lower stratosphere in April, but it does not significantly penetrate into the troposphere.

Regarding the RFW mode (Fig. 5b), weak but discernible anomaly signals are present in November, with a positive anomaly in the stratosphere and a negative anomaly in the troposphere. This positive anomaly descends while gaining strength, reaching the tropopause region and influencing the troposphere in December. Concurrently, a robust negative anomaly begins to form in the upper stratosphere. This negative anomaly propagates downward, covering the entire stratosphere from mid-January to mid-April while maintaining its intensity, indicating a persistently strong polar vortex throughout winter. From January to April, the tropospheric surface experiences the effects of this robust polar vortex, as anomalies persist just above the tropopause, facilitating their spread into the troposphere. It is important to note that this scenario represents the average evolution of only five winters, making this result statistically less robust than others. Notably, the surface is strongly influenced by the final stages of the wintertime stratospheric circulation in April, coinciding with the occurrence of the radiative FSW.

In the next section, we delve into the surface impact analysis for both sub-modes, examining the affected regions over the course of several months.

## 5.2 Impacts on surface pressure

Figure 6 illustrates the monthly mean MSLP anomay from November to April for both the DFW and RFW modes.

Regarding the DFW mode, in November (Fig. 6a), surface anomaly signals exhibit very significant statistically anomalies, albeit not with a strong magnitude, with negative signals over Siberia and Atlantic Ocean and positive signal in Pacific Ocean. In December (Fig. 6b), these significant negative and positive signals persist while being shifted above north-west Europe and Northern America, respectively. Noticeably, this pattern is similar to the dipole structure observed in the January mode but covering a shorter region with a lower magnitude. These early winter patterns constitute potential precursors of the absence

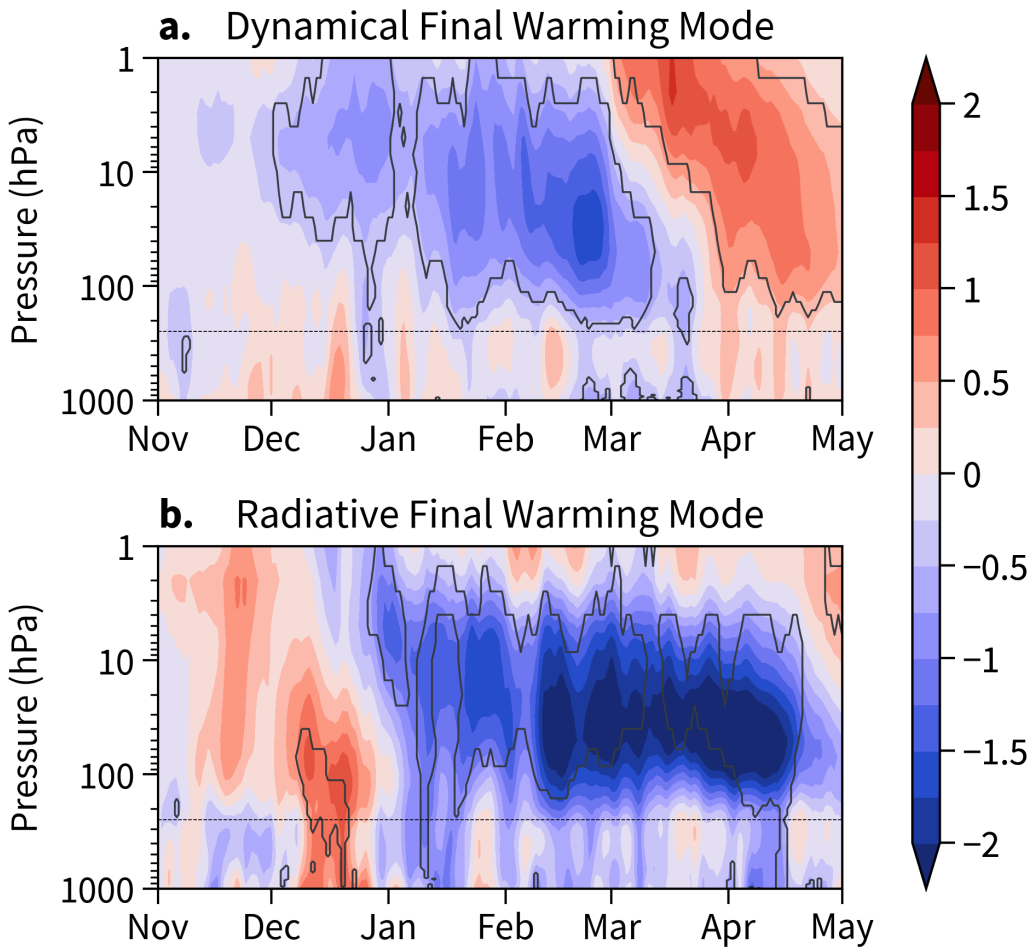


**Figure 5.** Mean time-height development of the northern annular mode indices for the winters associated with the two sub-modes composing the unperturbed scenario: the Dynamical Final Warming Mode (a) and the Radiative Final Warming Mode (b). The indices have daily resolution and are non-dimensional. Negative values (blue) corresponds to a strong polar vortex and positive values (red) to a weak polar vortex. The black lines contour areas with statistical confidence at the 95% level according to a Wilcoxon signed-rank test. The horizontal black dashed lines indicate the approximate delimitation between the troposphere and the stratosphere.

of occurrence of ISSWs in the following months. In January (Fig. 6c), these important harbingers disappear indicating that surface anomalies are probably neither driven anymore by regular surface anomaly and nor by stratospheric anomaly propagating into the troposphere. Then, significant anomalies are observed at the surface in February and March (Fig. 6d-e). In both months, a substantial negative anomaly is present at the pole and north of America, while a positive anomaly is observed in central Europe and northern Europe in February and March, respectively. Additionally, a notable negative anomaly tends to appear in the Pacific Ocean in March (Fig. 6e). Thus, these two months share a similar pattern, characteristic of a positive phase of the AO. The positive AO phase in the DFW mode is very likely induced by a downward propagation of stratospheric anomalies, confirming their connection with strong polar vortex events. Furthermore, the surface signal in the DFW mode exhibits a wave-1-like pattern, consistent with the wave activity diagnosed in the stratosphere during this period (Mariaccia, Keckhut, & Hauchecorne, 2022), indicating a vertical connection from the surface to the upper stratosphere. This persistent wave-1 activity is likely the cause of the dynamical FSW occurring before mid-April, similar to the disturbed scenarios. However, unlike wave-1-driven ISSWs occurring in January mode, the final pattern in April (Fig. 6f) is not influenced by the positive stratospheric anomaly generated by the dynamical FSW, as seen in the NAM evolution (Fig. 5).

Although the RFW mode is constructed with only five winters, it is still interesting to analyze the surface anomalies of this mode when significant signals spreading over large regions are found. Noticeably, the RFW mode exhibits significant positive anomaly signals over North America, Pacific Ocean and Greenland in November (Fig. 6g), different, albeit not opposite, to the signals found in the DFW mode at the same period. In December and January (Fig. 6h-i), only small regions are covered by statistically significant signals hampering to establish a real trend among the associated winters. In February (Fig. 6j), the signals start to dissociate sharply from the positive AO found in the DFW mode. Notably, we found two negative anomalies covering the Northern Europe and in the Pacific below the Bering Sea and positive anomalies over the Pacific near the U.S. west coast and in western Europe. In March (Fig. 6k), the preceding negative anomalies shift slightly to northern Europe and Russia's east coast, respectively, while the previous positive anomaly over western Europe diminishes, and the one in the Pacific moves westward and spreads over Alaska. Oppositely to the DFW mode, the RFW mode's NAM evolution suggests that the surface patterns in February and March are less affected by the stratosphere due to the less significant descent of anomalies during these months. Therefore, as for perturbed scenarios, these signals result potentially from a regular quasi-stationary wave shaping the surface temperature anomalies.

This hypothesis is strengthened with regard to the surface signal in March exhibiting a wave-2-like pattern that aligns with the peak of wave-2 activity found in the stratosphere during this period (Mariaccia, Keckhut, & Hauchecorne, 2022). This result also confirms the vertical connection through wave activity when the polar vortex is strong, characterized by westerly winds that enable planetary wave propagation. However, despite significant wave-2 activity in March, there is no generation of stratospheric anomalies associated with triggering an ISSW, supporting the essential role of wave-1, which exhibits low activity during this period. In April (Fig. 6l), a strong and significant negative anomaly is found at the pole, while positive anomalies are observed over the Bering Sea and the center of Siberia and China. This pattern reflects a positive phase of the AO, similar to what is found in February and March of the DFW mode. It aligns with the last observed anomaly descent in the NAM evolution. Beyond April, no further stratospheric anomalies are present due to the return of solar radiation, dissipating the polar vortex.

To summarise, the winters associated with the two sub-modes of the unperturbed scenario exhibit diverse surface pressure anomalies in November and comparable ones in the latter winter months. Nevertheless, there is a one-month time lag relating to the incidence date of the FSW. Notably, in November, the DFW mode demonstrates a negative anomaly

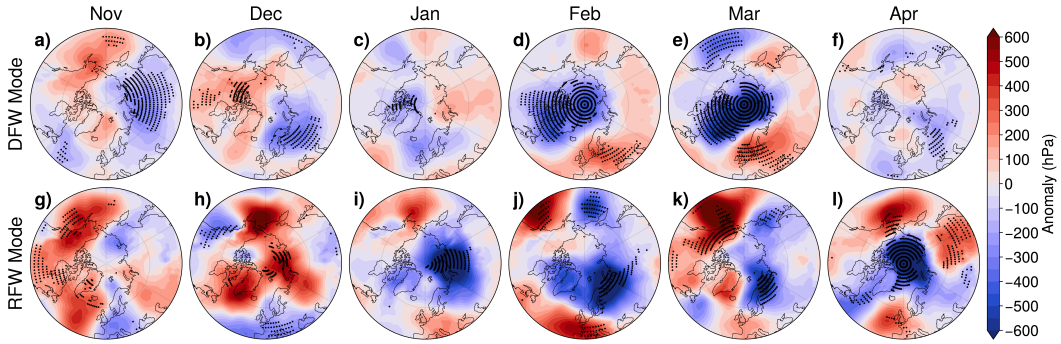


**Figure 6.** Monthly mean of MSLP anomaly from 40°N poleward in the northern hemisphere for the two sub-modes composing the unperturbed scenario from November to March. Blue and red shaded regions respectively correspond to negative and positive MSLP anomalies. Stippled areas show statistical confidence at the 95% level according to a Wilcoxon signed-rank test.

over Siberia, whilst the RFW mode displays a positive anomaly in Northern America. Although not conflicting, the varied trends in the initial surface anomalies imply that the polar vortex will maintain strength, potentially influencing the timing of the forthcoming FSW. Additionally, it is notable that a positive AO arises on the surface during FSW in both DFW and RFW modes. The surface patterns differ significantly from those acquired in the three perturbed scenarios at the same point, which exhibit either negative AO patterns after ISSWs or no noteworthy signals. Thus, the positive AO patterns detected in late winter months for the DFW and RFW modes indicate the vanishing of the polar vortex. This discovery validates that the timing and nature of FSWs are pivotal in comprehending the temporal shift in observed ground impacts. The next section explores the influence on the tropospheric climate by examining surface temperature anomalies for each scenario.

## 6 Impacts on Surface Temperature

To examine the impact of various scenarios on winter climate, which is critical for forecasting weather on a seasonal scale, we present the monthly average 2m temperature anomaly from December to March in the northern hemisphere for each scenario (see Fig. 7). Generally, negative (positive) temperature anomalies accompany positive (negative) pressure anomalies during the same period.

During November and December, it is unsurprising to discover opposing dipole signals in the January and February modes (Fig. 7a-b-f-g), which are consistent with the previously shown mean pressure anomaly for these months. Furthermore, December's surface signals indicate an intensification of the quasi-stationary wave responsible for observed temperature anomalies. In December, the January mode exhibits negative temperature anomalies ranging from -1 to -3 K across Eurasia, while positive anomalies of +1 to +2.5 K are observed in North America and Greenland (see Fig. 7b). It is worth noting that this temperature anomaly pattern over Eurasia in December presents similarities, but with higher significance, to the surface temperature anomalies found in the -30 to 0-day period before Displacement SSW events (Mitchell et al., 2013). By contrast, the February mode displays weaker signals (Fig. 7g), with temperature anomalies peaking at +1.5 K in Siberia and dropping to -1.5 K in North America.

Interestingly, the mean temperature anomaly patterns observed in December and January for the February mode (see Fig. 7g-h) do not correspond to the precursor stage for Displaced or Splitting events, suggesting a mixed signal. While for the Double mode, the

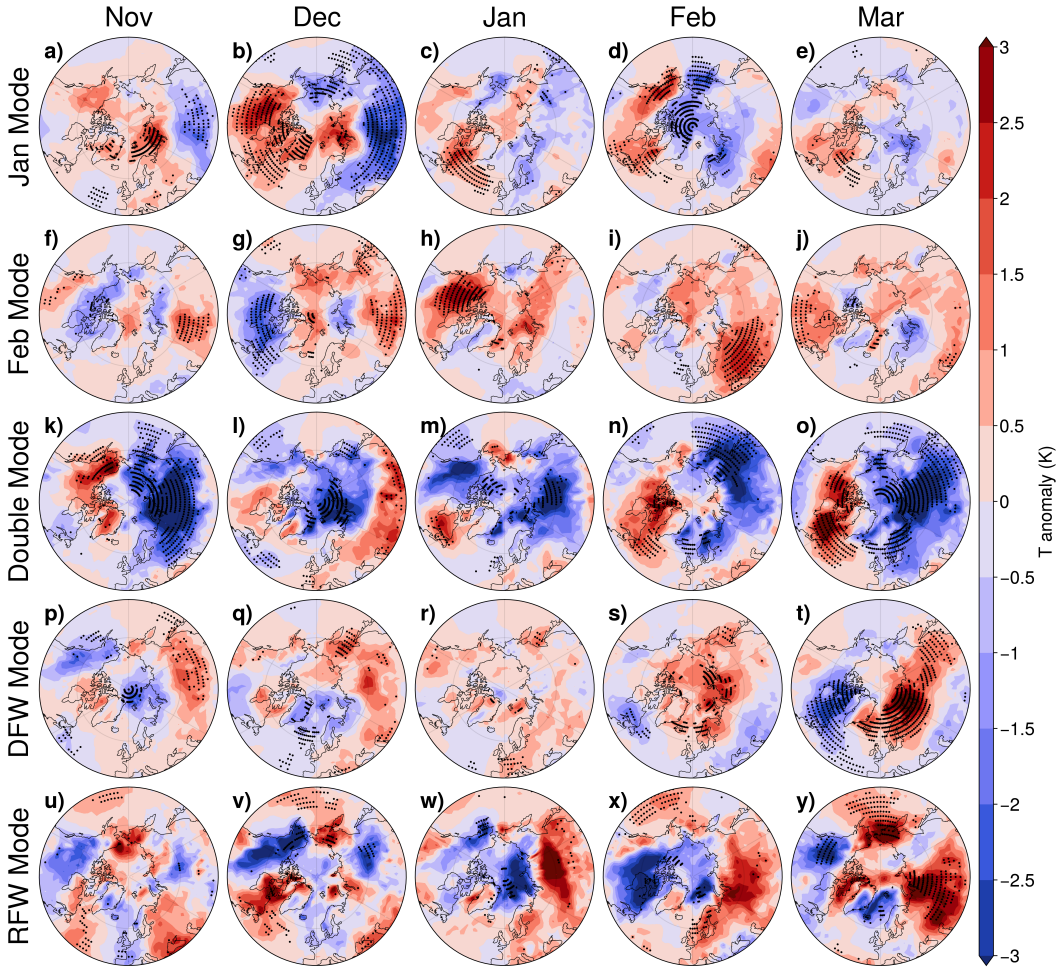


**Figure 7.** Monthly mean of 2m temperature anomaly from 40°N poleward in the northern hemisphere for each scenario in December and March. Stippled areas show statistical confidence at the 95% level according to a Wilcoxon signed-rank test.

temperature anomaly observed in November (Fig. 7k) is similar to the one observed in December for the January mode (Fig. 7b), but with stronger negative anomalies over a large part of Eurasia exceeding -3 K, and positive anomalies of +1.5 K mainly covering North West America and Greenland. Despite the weaker significance in December (Fig. 7l), the Double mode exhibits positive and negative temperature anomalies in the south and north of Siberia, respectively, indicating a warming of the Eurasia region when the first SSW of this scenario occurs in the stratosphere.

Therefore, these surface temperature patterns, similar to the MSLP anomaly patterns (Fig. 4), can be considered precursors of these perturbed scenarios, indicating that the upcoming northern hemisphere stratospheric state can be anticipated in early winter. These findings provide new insights with potential applications for seasonal prediction.

Subsequently, temperature anomalies evolutions in January, February and March months for the January and February modes display interesting patterns (Fig. 7c-d-e-h-i-j). While pressure anomalies display a strong negative AO both in January and February months for the January mode (Fig. 4c-d), associated temperature anomalies are, seemingly, only observed in February month with negative temperature anomalies over the pole (Fig. 7d). Differently, the February mode only exhibits positive temperature anomalies over Northwest America (+2.5 K) in January (Fig. 7h) and then over Eastern Europe (+2 K) in February (Fig. 7i), and finally again over North America (+1.5 K) in March (Fig. 7j), suggesting a rotation-like motion of this anomaly without any stratospheric influences. Thus, these different surface impacts confirm that ISSWs occurring in January impact more the tropospheric climate than those occurring in February. These results support therefore the role of the timing of ISSWs in the surface impacts as already reported in Monnin et al. (2022). Nonetheless, these results show that ISSWs in the January mode, even with an early timing, do not influence the surface temperature more than one month. Additionally, the regular surface temperature anomaly observed in the February mode suggest that overall the tropospheric weather is strongly influenced by initial surface anomalies throughout winter months.

In March, the January and February modes exhibit similarities but do not show mean temperature anomalies with high significance over large regions (Fig. 7e-j), suggesting that the surface climate at this period is no longer influenced by stratospheric anomalies, which aligns with the observed NAM evolutions (Fig. 3a-b). Hence, surface precursors can anticipate these two scenarios in December, but they are not indicative of a specific surface climate at the end of winter. It is noteworthy that their surface patterns in March are similar to those, not very different between them, observed for Splitting and Displacement events in their decay phase (Mitchell et al., 2013). Although not enabling to infer their mean associated polar vortex geometry, this result emphasizes that it is impossible with this classification to predict surface temperature anomalies from March for winters with a single warming.

Noticeably, the Double mode shows nearly identical surface signals in February and March (Fig. 7n-o) as those observed in November (Fig. 7k), but with positive temperature anomalies covering a larger area in North East America exceeding +2 K. Thus, the surface harbinger found in November associated with the Double mode is similar to the effect generated by the second SSW occurring at the end of February. Consequently, the Double mode is a unique mode with a strong impact on the northern hemisphere's surface climate from November to March.

Regarding the unperturbed scenario, a few statistically significant temperature anomalies are overall observed up to January for both sub-modes (Fig. 7p-q-r-u-v-w). Indeed, only the DFW mode seems to display notable positive temperature anomalies (+1.5 K) over Siberia in November (Fig. 7p) consistent with the negative pressure anomaly diagnosed previously at the same period (Fig. 6a). One can note that this signal bears similarities with the one of the February mode at the same month, even though, however, this

resemblance does not persist afterward. As a result, the DFW mode possesses a typical temperature anomaly in early winter that may play the role of a precursor of its FSW's nature and timing. Regarding the RFW mode, despite the positive pressure anomalies found over North America in November (Fig. 7g), the tropospheric temperature anomaly in first winter months does not follow any repetitive patterns. Consequently, the absence of temperature anomaly patterns similar to those found for the perturbed scenarios in early winter may indicate that the winter is following an unperturbed scenario. Testing these results by providing an example for the use in seasonal forecasting would be insightful, but is outside the scope of this study.

In February, the DFW mode starts exhibiting positive temperature anomaly (+1.5K) over the north pole (Fig. 7s) in agreement with the positive AO pattern found previously in 6d while the RFW mode still does not display significant signals (Fig. 7x). Finally, in March, the surface signals observed for the DFW and RFW modes (Fig. 7t-y) are somewhat opposite to those found for the Double mode (Fig. 7o) but similar to those observed in December for the February mode (Fig. 7g). The DFW mode shows a significant positive temperature anomaly exceeding +3 K over the Barents Sea region, ranging between 1 and 2 K in East Siberia, and negative anomalies averaging -1.5 K over North-East America (Fig. 7t). Similarly, the RFW mode exhibits positive anomalies exceeding +2.5 K on average over the center of Siberia and the Bering Sea region, while substantial negative temperature anomalies of -3 K and below are found over West America, Iceland, and Svalbard (Fig. 7y). Consequently, the similar temperature surface patterns between the DFW and RFW modes indicate that the type of final stratospheric warming does not determine a specific meteorological impact.

In general, these different early winter surface harbingers may provide information on the current and future stratospheric state confirming the importance of the tropospheric weather at this period in the upcoming winter stratosphere unfolding. In mid- and late winter, the tropospheric climate can undergo both the influence from downward propagating stratospheric anomaly and/or regular surface anomaly persisting throughout winter. These results bring therefore a new picture of the stratosphere-troposphere coupling in the northern hemisphere during wintertime with potential implications for seasonal forecasting.

## 7 Summary and perspectives

In this investigation, we analysed the coupling between the stratosphere and troposphere during the winter months of the four established winter stratosphere scenarios as outlined by Mariaccia, Keckhut, and Hauchecorne (2022). By analyzing the time-height evolutions of the mass-weighted divergence anomaly of the Eliassen-Palm flux, averaged in the latitude range of 50-70°N, we have found that the mean eddy heat and momentum flux primarily influence the upper stratosphere. Moreover, zonal mean temperature and zonal mean zonal wind evolutions at 10 hPa and averaged over 50-70°N are consistent with divergence signs found at this altitude. The analysis of contributions from Wave-1 and Wave-2 has shown the existence of clear tropospheric signals in early winter among the scenarios. Interestingly, opposing signals from Wave-1 occur in December between the January and February modes, revealing dynamic dissimilarities. Consequently, these divergent signals may suggest the initial signs of future dynamical activity in the stratosphere and, therefore, the timing of upcoming ISSWs. Additionally, they present distinct interferences between Wave-1 and Wave-2, either constructive or destructive, during ISSW events in both the stratosphere and troposphere. This finding underscores that ISSWs in these perturbed scenarios may be the result of different dynamical interactions.

Regarding the unperturbed scenario, we have identified frequent oscillations in the sign of the divergence in the upper stratosphere. These oscillations provide a physical explanation as to why the polar vortex remains strong during this scenario. Notably, the analysis of Wave-1 and Wave-2 contributions related to these sub-modes revealed that they possess

very different wave activity signals in both the stratosphere and troposphere. Noticeably, in early winter, the DFW mode exhibits a strong Wave-1 signal whereas the RFW mode displays oscillations. These results allude that early FSWs for winters without ISSWs can be potentially predicted by the dynamical behavior observed in the previous months in the troposphere. Although it is challenging to assess the mutual dynamical influence between the troposphere and stratosphere, these wave activity diagnoses enhance our understanding of the distinct dynamical behaviors exhibited by these scenarios and their impact on polar vortexes. Such inferences are crucial for potential simulations of these scenarios using mechanistic models.

We have also found that the time-height Northern Annular Mode (NAM) evolutions associated with each scenario align temporally with the phases of reinforcement and weakening of the polar vortex caused by ISSWs and FSWs. The discrepancies observed in these NAM evolutions, particularly in the descent of stratospheric anomalies caused by ISSWs or strong polar vortex events, provide confirmation that these stratospheric scenarios affect the troposphere differently throughout the winter. Moreover, consistent with most studies, our results suggest that downward propagation toward the tropopause is crucial for enabling the descent of stratospheric anomalies to the surface, irrespective of their sign. Importantly, these NAM evolutions also revealed significant signals in the troposphere in November and December that can represent precursors of the upcoming stratospheric states. In a broader sense, these outcomes verify that these scenarios not only represent a wind and temperature evolution at the edge of the polar vortex but also distinct stratosphere-troposphere couplings during the winter months in the northern hemisphere.

After examining the surface patterns of pressure and temperature anomalies, several important findings emerge regarding the precursors and tropospheric responses during winter for each scenario:

1. **January mode:**
   - In December, there is a dipole structure of mean pressure anomalies, with positive anomalies over Eurasia and negative anomalies over North-West America. This pattern is accompanied by mean temperature anomalies of -2 K over Eurasia and +2 K over North America. These wave-1-like surface patterns act as a precursor to the occurrence of an ISSW in January.
   - In January and February, a negative phase of the AO is observed at the surface due to the descent of positive stratospheric anomalies generated by the ISSW. Solely observed in February, this stratospheric penetration tends to generate cold air anomaly of -1.5 K over the north pole, northern Europe and Bering sea.
2. **February mode:**
   - In December, an opposite signal to the January mode is observed, with negative pressure anomalies over Siberia and West Greenland, and positive anomalies over the U.S. West Coast. This surface signal exhibits a wave-2-like pattern, acting as a harbinger of the ISSW in February. Associated temperature anomalies reach, on average, +1.5 K over Siberia and -1.5 K over North America.
   - In January, a positive phase of AO appears at the surface due to the descent of negative stratospheric anomalies, indicating the presence of a strong polar vortex. From February onwards, no significant signals indicate that the stratosphere no longer influences the surface.
3. **Double mode:**
   - In November, the mean pressure anomaly shows positive anomalies over the pole and the Barents Sea, and negative anomalies over southern western Europe and the Bering Sea. This signal shares similarities with the December pattern observed for the January mode. Associated with these anomalies are surface temperature anomalies exceeding -3 K over Eurasia and around +1.5 K over North West Amer-

ica and Greenland. These patterns exhibit a wave-1-like structure, acting as a precursor for the Double mode.

- In January and February, the first ISSW causes the descent of the stratospheric anomaly into the troposphere. This leads to positive pressure anomalies over Greenland and the Barents Sea, and negative anomalies over western Europe and China in January, and the Bering Sea in February.
- In March, the second ISSW generates a significant descent of the stratospheric anomaly, resulting in a substantial negative AO phase. This is associated with temperature anomalies exceeding +3 K over North East America and -3 K over Eurasia.

4. **DFW mode:**
   - In November, a negative pressure anomaly over Siberia associated to a positive temperature anomaly (+1.5 K) are found. The pressure signal in December is similar but not the temperature one.
   - In February and March, a positive AO phase is observed, accompanied by a positive pressure anomaly concentrated in Western Europe. In March, this surface pattern is associated with temperature anomalies exceeding +3 K over the Barents Sea region, and on average, +1.5 K over East Siberia. Negative anomalies of -1.5 K, on average, are found over North-East America.
5. **RFW mode:**
   - In November, a significant positive pressure anomaly is observed over North America, however, this signal is not associated with a marked temperature anomaly.
   - From February to March, a wave-2-like pattern emerges with positive pressure anomalies over the U.S. West coast and western Europe, and negative anomalies over the Barents Sea region and Siberia's East coast.
   - Finally, in April, a pronounced positive phase of the AO emerges when the polar vortex disappears.

We have discovered compelling indications during early winter, specifically in November and December, to suggest perturbed scenarios that may lead to subsequent stratospheric changes. Interestingly, in early winters the January and February modes demonstrate opposite surface patterns which align with the opposite divergence Wave-1 signals observed during the same time period. This confirms that they represent distinct atmospheric regimes. Our findings suggest that ISSWs occurring in mid-winter may be pre-conditioned in the preceding months. Additionally, on average, winter seasons displaying ISSWs followed by greater tropospheric impacts are associated with the January and Double modes. In contrast, winter seasons that exhibit independent tropospheric evolutions correspond to the February mode. These findings validate the significance of the timing of ISSWs in shaping surface impacts, which was emphasised earlier by Monnin et al. (2022), i.e. SSWs that occur in early winter months (Dec/Jan) have a more substantial effect on the surface than those occurring in later winter months (Feb/Mar). However, although there is propagation into the troposphere, it does not necessarily mean that it is solely or primarily caused by this stratospheric anomaly. Our findings reveal that tropospheric anomalies can also be caused by a quasi-stationary wave and, at times, by the descending stratospheric anomaly generated by ISSW. In terms of the undisturbed sub-modes, it should be noted that solely the DFW mode portrays repetitive pressure anomalies during early winter, albeit affecting surface temperature in November exclusively. On the other hand, the RFW mode does not demonstrate remarkable temperature anomalies extending over vast regions during early winter. As a result, although only the DFW mode exhibits marked early signals, identifying distinct precursors for these undisturbed modes is challenging. Nevertheless, they present similar strong surface impacts with a one-month time lag when the FSW arises. Therefore, our findings substantiate the significance of comprehending the timing of the FSW to enhance our understanding of how the undisturbed winter impacts the troposphere.

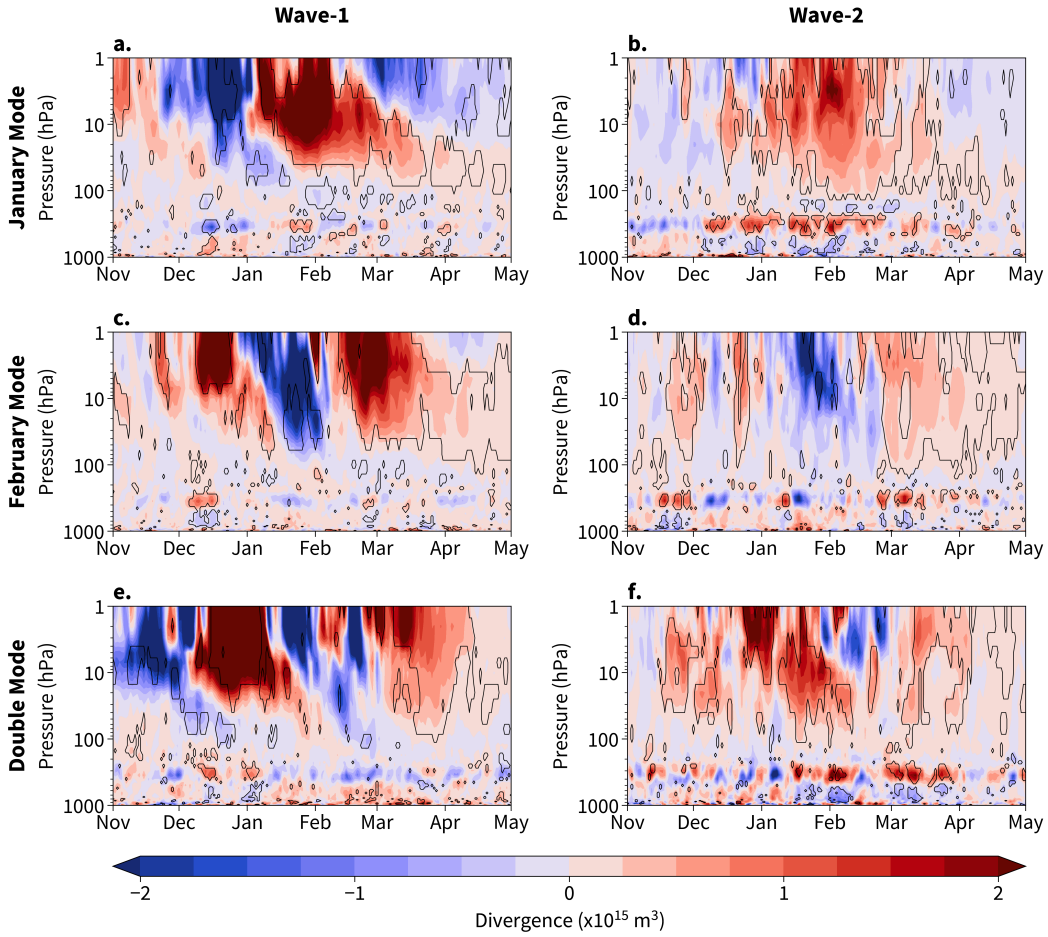


**Figure A1.** Contributions from Wave-1 and Wave-2 in the mean time-height development of the anomaly of the mass weighted divergence of Eliassen-Palm flux in the latitude range 50-70°N for the three perturbed scenarios. Shaded negative (blue) and positive (red) values correspond to a deceleration and acceleration of the zonal wind, respectively. The black lines contour areas with statistical confidence at the 95% level according to a Wilcoxon signed-rank test.

These findings significantly contribute to our understanding of stratosphere-troposphere coupling during the winter in the northern hemisphere, with potential applications for sub-seasonal to seasonal climate forecasts. Future research should employ mechanistic models to test whether these precursors and specific wave activities associated with each scenario can simulate ISSWs with the expected timing. Furthermore, investigating the causes of stratospheric anomaly entry into the troposphere would be beneficial. Additional investigations are necessary to better comprehend the triggers for each scenario, with one potential avenue being to explore links with sea ice concentrations and thicknesses at the beginning of winter.

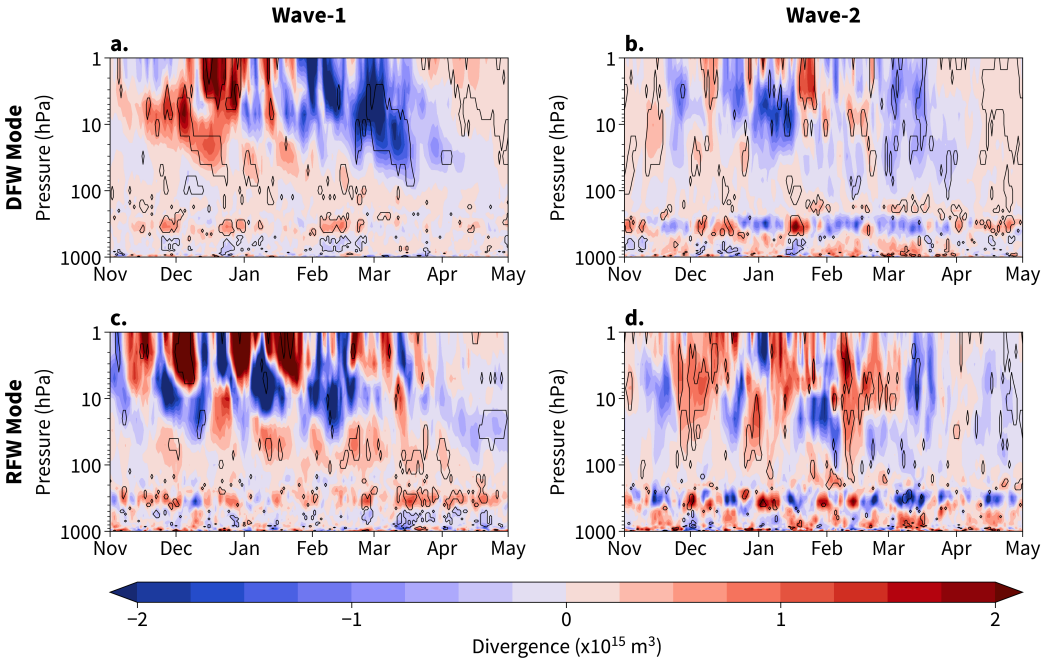


**Figure A2.** Contributions from Wave-1 and Wave-2 in the mean time-height development of the anomaly of the mass weighted divergence of Eliassen-Palm flux in the latitude range 50-70°N for the two sub-modes composing the unperturbed scenario. Shaded negative (blue) and positive (red) values correspond to a deceleration and acceleration of the zonal wind, respectively. The black lines contour areas with statistical confidence at the 95% level according to a Wilcoxon signed-rank test.

## Appendix A Contributions from Wave-1 and Wave-2 in the divergence of Eliassen-Palm flux

**Acknowledgments**

This work was performed within the framework of the European ARISE project and was funded by the French Educational Ministry with EUR IPSL. Copernicus Climate Change Service (C3S): ERA5: Fifth generation of ECMWF atmospheric reanalyses of the global climate. Copernicus Climate Change Service Climate Data Store (CDS), accessible at: `https://cds.climate.copernicus.eu/cdsapp#!/home`.

## References

Afargan-Gerstman, H., & Domeisen, D. I. V. (2020). Pacific modulation of the north atlantic storm track response to sudden stratospheric warming events. *Geophysical Research Letters*, *47*(2), e2019GL085007. doi: https://doi.org/10.1029/2019GL085007

Andrews, D. G., Mahlman, J. D., & Sinclair, R. W. (1983). Eliassen-palm diagnostics of wave-mean flow interaction in the gfdl "skyhi" general circulation model. *Journal of Atmospheric Sciences*, *40*(12), 2768 - 2784. doi: https://doi.org/10.1175/1520-0469(1983)040⟨2768:ETWATM⟩2.0.CO;2

Ayarzagüena, B., Langematz, U., & Serrano, E. (2011). Tropospheric forcing of the stratosphere: A comparative study of the two different major stratospheric warmings in 2009 and 2010. *Journal of Geophysical Research: Atmospheres*, *116*(D18). doi: https://doi.org/10.1029/2010JD015023

Baldwin, M. P., & Dunkerton, T. J. (2001). Stratospheric harbingers of anomalous weather regimes. *Science*, *294*(5542), 581-584. doi: 10.1126/science.1063315

Baldwin, M. P., & Thompson, D. W. (2009). A critical comparison of stratosphere–troposphere coupling indices. *Quarterly Journal of the Royal Meteorological Society*, *135*(644), 1661-1672. doi: https://doi.org/10.1002/qj.479

Bell, B., Hersbach, H., Simmons, A., Berrisford, P., Dahlgren, P., Horányi, A., ... Thépaut, J.-N. (2021). The era5 global reanalysis: Preliminary extension to 1950. *Quarterly Journal of the Royal Meteorological Society*, *147*(741), 4186-4227. doi: https://doi.org/10.1002/qj.4174

Black, R. X., & McDaniel, B. A. (2004). Diagnostic case studies of the northern annular mode. *Journal of Climate*, *17*(20), 3990 - 4004. doi: https://doi.org/10.1175/1520-0442(2004)017⟨3990:DCSOTN⟩2.0.CO;2

Butler, A. H., & Domeisen, D. I. V. (2021). The wave geometry of final stratospheric warming events. *Weather and Climate Dynamics*, *2*(2), 453–474. doi: 10.5194/wcd-2-453-2021

Butler, A. H., & Gerber, E. P. (2018). Optimizing the definition of a sudden stratospheric warming. *Journal of Climate*, *31*(6), 2337 - 2344. doi: https://doi.org/10.1175/JCLI-D-17-0648.1

Butler, A. H., Seidel, D. J., Hardiman, S. C., Butchart, N., Birner, T., & Match, A. (2015). Defining sudden stratospheric warmings. *Bulletin of the American Meteorological Society*, *96*(11), 1913 - 1928. doi: https://doi.org/10.1175/BAMS-D-13-00173.1

Butler, A. H., Sjoberg, J. P., Seidel, D. J., & Rosenlof, K. H. (2017). A sudden stratospheric warming compendium. *Earth System Science Data*, *9*(1), 63–76. doi: 10.5194/essd-9-63-2017

Charlton, A. J., & Polvani, L. M. (2007). A new look at stratospheric sudden warmings. part i: Climatology and modeling benchmarks. *Journal of Climate*, *20*(3), 449 - 469. doi: https://doi.org/10.1175/JCLI3996.1

Cohen, J., & Jones, J. (2011). Tropospheric precursors and stratospheric warmings. *Journal of Climate*, *24*(24), 6562 - 6572. doi: https://doi.org/10.1175/2011JCLI4160.1

Copernicus. (2023). *Hourly weather and climate snapshots now available from 1940.* Retrieved from `https://climate.copernicus.eu/hourly-weather-and-climate`

-snapshots-now-available-1940

de Wit, R. J., Hibbins, R. E., Espy, P. J., & Hennum, E. A. (2015). Coupling in the middle atmosphere related to the 2013 major sudden stratospheric warming. *Annales Geophysicae*, *33*(3), 309–319. doi: 10.5194/angeo-33-309-2015

Domeisen, D. I. (2019). Estimating the frequency of sudden stratospheric warming events from surface observations of the north atlantic oscillation. *Journal of Geophysical Research: Atmospheres*, *124*(6), 3180-3194. doi: https://doi.org/10.1029/2018JD030077

Domeisen, D. I., Butler, A. H., Charlton-Perez, A. J., Ayarzagüena, B., Baldwin, M. P., Dunn-Sigouin, E., ... Taguchi, M. (2020). The role of the stratosphere in subseasonal to seasonal prediction: 1. predictability of the stratosphere. *Journal of Geophysical Research: Atmospheres*, *125*(2), e2019JD030920. (e2019JD030920 10.1029/2019JD030920) doi: https://doi.org/10.1029/2019JD030920

Edmon, H. J., Hoskins, B. J., & McIntyre, M. E. (1980). Eliassen-palm cross sections for the troposphere. *Journal of Atmospheric Sciences*, *37*(12), 2600 - 2616. doi: https://doi.org/10.1175/1520-0469(1980)037⟨2600:EPCSFT⟩2.0.CO;2

Eliassen, A., & Palm, E. (1961). On the transfer of energy in stationary mountain waves. *Geofys. Publ.*, *22*, 1–23.

Esler, J. G., & Scott, R. K. (2005). Excitation of transient rossby waves on the stratospheric polar vortex and the barotropic sudden warming. *Journal of the Atmospheric Sciences*, *62*(10), 3661 - 3682. doi: https://doi.org/10.1175/JAS3557.1

Fritz, S., & Soules, S. D. (1970). Large-scale temperature changes in the stratosphere observed from nimbus iii. *Journal of Atmospheric Sciences*, *27*(7), 1091 - 1097. doi: https://doi.org/10.1175/1520-0469(1970)027⟨1091:LSTCIT⟩2.0.CO;2

Hauchecorne, A., Claud, C., Keckhut, P., & Mariaccia, A. (2022). Stratospheric final warmings fall into two categories with different evolution over the course of the year. *Communications Earth & Environment*, *3*(1), 4. doi: https://doi.org/10.1038/s43247-021-00335-z

Hersbach, H., Bell, B., Berrisford, P., Hirahara, S., Horányi, A., Muñoz-Sabater, J., ... Thépaut, J.-N. (2020). The era5 global reanalysis. *Quarterly Journal of the Royal Meteorological Society*, *146*(730), 1999-2049. doi: https://doi.org/10.1002/qj.3803

Hitchcock, P., Shepherd, T. G., & Manney, G. L. (2013). Statistical characterization of arctic polar-night jet oscillation events. *Journal of Climate*, *26*(6), 2096 - 2116. doi: https://doi.org/10.1175/JCLI-D-12-00202.1

Jucker, M. (2021). Scaling of eliassen-palm flux vectors. *Atmospheric Science Letters*, *22*(4), e1020. doi: https://doi.org/10.1002/asl.1020

Karpechko, A. Y., Hitchcock, P., Peters, D. H. W., & Schneidereit, A. (2017). Predictability of downward propagation of major sudden stratospheric warmings. *Quarterly Journal of the Royal Meteorological Society*, *143*(704), 1459-1470. doi: https://doi.org/10.1002/qj.3017

Kelleher, M. E., Ayarzagüena, B., & Screen, J. A. (2020). Interseasonal connections between the timing of the stratospheric final warming and arctic sea ice. *Journal of Climate*, *33*(8), 3079 - 3092. doi: https://doi.org/10.1175/JCLI-D-19-0064.1

Kidston, J., Scaife, A. A., Hardiman, S. C., Mitchell, D. M., Butchart, N., Baldwin, M. P., & Gray, L. J. (2015). Stratospheric influence on tropospheric jet streams, storm tracks and surface weather. *Nature Geoscience*, *8*(6), 433–440. doi: https://doi.org/10.1038/ngeo2424

Kodera, K., Funatsu, B. M., Claud, C., & Eguchi, N. (2015). The role of convective overshooting clouds in tropical stratosphere–troposphere dynamical coupling. *Atmospheric Chemistry and Physics*, *15*(12), 6767–6774. doi: 10.5194/acp-15-6767-2015

Kodera, K., Mukougawa, H., Maury, P., Ueda, M., & Claud, C. (2016). Absorbing and reflecting sudden stratospheric warming events and their relationship with tropospheric circulation. *Journal of Geophysical Research: Atmospheres*, *121*(1), 80-94. doi: https://doi.org/10.1002/2015JD023359

Kuroda, Y., & Kodera, K. (1999). Role of planetary waves in the stratosphere-troposphere

coupled variability in the northern hemisphere winter. *Geophysical Research Letters*, *26*(15), 2375-2378. doi: https://doi.org/10.1029/1999GL900507

Lehtonen, I., & Karpechko, A. Y. (2016). Observed and modeled tropospheric cold anomalies associated with sudden stratospheric warmings. *Journal of Geophysical Research: Atmospheres*, *121*(4), 1591-1610. doi: https://doi.org/10.1002/2015JD023860

Mariaccia, A., Keckhut, P., & Hauchecorne, A. (2022). Classification of stratosphere winter evolutions into four different scenarios in the northern hemisphere. *Journal of Geophysical Research: Atmospheres*, *127*(13), e2022JD036662. doi: https://doi.org/10.1029/2022JD036662

Mariaccia, A., Keckhut, P., Hauchecorne, A., Claud, C., Le Pichon, A., Meftah, M., & Khaykin, S. (2022). Assessment of era-5 temperature variability in the middle atmosphere using rayleigh lidar measurements between 2005 and 2020. *Atmosphere*, *13*(2). doi: 10.3390/atmos13020242

Marlton, G., Charlton-Perez, A., Harrison, G., Polichtchouk, I., Hauchecorne, A., Keckhut, P., ... Steinbrecht, W. (2021). Using a network of temperature lidars to identify temperature biases in the upper stratosphere in ecmwf reanalyses. *Atmospheric Chemistry and Physics*, *21*(8), 6079–6092. doi: 10.5194/acp-21-6079-2021

Matsuno, T. (1971). A dynamical model of the stratospheric sudden warming. *Journal of Atmospheric Sciences*, *28*(8), 1479 - 1494. doi: https://doi.org/10.1175/1520-0469(1971)028⟨1479:ADMOTS⟩2.0.CO;2

Maury, P., Claud, C., Manzini, E., Hauchecorne, A., & Keckhut, P. (2016). Characteristics of stratospheric warming events during northern winter. *Journal of Geophysical Research: Atmospheres*, *121*(10), 5368-5380. doi: https://doi.org/10.1002/2015JD024226

Maycock, A. C., & Hitchcock, P. (2015). Do split and displacement sudden stratospheric warmings have different annular mode signatures? *Geophysical Research Letters*, *42*(24), 10,943-10,951. doi: https://doi.org/10.1002/2015GL066754

Mitchell, D. M., Gray, L. J., Anstey, J., Baldwin, M. P., & Charlton-Perez, A. J. (2013). The influence of stratospheric vortex displacements and splits on surface climate. *Journal of Climate*, *26*(8), 2668 - 2682. doi: https://doi.org/10.1175/JCLI-D-12-00030.1

Monnin, E., Kretschmer, M., & Polichtchouk, I. (2022). The role of the timing of sudden stratospheric warmings for precipitation and temperature anomalies in europe. *International Journal of Climatology*, *42*(6), 3448-3462. doi: https://doi.org/10.1002/joc.7426

Nakagawa, K. I., & Yamazaki, K. (2006). What kind of stratospheric sudden warming propagates to the troposphere? *Geophysical Research Letters*, *33*(4). doi: https://doi.org/10.1029/2005GL024784

Plumb, R. A. (2002). Stratospheric transport. *Journal of the Meteorological Society of Japan*, *80*(4B), 793-809. doi: 10.2151/jmsj.80.793

Runde, T., Dameris, M., Garny, H., & Kinnison, D. E. (2016). Classification of stratospheric extreme events according to their downward propagation to the troposphere. *Geophysical Research Letters*, *43*(12), 6665-6672. doi: https://doi.org/10.1002/2016GL069569

Seviour, W. J. M., Mitchell, D. M., & Gray, L. J. (2013). A practical method to identify displaced and split stratospheric polar vortex events. *Geophysical Research Letters*, *40*(19), 5268-5273. doi: https://doi.org/10.1002/grl.50927

Sigmond, M., Scinocca, J., Kharin, V., & Shepherd, T. (2013). Enhanced seasonal forecast skill following stratospheric sudden warmings. *Nature Geoscience*, *6*(2), 98–102. doi: https://doi.org/10.1038/ngeo1698

Thompson, D. W. J., & Wallace, J. M. (2001). Regional climate impacts of the northern hemisphere annular mode. *Science*, *293*(5527), 85-89. doi: 10.1126/science.1058958

Tripathi, O. P., Baldwin, M., Charlton-Perez, A., Charron, M., Eckermann, S. D., Gerber, E., ... Son, S.-W. (2015). The predictability of the extratropical stratosphere on monthly time-scales and its impact on the skill of tropospheric forecasts. *Quarterly Journal of the Royal Meteorological Society*, *141*(689), 987-1003. doi: https://doi.org/10.1002/qj.2432

Vargin, P., Luk'yanov, A., & Kiryushov, B. (2020). Dynamic processes in the arctic strato-

## 6.3 . Conclusions

Ces derniers résultats démontrent le caractère unique du couplage stratosphère-troposphère se produisant au cours de l'hiver pour chaque scénario. En effet, les évolutions des indices de NAM révèlent de fortes disparités entre les scénarios, notamment dans la descente de l'anomalie stratosphérique survenant après l'apparition d'échauffements. Il est intéressant de noter que la comparaison avec les résultats reportés par Mitchell et al. (2013) mènent à penser que la géométrie du vortex polaire n'est pas le critère déterminant dans la propagation de l'anomalie au sein de la troposphère. Par conséquent, le timing des échauffements apparaît décisif non seulement dans le déroulé de l'hiver mais également sur les impacts sur la circulation troposphérique (Monnin et al., 2022).

De plus, l'analyse de la divergence du flux d'Eliassen-Palm améliore notre compréhension de l'effet des ondes planétaires, ondes 1 et 2, sur la dynamique atmosphérique de chaque scénario au bord du vortex polaire. En effet, connaître les différentes contributions des ondes 1 et 2, accélérant ou décélérant, au renforcement ou affaiblissement du vortex polaire sont essentielles pour bien simuler les scénarios par des modèles. D'autre part, le bon accord temporel, notamment en début d'hiver, entre les structures en forme d'onde 1 ou 2 trouvées au sol sur les cartes d'anomalies de géopotentiel et les amplitudes d'ondes dans la stratosphère confirme la connexion verticale entre les couches. Tout particulièrement en Décembre pour les scénarios perturbés où les cartes au sol admettent des signaux significatifs qui représentent de potentiels précurseurs des échauffements se produisant les mois suivants.

Les précurseurs trouvés suggèrent ainsi que le déroulé de l'hiver est en quelque sorte décidé en début d'hiver. Ceux-ci établissent la connexion entre le début d'hiver et la fin d'hiver et entre la troposphère et la stratosphère.

Ces résultats renforcent notre capacité à anticiper le déroulé de l'hiver au sein de la troposphère et de la stratosphère pouvant aider à améliorer la prévision à l'échelle saisonnière dans l'hémisphère nord. Dans la prolongation de ce travail, l'utilisation de

modèles mécaniques est nécessaire afin de tester la force de ces précurseurs en essayant de simuler des échauffements avec le bon timing.

Néanmoins, de futures recherches restent à mener pour comprendre les causes principales responsables du déclenchement des scénarios ou encore des conditions favorables à propagation ou non de l'anomalie stratosphérique au sein de la troposphère.

# Conclusions générales et perspectives

## 6.4 . Synthèse

Au fil de cette étude, notre intérêt s'est porté sur deux phénomènes résultant des interactions entre les ondes et l'écoulement moyen, et qui sont responsables de la majeure partie de la variabilité observée au sein de la moyenne atmosphère : les échauffements stratosphériques soudains (ESS) et les inversions de température mésosphériques (ITM). Cependant, il convient de noter que les données de température, caractérisées par une résolution verticale adéquate, se font rares pour décrire la moyenne atmosphère. Quant à la variable du vent, elle n'est observée que dans la basse stratosphère, principalement à travers les radiosondages, tandis que l'utilisation des fusées pour de telles observations a été interrompue dans les années 1990. Dans ce contexte, les données LiDAR se révèlent particulièrement précieuses, bien qu'elles ne soient disponibles que sur quelques sites.

Une évaluation de la capacité des réanalyses de dernière génération ERA5 à reproduire la variabilité observée dans la haute stratosphère et la mésosphère a été entreprise en les comparant à quinze années d'observations LiDAR de température acquises à l'OHP. Les résultats statistiques montrent que les réanalyses ERA5 sont excellentes dans la stratosphère en hiver où elles capturent avec une grande justesse la variabilité générale ainsi que celle générée par les échauffements. Ce résultat suggère entre autre une bonne assimilation d'observations et des bonnes paramétrisations au sein du modèle des interactions entre les ondes planétaires et l'écoulement moyen dans la stratosphère d'hiver où réside le vortex polaire. Cependant, cette aptitude n'est pas retrouvée dans la stratosphère d'été où la variabilité naturelle reste faible. De même, la variabilité de la mésosphère n'est jamais reproduite correctement par incapacité à simuler précisément les ITMs. Les principales causes sont avant tout l'absence d'observations assimilées dans

cette région par le modèle, la faible résolution d'ERA5 dans la mésosphère et la couche éponge située au-dessus de 50 km filtrant la propagation des ondes de gravité nécessaires à l'apparition des inversions mésosphériques. Cependant, les simulations des inversions mésosphériques dans les réanalyses ERA5, bien qu'imprécises, démontrent que leurs paramétrisations existent dans le modèle alors que le mécanisme d'apparition de ces événements n'est pas encore compris entièrement. Aussi, comme la plupart des théories proposées suggèrent que les ondes de gravité jouent systématiquement un rôle important dans l'apparition de ce phénomène, les résultats obtenus montrent que les réanalyses ERA5 peuvent reproduire l'effet associé à leur propagation.

Dans le but d'une documentation plus approfondie des inversions de température mésosphériques ainsi que d'une meilleure compréhension de leurs mécanismes de formation, nous avons rapporté des informations jusqu'alors absentes concernant les structures de vents dans la moyenne atmosphère au moment de la survenue de ce phénomène.

Ainsi, pour la première fois, des observations de vent-température co-localisées lors d'événements d'inversions mésosphériques ont été décrites dans ce travail. Les profils montrent qu'un fort ralentissement du vent zonal se produit systématiquement dans la même gamme d'altitude où la température croît. Ce résultat conforte l'idée introduite initialement par Hauchecorne et al. (1987) selon laquelle les ITMs seraient générées par le déferlement des ondes de gravité et leur transfert de quantité de mouvement associé.

De façon surprenante, les réanalyses ERA5 réussissent parfois à reproduire le ralentissement du vent lors de certaines inversions mésosphériques suggérant que le mécanisme est bien présent dans le modèle. Cependant, la plupart des événements restent mal ou pas simulés par le modèle. Néanmoins, les réanalyses ERA5 restent une excellente base de données pour étudier les échauffements stratosphériques soudains et leurs impacts sur la stratosphère et la troposphère d'hiver.

Le travail de mémoire stratosphérique que nous avons initié dans l'étude Hauche-

corne et al. (2022) a montré que la fin de l'hiver est influencée à la fois par l'apparition et par l'absence d'échauffement en milieu d'hiver. Cette étude a été poursuivie en diagnostiquant les principaux modes de variabilité des vents zonaux à 60°N-10hPa des 70 hivers allant de 1950 à 2020 extraits des réanalyses ERA5. Une nouvelle approche, prenant en compte l'ensemble des échauffements dits importants, englobant les échauffements majeurs et mineurs, a été entreprise afin de classifier les hivers selon leurs typologies. A l'issue de cette analyse, il apparaît que la stratosphère d'hiver tend à suivre quatre scénarios influencés par le timing des échauffements stratosphériques soudains et finaux. Trois de ces scénarios correspondent à des hivers dits "perturbés" au cours desquels des échauffements stratosphériques se sont produits en milieu d'hiver affaiblissant le vortex polaire. Le dernier scénario représente les hivers dits "non perturbés" au cours desquels le vortex polaire est resté fort et finissant généralement avec un échauffement final tôt et dynamique. Ces nouveaux résultats confirment notamment les conclusions établies par Hauchecorne et al. (2022), i.e., les hivers non perturbés tendent à avoir un échauffement final dynamique et que le vortex des hivers perturbés est anticorrélé avec son état 2-3 mois auparavant. De manière cohérente, les hivers ayant un ESS en janvier ont davantage d'échauffements finaux dynamiques que ceux avec un ESS en février finissant majoritairement radiativement. En effet, plus les échauffements de milieu d'hiver se produisent tardivement, moins le vortex polaire dispose du temps caractéristique nécessaire pour se reformer et permettre la propagation des ondes planétaires essentielles pour déclencher un échauffement final dynamique. Ces résultats soulignent ainsi l'importance du timing des échauffements stratosphériques dans le déroulé des hivers et permettent de connecter le milieu avec la fin d'hiver. L'examen de l'activité des ondes planétaires de nombre d'ondes 1 et 2 associée à chaque scénario révèle également le caractère singulier de leur comportement dynamique. De manière intéressante, les hivers ayant un ESS en janvier (février) semblent principalement pilotés par l'onde 1 (onde 1 et onde 2). De plus, la séparation des évolutions de l'onde 1 entre les différents scénarios au début du mois de

décembre suggère que les facteurs influençant le déroulé de l'hiver agissent dans les mois précédents. Cependant, la comparaison avec les précédentes classifications n'a pas permis d'établir une correspondance claire entre les scénarios et de spécifiques géométries de vortex polaire, soit déplacé ou scindé en deux tourbillons, ou de géométries d'ondes, ondes 1 ou 2, ou encore une certaine phase de l'oscillation sud de El Niño.

Dans le but de confirmer cette tendance naturelle de la stratosphère à suivre ces scénarios mais également cette connexion au sein de l'atmosphère tout au long de l'hiver, cette étude a été poursuivie. Pour cela, une analyse approfondie de la dynamique et du couplage stratosphère-troposphère au cours de l'hiver a été menée pour chaque scénario ainsi qu'une recherche d'éventuels précurseurs dans les premiers mois d'hiver. Tout d'abord, l'examen de la divergence du flux d'Eliassen-Palm associé aux scénarios a montré que les flux de chaleur et de quantité de mouvement influencent avant tout la haute stratosphère. De plus, l'analyse des contributions de l'onde 1 et onde 2 démontrent que les scénarios possèdent des régimes dynamiques distincts dès le début d'hiver à la fois dans la stratosphère et la troposphère. Ces résultats soutiennent l'idée d'un préconditionnement atmosphérique influençant la dynamique future de la stratosphère et d'une certaine façon le timing des échauffements stratosphériques dans les prochains mois.

Les évolutions des modes annulaires du nord démontrent que la connexion verticale entre la troposphère et la stratosphère au cours de l'hiver est propre à chaque scénario. En effet, les divergences observées dans les descentes des anomalies stratosphériques, générées soient par les échauffements stratosphériques importants ou des vortex polaires forts, confirment que la stratosphère et la troposphère sont impactées différemment en fonction des scénarios. Ces résultats confortent le caractère important du timing des échauffements, d'une part, sur l'évolution de la stratosphère et d'autre part sur les potentiels impacts à la surface suivant un ESS. Notamment, on trouve que les ESSs survenant en janvier se propagent davantage dans la troposphère que ceux se produisant

en février suggérant des réponses troposphériques plus fortes pour les ESSs de janvier. D'autre part, ces évolutions de modes annulaires du nord soulignent également l'importance de la propagation de l'anomalie vers la tropopause pour pénétrer ensuite dans la troposphère en accord avec les précédentes études (Black and McDaniel, 2004; Karpechko et al., 2017). La comparaison à nouveau avec les résultats de Mitchell et al. (2013) confirment l'impossibilité d'attribuer une spécifique géométrie de vortex polaire, déplacé ou scindé en deux tourbillons, à chaque scénario perturbé.

Enfin, l'analyse des champs moyens mensuels d'anomalies de pression et de température au sol au cours de l'hiver pour chaque scénario a révélé des structures significatives en début et en fin d'hiver révélant l'existence de précurseurs et, pour certains, de réponses troposphériques. Concernant les précurseurs, des signaux importants très significatifs sont présents en début d'hiver en novembre et en décembre, confortant l'idée reportée précédemment selon laquelle les déroulés des hivers dans la stratosphère sont décidés en début d'hiver. L'une des trouvailles les plus intéressantes est l'opposition des signaux au sol en Décembre entre différents modes perturbés confirmant que l'état de l'atmosphère en début d'hiver conditionne potentiellement le timing des échauffements survenant dans les semaines suivantes. De plus ces champs admettent des structures de la forme d'ondes en accord avec l'activité ondulatoire diagnostiquée dans la stratosphère confirmant la connexion verticale au sein de l'atmosphère. Au delà du mois de décembre, certains scénarios affichent des signaux d'anomalies au sol typiques correspondant à des phases négatives de l'oscillation Arctique Nord se produisant après l'occurrence d'échauffements stratosphériques. On remarque que les échauffements se produisant en février impactent moins le temps dans la troposphère par rapport à ceux se produisant en janvier en accord avec les résultats de Monnin et al. (2022). Ces derniers ont rapportés que les plus fortes anomalies de vortex en début d'hiver causées par un état moyen plus fort sont responsables de cette différence d'impact. A l'aide de ces potentiels précurseurs, il nous est donc possible de connecter la troposphère de début d'hiver avec un déroulé spé-

cifique de la circulation stratosphérique comprenant un certain timing d'échauffement stratosphérique. Ce dernier joue ensuite un rôle dans l'influence qu'aura l'anomalie stratosphérique générée sur la troposphère. Ainsi, ces résultats constituent de potentielles applications pour l'amélioration de nos aptitudes à prédire le climat à l'échelle saisonnière dans l'hémisphère nord.

## 6.5 . Perspectives

Tout d'abord, concernant le phénomène des inversions de température mésosphériques, une première étape serait de confirmer le mécanisme d'apparition introduit par Hauchecorne et al. (1987) par simulation telle que celle réalisée par Hauchecorne and Maillard (1990) mais en utilisant un nouveau modèle 3D mécaniste possédant une meilleure résolution verticale. Le modèle mécaniste RACCORD pourra être utilisé pour cet objectif en forçant la troposphère et la stratosphère avec des données ERA5. Aussi, d'autres observations simultanées de vent-température dans la moyenne atmosphère en présence d'inversions mésosphériques sont nécessaires afin de rendre plus robuste la statistique établie ici. Notamment dans le but de pouvoir caractériser plus précisément le ralentissement de vent associé à une élévation de température dans la mésosphère. Pour cela, davantage d'observations de vent doivent être conduites simultanément à celles de température dans la moyenne atmosphère. Cet objectif passe par le développement de la technologie LiDAR Doppler et l'amélioration de la technique afin de réduire les erreurs instrumentales associées et d'obtenir de meilleure portée verticale pour les données LiDAR vent.

D'autre part, concernant les travaux sur la mémoire atmosphérique, on pourra tirer profit de la nouvelle classification des hivers établie dans ce travail afin de tester leur potentiel prédicatif de l'apparition d'un échauffement stratosphérique. En effet, une forte motivation à la poursuite de cette étude sont les évolutions moyennes des vents zonaux à 10hPa-60°N des derniers hivers (voir Figure 6.1) : 2020/2021, 2021/2022 et 2022/2023, qui,

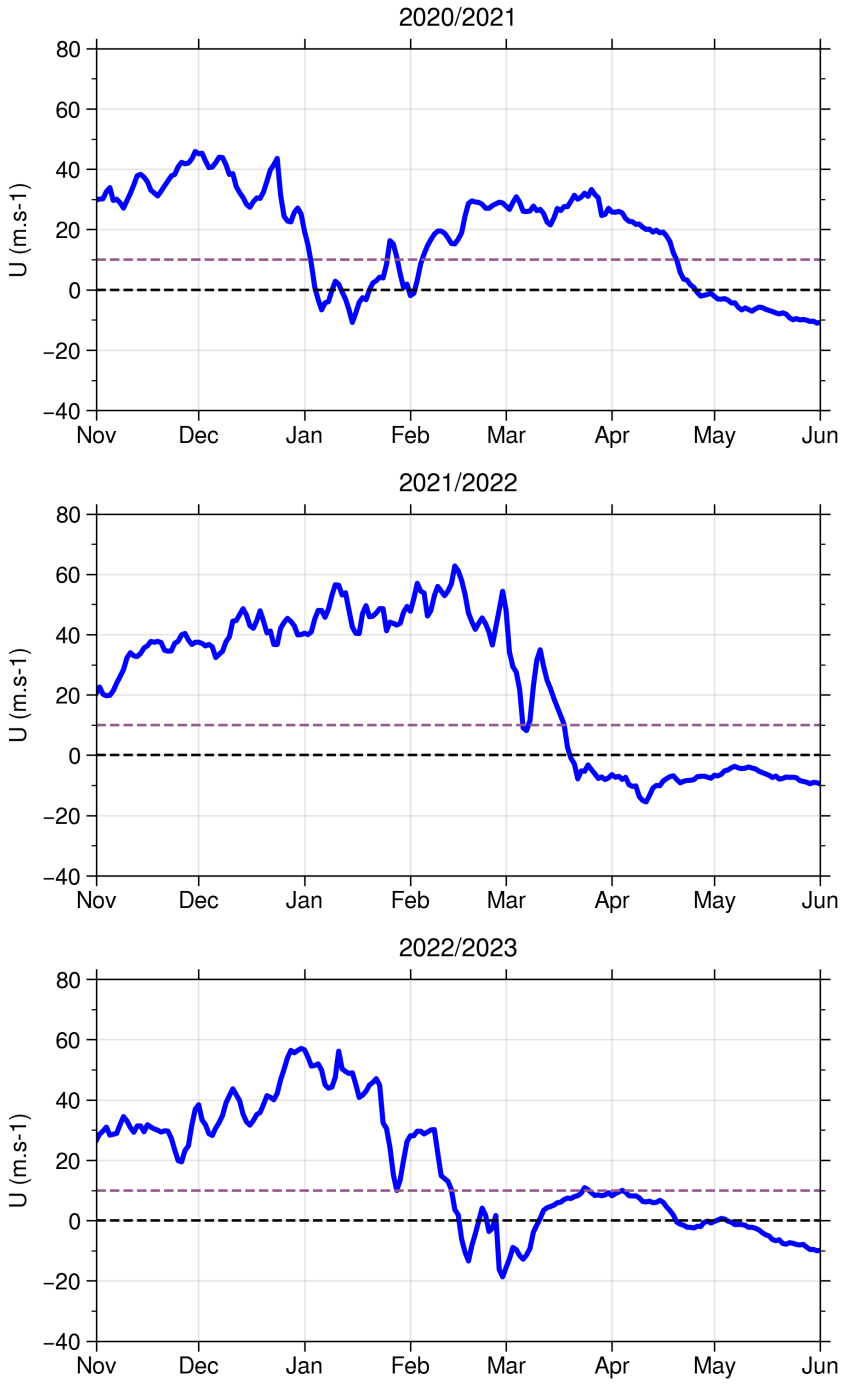


Figure 6.1 – Évolution journalière du vent zonal moyen à 60°N-10hPa des trois hivers : 2020/2021, 2021/2022 et 2022/2023. Les lignes pointillées violettes et noires correspondent aux seuils de 10 m/s (échauffement important) et 0 m/s (échauffement majeur), respectivement.

à première vue, peuvent être classifiés respectivement comme appartenant au mode Janvier, au mode DFW et au mode Février. La Figure 6.2 révèle les évolutions au sol des anomalies de pression de ces trois derniers hivers en indiquant les régions significatives associées à leur potentiel scénario. Il apparaît que les que les hivers 2020/2021 et 2021/2022 suivent fidèlement les scénarios qui leurs ont été associés. En revanche, le dernier hiver 2022/2023 ne semble pas suivre l'évolution du mode de Février. Notamment, on remarque que les signaux présents en novembre et décembre présentent quelques similarités avec à ceux du mode de Janvier. Cette évolution peut éventuellement être associée à la première chute de vent survenant en Janvier de cet hiver. Cependant le signal à partir de janvier diverge de celui du mode de Janvier empêchant une correspondance totale en début d'hiver. Ainsi, l'hiver 2022/2023 ne semble pas suivre une évolution typique au sol.

Par conséquent, le relation timing des échauffements avec le sol du début d'hiver établie ici semble posséder un réel potentiel pour les prévisions saisonnières. Cependant, il subsiste des évolutions atypiques au sein de certains hivers ne rentrant pas dans cette classification confirmant que ces principaux scénarios rapportés ici ne sont pas suivis systématiquement. Des investigations supplémentaires sont nécessaires afin de comprendre quels facteurs sont responsables de l'apparition des ces anomalies typiques en début d'hiver.

Pour cette tâche, l'utilisation d'un modèle mécaniste simulant le déroulé de l'hiver dans la stratosphère en forçant la troposphère avec des conditions météorologiques typiques (géopotentiel, température, vent, activité ondulatoire) de l'un des scénarios peut-être une première étape. Ainsi, ces simulations pourraient apporter une preuve que certains timings d'échauffements stratosphériques sont bien influencés par des précurseurs troposphériques dans les semaines qui précédent l'événement. De façon similaire, une autre simulation pourra être conçue afin de tenter de reproduire les mêmes impacts sur la troposphère que ceux observés dans chaque scénario après l'apparition d'un échauffement. De plus cette classification peut-être utilisée comme une référence afin d'éva-

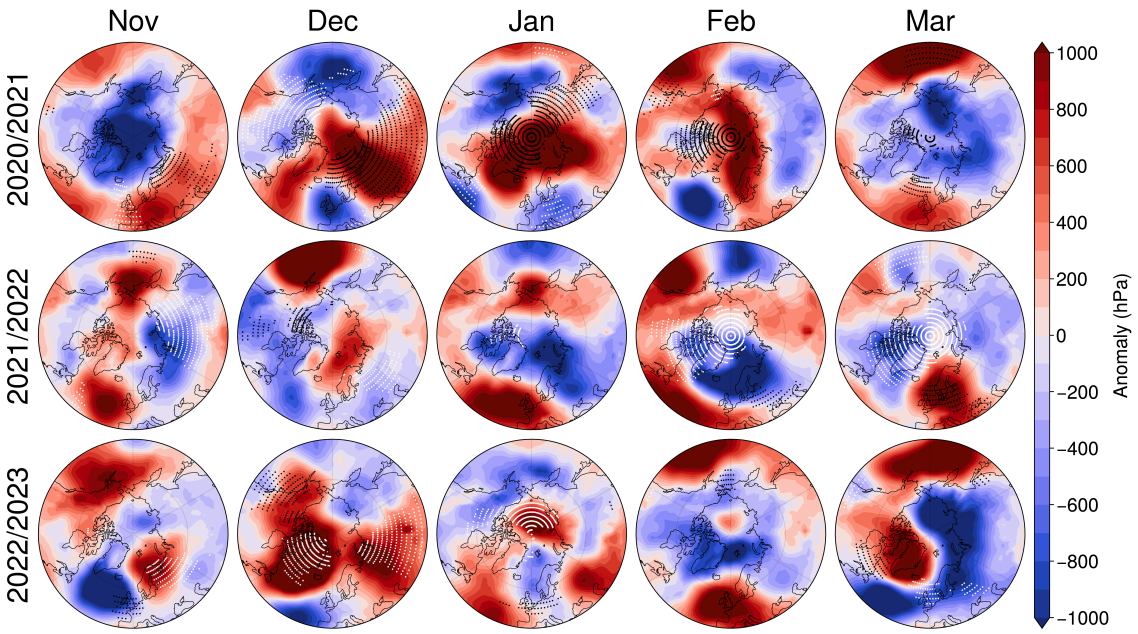


Figure 6.2 – Moyenne mensuelle de l'anomalie MSLP à partir de 40°N dans l'hémisphère nord pour les trois hivers : 2020/2021 (considéré comme le mode janvier), 2021/2022 (considéré comme le mode DFW) et 2022/2023 (considéré comme le mode février). Les régions ombrées en bleu et en rouge correspondent respectivement aux anomalies MSLP négatives et positives. Les zones pointillées blanches et noires indiquent la confiance statistique au niveau de 95% selon un test de Wilcoxon signé du signal négatif et positif, respectivement, du mode associé.

luer les modèles de climat appartenant au groupe de CMIP6. D'une façon globale, des recherches supplémentaires sont requises afin de comprendre quelles sont les réelles causes responsables du timing de l'échauffement stratosphérique final ou encore de la descente de l'anomalie stratosphérique dans la troposphère.

Une amélioration éventuelle de la classification est également envisageable en se basant désormais sur les conditions au sol en début d'hiver qui dépeignent un aspect physique de l'état troposphérique. Enfin, il serait intéressant d'étudier le rôle de la mésosphère dans l'apparition des anomalies au sein de la stratosphère qui tendent à apparaître dans la haute stratosphère. Pour cela, davantage de données globales de température dans la mésosphère à partir de sondage au limbe dans le même modèle qu'avec GOMOS (Hauchecorne et al., 2007) pourraient être réalisées à partir d'une constellation de CubeSat (Keckhut et al., 2021).

# Bibliographie

V. J. Abreu and J. H. Yee. Diurnal and seasonal variation of the nighttime oh (8-3) emission at low latitudes. *Journal of Geophysical Research : Space Physics*, 94(A9) :11949–11957, 1989. doi : https://doi.org/10.1029/JA094iA09p11949.

H. Afargan-Gerstman and D. I. V. Domeisen. Pacific modulation of the north atlantic storm track response to sudden stratospheric warming events. *Geophysical Research Letters*, 47(2) :e2019GL085007, 2020. doi : https://doi.org/10.1029/2019GL085007. e2019GL085007 10.1029/2019GL085007.

D. Andrews, J. Holton, and C. Leovy. *Middle Atmosphere Dynamics*. International Geophysics. Elsevier Science, 1987. ISBN 9780120585762.

D. G. Andrews. On the interpretation of the eliassen-palm flux divergence. *Quarterly Journal of the Royal Meteorological Society*, 113(475) :323–338, 1987. doi : https://doi.org/10.1002/qj.49711347518.

D. G. Andrews and M. E. McIntyre. Planetary waves in horizontal and vertical shear : The generalized eliassen-palm relation and the mean zonal acceleration. *Journal of Atmospheric Sciences*, 33(11) :2031 – 2048, 1976. doi : https://doi.org/10.1175/1520-0469(1976)033<2031:PWIHAV>2.0.CO;2.

D. G. Andrews and M. E. McIntyre. Generalized eliassen-palm and charney-drazin theorems for waves on axismmetric mean flows in compressible atmospheres. *Journal of Atmospheric Sciences*, 35(2) :175 – 185, 1978. doi : https://doi.org/10.1175/1520-0469(1978)035<0175:GEPACD>2.0.CO;2.

B. Ayarzagüena, A. J. Charlton-Perez, A. H. Butler, P. Hitchcock, I. R. Simpson, L. M. Pol-

vani, N. Butchart, E. P. Gerber, L. Gray, B. Hassler, P. Lin, F. Lott, E. Manzini, R. Mizuta, C. Orbe, S. Osprey, D. Saint-Martin, M. Sigmond, M. Taguchi, E. M. Volodin, and S. Watanabe. Uncertainty in the response of sudden stratospheric warmings and stratosphere-troposphere coupling to quadrupled co2 concentrations in cmip6 models. *Journal of Geophysical Research : Atmospheres*, 125(6) :e2019JD032345, 2020. doi : https://doi.org/10.1029/2019JD032345. e2019JD032345 2019JD032345.

M. P. Baldwin and T. J. Dunkerton. Stratospheric harbingers of anomalous weather regimes. *Science*, 294(5542) :581–584, 2001. doi : 10.1126/science.1063315.

M. P. Baldwin, D. W. J. Thompson, E. F. Shuckburgh, W. A. Norton, and N. P. Gillett. Weather from the stratosphere? *Science*, 301(5631) :317–319, 2003. doi : 10.1126/science.1085688.

S. Bancalá, K. Krüger, and M. Giorgetta. The preconditioning of major sudden stratospheric warmings. *Journal of Geophysical Research : Atmospheres*, 117(D4), 2012. doi : https://doi.org/10.1029/2011JD016769.

D. Barriopedro and N. Calvo. On the relationship between enso, stratospheric sudden warmings, and blocking. *Journal of Climate*, 27(12) :4704 – 4720, 2014. doi : https://doi.org/10.1175/JCLI-D-13-00770.1.

Bellisario, Christophe, Simoneau, Pierre, Keckhut, Philippe, and Hauchecorne, Alain. Comparisons of spectrally resolved nightglow emission locally simulated with space and ground level observations. *J. Space Weather Space Clim.*, 10 :21, 2020. doi : 10.1051/swsc/2020017.

R. X. Black and B. A. McDaniel. Diagnostic case studies of the northern annular mode. *Journal of Climate*, 17(20) :3990 – 4004, 2004. doi : https://doi.org/10.1175/1520-0442(2004)017<3990:DCSOTN>2.0.CO;2.

A. W. Brewer. Evidence for a world circulation provided by the measurements of helium

and water vapour distribution in the stratosphere. *Quarterly Journal of the Royal Meteorological Society*, 75(326) :351–363, 1949. doi : https://doi.org/10.1002/qj.49707532603.

N. Butchart. The brewer-dobson circulation. *Reviews of Geophysics*, 52(2) :157–184, 2014. doi : https://doi.org/10.1002/2013RG000448.

A. H. Butler, D. J. Seidel, S. C. Hardiman, N. Butchart, T. Birner, and A. Match. Defining sudden stratospheric warmings. *Bulletin of the American Meteorological Society*, 96(11) : 1913 – 1928, 2015. doi : https://doi.org/10.1175/BAMS-D-13-00173.1.

A. H. Butler, J. P. Sjoberg, D. J. Seidel, and K. H. Rosenlof. A sudden stratospheric warming compendium. *Earth System Science Data*, 9(1) :63–76, 2017. doi : 10.5194/essd-9-63-2017.

A. J. Charlton and L. M. Polvani. A new look at stratospheric sudden warmings. part i : Climatology and modeling benchmarks. *Journal of Climate*, 20(3) :449 – 469, 2007. doi : https://doi.org/10.1175/JCLI3996.1.

A. J. Charlton, A. O'neill, W. A. Lahoz, and A. C. Massacand. Sensitivity of tropospheric forecasts to stratospheric initial conditions. *Quarterly Journal of the Royal Meteorological Society*, 130(600) :1771–1792, 2004. doi : https://doi.org/10.1256/qj.03.167.

A. J. Charlton, A. O'Neill, W. A. Lahoz, and P. Berrisford. The splitting of the stratospheric polar vortex in the southern hemisphere, september 2002 : Dynamical evolution. *Journal of the Atmospheric Sciences*, 62(3) :590 – 602, 2005. doi : https://doi.org/10.1175/JAS-3318.1.

A. J. Charlton-Perez, M. P. Baldwin, T. Birner, R. X. Black, A. H. Butler, N. Calvo, N. A. Davis, E. P. Gerber, N. Gillett, S. Hardiman, J. Kim, K. Krüger, Y.-Y. Lee, E. Manzini, B. A. McDaniel, L. Polvani, T. Reichler, T. A. Shaw, M. Sigmond, S.-W. Son, M. Toohey, L. Wilcox, S. Yoden, B. Christiansen, F. Lott, D. Shindell, S. Yukimoto, and S. Watanabe. On the lack of stratospheric dynamical variability in low-top versions of the cmip5 mo-

dels. *Journal of Geophysical Research : Atmospheres*, 118(6) :2494–2505, 2013. doi : https://doi.org/10.1002/jgrd.50125.

J. G. Charney and P. G. Drazin. Propagation of planetary-scale disturbances from the lower into the upper atmosphere. *Journal of Geophysical Research (1896-1977)*, 66(1) :83–109, 1961. doi : https://doi.org/10.1029/JZ066i001p00083.

R. T. H. Collis. Lidar. *Appl. Opt.*, 9(8) :1782–1788, Aug 1970. doi : 10.1364/AO.9.001782.

D. P. Dee, S. M. Uppala, A. J. Simmons, P. Berrisford, P. Poli, S. Kobayashi, U. Andrae, M. A. Balmaseda, G. Balsamo, P. Bauer, P. Bechtold, A. C. M. Beljaars, L. van de Berg, J. Bidlot, N. Bormann, C. Delsol, R. Dragani, M. Fuentes, A. J. Geer, L. Haimberger, S. B. Healy, H. Hersbach, E. V. Hólm, L. Isaksen, P. Kållberg, M. Köhler, M. Matricardi, A. P. McNally, B. M. Monge-Sanz, J.-J. Morcrette, B.-K. Park, C. Peubey, P. de Rosnay, C. Tavolato, J.-N. Thépaut, and F. Vitart. The era-interim reanalysis : configuration and performance of the data assimilation system. *Quarterly Journal of the Royal Meteorological Society*, 137 (656) :553–597, 2011. doi : https://doi.org/10.1002/qj.828.

G. M. B. Dobson. Origin and distribution of the polyatomic molecules in the atmosphere. *Proceedings of the Royal Society of London. Series A, Mathematical and Physical Sciences*, 236(1205) :187–193, 1956. ISSN 00804630.

D. I. Domeisen. Estimating the frequency of sudden stratospheric warming events from surface observations of the north atlantic oscillation. *Journal of Geophysical Research : Atmospheres*, 124(6) :3180–3194, 2019. doi : https://doi.org/10.1029/2018JD030077.

T. J. Duck, D. P. Sipler, J. E. Salah, and J. W. Meriwether. Rayleigh lidar observations of a mesospheric inversion layer during night and day. *Geophysical Research Letters*, 28(18) : 3597–3600, 2001. doi : https://doi.org/10.1029/2001GL013409.

F. G. Finger, M. Gelman, J. Wild, M.-L. Chanin, A. Hauchecorne, and A. Miller. Evaluation of nmc upper-stratospheric temperature analyses using rocketsonde and lidar data.

*Bulletin of the American Meteorological Society*, 74(5) :789–800, 1993. doi : https://doi.org/10.1175/1520-0477(1993)074<0789:EONUST>2.0.CO;2.

E. L. Fleming, S. Chandra, J. Barnett, and M. Corney. Zonal mean temperature, pressure, zonal wind and geopotential height as functions of latitude. *Advances in Space Research*, 10(12) :11–59, 1990. ISSN 0273-1177. doi : https://doi.org/10.1016/0273-1177(90)90386-E.

J. M. Forbes. *Tidal and Planetary Waves*, pages 67–87. American Geophysical Union (AGU), 1995. ISBN 9781118664247. doi : https://doi.org/10.1029/GM087p0067.

J. A. France, V. L. Harvey, C. E. Randall, R. L. Collins, A. K. Smith, E. D. Peck, and X. Fang. A climatology of planetary wave-driven mesospheric inversion layers in the extratropical winter. *Journal of Geophysical Research : Atmospheres*, 120(2) :399–413, 2015. doi : https://doi.org/10.1002/2014JD022244.

A. Friker and F.-J. Lübken. Neutral air density and temperature measurements by the total instrument aboard the rose payloads. *Journal of Atmospheric and Terrestrial Physics*, 54 (6) :693–701, 1992. ISSN 0021-9169. doi : https://doi.org/10.1016/0021-9169(92)90107-V. E-Region Irregularities.

B. M. Funatsu, C. Claud, P. Keckhut, W. Steinbrecht, and A. Hauchecorne. Investigations of stratospheric temperature regional variability with lidar and advanced microwave sounding unit. *Journal of Geophysical Research : Atmospheres*, 116(D8), 2011. doi : https://doi.org/10.1029/2010JD014974.

B. M. Funatsu, C. Claud, P. Keckhut, A. Hauchecorne, and T. Leblanc. Regional and seasonal stratospheric temperature trends in the last decade (2002–2014) from amsu observations. *Journal of Geophysical Research : Atmospheres*, 121(14) :8172–8185, 2016. doi : https://doi.org/10.1002/2015JD024305.

A. Hauchecorne and M.-L. Chanin. Density and temperature profiles obtained by lidar

between 35 and 70 km. *Geophysical Research Letters*, 7(8) :565–568, 1980. doi : https://doi.org/10.1029/GL007i008p00565.

A. Hauchecorne and A. Maillard. A 2-d dynamical model of mesospheric temperature inversions in winter. *Geophysical Research Letters*, 17(12) :2197–2200, 1990. doi : https://doi.org/10.1029/GL017i012p02197.

A. Hauchecorne, M. L. Chanin, and R. Wilson. Mesospheric temperature inversion and gravity wave breaking. *Geophysical Research Letters*, 14(9) :933–936, 1987. doi : https://doi.org/10.1029/GL014i009p00933.

A. Hauchecorne, M.-L. Chanin, and P. Keckhut. Climatology and trends of the middle atmospheric temperature (33–87 km) as seen by rayleigh lidar over the south of france. *Journal of Geophysical Research : Atmospheres*, 96(D8) :15297–15309, 1991. doi : https://doi.org/10.1029/91JD01213.

A. Hauchecorne, J. L. Bertaux, and R. Lallement. *Impact of Solar Activity on Stratospheric Ozone and No2 Observed by GOMOS/ENVISAT*, pages 393–402. Springer New York, New York, NY, 2007. ISBN 978-0-387-48341-2. doi : 10.1007/978-0-387-48341-2_31.

A. Hauchecorne, C. Claud, P. Keckhut, and A. Mariaccia. Stratospheric final warmings fall into two categories with different evolution over the course of the year. *Communications Earth & Environment*, 3(1) :4, 2022. doi : https://doi.org/10.1038/s43247-021-00335-z.

P. H. Haynes, M. E. McIntyre, T. G. Shepherd, C. J. Marks, and K. P. Shine. On the "downward control" of extratropical diabatic circulations by eddy-induced mean zonal forces. *Journal of Atmospheric Sciences*, 48(4) :651 – 678, 1991. doi : https://doi.org/10.1175/1520-0469(1991)048<0651:OTCOED>2.0.CO;2.

A. E. Hedin. Msis-86 thermospheric model. *Journal of Geophysical Research : Space Physics*, 92(A5) :4649–4662, 1987. doi : https://doi.org/10.1029/JA092iA05p04649.

H. Hersbach, B. Bell, P. Berrisford, S. Hirahara, A. Horányi, J. Muñoz-Sabater, J. Nicolas, C. Peubey, R. Radu, D. Schepers, A. Simmons, C. Soci, S. Abdalla, X. Abellan, G. Balsamo, P. Bechtold, G. Biavati, J. Bidlot, M. Bonavita, G. De Chiara, P. Dahlgren, D. Dee, M. Diamantakis, R. Dragani, J. Flemming, R. Forbes, M. Fuentes, A. Geer, L. Haimberger, S. Healy, R. J. Hogan, E. Hólm, M. Janisková, S. Keeley, P. Laloyaux, P. Lopez, C. Lupu, G. Radnoti, P. de Rosnay, I. Rozum, F. Vamborg, S. Villaume, and J.-N. Thépaut. The era5 global reanalysis. *Quarterly Journal of the Royal Meteorological Society*, 146(730) : 1999–2049, 2020. doi : https://doi.org/10.1002/qj.3803.

C. O. Hines. Internal atmospheric gravity waves at ionospheric heights. *Canadian Journal of Physics*, 38(11) :1441–1481, 1960. doi : 10.1139/p60-150.

R. R. Hodges Jr. Eddy diffusion coefficients due to instabilities in internal gravity waves. *Journal of Geophysical Research (1896-1977)*, 74(16) :4087–4090, 1969. doi : https://doi.org/10.1029/JA074i016p04087.

J. R. Holton. The dynamics of sudden stratospheric warmings. *Annual Review of Earth and Planetary Sciences*, 8(1) :169–190, 1980. doi : 10.1146/annurev.ea.08.050180.001125.

E. Kalnay, M. Kanamitsu, R. Kistler, W. Collins, D. Deaven, L. Gandin, M. Iredell, S. Saha, G. White, J. Woollen, et al. The ncep/ncar 40-year reanalysis project. In *Renewable Energy*, pages Vol1_146–Vol1_194. Routledge, 2018.

F. Karbou, F. Aires, C. Prigent, and L. Eymard. Potential of advanced microwave sounding unit-a (amsu-a) and amsu-b measurements for atmospheric temperature and humidity profiling over land. *Journal of Geophysical Research : Atmospheres*, 110(D7), 2005. doi : https://doi.org/10.1029/2004JD005318.

A. Y. Karpechko, P. Hitchcock, D. H. W. Peters, and A. Schneidereit. Predictability of downward propagation of major sudden stratospheric warmings. *Quarterly Journal of the*

*Royal Meteorological Society*, 143(704) :1459–1470, 2017. doi : https://doi.org/10.1002/qj.3017.

P. Keckhut and K. Kodera. Long-term changes of the upper stratosphere as seen by japanese rocketsondes at ryori (39 n, 141 e). In *Annales Geophysicae*, volume 17, pages 1210–1217. Springer, 1999.

P. Keckhut, A. Hauchecorne, and M.-L. Chanin. A critical review of the database acquired for the long-term surveillance of the middle atmosphere by the french rayleigh lidars. *JOURNAL OF ATMOSPHERIC AND OCEANIC TECHNOLOGY*, 10 :850–867, 12 1993. doi : 10.1175/1520-0426(1993)010<0850:ACROTD>2.0.CO;2.

P. Keckhut, F. Schmidlin, A. Hauchecorne, and M. Chanin. Stratospheric and mesospheric cooling trend estimates from u.s. rocketsondes at low latitude stations (8°s–34°n), taking into account instrumental changes and natural variability. *Journal of Atmospheric and Solar-Terrestrial Physics*, 61(6) :447–459, 1999. ISSN 1364-6826. doi : https://doi.org/10.1016/S1364-6826(98)00139-4.

P. Keckhut, A. Hauchecorne, T. Kerzenmacher, and G. Angot. Modes of variability of the vertical temperature profile of the middle atmosphere at mid-latitude : Similarities with solar forcing. *Journal of Atmospheric and Solar-Terrestrial Physics*, 75-76 :92–97, 2012. ISSN 1364-6826. doi : https://doi.org/10.1016/j.jastp.2011.05.012. Atmospheric Coupling Processes in the Sun-Earth System.

P. Keckhut, A. Hauchecorne, M. Meftah, S. Khaykin, C. Claud, and P. Simoneau. Middle-atmosphere temperature monitoring addressed with a constellation of cubesats dedicated to climate issues. *Journal of Atmospheric and Oceanic Technology*, 38(3) :685 – 693, 2021. doi : https://doi.org/10.1175/JTECH-D-20-0046.1.

W. W. Kellogg and G. F. Schilling. A proposed model of the circulation in the upper stra-

tosphere. *Journal of Atmospheric Sciences*, 8(4) :222 – 230, 1951. doi : https://doi.org/10.1175/1520-0469(1951)008<0222:APMOTC>2.0.CO;2.

S. M. Khaykin, B. M. Funatsu, A. Hauchecorne, S. Godin-Beekmann, C. Claud, P. Keckhut, A. Pazmino, H. Gleisner, J. K. Nielsen, S. Syndergaard, and K. B. Lauritsen. Postmillennium changes in stratospheric temperature consistently resolved by gps radio occultation and amsu observations. *Geophysical Research Letters*, 44(14) :7510–7518, 2017. doi : https://doi.org/10.1002/2017GL074353.

S. KOBAYASHI, Y. OTA, Y. HARADA, A. EBITA, M. MORIYA, H. ONODA, K. ONOGI, H. KAMAHORI, C. KOBAYASHI, H. ENDO, K. MIYAOKA, and K. TAKAHASHI. The jra-55 reanalysis : General specifications and basic characteristics. *Journal of the Meteorological Society of Japan*, 93(1) :5–48, 2015. doi : 10.2151/jmsj.2015-001.

K. Kodera, H. Mukougawa, P. Maury, M. Ueda, and C. Claud. Absorbing and reflecting sudden stratospheric warming events and their relationship with tropospheric circulation. *Journal of Geophysical Research : Atmospheres*, 121(1) :80–94, 2016. doi : https://doi.org/10.1002/2015JD023359.

A. Kubicki, P. Keckhut, M.-L. Chanin, A. Hauchecorne, E. Lysenko, and G. S. Golitsyn. Temperature trends in the middle atmosphere as seen by historical russian rocket launches : Part 1, volgograd (48.68°n, 44.35°e). *Journal of Atmospheric and Solar-Terrestrial Physics*, 68(10) :1075–1086, 2006. ISSN 1364-6826. doi : https://doi.org/10.1016/j.jastp.2006.02.001.

Y.-H. KUO, T.-K. WEE, S. SOKOLOVSKIY, C. ROCKEN, W. SCHREINER, D. HUNT, and R. ANTHES. Inversion and error estimation of gps radio occultation data. *Journal of the Meteorological Society of Japan*, 82(1B) :507–531, 2004. doi : 10.2151/jmsj.2004.507.

K. Labitzke. Stratospheric-mesospheric midwinter disturbances : A summary of observed

characteristics. *Journal of Geophysical Research : Oceans*, 86(C10) :9665–9678, 1981. doi : https://doi.org/10.1029/JC086iC10p09665.

T. Le Du, P. Keckhut, A. Hauchecorne, and P. Simoneau. Observation of gravity wave vertical propagation through a mesospheric inversion layer. *Atmosphere*, 13(7), 2022. ISSN 2073-4433. doi : 10.3390/atmos13071003.

T. Leblanc and A. Hauchecorne. Recent observations of mesospheric temperature inversions. *Journal of Geophysical Research : Atmospheres*, 102(D16) :19471–19482, 1997. doi : https://doi.org/10.1029/97JD01445.

R. S. Lindzen. Thermally driven diurnal tide in the atmosphere. *Quarterly Journal of the Royal Meteorological Society*, 93(395) :18–42, 1967. doi : https://doi.org/10.1002/qj.49709339503.

R. S. Lindzen. Turbulence and stress owing to gravity wave and tidal breakdown. *Journal of Geophysical Research : Oceans*, 86(C10) :9707–9714, 1981. doi : https://doi.org/10.1029/JC086iC10p09707.

R. S. Lindzen and D. Blake. Internal gravity waves in atmospheres with realistic dissipation and temperature part ii. thermal tides excited below the mesopause. *Geophysical Fluid Dynamics*, 2(1) :31–61, 1971. doi : 10.1080/03091927108236051.

R. S. Lindzen and S. Chapman. The application of classical atmospheric tidal theory. *Proceedings of the Royal Society of London. Series A. Mathematical and Physical Sciences*, 303 (1474) :299–316, 1968. doi : https://doi.org/10.1098/rspa.1968.0052.

F.-J. Lübken, G. Baumgarten, J. Hildebrand, and F. J. Schmidlin. Simultaneous and co-located wind measurements in the middle atmosphere by lidar and rocket-borne techniques. *Atmospheric Measurement Techniques*, 9(8) :3911–3919, 2016. doi : 10.5194/amt-9-3911-2016.

F.-J. Lübken, W. Hillert, G. Lehmacher, U. Zahn, M. Bittner, D. Offermann, F. Schmidlin, A. Hauchecorne, M. Mourier, and P. Czechowsky. Intercomparison of density and temperature profiles obtained by lidar, ionization gauges, falling spheres, datasondes and radiosondes during the dyana campaign. *Journal of Atmospheric and Terrestrial Physics*, 56(13) :1969–1984, 1994. ISSN 0021-9169. doi : https://doi.org/10.1016/0021-9169(94)90023-X. Dynamic Adapted Network for the the Atmosphere.

T. Matsuno. A dynamical model of the stratospheric sudden warming. *Journal of Atmospheric Sciences*, 28(8) :1479 – 1494, 1971. doi : https://doi.org/10.1175/1520-0469(1971)028<1479:ADMOTS>2.0.CO;2.

P. Maury, C. Claud, E. Manzini, A. Hauchecorne, and P. Keckhut. Characteristics of stratospheric warming events during northern winter. *Journal of Geophysical Research : Atmospheres*, 121(10) :5368–5380, 2016. doi : https://doi.org/10.1002/2015JD024226.

M. E. McIntyre and T. Palmer. Breaking planetary waves in the stratosphere. *Nature*, 305 (5935) :593–600, 1983.

C. McLandress. On the importance of gravity waves in the middle atmosphere and their parameterization in general circulation models. *Journal of Atmospheric and Solar-Terrestrial Physics*, 60(14) :1357–1383, 1998. ISSN 1364-6826. doi : https://doi.org/10.1016/S1364-6826(98)00061-3.

J. W. Meriwether and C. S. Gardner. A review of the mesosphere inversion layer phenomenon. *Journal of Geophysical Research : Atmospheres*, 105(D10) :12405–12416, 2000. doi : https://doi.org/10.1029/2000JD900163.

J. W. Meriwether and A. J. Gerrard. Mesosphere inversion layers and stratosphere temperature enhancements. *Reviews of Geophysics*, 42(3), 2004. doi : https://doi.org/10.1029/2003RG000133.

J. W. Meriwether and M. G. Mlynczak. Is chemical heating a major cause of the mesosphere inversion layer? *Journal of Geophysical Research : Atmospheres*, 100(D1) :1379–1387, 1995. doi : https://doi.org/10.1029/94JD01736.

D. M. Mitchell, L. J. Gray, J. Anstey, M. P. Baldwin, and A. J. Charlton-Perez. The influence of stratospheric vortex displacements and splits on surface climate. *Journal of Climate*, 26(8) :2668 – 2682, 2013. doi : https://doi.org/10.1175/JCLI-D-12-00030.1.

E. Monnin, M. Kretschmer, and I. Polichtchouk. The role of the timing of sudden stratospheric warmings for precipitation and temperature anomalies in europe. *International Journal of Climatology*, 42(6) :3448–3462, 2022. doi : https://doi.org/10.1002/joc.7426.

N. Mzé, A. Hauchecorne, P. Keckhut, and M. Thétis. Vertical distribution of gravity wave potential energy from long-term rayleigh lidar data at a northern middle-latitude site. *Journal of Geophysical Research : Atmospheres*, 119(21) :12,069–12,083, 2014. doi : https://doi.org/10.1002/2014JD022035.

K. I. Nakagawa and K. Yamazaki. What kind of stratospheric sudden warming propagates to the troposphere? *Geophysical Research Letters*, 33(4), 2006. doi : https://doi.org/10.1029/2005GL024784.

C. J. Nappo. Fundamentals. In C. J. Nappo, editor, *An Introduction to Atmospheric Gravity Waves*, volume 102 of *International Geophysics*, pages 1–28. Academic Press, 2012a. doi : https://doi.org/10.1016/B978-0-12-385223-6.00001-X.

C. J. Nappo. The linear theory. In C. J. Nappo, editor, *An Introduction to Atmospheric Gravity Waves*, volume 102 of *International Geophysics*, pages 29–56. Academic Press, 2012b. doi : https://doi.org/10.1016/B978-0-12-385223-6.00002-1.

I. M. Navon. Data assimilation for numerical weather prediction : a review. *Data assimilation for atmospheric, oceanic and hydrologic applications*, pages 21–65, 2009.

B. C. O'Neill, C. Tebaldi, D. P. van Vuuren, V. Eyring, P. Friedlingstein, G. Hurtt, R. Knutti, E. Kriegler, J.-F. Lamarque, J. Lowe, G. A. Meehl, R. Moss, K. Riahi, and B. M. Sanderson. The scenario model intercomparison project (scenariomip) for cmip6. *Geoscientific Model Development*, 9(9) :3461–3482, 2016. doi : 10.5194/gmd-9-3461-2016.

R. A. Plumb. Stratospheric transport. *Journal of the Meteorological Society of Japan*, 80(4B) : 793–809, 2002. doi : 10.2151/jmsj.80.793.

R. S. Quiroz. Tropospheric-stratospheric interaction in the major warming event of january-february 1979. *Geophysical Research Letters*, 6(8) :645–648, 1979. doi : https://doi.org/10.1029/GL006i008p00645.

J. Rao, C. I. Garfinkel, I. P. White, and C. Schwartz. The southern hemisphere minor sudden stratospheric warming in september 2019 and its predictions in s2s models. *Journal of Geophysical Research : Atmospheres*, 125(14) :e2020JD032723, 2020. doi : https://doi.org/10.1029/2020JD032723. e2020JD032723 2020JD032723.

R. J. Reed, W. J. Campbell, L. A. Rasmussen, and D. G. Rogers. Evidence of a downward-propagating, annual wind reversal in the equatorial stratosphere. *Journal of Geophysical Research (1896-1977)*, 66(3) :813–818, 1961. doi : https://doi.org/10.1029/JZ066i003p00813.

M. Salby. *Physics of the Atmosphere and Climate*. Physics of the Atmosphere and Climate. Cambridge University Press, 2012. ISBN 9780521767187.

M. Salby, F. Sassi, P. Callaghan, D. Wu, P. Keckhut, and A. Hauchecorne. Mesospheric inversions and their relationship to planetary wave structure. *Journal of Geophysical Research : Atmospheres*, 107(D4) :ACL 4–1–ACL 4–13, 2002. doi : https://doi.org/10.1029/2001JD000756.

F. Sassi, R. R. Garcia, B. A. Boville, and H. Liu. On temperature inversions and the mesospheric surf zone. *Journal of Geophysical Research : Atmospheres*, 107(D19) :ACL 8–1–ACL 8–11, 2002. doi : https://doi.org/10.1029/2001JD001525.

R. Scherhag. Die explosinonsartigen stratospharen warmungen des stratintere 1951/52. *Deutsch. Wetterdienstes US-Zone, Berlin*, 6, 1952.

F. J. Schmidlin. Temperature inversions near 75 km. *Geophysical Research Letters*, 3(3) : 173–176, 1976. doi : https://doi.org/10.1029/GL003i003p00173.

F. J. Schmidlin. Repeatability and measurement uncertainty of the united states meteorological rocketsonde. *Journal of Geophysical Research : Oceans*, 86(C10) :9599–9603, 1981. doi : https://doi.org/10.1029/JC086iC10p09599.

F. J. Schmidlin, H. S. Lee, and W. Michel. The inflatable sphere : A technique for the accurate measurement of middle atmosphere temperatures. *Journal of Geophysical Research : Atmospheres*, 96(D12) :22673–22682, 1991. doi : https://doi.org/10.1029/91JD02395.

M. R. Schoeberl. Stratospheric warmings : Observations and theory. *Reviews of Geophysics*, 16(4) :521–538, 1978. doi : https://doi.org/10.1029/RG016i004p00521.

W. Schreiner, J. Weiss, R. Anthes, J. Braun, V. Chu, J. Fong, D. Hunt, Y.-H. Kuo, T. Meehan, W. Serafino, J. Sjoberg, S. Sokolovskiy, E. Talaat, T. Wee, and Z. Zeng. Cosmic-2 radio occultation constellation : First results. *Geophysical Research Letters*, 47(4) :e2019GL086841, 2020. doi : https://doi.org/10.1029/2019GL086841. e2019GL086841 2019GL086841.

G. Seibert and B. T. Battrick. *The history of sounding rockets and their contribution to European space research*. ESA Publications division Noordwijk, 2006.

J. Seinfeld and S. Pandis. *Atmospheric Chemistry and Physics : From Air Pollution to Climate Change*. Wiley, 2016. ISBN 9781118947401.

T. G. Shepherd. The middle atmosphere. *Journal of Atmospheric and Solar-Terrestrial Physics*, 62(17) :1587–1601, 2000. ISSN 1364-6826. doi : https://doi.org/10.1016/S1364-6826(00)00114-0.

T. G. Shepherd. Transport in the middle atmosphere. *Journal of the Meteorological Society of Japan. Ser. II*, 85B :165–191, 2007. doi : 10.2151/jmsj.85B.165.

R. J. States and C. S. Gardner. Thermal structure of the mesopause region (80–105 km) at 40°n latitude. part i : Seasonal variations. *Journal of the Atmospheric Sciences*, 57(1) :66 – 77, 2000. doi : https://doi.org/10.1175/1520-0469(2000)057<0066:TSOTMR>2.0.CO;2.

W. G. Stroud, W. Nordberg, W. R. Bandeen, F. L. Bartman, and P. Titus. Rocket-grenade measurements of temperatures and winds in the mesosphere over churchill, canada. *Journal of Geophysical Research (1896-1977)*, 65(8) :2307–2323, 1960. doi : https://doi.org/10.1029/JZ065i008p02307.

K. E. Trenberth, T. Koike, and K. Onogi. Progress and prospects for reanalysis for weather and climate. *Eos, Transactions American Geophysical Union*, 89(26) :234–235, 2008. doi : https://doi.org/10.1029/2008EO260002.

D. W. Waugh and P.-P. Rong. Interannual variability in the decay of lower stratospheric arctic vortices. *Journal of the Meteorological Society of Japan. Ser. II*, 80(4B) :997–1012, 2002. doi : 10.2151/jmsj.80.997.

D. W. Waugh, A. H. Sobel, and L. M. Polvani. What is the polar vortex and how does it influence weather? *Bulletin of the American Meteorological Society*, 98(1) :37 – 44, 2017. doi : https://doi.org/10.1175/BAMS-D-15-00212.1.

R. Wing, A. Hauchecorne, P. Keckhut, S. Godin-Beekmann, S. Khaykin, and E. M. McCullough. Lidar temperature series in the middle atmosphere as a reference data set – part 2 : Assessment of temperature observations from mls/aura and saber/timed satellites. *Atmospheric Measurement Techniques*, 11(12) :6703–6717, 2018a. doi : 10.5194/amt-11-6703-2018.

R. Wing, A. Hauchecorne, P. Keckhut, S. Godin-Beekmann, S. Khaykin, E. M. McCullough, J.-F. Mariscal, and E. d'Almeida. Lidar temperature series in the middle atmosphere as

a reference data set – part 1 : Improved retrievals and a 20-year cross-validation of two co-located french lidars. *Atmospheric Measurement Techniques*, 11(10) :5531–5547, 2018b. doi : 10.5194/amt-11-5531-2018.

R. Wing, M. Martic, A. Hauchecorne, J. Porteneuve, P. Keckhut, Y. Courcoux, L. Yung, P. Retailleau, and D. Cocuron. Atmospheric density and temperature vertical profile retrieval for flight-tests with a rayleigh lidar on-board the french advanced test range ship monge. *Atmosphere*, 11(1), 2020. ISSN 2073-4433. doi : 10.3390/atmos11010075.

Z. Wu and T. Reichler. Variations in the frequency of stratospheric sudden warmings in cmip5 and cmip6 and possible causes. *Journal of Climate*, 33(23) :10305 – 10320, 2020. doi : https://doi.org/10.1175/JCLI-D-20-0104.1.

W. Zhong and J. D. Haigh. The greenhouse effect and carbon dioxide. *Weather*, 68(4) : 100–105, 2013.

# A - Équations de la dynamique de la moyenne atmosphère

## A.1 . Équations primitives sur le plan Beta

Afin d'étudier les mouvements à plus larges échelles et plus lents, notamment dans les régions extra-tropicales, il est possible d'introduire plusieurs simplifications aux équations primitives décrites. Pour cela, on remplace les coordonnées sphériques ($\lambda$, $\phi$) par les coordonnées cartésiennes ($x$, $y$) indiquant l'est et le nord. L'avantage est de restreindre le domaine d'étude au voisinage de la latitude $\phi_0$. Les équations primitives prennent alors la forme suivante :

$$\frac{Du}{Dt} - fv + \Phi_x = X, \tag{A.1}$$

$$\frac{Dv}{Dt} + fu + \Phi_y = Y, \tag{A.2}$$

$$\Phi_z = H^{-1} R\Theta e^{-\kappa z/H}, \tag{A.3}$$

$$u_x + v_y + \rho_0^{-1}(\rho_0 w)_z = 0, \tag{A.4}$$

$$\frac{D\theta}{Dt} = Q, \tag{A.5}$$

où

$$\frac{D}{Dt} = \frac{\partial}{\partial t} + u\frac{\partial}{\partial x} + v\frac{\partial}{\partial y} + z\frac{\partial}{\partial z}.$$

Ici les distances vers l'est et ne nord sont représentées par les variables $x$ et $y$ à partir d'un point d'origine ($\lambda_0$, $\phi_0$), les indices dénotent les dérivations partielles et le paramètre

de Coriolis s'écrit :

$$f = f_0 + \beta y \tag{A.6}$$

où $f_0 = 2\Omega \sin \phi_0$, et $\beta = 2\Omega a^{-1} \cos \phi_0$. Ainsi, la variation linéaire de $f$ avec $y$ permet de capturer l'effet dynamique le plus important de la variation du paramètre de Coriolis. Cet effet fut découvert la première fois par Rossby (1939).

## A.2 . Fluide Quasi-Géostrophique

Pour décrire les mouvements de basses fréquences et larges échelles, plusieurs approximations peuvent être faites en décrivant tout d'abord le vent comme étant la somme de composantes géostrophique et agéostrophique. De plus, que le nombre de Rossby (Ro $= U/f_0 L$) soit petit, que les dérivées temporelles soient petites par rapport au terme de Coriolis $f_0$, d'utiliser $f_0$ au lieu de $f$ et enfin que la friction soit petite. En suivant ces conditions il est possible de d'obtenir un nouvel ensemble d'équations à partir des équations sur le plan beta appelées équations quasi-géostrophiques.

$$D_g u_g - f_0 v_a - \beta y v_g = X, \tag{A.7}$$

$$D_g v_g + f_0 u_a + \beta y u_g = Y, \tag{A.8}$$

$$u_{ax} + v_{ay} + \rho_0^{-1} (\rho_0 w_a)_z = 0, \tag{A.9}$$

$$D_g \Theta_e + w_a \Theta_{0z} = Q, \tag{A.10}$$

où

$$D_g = \frac{\partial}{\partial t} + u_g \frac{\partial}{\partial x} + v_g \frac{\partial}{\partial y}$$